



MINISTÉRIO DA CIÊNCIA, TECNOLOGIA, INOVAÇÕES E COMUNICAÇÕES  
**INSTITUTO NACIONAL DE PESQUISAS ESPACIAIS**

sid.inpe.br/mtc-m21b/2017/05.23.23.55-TDI

**ANGLE OF ATTACK EFFECT IN THE  
AEROTHERMODYNAMICS OF A HYPERSONIC  
VEHICLE WITH A SURFACE DISCONTINUITY OF  
GAP TYPE**

Luis Carlos Roldan Torres

Master's Dissertation of the Graduate Course in Engineering and Space Technology, guided by Dr. Wilson Fernando Nogueira dos Santos, approved in March 29, 2017.

URL of the original document:

<<http://urlib.net/8JMKD3MGP3W34P/3NU8MJS>>

INPE  
São José dos Campos  
2017

**PUBLISHED BY:**

Instituto Nacional de Pesquisas Espaciais - INPE

Gabinete do Diretor (GB)

Serviço de Informação e Documentação (SID)

Caixa Postal 515 - CEP 12.245-970

São José dos Campos - SP - Brasil

Tel.:(012) 3208-6923/6921

E-mail: pubtc@inpe.br

**COMMISSION OF BOARD OF PUBLISHING AND PRESERVATION  
OF INPE INTELLECTUAL PRODUCTION (DE/DIR-544):**

**Chairperson:**

Maria do Carmo de Andrade Nono - Conselho de Pós-Graduação (CPG)

**Members:**

Dr. Plínio Carlos Alvalá - Centro de Ciência do Sistema Terrestre (CST)

Dr. André de Castro Milone - Coordenação de Ciências Espaciais e Atmosféricas  
(CEA)

Dra. Carina de Barros Melo - Coordenação de Laboratórios Associados (CTE)

Dr. Evandro Marconi Rocco - Coordenação de Engenharia e Tecnologia Espacial  
(ETE)

Dr. Hermann Johann Heinrich Kux - Coordenação de Observação da Terra (OBT)

Dr. Marley Cavalcante de Lima Moscati - Centro de Previsão de Tempo e Estudos  
Climáticos (CPT)

Silvia Castro Marcelino - Serviço de Informação e Documentação (SID) **DIGITAL  
LIBRARY:**

Dr. Gerald Jean Francis Banon

Clayton Martins Pereira - Serviço de Informação e Documentação (SID)

**DOCUMENT REVIEW:**

Simone Angélica Del Ducca Barbedo - Serviço de Informação e Documentação  
(SID)

Yolanda Ribeiro da Silva Souza - Serviço de Informação e Documentação (SID)

**ELECTRONIC EDITING:**

Marcelo de Castro Pazos - Serviço de Informação e Documentação (SID)

André Luis Dias Fernandes - Serviço de Informação e Documentação (SID)



MINISTÉRIO DA CIÊNCIA, TECNOLOGIA, INOVAÇÕES E COMUNICAÇÕES  
**INSTITUTO NACIONAL DE PESQUISAS ESPACIAIS**

sid.inpe.br/mtc-m21b/2017/05.23.23.55-TDI

**ANGLE OF ATTACK EFFECT IN THE  
AEROTHERMODYNAMICS OF A HYPERSONIC  
VEHICLE WITH A SURFACE DISCONTINUITY OF  
GAP TYPE**

Luis Carlos Roldan Torres

Master's Dissertation of the Graduate Course in Engineering and Space Technology, guided by Dr. Wilson Fernando Nogueira dos Santos, approved in March 29, 2017.

URL of the original document:

<<http://urlib.net/8JMKD3MGP3W34P/3NU8MJS>>

INPE  
São José dos Campos  
2017

Cataloging in Publication Data

---

Torres, Luis Carlos Roldan.

T636a Angle of attack effect in the aerothermodynamics of a hypersonic vehicle with a surface discontinuity of gap type / Luis Carlos Roldan Torres. – São José dos Campos : INPE, 2017. xxviii + 156 p. ; (sid.inpe.br/mtc-m21b/2017/05.23.23.55-TDI)

Dissertation (Master in Engineering and Space Technology) – Instituto Nacional de Pesquisas Espaciais, São José dos Campos, 2017.

Guiding : Dr. Wilson Fernando Nogueira dos Santos.

1. Direct simulation Monte Carlo. 2. Hypersonic flow. 3. Rarefied flow. 4. Gap flow. 5. Hypersonic vehicle. I.Title.

CDU 519.87:629.7.016.55

---



Esta obra foi licenciada sob uma Licença [Creative Commons Atribuição-NãoComercial 3.0 Não Adaptada](https://creativecommons.org/licenses/by-nc/3.0/).

This work is licensed under a [Creative Commons Attribution-NonCommercial 3.0 Unported License](https://creativecommons.org/licenses/by-nc/3.0/).

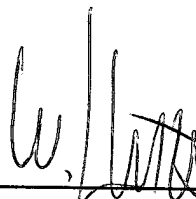
Aluno (a): **Luis Carlos Roldan Torres**

Título: "ANGLE OF ATTACK EFFECT IN THE AEROTHERMODYNAMICS OF A  
HYPERSONIC VEHICLE WITH A SURFACE DISCONTINUITY OF GAP TYPE".

Aprovado (a) pela Banca Examinadora  
em cumprimento ao requisito exigido para  
obtenção do Título de **Mestre** em

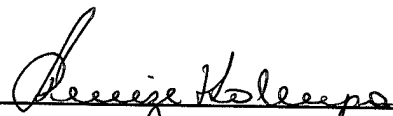
**Engenharia e Tecnologia**  
**Espaciais/Combustão e Propulsão**

Dr. **Wilson Fernando Nogueira dos  
Santos**



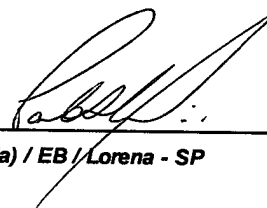
\_\_\_\_\_  
*Presidente / Orientador(a) / INPE / Cachoeira Paulista - SP*

Dra. **Denize Kalempa**



\_\_\_\_\_  
*Membro da Banca / USP / Lorena - SP*

Dr. **Paulo Henrique Mineiro Leite**



\_\_\_\_\_  
*Convidado(a) / EB / Lorena - SP*

*Este trabalho foi aprovado por:*

*maioria simples*

*unanimidade*

**São José dos Campos, 29 de Março de 2017**



*“The most beautiful experience we can have is the mysterious. It is the fundamental emotion that stands at the cradle of true art and true science.”*

ALBERT EINSTEIN



*This work is dedicated to my family **Roldan Torres** and  
**Natalia Botia.***



## ACKNOWLEDGEMENTS

Firstly, to God for the opportunities offered in my life, and for allowing me to finish this stage in my life.

To my parents, Napoleon Roldan and Liliana Torres for their unconditional support throughout in my professional training.

To my advisor, Dr. Wilson F. N. Santos, for the orientation in my Master course, and for the help in the development of this research.

To Natalia Botia, for the support, patience and motivation in each instance these process.

To my friends, Daimer Ospina, Luis Thiago Lucci Correa, Minella Martins, Maycol Vargas, Paulo Henrique Mineiro, families Ospina and Lucci Paolicchi because you were fundamental in this process, as they helped me overcome the obstacles that arose during this research.



## ABSTRACT

The development of hypersonic vehicles has become a topic of interest in recent years, since has made it possible to reach inaccessible places such as orbital flights. The construction of these vehicles must be made with specials materials, and must have an efficient aerodynamic shape to withstand high speeds, high temperatures and significant pressure changes. The study described in this dissertation was undertaken with the objective to investigate the impact of discontinuities present on the surface of hypersonic space vehicles. In pursuit of this goal, computational simulations of a low-density hypersonic flow over a flat plate with a gap has been performed by using the Direct Simulation Monte Carlo method. The simulations provided information about the nature of the flowfield structure and the aerodynamic surface properties on the gap resulting from variations in the length-to-depth ( $L/H$ ) ratio and variations in the angle of attack. A description of the flowfield properties, such as velocity, density, pressure and temperature, and aerodynamics surface quantities, such as, number flux, heat transfer, pressure and skin friction, were obtained by a numerical method that properly account for non-equilibrium effects in the transition flow regime. Results for a gap defined by  $L/H$  ratio of 1, 1/2, 1/3 and 1/4, and flow with angle of attack of 10, 15 and 20 degrees, were compared to those of a flat plate without a gap with zero-degree angle of incidence. The analysis showed that the flow topology inside the gap with incidence is slightly different from that for zero-degree angle of incidence for the  $L/H$  ratio investigated. It was found that the maximum values for the heat transfer, pressure and skin friction coefficients inside the gap took place on the gap forward face. It was also found that, maximum values for heat transfer coefficient inside the gaps increased with increasing the angle of attack  $\alpha$ . Nevertheless, it was observed that these maximum values are smaller than those observed in a flat-plate without a gap for the corresponding angle of attack. As a result, in terms of pressure, the presence of the gap on the vehicle surface can not be ignored in the vehicle design.

Keywords: Direct Simulation Monte Carlo. Hypersonic Flow. Rarefied Flow. Gap Flow. Hypersonic Vehicle.



# EFEITO DO ÂNGULO DE ATAQUE NA AEROTERMODINÂMICA DE UM VEÍCULO HIPERSÔNICO COM DESCONTINUIDADE NA SUPERFÍCIE DO TIPO FILETE.

## RESUMO

O desenvolvimento de veículos hipersônicos tem se tornado um tema de interesse nos últimos anos, considerando-se a possibilidade de se chegar com tais veículos a locais até então inacessíveis como os voos orbitais. A construção desses veículos exige materiais especiais e deve apresentar uma forma aerodinâmica eficiente para resistir altas velocidades além de temperaturas elevadas e mudanças de pressão significativas. O estudo descrito nesta dissertação foi realizado com o objetivo de investigar o impacto de descontinuidades presentes na superfície de veículos espaciais hipersônicos. Em busca deste objetivo, simulações computacionais de um escoamento hipersônico rarefeito sobre uma placa plana, foi realizada usando-se o método Direct Simulation Monte Carlo. As simulações forneceram informações sobre a natureza da estrutura do escoamento, propriedades primárias e propriedades aerodinâmicas, devido a variações na razão comprimento-profundidade ( $L/H$ ), e variações no ângulo de ataque. Uma descrição das propriedades primárias, tais como velocidade, massa específica, pressão e temperatura, e das quantidades aerodinâmica, tais como transferência de calor, pressão e atrito na superfície, foi obtida por um método numérico que leva em conta os efeitos de não-equilíbrio no regime de transição. Os resultados para um filete definido por uma razão  $L/H$  de 1,  $1/2$ ,  $1/3$  e  $1/4$ , e com ângulo de ataque do escoamento de 10, 15 e 20 graus, foram comparados com os de uma placa plana sem a presença de um filete. A análise mostrou que a estrutura do escoamento dentro do filete com ângulo de ataque é ligeiramente diferente daquela com zero grau de incidência para cada razão  $L/H$  investigada. Verificou-se que os valores máximos para os coeficientes de transferência de calor, pressão e coeficiente de atrito ocorreram na superfície a montante do escoamento dentro do filete. Verificou-se também que, os valores máximos para o coeficiente de transferência de calor dentro do filete aumentaram com o aumento do ângulo de ataque  $\alpha$ . Como resultado, em termos de pressão, a presença do filete sobre a superfície do veículo não pode ser ignorada no projeto do veículo.

Palavras-chave: Direct Simulation Monte Carlo. Escoamento hipersônicos. Escoamento rarefeito. Filete. Veículos hipersônicos.



## LIST OF FIGURES

	<u>Page</u>
1.1 Drawing illustrating the Thermal Protection System of the Space Shuttle orbiter. . . . .	2
1.2 (a) TPS of Space Shuttle Endeavour in orbit,(b) TPS of Space Shuttle Endeavour after the reentry in the Earth . . . . .	3
1.3 Flow regimes as a function of the Knudsen number. . . . .	6
1.4 Drawing illustrating the flowfield structure inside a gap. . . . .	10
1.5 Streamline traces inside the gaps for $L/H$ of 1, 1/2, 1/3, 1/4. $Y$ is the depth $H$ of the gap normalized by the freestream mean free path $\lambda_\infty$ . . .	11
2.1 Validity of the conventional mathematical models as function of local Knudsen number. . . . .	14
2.2 Flowchart of DSMC Method. . . . .	19
2.3 Typical intermolecular force field. . . . .	21
2.4 Schematic of the binary collisions. (a) Representation of a planar collision. (b) Binary collision in the center of mass frame of reference, and (c) Interaction of reduced mass particle with a fixed scattering center. . .	32
2.5 Drawing illustrating the Maxwell reflection model and CLL reflection model. . . . .	39
3.1 Drawing illustrating the gap configuration. . . . .	43
3.2 Drawing illustrating the computational domain. . . . .	46
4.1 Drawing illustrating the flat-plate computational domain. . . . .	55
4.2 Effect of altering the cell size in $x$ -direction on pressure (top), skin friction (middle) and heat transfer (bottom) coefficients. . . . .	58
4.3 Effect of altering the cell size in $y$ -direction on pressure (top), skin friction (middle) and heat transfer (bottom) coefficients. . . . .	59
4.4 Effect of altering the number of simulated particles on pressure (top), skin friction (middle) and heat transfer (bottom) coefficients. . . . .	60
4.5 Effect of altering the length of the flat-plate on pressure (top), skin friction (middle) and heat transfer (bottom) coefficients. . . . .	61
4.6 Density ratio ( $\rho/\rho_\infty$ ) profile at section $x/L = 1.5$ along the flat plate surface. . . . .	63
4.7 Wall pressure ( $p_w/p_\infty$ ) distribution along the flat plate surface. . . . .	64
4.8 Translational ( $T_T/T_\infty$ ) and rotational ( $T_R/T_\infty$ ) temperature distribution along the flat plate surface. . . . .	65

4.9	Density ratio ( $\rho/\rho_\infty$ ) profiles normal to the plate surface for three locations along the plate surface. . . . .	66
4.11	Tangential velocity ratio ( $u/U_\infty \cos\alpha$ ) profiles normal to the plate surface for three locations along the plate surface. . . . .	66
4.10	Overall kinetic temperature ratio ( $T_O/T_\infty$ ) profiles normal to the plate surface for three locations along the plate surface. . . . .	67
4.12	Effect of variation in the cell size in the $x$ -direction in pressure coefficient for $L/H = 1$ case. . . . .	70
4.13	Effect of variation in the cell size in the $x$ -direction in skin friction coefficient for $L/H = 1$ case. . . . .	71
4.14	Effect of variation in the cell size in the $x$ -direction in heat transfer coefficient for $L/H = 1$ case. . . . .	72
4.15	Effect of variation in the cell size in the $y$ -direction in pressure coefficient for $L/H = 1$ case. . . . .	73
4.16	Effect of variation in the cell size in the $y$ -direction in skin friction coefficient for $L/H = 1$ case. . . . .	74
4.17	Effect of variation in the cell size in the $y$ -direction in heat transfer coefficient for $L/H = 1$ case. . . . .	75
4.18	Effect of variation in the number of molecules in pressure coefficient for $L/H = 1$ . . . . .	76
4.19	Effect of variation in the number of molecules in skin friction coefficient for $L/H = 1$ . . . . .	77
4.20	Effect of variation in the number of molecules in heat transfer coefficient for $L/H = 1$ . . . . .	78
4.21	A Drawing illustrating the cell distribution for (a) the standard mesh for the gap configuration with $L/H = 1$ and 10-degree angle of attack, and (b) a magnified view of region R5. . . . .	79
5.1	Tangential velocity ratio ( $u/U_\infty$ ) profiles for two sections outside the gaps and for angle of attack $\alpha$ of 10, 15 and 20 degrees, parameterized by the gap $L/H$ ratio. . . . .	83
5.2	Tangential velocity ratio ( $u/(U_\infty \cos\alpha)$ ) profiles for two sections outside the gaps and for $L/H$ ratio of 1, 1/2, and 1/4, parameterized by the angle of attack $\alpha$ . . . . .	84
5.3	Tangential velocity ratio ( $u/U_\infty$ ) profiles for three sections inside the gaps as a function of the dimensionless height $Y_H$ , parameterized by the gap $L/H$ ratio. Left- and right-column plots correspond to angle of attack $\alpha$ of 10 and 20 degrees, respectively. . . . .	86

5.4	Tangential velocity ratio ( $u/U_\infty$ ) profiles for three sections inside the gaps as a function of the dimensionless height $Y_H$ , parameterized by the angle of attack $\alpha$ . Left- and right-column plots correspond to gap $L/H$ ratio of 1 and 1/2, respectively. . . . .	87
5.5	Tangential velocity ratio ( $u/U_\infty$ ) profiles for three sections inside the gaps as a function of the dimensionless height $Y_H$ , parameterized by the angle of attack $\alpha$ . Left- and right-column plots correspond to gap $L/H$ ratio of 1/3 and 1/4, respectively. . . . .	88
5.6	Normal velocity ratio ( $v/U_\infty$ ) profiles for three transverse sections inside the gaps as a function of the dimensionless length $X'_L$ , parameterized by the gap $L/H$ ratio. Left- and right-column plots correspond to angle of attack $\alpha$ of 10 and 20 degrees, respectively. . . . .	89
5.7	Normal velocity ratio ( $v/U_\infty$ ) profiles for three transverse sections inside the gaps as a function of the dimensionless length $X'_L$ , parameterized by the angle of attack $\alpha$ . Left- and right-column plots correspond to gap $L/H$ ratio of 1 and 1/2, respectively. . . . .	91
5.8	Normal velocity ratio ( $v/U_\infty$ ) profiles for three transverse sections inside the gaps as a function of the dimensionless length $X'_L$ , parameterized by the angle of attack $\alpha$ . Left- and right-column plots correspond to gap $L/H$ ratio of 1/3 and 1/4, respectively. . . . .	92
5.9	Distribution of streamline traces inside the gaps for $L/H$ of 1 (left), 1/2, 1/3, and 1/4 (right), with angle attack $\alpha$ of 10 (top), 15, and 20 (bottom) degrees. . . . .	93
5.10	Density ratio ( $\rho/\rho_\infty$ ) profiles for two sections outside the gaps and for angle of attack $\alpha$ of 10, 15 and 20 degrees, parameterized by the gap $L/H$ ratio. . . . .	95
5.11	Density ratio ( $\rho/\rho_\infty$ ) profiles for two sections outside the gaps and for $L/H$ ratio of 1, 1/2, and 1/4, parameterized by the angle of attack $\alpha$ . . . . .	96
5.12	Density ratio ( $\rho/\rho_\infty$ ) profiles for three sections inside the gaps as a function of the dimensionless height $Y_H$ , parameterized by the gap $L/H$ ratio. Left- and right-column plots correspond to angle of attack $\alpha$ of 10 and 20 degrees, respectively. . . . .	98
5.13	Density ratio ( $\rho/\rho_\infty$ ) profiles for three sections inside the gaps as a function of the dimensionless height $Y_H$ , parameterized by the angle of attack $\alpha$ . Left- and right-column plots correspond to gap $L/H$ ratio of 1 and 1/2, respectively. . . . .	99

5.14	Density ratio ( $\rho/\rho_\infty$ ) profiles for three sections inside the gaps as a function of the dimensionless height $Y_H$ , parameterized by the angle of attack $\alpha$ . Left- and right-column plots correspond to gap $L/H$ ratio of 1/3 and 1/4, respectively. . . . .	100
5.15	Distribution of density ratio ( $\rho/\rho_\infty$ ) along with streamline traces inside the gaps for $L/H$ ratio of 1 (left), 1/2, 1/3 and 1/4 (right), with angle attack $\alpha$ of 10 (top), 15, and 20 degrees (bottom). . . . .	101
5.16	Pressure ratio ( $p/p_\infty$ ) profiles for two sections outside the gaps and for angle of attack $\alpha$ of 10, 15 and 20 degrees, parameterized by the gap $L/H$ ratio. . . . .	103
5.17	Pressure ratio ( $p/p_\infty$ ) profiles for two sections outside the gaps and for $L/H$ ratio of 1, 1/2, and 1/4, parameterized by the angle of attack $\alpha$ . . . . .	104
5.18	Pressure ratio ( $p/p_\infty$ ) profiles for three sections inside the gaps as a function of the dimensionless height $Y_H$ , parameterized by the gap $L/H$ ratio. Left- and right-column plots correspond to angle of attack $\alpha$ of 10 and 20 degrees, respectively. . . . .	105
5.19	Pressure ratio ( $p/p_\infty$ ) profiles for three sections inside the gaps as a function of the dimensionless height $Y_H$ , parameterized by the angle of attack $\alpha$ . Left- and right-column plots correspond to gap $L/H$ ratio of 1 and 1/2, respectively. . . . .	107
5.20	Pressure ratio ( $p/p_\infty$ ) profiles for three sections inside the gaps as a function of the dimensionless height $Y_H$ , parameterized by the angle of attack $\alpha$ . Left- and right-column plots correspond to gap $L/H$ ratio of 1/3 and 1/4, respectively. . . . .	108
5.21	Distribution of pressure ratio ( $p/p_\infty$ ) along with streamline traces inside the gaps for $L/H$ ratio of 1 (left), 1/2, 1/3 and 1/4 (right), with angle attack $\alpha$ of 10 (top), 15, and 20 degrees (bottom). . . . .	109
5.22	Kinetic temperature ratio ( $T/T_\infty$ ) profiles for two sections outside the gaps and for angle of attack $\alpha$ of 10, 15 and 20 degrees, parameterized by the gap $L/H$ ratio. . . . .	113
5.23	Comparison of the kinetic temperature ratio ( $T/T_\infty$ ) profiles for the gap $L/H$ ratio of 1 and the flat-plate at two sections outside the gap for angle of attack $\alpha$ of 10, 15 and 20 degrees. . . . .	114
5.24	Kinetic temperature ratio ( $T/T_\infty$ ) profiles for three sections inside the gaps as a function of the dimensionless height $Y_H$ , parameterized by the gap $L/H$ ratio. Left- and right-column plots correspond to angle of attack of 10 and 20 degrees, respectively. . . . .	115

5.25	Distribution of overall temperature ratio ( $T_O/T_\infty$ ) along with streamline traces inside the gaps for $L/H$ ratio of 1 (left), 1/2, 1/3 and 1/4 (right), with angle attack $\alpha$ of 10 (top), 15, and 20 degrees (bottom). . . . .	116
5.26	Dimensionless number flux ( $N_f$ ) distribution along the gap surfaces parameterized by the gap $L/H$ ratio for 10-degree angle of attack. . . . .	119
5.27	Dimensionless number flux ( $N_f$ ) distribution along the gap surfaces parameterized by the gap $L/H$ ratio for 20-degree angle of attack. . . . .	120
5.28	Dimensionless number flux ( $N_f$ ) distribution along the gap surfaces parameterized by the angle of attack $\alpha$ for gap $L/H$ ratio of 1. . . . .	121
5.29	Dimensionless number flux ( $N_f$ ) distribution along the gap surfaces parameterized by the angle of attack $\alpha$ for gap $L/H$ ratio of 1/4. . . . .	122
5.30	Pressure coefficient ( $C_p$ ) distribution along the gap surfaces parameterized by the gap $L/H$ ratio for 10-degree angle of attack. . . . .	125
5.31	Pressure coefficient ( $C_p$ ) distribution along the gap surfaces parameterized by the gap $L/H$ ratio for 20-degree angle of attack. . . . .	126
5.32	Pressure coefficient ( $C_p$ ) distribution along the gap surfaces parameterized by the angle of attack $\alpha$ for gap $L/H$ ratio of 1. . . . .	127
5.33	Pressure coefficient ( $C_p$ ) distribution along the gap surfaces parameterized by the angle of attack $\alpha$ for gap $L/H$ ratio of 1/4. . . . .	128
5.34	Skin friction coefficient ( $C_f$ ) distribution along the gap surfaces parameterized by the gap $L/H$ ratio for 10-degree angle of attack. . . . .	131
5.35	Skin friction coefficient ( $C_f$ ) distribution along the gap surfaces parameterized by the gap $L/H$ ratio for 20-degree angle of attack. . . . .	132
5.36	Skin friction coefficient ( $C_f$ ) distribution along the gap surfaces parameterized by the angle of attack $\alpha$ for gap $L/H$ ratio of 1. . . . .	133
5.37	Skin friction coefficient ( $C_f$ ) distribution along the gap surfaces parameterized by the angle of attack $\alpha$ for gap $L/H$ ratio of 1/4. . . . .	134
5.38	Heat transfer coefficient ( $C_h$ ) distribution along the gap surfaces parameterized by the gap $L/H$ ratio for 10-degree angle of attack. . . . .	137
5.39	Heat transfer coefficient ( $C_h$ ) distribution along the gap surfaces parameterized by the gap $L/H$ ratio for 20-degree angle of attack. . . . .	138
5.40	Heat transfer coefficient ( $C_h$ ) distribution along the gap surfaces parameterized by the angle of attack $\alpha$ for gap $L/H$ ratio of 1. . . . .	139
5.41	Heat transfer coefficient ( $C_h$ ) distribution along the gap surfaces parameterized by the angle of attack $\alpha$ for gap $L/H$ ratio of 1/4. . . . .	140



## LIST OF TABLES

	<u>Page</u>
3.1 Geometric characteristics for the gaps. . . . .	44
3.2 Working fluid properties for DSMC simulations. . . . .	45
3.3 Freestream flow conditions. . . . .	47
4.1 Freestream flow conditions . . . . .	53
4.2 Freestream flow conditions . . . . .	54
4.3 Number of cells in the ( $x$ -direction) and [ $y$ -direction] for the flat-plate case. . . . .	56
4.4 Number of cells in the ( $x$ -direction) and [ $y$ -direction] for the gap case of the $L/H = 1$ and 10-degree angle of attack. . . . .	69



# NOMENCLATURE

$a$	Speed of sound $m/s$
$A$	Area, $m^2$
$C_f$	Skin friction coefficient, $\tau_w/(\frac{1}{2}\rho_\infty U_\infty^2)$
$C_h$	Heat transfer coefficient, $q_w/(\frac{1}{2}\rho_\infty U_\infty^3)$
$C_p$	Pressure coefficient, $(p_w - p_\infty)/(\frac{1}{2}\rho_\infty U_\infty^2)$
$\mathbf{c}$	Molecular velocity vector, $m/s$
$\mathbf{c}'$	Thermal molecular velocity, $m/s$
$e$	Specific molecular energy, $J/kg$
$d$	Molecular diameter, $m$
$D$	Diffusion coefficient, $m^2/s$
$F$	Force, $N$
$F_n$	Intermolecular force potential
$F_N$	Number of real molecules represented by a single simulated molecule
$H$	Gap depth, $m$
$k$	Molecular characteristic constant; Boltzmann constant, $1.3806488 \times 10^{-23} J_s$
$Kn$	Knudsen number, $\lambda/L$
$L$	Characteristic length scale, Gap length, $m$
$l$	Characteristic length scale, $m$
$M$	Mach number, $ v /a$
$m$	Molecular mass, $kg$
$n$	Number density, $m^{-3}$
$N$	Number of particles
$N_{coll}$	Number of collisions
$N_f$	Dimensionless number flux
$p$	Pressure, $N/m^2$
$P$	A probability
$q$	Heat flux, $W/m^2$
$Re$	Reynolds number, $(\rho_\infty U_\infty l)/\mu_\infty$
$r$	Position vector; Intermolecular separation, $m$
$R$	Ordinary gas constant, $J/Kmol$
$R_F$	Random number between 0 and 1
$t$	Time, $s$
$T$	Temperature, $K$
$u$	Tangential velocity, $m/s$
$V_C$	Cell volume, $m^3$

$v$	Normal velocity, $m/s$
$X$	Dimensionless length, $x/\lambda_\infty$
$X'_L$	Dimensionless length, $(x - L_u)/L$
$Y$	Dimensionless height, $y/\lambda_\infty$
$Y_H$	Dimensionless height, $y/H$
$Z$	Relaxation collision number

## GREEK SYMBOLS

$\alpha$	Accommodation coefficient; Angle of attack, degree
$\Delta$	Increment
$\delta t$	Time counter
$\eta$	Molecular characteristic constant; Power law
$\lambda$	Mean free path, $m$
$\mu$	Viscosity coefficient, $kg/m.s$
$\omega$	Viscosity-temperature index
$\phi$	Potential energy of interaction; Average probability
$\varphi$	Gas property
$\rho$	Gas density, $kg/m^3$
$\sigma$	Collision cross-section, $m$
$\sigma_T$	Total collision cross-section
$\tau$	Relaxation time, $s$ ; Shear stress, $N/m^2$
$\tau_c$	Mean collision time, $s$
$\Theta$	Characteristic temperature, $K$
$\zeta$	Number of degrees of freedom

## SUBSCRIPTS AND SUPERSCRIPTS

$d$	Refers to downstream
$H$	Refers to gap depth
$i$	Refers to incident
$L$	Refers to gap length
$m$	Refers to center of mass
$n$	Refers to normal
$O$	Refers to overall
$r$	Refers to rotational; reduced; relative; Reflect
$ref$	Refers to reference values

$t$	Refers to translational
$u$	Refers to upstream
$v$	Refers to vibrational
$w$	Refers to wall conditions
$x, y, z$	Refers to x-,y-, and z- cartesian axes
1, 2	Refers to species
$\infty$	Refers to the freestream
*	Refers to post-collision



# CONTENTS

	<u>Page</u>
<b>1 INTRODUCTION</b> . . . . .	<b>1</b>
1.1 Motivation . . . . .	1
1.2 Reentry Flow Regimes . . . . .	4
1.3 Previous Work . . . . .	7
1.4 Problem Definition and Scope of Current Work . . . . .	11
<b>2 COMPUTATIONAL METHOD</b> . . . . .	<b>13</b>
2.1 Methods for Modeling Transition Flows . . . . .	13
2.2 Direct Simulation Monte Carlo (DSMC) Method . . . . .	16
2.2.1 DSMC Methodology . . . . .	18
2.2.2 Molecular Model . . . . .	20
2.2.2.1 Variable Hard-Sphere (VHS) model . . . . .	22
2.2.3 Collision Models . . . . .	26
2.2.4 Binary Elastic Collisions . . . . .	28
2.2.5 Internal Degrees-of-Freedom . . . . .	31
2.2.6 Relaxation Rate . . . . .	33
2.2.6.1 Rotational Relaxation Rate . . . . .	34
2.2.6.2 Vibrational Relaxation Rate . . . . .	35
2.2.7 Boundary Conditions . . . . .	38
<b>3 COMPUTATIONAL PROCEDURE</b> . . . . .	<b>43</b>
3.1 Geometry Definition . . . . .	43
3.2 Numerical Simulation Conditions . . . . .	44
3.3 Freestream and Flow Conditions . . . . .	47
<b>4 VERIFICATION AND VALIDATION PROCESS</b> . . . . .	<b>49</b>
4.1 Computational Requirements . . . . .	49
4.2 Computational Mesh Generation . . . . .	51
4.3 Computational Mesh Adaption . . . . .	51
4.4 DSMC Test Case . . . . .	52
4.4.1 Effect of Mesh Resolution . . . . .	55
4.4.2 Effect of Variation on the Number of Simulated Particles . . . . .	57
4.4.3 Effect of Downstream Boundary Condition . . . . .	57

4.5	Experimental and Numerical Comparisons . . . . .	57
4.5.1	First Test Case . . . . .	62
4.5.2	Second Test Case . . . . .	64
4.6	Gap Case . . . . .	67
<b>5</b>	<b>COMPUTATIONAL RESULTS AND DISCUSSION . . . . .</b>	<b>81</b>
5.1	Flowfield Structure . . . . .	81
5.1.1	Velocity Field . . . . .	81
5.1.2	Density Field . . . . .	94
5.1.3	Pressure Field . . . . .	102
5.1.4	Kinetic Temperature Field . . . . .	110
5.2	Aerodynamic Surface Quantities . . . . .	117
5.2.1	Number Flux . . . . .	117
5.2.2	Pressure Coefficient . . . . .	123
5.2.3	Skin Friction Coefficient . . . . .	129
5.2.4	Heat Transfer Coefficient . . . . .	135
<b>6</b>	<b>CONCLUSIONS . . . . .</b>	<b>143</b>
6.1	Concluding Remarks . . . . .	143
6.2	Future Work . . . . .	144
	<b>REFERENCES . . . . .</b>	<b>145</b>

# 1 INTRODUCTION

## 1.1 Motivation

Development of hypersonic flight vehicles is a current topic of interest for scientific, military, and commercial applications. The study of these vehicles has been of great interest to science because high velocity is necessary to achieve rapid access to space and rapid global reach. The design of hypersonic vehicles requires accurate prediction of the flowfield structure and surface properties, such as heat flux, shear stress, and pressure, along the entire vehicle surface and throughout all possible flight trajectories. These quantities determine not only the aerodynamic performance of each vehicle, which is necessary for guidance, navigation, and control, but also the thermodynamic performance, which determines the type and sizing of the Thermal Protection System (TPS) that is required to guarantee that the vehicle survives the intense heat transfer from the surrounding flow.

An important issue for the design and development of hypersonic vehicles is the effect of various flow phenomena on aerodynamic performance and aeroheating characteristics. Of particular concern are separated and/or reattached flows, which can occur in a variety of ways. Separated flows increase pressure losses and also increase heat transfer in the region near separation and reattachment.

Discontinuities present on the surface of hypersonic vehicles, such as protuberances, notches, steps, cavities or gaps, may generate separated and/or reattached flows. The presence of these discontinuities in hypersonic configurations may occur as a desired or undesired design feature. For instance, the TPS on the windward side of the Space Shuttle Orbiter consists of many ceramic tiles, as illustrated in Figure 1.1. The tiles are arranged with small gaps between the tiles to accommodate thermal expansion and deflection of the primary structure. Tile arrays are oriented to minimize the ingress of hot boundary-layer gases into the tile gaps. The hot boundary-layer gases penetrate into the gaps between the tiles and produce high local heating levels, which may result in tile degradation or excessive structural temperatures.

It is usually accepted without question that reentry hypersonic vehicles, such as the Space Shuttle Orbiter, are exposed to extreme flight conditions with heavy thermal and mechanical loads acting on the surface of the vehicles during their mission. Unfortunately, the accident of the Space Shuttle Orbiter Columbia, during its reentry from orbit on February 1, 2003, has been a reminder of how severe the aerothermodynamic environment is for a vehicle traveling at hypersonic speeds.

Figure 1.1 - Drawing illustrating the Thermal Protection System of the Space Shuttle orbiter.



(a) Windward side of the Space Shuttle Orbiter



(b) Ceramic tiles

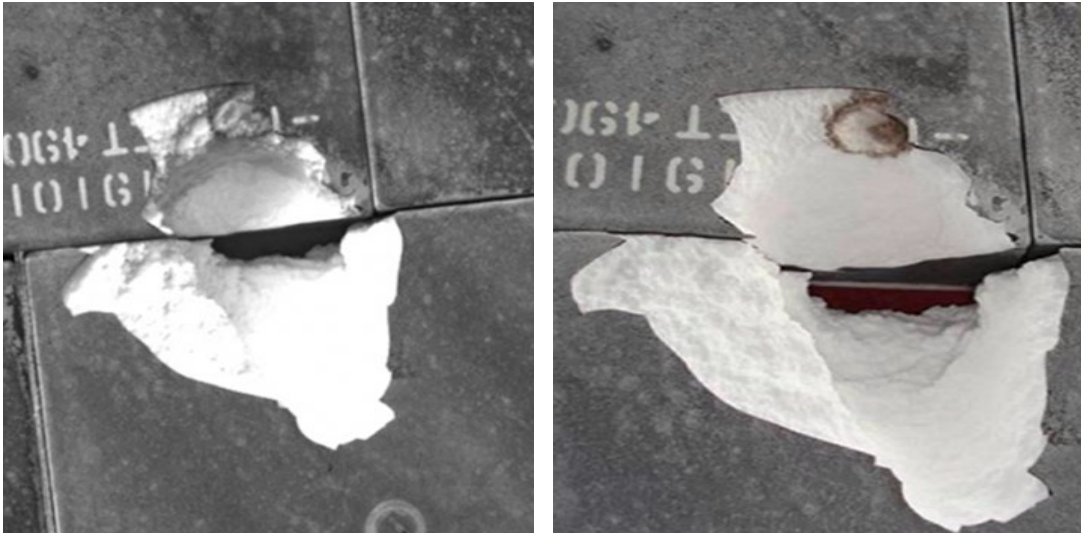


(c) A single tile

SOURCE: (ATKINSON, 2015).

According to the final report of the Columbia Accident Investigation Board (CAIB), a piece of insulating foam produced a breach in the TPS of the leading edge of the left wing. It is believed that this small breach in the TPS provided a path for the hot gases, which reached the interior of the left wing during the severe aerothermodynamic environment in the reentry trajectory of the Columbia during its mission STS-107 (BERTIN; CUMMINGS, 2006).

Figure 1.2 - (a) TPS of Space Shuttle Endeavour in orbit,(b) TPS of Space Shuttle Endeavour after the reentry in the Earth



SOURCE: PALMER et al. (2009).

Four years later, a similar situation occurred with the Space Shuttle Endeavour in its mission to the International Space Station (ISS). During its mission STS-118 in August 2007 (PALMER et al., 2009), a piece of foam insulation was released from the external tank of the Space Shuttle Endeavour. The impact of the foam in the TPS tile caused a defect, such as a cavity, 8.9 cm long and 5.1 cm wide, designated as damage site D-118, as illustrated in Fig. 1.2 (a). The photograph shown in Fig. 1.2 (a) was produced during the damage site inspection performed when the Orbiter Endeavour was docked to the ISS. A group of analysts, scientists from the NASA Ames and NASA Langley Research Centers, known as the Damage Assessment Team (DAT), performed Computational Fluid Dynamic (CFD) simulations in order to provide insight into the flow structures and flow physics in the interior of the cavity. Based on the detailed CFD solutions generated by the DAT, it was decided not to perform a spacewalk to repair the damage site but rather to fly Space Shuttle Endeavour back to Earth with the damage site. Fortunately, the Space Shuttle Endeavour successfully reentered the Earth's atmosphere and landed on August 21, 2007. The final condition of the piece of insulation, after the reentry phase, is shown in Fig. 1.2 (b).

As indeed is clear from these two examples, the investigation of discontinuities or

imperfections on the surface of hypersonic vehicles becomes imperative. Hypersonic flow past a gap or cavity is a challenging problem due to complex flow characteristics, such as hypersonic flow separation and reattachment. The presence of flow separation is important for the heat transfer problem since the aerodynamic heat load varies spatially as the flow passes over the damaged tile represented by a gap or cavity. In addition, the effects on the flowfield due to these changes in the surface slope depend on its geometry, on its dimensions relative to the boundary-layer thickness, as well as on the characteristics of the boundary layer.

## 1.2 Reentry Flow Regimes

Launch, cruise and entry vehicles are three major types of vehicles that cross the atmosphere. High lift-to-drag ratio, therefore efficient aerodynamics, becomes imperative for launch and cruise vehicles. Conversely, high drag for optimum aerobraking at higher altitudes is desirable for entry vehicles. In addition, vehicles that return to the atmosphere that they came from are defined as reentry vehicles.

Hypersonic flows around spatial vehicles during their reentry phase in planetary atmosphere are characterized by intense aerothermal phenomena. The prediction of aerodynamic heating of a spacecraft during the descent phase into Earth's atmosphere is essential for a successful space mission and a safe return.

During the descent phase, important physical interactions arise between the vehicle and the environment around the space vehicle. At the highest altitudes, the interaction of the vehicle with the atmospheric air is characterized by the free molecular flow. In this regime, the molecules of the environment collide with the vehicle surface, interact with the surface and are reflected from the surface. However, collisions of reflected molecules with incoming molecules from the freestream are not frequently in this flow regime. Consequently, they are ignored.

As the space vehicle enters a little deeper into the dense atmosphere, the mean free path between incoming atmosphere molecules decreases, and collisions between molecules reflected from the vehicle surface and the molecules incoming from the freestream can no longer be ignored. As a result, the flow in this condition defines the transition flow regime, i.e., transition between the collisionless flow regime and the continuum flow regime. In the transition flow regime, the contribution of aerodynamic forces and heat flux to the vehicle surface start increasing rapidly with decreasing altitude, causing large changes in the aerodynamic characteristics of the vehicle when compared with those observed in the free molecular flow.

As the space vehicle continues to enter into the atmosphere, it finally reaches the continuum flow regime. In this regime, the flow around the space vehicle is treated by a macroscopic model that considers the air as a continuum, and the description of the flow is made in terms of spatial and temporal variations of the primary properties, such as velocity, pressure, density and temperature.

In order to define quantitative limits for each flow regime, the degree of rarefaction of a flow is expressed by a dimensionless parameter named Knudsen number,  $Kn$ , defined as:

$$Kn = \frac{\lambda}{l} \quad (1.1)$$

where  $\lambda$  is the molecular mean free path and  $l$  is a characteristic length.

The mean free path  $\lambda$  is the distance traveled by molecules between collisions. For a gas in thermodynamic equilibrium, it depends on the number density of the gas,  $n$ , which varies with the altitude of the reentry vehicle, and with the diameter  $d$  of the gas molecule according to the following equation:

$$\lambda = \frac{1}{\sqrt{2}\pi d^2 n} \quad (1.2)$$

Also of great significance is the characteristic length  $l$ . At first, one might be tempted to select the characteristic length scale as some overall flow dimension in order to determine an overall Knudsen number. However, a better description is possible if a local Knudsen number is defined with  $l$  as the gradient length scale of a macroscopic quantity  $\phi$  given by:

$$l = \frac{\phi}{|\nabla\phi|} \quad (1.3)$$

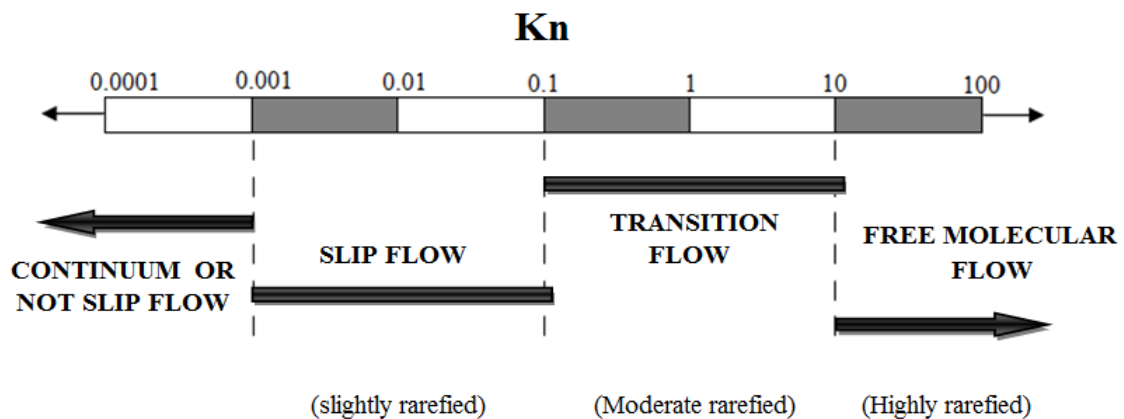
where  $\phi$  may represent the local velocity, density, pressure or temperature.

This equation shows that small values of  $l$  can be obtained by strong gradients in the flow. Consequently, the local Knudsen number is defined by the ratio of the local  $\lambda$  to the local  $l$ . Therefore, it is evident that in a steady state flow  $Kn$  may change spatially and also according to the macroscopic property considered.

A flow is defined in the continuum flow regime when the Knudsen number tends to zero. In this situation, molecules are considered to be so densely packed that the mean free path is insignificant compared with the flow dimensions. On the other hand, a flow is defined in the free molecular flow as the Knudsen number goes to infinity.

For completeness, the classification of flow regimes as a function of the overall Knudsen number is illustrated in Fig. 1.3. This subdivision is desirable because the four flow regimes exhibit quite different phenomena, and the basic theoretical approaches are entirely different. According to Fig. 1.3, the Knudsen number range,  $0.001 < Kn < 0.1$ , is defined as the slip flow regime. The name derived from the fact that under these conditions, the gas layer immediately adjacent to the vehicle surface does not adhere to the surface, but slips along with a velocity proportional to the mean free path (McCARTY, 1969).

Figure 1.3 - Flow regimes as a function of the Knudsen number.



SOURCE: GAD-EL-HAK (1999).

Techniques used to analyze the flowfield structure of a hypersonic flow around reentry vehicles depend to a considerable degree on the shape of the vehicle and on a predicted atmospheric trajectory. As a result, several regimes may be required to define the flow structure for a given flight conditions. For flows around reentry space vehicles in the range from 120 to 60 *km* of altitude, the molecular mean free path  $\lambda$  may be of the order of a dimension of gaps, cavities, or steps related to a

discontinuity on the vehicles surfaces. Consequently, the Knudsen number, which indicates the degree of flow rarefaction, may be in the range of the transition flow regime, i.e., between the continuum regime and the collisionless regime.

As an illustrative example, the depth  $H$  or length  $L$  for gaps or cavities, which represent a discontinuity on the vehicle surface, is usually on the order of 3 to 6  $mm$  (WEINSTEIN et al., 1975; GAI; MILTHORPE, 1995; EVERHART et al., 2006). In addition, for 90, 80, 70 and 60  $km$  of altitude, the molecular mean free path  $\lambda$  is 26.03, 4.11, 0.929 and 0.265  $mm$ , respectively. As a result, for  $H$  (or  $L$ ) of 3  $mm$ , the overall Knudsen number is the order of 8.67, 1.37, 0.31 and 0.088, for altitudes of 90, 80, 70 and 60  $km$ , respectively. By considering  $H$  (or  $L$ ) of 6  $mm$ , the overall Knudsen number is reduced by half. In this manner, the overall Knudsen number is in the transition flow regime, usually defined by the range  $0.1 < Kn < 10$ , as shown in Fig. 1.3. Under the aforementioned assumptions, in the transition flow regime, the concepts of the continuum hypothesis can not be applied, and the molecular structure of the gas must be considered.

### 1.3 Previous Work

In aerospace engineering applications, surface discontinuity arises as design features in modern aerodynamic configurations. According to the current literature, a considerable amount of attention has been given to surface discontinuity on aerospace vehicle in the last decades. The extensive literature on this subject – mostly, but not entirely, experimental studies – is devoted primarily to investigate the impact of surface discontinuities on the flowfield structure of aerospace vehicles, among others, such as, distortions (BERTRAM; WIGGS, 1963; BERTRAN et al., 1967), protuberances (MAZAHERI; WOOD, 2009), gaps (WEI et al., 2006; JACKSON et al., 1999; CATLETT, 2010; LIN et al., 2011; BREWER et al., 1973; BERTIN; KEISNER, 1978; WEINSTEIN et al., 1975; NARIS; VALOUGEORGIS, 2005; HAO et al., 2013; DUNAVANT; THROCKMORTON, 1974; WEINSTEIN et al., 1975; SCOTT; MARAIA, 1979; HINDERKS et al., 2004; TRAINEAU et al., 2005; HINDERSKS; RADESPIEL, 2006; PATIL et al., 2006; XU et al., 2015), cavities (OHMACHI; SUZUKI, 2011; NICOLL, 1964; ESTEVE et al., 2000; ATVARS et al., 2009; ZDANSKI et al., 2006), or step (BOGDONOFF; KEPLER, 1955; GADD, 1957; ROM; SEGNER, 1964; NESTLER et al., 1969; JAKUBOWSKI; LEWIS, 1973; PULLIN; HARVEY, 1977; GAI; MILTHORPE, 1995; GROTOWSKY; BALLMANN, 2000).

In general, these studies have been conducted in order to understand the physical aspects of a subsonic, supersonic, or hypersonic flow past to these types of surface discontinuities mostly in the continuum flow regime. Given the number of studies

on this subject, this introduction will focus on the more limited subject of gaps.

Dunavant and Throckmorton ([DUNAVANT; THROCKMORTON, 1974](#)) conducted an experimental investigation on heat transfer to RSI (Reusable Surface Insulation) tile surfaces with gap intersections. They found on the tile surface heating rates as high as 75% above the reference undisturbed value. Also, no appreciable increase in heating was observed where the boundary-layer bridges the gap and reattaches at the forward lip of the tile. The average heating rate to the surface was 24% greater than that to the same area on the undisturbed plate. Moreover, as expected, surface mismatch caused the worst heating condition with heating rated as high as three times the undisturbed value measured on the 0.1 inch protruding tile.

Weinstein *et al.* ([WEINSTEIN et al., 1975](#)) conducted an experimental investigation on aerodynamic heating in a RSI tile array in a turbulent flow at Mach 6.6. Results indicated that the maximum heating rate to an in-line tile arrangement occurred at the largest gap width, and was 1.8 times the local flat-plate value. The maximum heating for this tile arrangement consistently occurred on the top of the tile just behind the leading-edge radius. The heating along the center line for this arrangement was only mildly affected by variations in both gap width and boundary-layer displacement thickness. The maximum heating rate to a staggered tile arrangement was approximately 2.9 times the local flat plate value.

Scott and Maraia ([SCOTT; MARAIA, 1979](#)) have investigated the heating rate distribution and the temperature response on the gap walls of protection tiles. The analysis showed that the hottest location measured in the gap was at 0.75 inch from the upstream transverse gap, and the heat flux distribution in the gap was not constant in time, since the convective heating rate depended on the wall temperature of the gap. In addition, they have demonstrated that the heating rate depended on the gap length.

Bertin and Goodrich ([BERTIN; GOODRICH, 1980](#)) measured heating rates by considering laminar and transitional flow (from laminar to turbulent flow) in slots (very narrow cavities) and gaps relative to shuttle tile installation. In general, the heating measurements were obtained with sparsely spaced discrete sensors that miss much of the three-dimensional nature of the surface heating profile or the important peak heating value.

Hinderks *et al.* ([HINDERKS et al., 2004](#)) have investigated the gap flow structure. They showed that exist a complex flow within the gap, consisting of a vortex super-

posed by an axial flow. The analysis showed that the heat flux transferred to the structure depends on the thermal state of the structure. Also, effects due to changes in the gap geometry caused by deformations in the gap structure demonstrated that deformations should be considered in the design analysis.

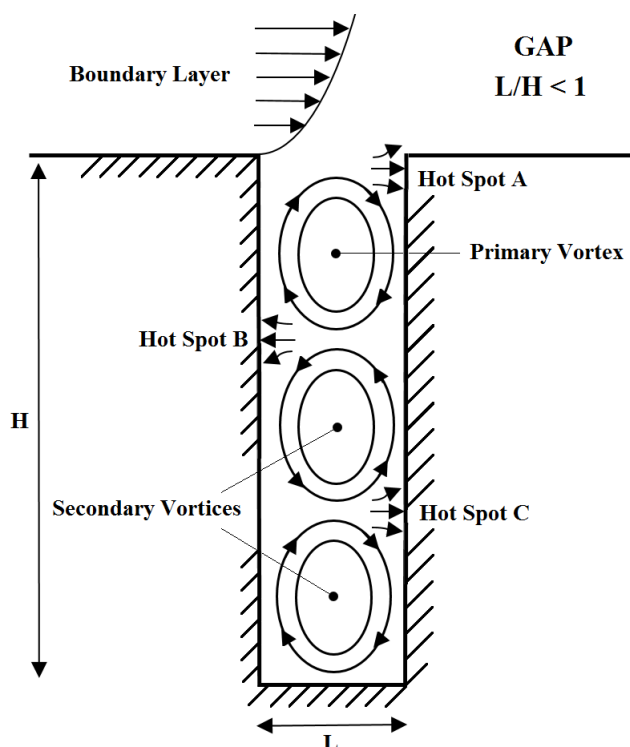
Traineau *et al.* (TRAINEAU *et al.*, 2005) presented new recommendations on the gap heating prediction methodology based in experimental and numerical investigations. It was verified that heating in the transverse gap and in the tee-gap regions was different, and depended on the nature of flow, i.e., laminar or turbulent flow, for a range of Mach number from 3.2 to 6.5. Also, they found that an increase in the angle of attack of 10 to 15 degrees, for the same case studied, generated a 48% increase in pressure at the surface and 22% increase in heat transfer. They also showed that increasing the depth and length of the gaps caused a significant increase in temperature. Furthermore, studies have found that three-dimensional effects are important to the size of the vertical flow zone at the top of the gap, where the 3-D size is much smaller than that in 2-D.

Based on a survey, Everhart *et al.* (EVERHART *et al.*, 2006) have pointed out that a gap is defined as being a very short or deep cavity defined by length-to-depth ( $L/H$ ) ratio less than 1, i.e.,  $L/H < 1$ . In the continuum flow regime, the gap flow topology is usually defined by the development of a column of counter-rotating vortices within the gap caused by the main stream flow, where the number of vortices is approximately given by  $H/L$  ratio. In addition, alternating hot spots are developed in the gap when the vortices directionally align and impinge on the gap sidewall. Figure. 1.4 illustrates the flow topology in a gap.

Patil *et al.* (PATIL *et al.*, 2006) simulated a lid-driven flow in rectangular deep cavities for several Reynolds number. They concluded that as the Reynolds number increases, the center of the primary recirculation begins to move downwards at first, with respect to the top lid. However, as the Reynolds number increases beyond a value of 1000, the center of the primary vortex remains at almost a constant depth for both cases of rectangular cavity  $L/H$  ratio investigated. For the second primary vortex, when Reynolds number is low, it is located at the mid-plane i.e.  $X_C = L/2$  but at higher Reynolds number it drifts towards the left walls i.e.  $X_C < L/2$ . Another observation was that increasing the depth of the cavity does not affect the structure of the primary vortex nearest to the lid. Finally, it was found that the center of two successive primary eddies are spaced at a vertical distance of  $\sim 1.355L$ .

Paolicchi (PAOLICCHI, 2010) has studied gaps situated in a rarefied hypersonic flow

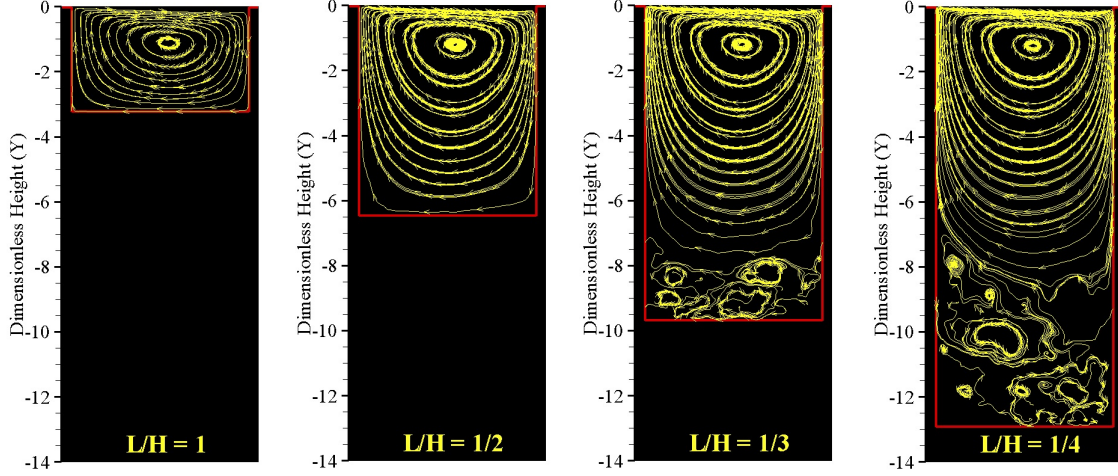
Figure 1.4 - Drawing illustrating the flowfield structure inside a gap.



SOURCE: Adapted from Everhart et al. [EVERHART et al. \(2006\)](#).

by employing the Direct Simulation Monte Carlo (DSMC) method. The work was motivated by the interest in investigating the length-to-depth ( $L/H$ ) ratio effects on the flowfield structure and on the aerodynamic surface quantities for a family of gaps defined by  $L/H$  of 1,  $1/2$ ,  $1/3$  and  $1/4$ . The primary emphasis was to examine the behavior of the primary properties, such as velocity, density, pressure and temperature, as well as pressure, skin friction and heat transfer coefficients, due to changes on the gap  $L/H$  ratio. It was observed the formation of only one recirculation for  $L/H$  ratio of 1,  $1/2$ ,  $1/3$  and  $1/4$ . Results showed that gap flow behavior in the transition flow regime differs from that found in the continuum flow regime for the conditions investigated. The analysis showed that the recirculation region inside the gaps is a function of the  $L/H$  ratio. It was found that, for the  $L/H$  of 1 and  $1/2$  cases, the flow structure was characterized by a primary vortex system, with the recirculation region filling the entire gaps. Otherwise, for the  $L/H$  of  $1/3$  and  $1/4$  cases, it was observed that the recirculation region does not fill the entire gaps. In addition, as expected, the external stream does not reattach

Figure 1.5 - Streamline traces inside the gaps for  $L/H$  of 1, 1/2, 1/3, 1/4.  $Y$  is the depth  $H$  of the gap normalized by the freestream mean free path  $\lambda_\infty$ .



SOURCE: PAOLICCHI (2010).

the bottom surface of the gaps. Figure 1.5 illustrates the flow topology inside the gaps. The analysis also showed that aerodynamic surface quantities presented a large dependence on the  $L/H$  ratio for the range investigated. It was found that heat transfer, pressure and skin friction coefficients presented the maximum values along the gap downstream face, more precisely, at the vicinity of the gap shoulder. Furthermore, simulations showed that pressure and heating loads are several times larger than those for a smooth surface.

Finally, Xu *et al.* (XU *et al.*, 2015) simulated a 2- $D$  supersonic flow over a gap at incidence by employing the finite volume method in order to solve the Navier-Stokes equations. The numerical results revealed that the heat flux ratio presented a *U-shaped* distribution on the gap wall, and maximum value at the windward corner of the gap. The heat flux ratio decreased as the gap depth and Mach number increased. In addition, it increased with increasing the angle of attack.

#### 1.4 Problem Definition and Scope of Current Work

In the current study, effort is directed to expand the previous analysis of hypersonic gap flow by Paolicchi (PAOLICCHI, 2010) in the transition flow regime by investigating the impact of the angle of attack on the flowfield structure and on the

aerodynamic surfaces quantities.

In this manner, the present investigation was undertaken in an attempt to assess the behavior of the primary properties, such as velocity, density, pressure and temperature, as well as the heat transfer, pressure and skin friction coefficients due to changes on the angle of attack and on the gap  $L/H$  ratio. The focus of the present study is the low-density region in the upper atmosphere, characterized by the transition flow regime, i.e., between the continuum flow and the free collision flow regime. In such a circumstance, the DSMC method will be employed to calculate the hypersonic two-dimensional flow over the gaps.

In order to guide the reader, the purpose and contents of the following chapters are provided below.

Chapter 2: In this chapter, a description of the appropriate computational method is presented. Particular emphasis is placed on the DSMC methodology, molecular model, collision model, internal degrees of freedom and boundary conditions.

Chapter 3: The computational procedure is explored in this chapter. It includes the simulation conditions, the definition of the geometry analyzed in this research as well as the important geometric parameters.

Chapter 4: This chapter outlines the procedure for the verification and validation processes of the DSMC code employed in the simulations. These processes are applied in a test case defined by a flat-plate. The DSMC code is validated with simulation of a hypersonic flow over a flat-plate and comparisons with previous experimental and numerical results.

Chapter 5: The purpose of this chapter is to present the computational results and discussion. In this chapter, the major features of the primary properties, velocity, density, pressure and kinetic temperatures, are discussed in details. Moreover, the aerodynamic surface quantities, number flux to the surface, heat transfer, pressure, and shear stress, expressed in a coefficient form, are carefully examined.

Chapter 6: The final chapter of this dissertation contains a summary of the results obtained throughout the course of this work, and the conclusions that were drawn from them. Recommendations are made regarding further computational work that should be undertaken on the topic of this dissertation.

## 2 COMPUTATIONAL METHOD

### 2.1 Methods for Modeling Transition Flows

Hypersonic vehicles experience different flow regimes during the course of its flight trajectory, since density varies with altitude in the Earth's atmosphere. Hypersonic vehicles which operate in rarefied gas environments may encounter non-continuum flow conditions, which can have a significant influence on aerodynamic performance and vehicle surface heat flux.

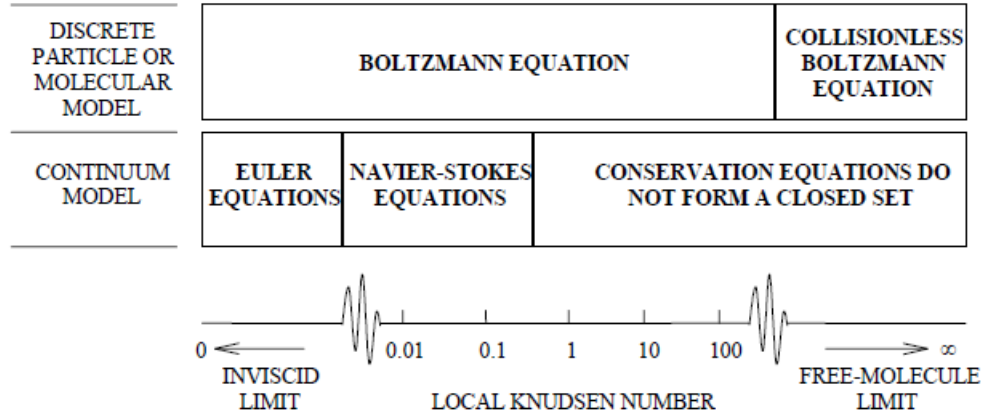
Difficulties of experimental devices for hypersonic flows of high enthalpy and low density, where several physical and chemical processes are relevant, have stimulated the development of various numerical methods to simulate these flows. Nevertheless, numerical techniques which fail to incorporate such non-equilibrium conditions miss out on an essential part of the flow physics surrounding the vehicle. Under such conditions, a particle-based method is required to capture the dilute flow environment.

The degree of rarefaction of a flow is usually expressed by the Knudsen number, as defined earlier by Eq. 1.1. Since the mean free path  $\lambda$  is inversely proportional to the flow density, then it should be recognized that it is not density alone that determines rarefaction, but its relation to some characteristic dimension of the geometry.

The conventional continuum flow assumption is valid when the overall Knudsen number tends to zero. In this flow regime, one can disregard its microscopic structure and consider only its macroscopic properties such as density, velocity or temperature. In the opposite limit, the overall Knudsen number tending to infinity, the flow regime corresponds to the free molecular flow. In this case, intermolecular collisions may be neglected and particle collisions with the body surface play the determining role. The range defined by  $0.1 < Kn < 10$  is referred to as the transition flow regime, where not only gas-surface collisions but also intermolecular collisions are important. In the transition flow regime, viscosity, heat conduction, relaxation, diffusion and chemical processes are important. The velocity distribution functions may be non-Maxwellian, thus resulting in strong thermal non-equilibrium. These Knudsen number limits on the conventional mathematical formulations are illustrated in Fig. 2.1.

In the macroscopic model or continuum flow model, the Euler equations for inviscid flow assume that the flow is in local thermodynamic equilibrium, with the velocity distribution everywhere equal to the local Maxwellian equilibrium distribution. This is the limiting case as the Knudsen number tends to zero. The continuum

Figure 2.1 - Validity of the conventional mathematical models as function of local Knudsen number.



SOURCE: Adapted from Bird BIRD (1986).

flow model, expressed by the Navier-Stokes equations, may be assumed to be valid when the Knudsen number is very small in comparison with unity. In this case, the velocity distribution function departs from the Maxwellian distribution. However, the departure is still sufficiently small for the Chapman-Enskog theory (CHAPMAN; COWLING, 1970) for the transport coefficients to be valid.

The departure from the Maxwellian distribution becomes important when the local Knudsen number  $Kn > 0.05$ . It means that both the Chapman-Enskog theory and the Navier-Stokes equations stop to be valid (BOYD et al., 1995). One alternative approach to this problem of the failure of the Navier-Stokes equations is to perform the Chapman-Enskog expansion to higher order to obtain the Burnett equations (BURNETT, 1936). Each level of approximation implies a different distribution function that deviates from the Maxwellian distribution.

Interest in the use of Burnett equations, based on the second order of the Chapman-Enskog expansion for calculating rarefied hypersonic flows, increased in the last decades (TANNEHILL; EISLER, 1976; FISCKO; CHAPMAN, 1988; FISCKO; CHAPMAN, 1989; LUMPKIN III; CHAPMAN, 1992; ZHONG et al., 1993; LEE, 1994; COMEAUX et al., 1995; KEON-YOUNG et al., 2001). However, applications of the Burnett equations face additional difficulties related to the correct formulation of the boundary conditions and linear instability of these equations to short-wave disturbances. In addition,

the Burnett equations increase the order of the differential equations that govern momentum and heat transport in the gas. These equations are more difficult to solve numerically, and fail when the degree of rarefaction is sufficiently high. Finally, the Burnett equations can also lead to second-law impossibilities in certain situations, such as a negative dissipation function or a heat flux in an isothermal gas (COMEAUX et al., 1995). Cheng and Emanuel (CHENG; EMMANUEL, 1995) present a more detailed description of the use of Burnett equations for rarefied hypersonic flows.

The microscopic or molecular model recognizes the particulate structure of the gas as a myriad of discrete molecules, providing information on the position, velocity, and state of the molecules at all times. The mathematical model requires solution of the Boltzmann equation (CERCIGNANI, 1988). Solutions of the Boltzmann equation are readily obtained in the free molecular limit as the Knudsen number tends to infinity. In this manner, analytical difficulties are faced at finite Knudsen numbers.

The Boltzmann equation is an integro-differential equation with the velocity distribution function as the only dependent variable. In contrast, the Navier-Stokes equations have the flow velocity and macroscopic thermodynamic properties as dependent variables. The reduction in the number of dependent variables is made at the expense of increasing the number of independent variables from those of physical space to those of phase space. In the simplest case of a monoatomic gas with no internal degrees of freedom, the additional dimensions of this phase space are the three velocity components of the molecules. An one-dimensional steady flow of such a gas becomes a three-dimensional problem in phase space (the velocity distribution is axially symmetric about the velocity component in the flow direction), while a two-dimensional steady flow becomes five-dimensional in phase space.

It is important to remark that analytical solutions of the Boltzmann equation are generally limited to flows involving a simple molecular model, one independent macroscopic variable and small disturbance. In addition, rarefied hypersonic flow problems often involve physical effects, such as chemical reactions and thermal radiation, which have not yet been incorporated into the Boltzmann formulation. Consequently, the mathematical difficulties associated with the direct solution of the Boltzmann equation have stimulated the development of physically-based numerical methods. In this context, the Boltzmann equation may be solved numerically by the following approaches: molecular dynamics method (ALDER; WAINWRIGHT, 1957; ALDER; WAINWRIGHT, 1958; DOMINIK; JÜRIG, 2009; AKIRA, 2011), test particle method (HAVILAND; LAVIN, 1962; HAVILAND, 1965; FRENKEL; SMIT, 2009), direct

numerical integration method (YEN, 1971; YEN, 1984) and the Direct Simulation Monte Carlo method (BIRD, 1994; BIRD, 2013).

The DSMC method, originated by Bird (BIRD, 1994; BIRD, 2013) in the 1960s, is the dominant numerical method for applications involving rarefied gas flow. For the purpose of this dissertation only the DSMC method will be discussed, since it is the method used in the present work.

## 2.2 Direct Simulation Monte Carlo (DSMC) Method

The Direct Simulation Monte Carlo (DSMC) method (BIRD, 1976; BIRD, 1994; BIRD, 2013), is a numerical method that provides a probabilistic physical simulation of a gas flow by simultaneously following the motion of representative molecules in physical space, quite different from the finite-difference method (YOSHIO, 2007). It is a numerical scheme for solving the nonlinear Boltzmann equation for a hard sphere. The DSMC method is based on the study of the physical concepts of rarefied gases and on physical assumptions that form the basis for the phenomenological derivation of the Boltzmann equation. However, it is not derived from the Boltzmann equation itself.

The DSMC method and the Boltzmann equation are based on the classical kinetic theory, and both are subjected to the same hypothesis, i.e., the hypothesis of molecular chaos and dilute gases. The relationship between the Boltzmann equation and DSMC method was investigated by Bird (BIRD, 1970). The convergence of the DSMC method to the Boltzmann equation, as the number of molecules tends to infinity, was demonstrated by Wagner (WAGNER, 1992).

Currently, the DSMC method is recognized as an extremely powerful technique capable of predicting an almost unlimited variety of rarefied flowfields in the regimes where neither the Navier-Stokes nor the free molecular approaches are appropriate. The method has been tested for high Knudsen number flows in the last 50 years. The results have shown an optimal agreement with experimental data (HARVEY, 1986; HARVEY, 2003; HARVEY; GALLIS, 2000; HOLDEN; P., 2003). Thus, comparison with experiments has given acceptance and credibility to the method.

The DSMC method models the flow as a collection of simulated molecules. Each simulated molecule represents a large number of real molecules, since it is not possible to simulate the real number of molecules in the physical domain. Each simulated molecule has a position, velocity and internal energy. The state of these simulated

molecules is modified over time whenever the molecules move, collide and interact with simulated physical space. The hypothesis of a dilute gas, which means that the mean molecular diameter is much less than the mean molecular spacing of molecules in the gas, allows for the molecular motion to be decoupled from the molecular collisions. The movement of simulated molecules is modeled deterministically, and the collisions are treated statistically. Simulations made by DSMC method can vary from thousands to millions of simulated molecules in rarefied flow problems.

In the DSMC method, a computational grid, which represents the physical space, is required for the execution of the method. The computational grid is divided into cells, and each cell is divided into subcells. The cell provides a convenient reference for the sampling of the macroscopic gas properties, and the subcell for the choice of the potential collision pairs. The dimension of the cells must be such that changes in flow properties across each cell be small. The linear dimensions of the cells should be small in comparison with the mean free path  $\lambda$  in the direction of primary gradients (BIRD, 1994). Studies (ALEXANDER et al., 1998; ALEXANDER et al., 2000) confirm that significant errors occur when the cell dimensions are larger than the mean free path  $\lambda$ . As the mean free path  $\lambda$  is inversely proportional to flow density, then high density flows demand more computational cells. This means that more molecules are simulated and more collisions are computed. The simulated molecules in the cell are considered as representative of the real molecules at the position of the cell, and the relative position of the molecules within the cell is ignored in the selection of a collision partner. Also, in order to minimize the smearing of gradients, the mean separation distance of the collision pair should be reduced.

An additional requirement of the DSMC method is related to the minimum number of simulated molecules in the cells. As mentioned earlier, the DSMC method uses the cell system for the sampling of the macroscopic properties and for the selection of collision partners. As the collision rate is a function of the number of molecules in the cells, it is desirable that each cell has the largest possible number of simulated molecules. However, the possible number of collision partners is a function of the number of simulated molecules in each cell. In this scenario, the greater the number of simulated molecules, the greater is the possible number of pairs to collide. As a result, for the collision process, it is desirable to have the number of simulated molecules per cell as small as possible.

In order to solve this conflict, Bird (BIRD, 1986) introduced the option of subdividing the cells into an arbitrary number of sub-cells for the selection of collision pairs. This

procedure improves the accuracy of the method by ensuring that collisions occur only between near neighbor simulated molecules. Thus, it is desirable that each cell has a minimum number around 20 to 30 molecules (BIRD, 1994). This procedure improves the accuracy of the method.

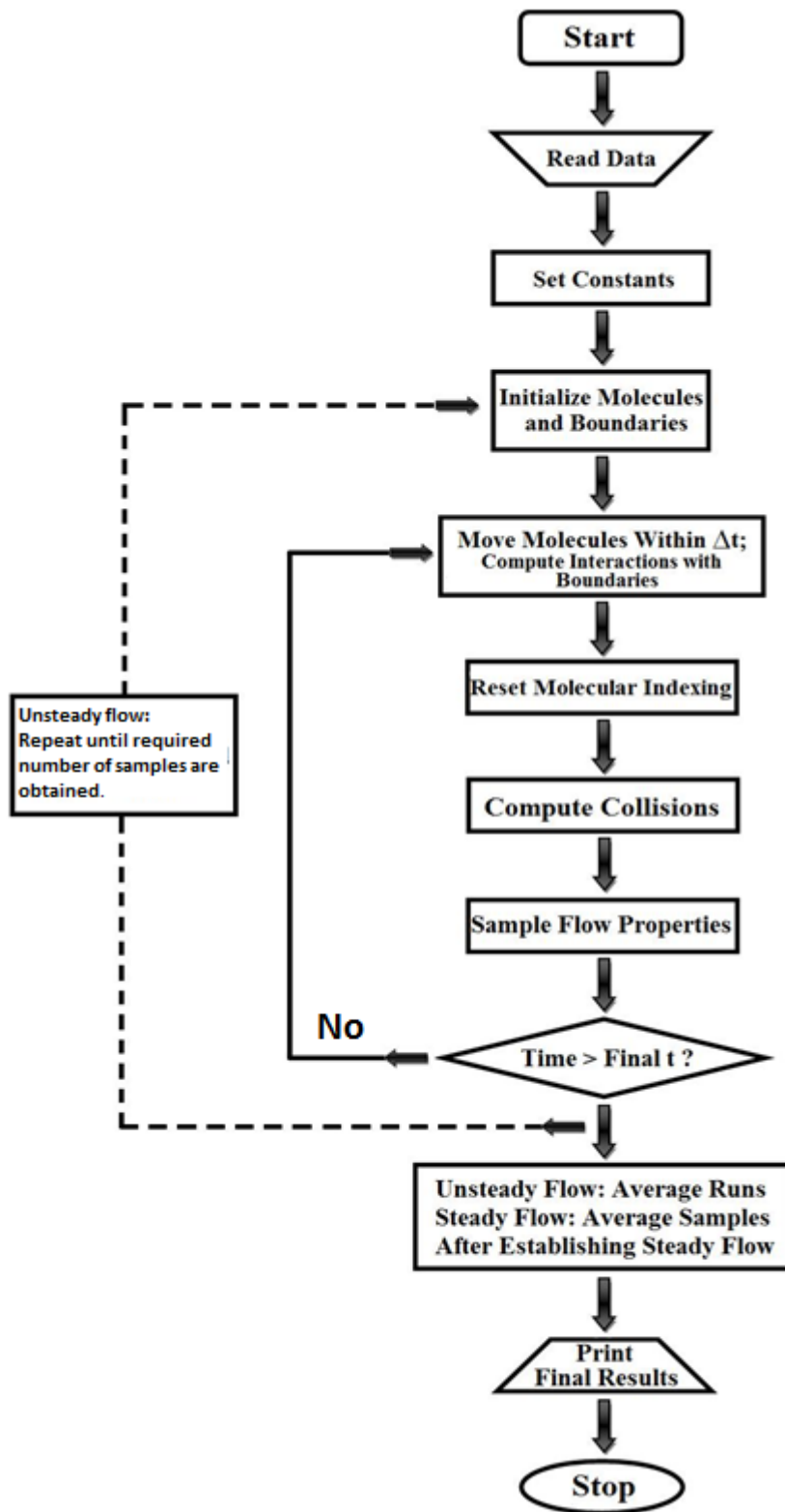
Finally, another requirement in the DSMC method is a proper time step  $\Delta t$ . The paths of the simulated molecules are traced out in physical space by decoupling motion from intermolecular collisions. The size of the time step over which decoupling occurs should be chosen to be significantly smaller than the mean time between collisions. A very small time step results in an inefficient advancement of the solution and accumulation of statistics. Most simulated molecules will take many time step to cross from one cell to another. As a result, the collision phase of each time step will involve the same group of simulated molecules as in the previous time step since almost no molecules leave or enter the cell. Also, a large time step allows the simulated molecules to move too far without the opportunity to participate in a collision. This causes a smearing of the properties of the flow, resulting in yielding inaccurate or non-physical results. In this manner, the time step should be chosen such that a typical simulated molecule moves about one fourth the cell dimension at each time step (LIU; YIN-KWEE, 2002). It should be remarked in this context that stability problems are completely absent in the DSMC method. Consequently, the DSMC method is not subject to a stability criterion such as the Courant-Friedrichs-Lewy condition of traditional Computational Fluid Dynamics (CFD).

### 2.2.1 DSMC Methodology

The DSMC method is a particle-based numerical modeling technique that computes the trajectories of a large number of simulated molecules and calculates macroscopic quantities by sampling simulated molecules properties. The flowchart of the method is displayed in Fig. 2.2. Based on this figure, the DSMC algorithm may be divided into four basic processes as follow:

The first process involves motion of the simulated molecules during a time interval of  $\Delta t$ . Because the simulated molecules will go through intermolecular collision, the time step  $\Delta t$  for simulation is chosen smaller than the mean collision time  $\Delta t_c$ . Once the simulated molecules are advanced in space, some of them may collide to solid surfaces or may leave the computational domain through the inflow/outflow boundaries. Hence, boundary conditions must be enforced at this level, and the macroscopic properties along the solid surfaces must be sampled. This is done by modeling the surface molecule interactions by applying the conservation laws on

Figure 2.2 - Flowchart of DSMC Method.



SOURCE: PAOLICCHI (2010).

individual molecules rather than using a velocity distribution function that is commonly utilized in the Boltzmann algorithms. This approach allows inclusion of many other physical processes, such as chemical reactions, radiation effects, three-body collisions, and ionized flow effects, without major modifications to the basic DSMC procedure (ORAN et al., 1998).

The second process is the indexing and tracking of the simulated molecules. This is necessary because the simulated molecules might have moved to new cell locations during the first stage. The new cell location of the simulated molecules is indexed, and thus the intermolecular collisions and flowfield sampling can be handled accurately. This is a crucial step for an efficient DSMC algorithm. The molecule indexing, molecule tracking, and data structuring algorithms should be carefully designed for the specific computing platforms, such as vector super computers and workstation architectures.

The third process is simulation of collisions via a probabilistic process. Because only a small portion of the molecules is simulated and the motion and collision processes are decoupled, probabilistic treatment becomes necessary. A common collision model is the no-time-counter (NTC) technique of Bird (BIRD, 1994) that is used in conjunction with the subcell technique where the collision rates are calculated within the cells and the collision pairs are selected within the subcell. This improves the accuracy of the method by maintaining the collisions of the simulated molecules with their closest neighbors (ORAN et al., 1998).

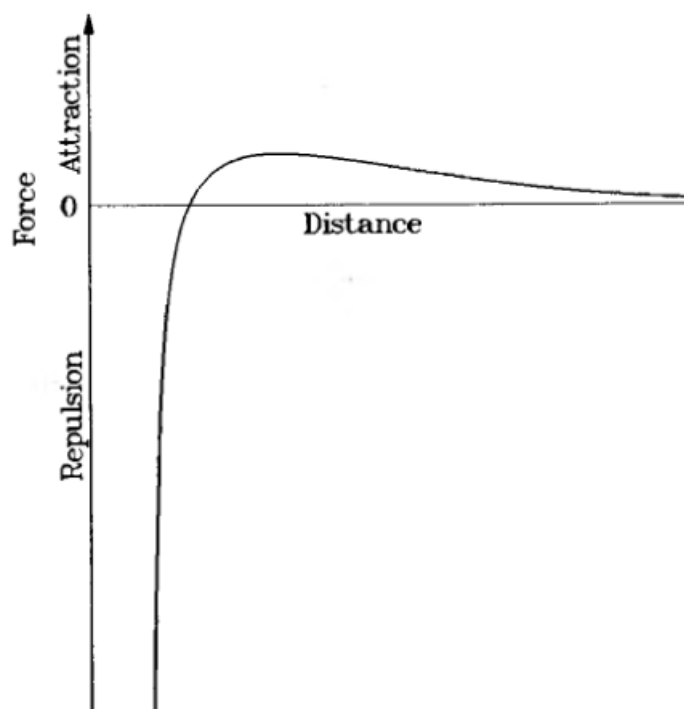
Finally, the fourth process is sampling of molecule properties. The calculation of appropriate flow properties as velocity, temperature, and density are obtained by sampling the microscopic state of all simulated particles in each cell.

### 2.2.2 Molecular Model

A molecular model is established through the definition of force or the potential energy of interaction (PRASANTH; KAKKASSERY, 2008). The force of interaction  $F(r)$  and the potential energy of interaction  $\phi(r)$  between two spherical non-polar molecules are a function of the intermolecular separation  $r$  as shown in the Fig. 2.3. These two are simply related as:

$$F_r = -\frac{d\phi}{dr}, \quad \phi(r) = \int_r^\infty F(r)dr \quad (2.1)$$

Figure 2.3 - Typical intermolecular force field.



SOURCE: BIRD (1994).

In selecting the form of an intermolecular potential to use in calculations, one must consider two factors: (i) the degree of realism desired and (ii) the numerical difficulties associated with the manipulation of the function. For DSMC applications, the first interaction potential used was the rigid impenetrable sphere model due to its simplicity. This empirical intermolecular potential functions may be expressed as:

$$\phi(r) = \begin{cases} \infty & \text{if } r < d, \\ 0 & \text{if } r > d. \end{cases}$$

This potential function represents rigid impenetrable spheres of a diameter  $d$ . Due to its simplicity, it is frequently used for exploratory calculations. It works on the simple premise that interaction occurs only when molecules come into actual physical contact. Although this model is handled very conveniently, it is not a very realistic model. It is well known that two molecules attract each other when they are far apart and repel each other when they come close together, as illustrated in Fig. 2.3.

However, for most applications, except for extremely low temperatures, the attractive component of the interaction potential may be neglected. This simplification gives the mathematically and computationally convenient inverse power law (IPL) potential or the point centers of repulsion model, which is expressed as:

$$\phi(r) = Kr^{-\zeta} \quad (2.2)$$

where  $K$  is a constant and  $\zeta$  is the index of repulsion. For most molecules,  $\zeta$  has a value between 9 and 15.

Among all the molecular models used in the collision routine of the DSMC method, for the purpose of this study, only the VHS model will be described. The VHS model has been the most popular molecular model used in DSMC applications. It has been recommended (BIRD, 1994) for engineering calculations, since for the most flows of interest, the variation in the collision cross section has a far greater influence on the structure of a flow than any variation in the molecular scattering characteristics.

### 2.2.2.1 Variable Hard-Sphere (VHS) model

As the temperature of the gas increases, both its relative molecular velocity and its translational kinetic energy also increases. It has been observed that as these quantities increase, the effective total collision cross-section decreases and this rate of decrease can be directly related to the change of coefficient of viscosity with temperature. Whereas, the rigid interaction potential does not capture the variation of viscosity with temperature accurately, the IPL interaction potential captures the rate to a reasonable accuracy at high temperatures (PRASANTH; KAKKASSERY, 2008). The IPL interaction potential or the point centre of repulsion model is described by a Force field  $F(r)$  of the form:

$$F(r) = \frac{k}{r^\eta} \quad (2.3)$$

where  $k$  is the constant and  $\eta$  is the exponent in the IPL.

This is a very useful interaction potential at high temperatures. For any finite value of the exponent, the force field extends to infinity and the total cross-section diverges.

For a fixed value of the relative molecular velocity, the total cross-section  $\sigma_T$  is obtained (SHEN, 2006) as:

$$\sigma_T = \pi W_m^2 \cdot \left( \frac{k}{2E_t} \right)^{\frac{2}{\eta-1}} \quad (2.4)$$

where  $W_m$  is a constant and  $E_t$  is the relative translational energy given by  $E_t = 0.5m_r c_r^2$ , where  $m_r$  calculated as  $m_1 m_2 / (m_1 + m_2)$ , is the reduced molecular mass of two colliding molecules of mass  $m_1$  and  $m_2$ .

The value of the constant  $W_m$  is arbitrary and, hence this expression is not suitable for setting the effective collision frequency or the mean free path. Thus, in the direct simulation of gas flows, though the IPL model was in use, it had to be replaced and researchers had to fall back to the rigid-sphere molecular model, which has a constant  $\sigma_T$ . However, as can be deduced from Eq. 2.4, in a realistic situation,  $\sigma_T$  is hardly a constant. It is inversely proportional to  $c_r^{4/(\eta-1)}$ . This led to the introduction of the variable hard-sphere model introduced by Bird (BIRD, 1981). This model incorporates the hard-sphere scattering law for collisions, but its cross-section is inversely proportional to the relative translational energy in the collision to the power  $2/(\eta-1)$ . Hence, for an equilibrium gas, the average total cross-section is related to the temperature as:

$$\bar{\sigma}_T \propto T^{-2/(\eta-1)} \quad (2.5)$$

The VHS model combines a finite cross-section with a realistic temperature exponent of the coefficient of viscosity. It has permitted the definition of a mean free path and a Knudsen number (BIRD, 1986) that accounts for the real temperature exponent of the coefficient of viscosity. The deflection angle is given by Eq. 2.6, where  $b$  is the impact parameter and  $d$  is the molecule diameter. The diameter  $d$  is a function of relative translational energy and varies according to Eq. 2.7.

$$\chi = 2 \cos^{-1} \left( \frac{b}{d} \right) \quad (2.6)$$

$$d = d_{ref} \left( \frac{c_{r,ref}}{c_r} \right)^{2/(\eta-1)} \quad (2.7)$$

In the VHS model, the reference values  $\sigma_{T,ref}$ ,  $d_{ref}$ ,  $c_{r,ref}$  and  $E_{t,ref}$  are introduced, which define the VHS model as:

$$\frac{\sigma_T}{\sigma_{T,ref}} = \left( \frac{d}{d_{ref}} \right)^2 = \left( \frac{c_r}{c_{r,ref}} \right)^{-2\zeta} = \left( \frac{E_t}{E_{t,ref}} \right)^{-\zeta} \quad (2.8)$$

where  $\sigma_{T,ref}$  and  $d_{ref}$  are the values of the total collision cross-section and the molecular diameter when the relative velocity is  $c_{r,ref}$  and the corresponding energy is  $E_{t,ref}$ . The index  $\zeta$  is the power of  $E_t$  in Eq. 2.4, i.e, this power law for variation of diameter with  $c_r$  corresponds to the power law for the variation of  $\sigma_T$  with  $c_r$ , as given by Eq. 2.4. In addition, it also permits for a variation of the coefficient of viscosity with temperature, in much the same way as that in the IPL model. This allows the cross-section in the VHS model to be determined from the viscosity coefficient. Incidentally, the viscosity cross-section and the momentum cross-section for this model have been found to be related to the total collision cross-section in the same way as they are related in the rigid-sphere model. These cross-sections are expressed by the following expressions:

$$\sigma_u = \frac{2}{3}\sigma_T = \frac{2}{3}\pi d^2 \quad (2.9)$$

$$\sigma_M = \sigma_T = \pi d^2 \quad (2.10)$$

Hence for this model, the coefficient of viscosity can be written in the following form (BIRD, 2013):

$$\mu = \frac{\frac{15}{8}\sqrt{\pi m k}(4k/m)^\xi T^{1/2+\xi}}{\Gamma(4-\xi)\sigma_{T,ref}c_{r,ref}^{2\xi}} \quad (2.11)$$

In this equation, the coefficient of viscosity is proportional to  $T$  to the power  $\omega=(1/2+\xi)$ , which is defined as the temperature index of the coefficient of viscosity. By adjusting the value of  $\xi$ , the correct dependence of  $\mu$  on  $T$  can be obtained by observing that,

$$\begin{aligned}\xi &= \frac{2}{\eta - 1} \\ \omega &= \frac{1}{2} \frac{\eta + 3}{\eta - 1}\end{aligned}\tag{2.12}$$

For the hard-sphere molecule,  $\omega = 1/2$ ,  $\eta \rightarrow \infty$ , and  $\xi = 0$ , and for the Maxwellian molecule, one has  $\omega = 1$  and  $\xi = 1/2$  (BIRD, 1981). The Maxwellian model finds wide application in analytical studies because it simplifies a lot of the mathematical calculations. However, the viscosity of a gas for Maxwellian molecules is linearly proportional to the temperature and, hence it is unrealistic. The hard-sphere model with  $\eta \rightarrow \infty$  is the most hard molecule and the Maxwellian molecule is the most soft among all molecular models (PRASANTH; KAKKASSERY, 2008).

For the unrealistic hard sphere molecular model, which the molecules has a fixed diameter  $d$  and the collision cross-section is  $\sigma = \pi d^2$ , the mean free-path in a equilibrium gas of number density  $n$  is given by:

$$\lambda = \frac{1}{\sqrt{2}n\sigma}\tag{2.13}$$

where  $n$  is the number density, and  $\sigma$  is the hard sphere collision cross section. In this sense, the Chapman-Enskog result for the coefficient of viscosity in a hard sphere gas, at a temperature  $T$ , was defined by:

$$\mu = \frac{5m}{16} \frac{(\pi RT)^{1/2}}{\sigma}\tag{2.14}$$

The cross section may be eliminated from Eqs.2.13 and 2.14 to give the standard result:

$$\lambda = \frac{16\mu (2\pi RT)^{-1/2}}{5\rho} \quad (2.15)$$

where  $\rho = nm$  is the gas density.

The inconsistency in the above procedure is that the coefficient of viscosity has a fixed temperature exponent of 1/2, while the real gas coefficient of viscosity yields to  $\mu \propto T^\omega$  where  $\omega$  is generally in the range 0.6 - 0.9. Therefore, as an alternative scheme, a consistent definition of the mean free path obtained through the variable cross-section hard sphere (VHS) was introduced by Bird (BIRD, 1994). The mean free path in a VHS is now defined by:

$$\lambda = \frac{2\mu (7 - 2\omega)(5 - 2\omega)(2\pi RT)^{-1/2}}{15\rho} \quad (2.16)$$

which can account for the real gas temperature exponent of the coefficient of viscosity.

### 2.2.3 Collision Models

In order to perform intermolecular collisions in the DSMC method, the total collision cross-section of the interacting particles becomes imperative. The total collision cross-section corresponds to the cross-section of an imaginary sphere surrounding a molecule into which the center of another molecule can not penetrate. This quantity is necessary for the calculation of the collision frequency, the collision probability and the mean free path of the molecules, which is used for setting the dimensions of the cell structure. In addition, the scattering angle is also estimated for the computation of the post-collision velocities of a colliding pair of molecules.

The total collision cross-section  $\sigma_T$  is expressed by (PRASANTH; KAKKASSERY, 2008):

$$\sigma_T = 2\pi \int_{b_1}^{b_2} b db \quad (2.17)$$

This equation is useful only when the relation between the deflection angle  $\chi$  and the parameter  $b$  is known so that the terms inside the integral sign could be expressed

in terms of  $\chi$ . The impact parameter  $b$  is the distance of closest approach of the trajectories of two particles in the center of mass frame of reference, unaffected yet by the intermolecular force. The specification of the impact parameter allows the deflection angle to be calculated. The smaller this parameter, the greater is the effect of interaction. When  $b$  exceeds a certain limit, the particles do not interact with each other.

In addition to the total cross-section, the so-called viscosity cross-section  $\sigma_u$  and the diffusion cross-section  $\sigma_M$  are also important. These are certain convergence integrals, which are encountered in the Chapman Enskog theory (HIRSCHFELDER et al., 1954) for the coefficients of viscosity, thermal conductivity and diffusion. Their expressions in terms of the impact parameter and deflection angle are:

$$\sigma_u = 2\pi \int_{b_1}^{b_2} \sin^2 \chi b db \quad (2.18)$$

$$\sigma_M = 2\pi \int_{b_1}^{b_2} (1 - \cos \chi) b db \quad (2.19)$$

The molecular diameter of reference for the estimation of the total collision cross-section in a particular molecular model is obtained by equating the temperature dependent expression for the coefficient of viscosity of that model to the experimentally observed coefficient of viscosity, at a particular reference temperature. In the transport theory of Chapman-Enskog, the first approximation to the coefficient of viscosity  $\mu$  at a temperature  $T$  of a gas is given by (VICENTI; KRUGER, 1967):

$$\mu = \frac{\frac{5}{8} \sqrt{\pi m k T}}{(m/4kT)^4 \int_0^\infty c_r^7 \sigma_u e^{-mc_r^2/4kT} dc_r} \quad (2.20)$$

where  $m$  is the molecular mass,  $k$  the Boltzmann constant and  $c_r$  the relative molecular speed. The evaluation of the quantities inside the integral sign depends on the molecular model under consideration, which results in different expressions for the coefficient of viscosity for different models.

In order to compute the collisions between simulated particles, several different collision-modeling schemes have been formulated and implemented in the DSMC method. All of them achieve a faster numerical performance than those in molecular dynamics (MD) by ignoring the influence of the relative positions of particles within

a cell in determining particles that collide. Among them, the time-counter (TC) technique (BIRD, 1976), Nanbu scheme (NANBU, 1986), null-collision (NC) technique (KOURA, 1986; KOURA, 1998), no-time-counter (NTC) technique (BIRD, 1989) and the generalized scheme (ABE, 1993) of the no-time-counter technique. NTC scheme (BIRD, 1989) is the most widely used collision scheme in which a number of particle pairs in a cell is formed and is given by:

$$N_c = \frac{1}{2}n\bar{N}(\sigma_T c_r)_{max}\Delta t \quad (2.21)$$

where  $n$  is the number density,  $\bar{N}$  is the average number of particles in a cell,  $\sigma_T$  is the total collision cross section, and  $c_r$  is the relative molecular speed. Each one of the  $N_c$  pairs of particles is formed at random regardless of position in the cell, and then a probability of collision for each pair is evaluated using:

$$P_c = \frac{\sigma_T c_r}{(\sigma_T c_r)_{max}} \quad (2.22)$$

where  $(\sigma_T c_r)_{max}$  is the product of the maximum value between the total collision cross section and the relative molecular speed.

This procedure reproduces the expected equilibrium collision rate under conditions of equilibrium. It is determined whether the particle pair actually collides by comparing the collision probability,  $P_c$ , to a random number  $R_F$ . When collision occurs, post-collision velocities are calculated using conservation of momentum and energy (BOYD, 2014).

#### 2.2.4 Binary Elastic Collisions

As mentioned in the previous sections, the DSMC method is subject to the restriction of the diluted gases. For dilute gases, intermolecular collisions are considered as being binary collisions. Also, an elastic collision is defined as one in which there is no energy exchange between translational and internal modes.

Pre-collision velocities of two molecules may be denoted by  $\vec{c}_1$  and  $\vec{c}_2$ . By knowing the physical properties of these two molecules and the orientation of their trajectories, it is possible to determine their pos-collision velocities  $\vec{c}_1^*$  and  $\vec{c}_2^*$ . By considering that linear momentum and energy must be conserved in the collision process, then the post-collision velocities  $\vec{c}_1^*$  and  $\vec{c}_2^*$  are obtained by the following equations,

$$m_1\vec{c}_1 + m_2\vec{c}_2 = m_1\vec{c}_1^* + m_2\vec{c}_2^* = (m_1 + m_2)\vec{c}_m \quad (2.23)$$

where  $m_1$  and  $m_2$  are the molecular masses of the molecules, and  $\vec{c}_m$  is the velocity of the center of mass of the pair of molecules.

$$m_1\vec{c}_1^2 + m_2\vec{c}_2^2 = m_1\vec{c}_1^{*2} + m_2\vec{c}_2^{*2} \quad (2.24)$$

According to Equation 2.23, the center of mass velocity  $c_m$  is not affected by the collision process. The values of pre- and post-collision, and the relative velocity between the molecules can be defined by:

$$\vec{c}_r = \vec{c}_1 - \vec{c}_2 \quad (2.25)$$

$$\vec{c}_r^* = \vec{c}_1^* - \vec{c}_2^* \quad (2.26)$$

By combining Equations 2.23, 2.24, and 2.25, one obtains the following expressions:

$$\vec{c}_1 = \vec{c}_m + \frac{m_2}{m_1 + m_2}\vec{c}_r \quad (2.27)$$

$$\vec{c}_2 = \vec{c}_m - \frac{m_1}{m_1 + m_2}\vec{c}_r \quad (2.28)$$

The pre-collision velocities relative to the center of mass are  $\vec{c}_1 - \vec{c}_m$  and  $\vec{c}_2 - \vec{c}_m$ .

Similarly, the post-collision, velocities are given by:

$$\vec{c}_1^* = \vec{c}_m + \frac{m_2}{m_1 + m_2}\vec{c}_r^* \quad (2.29)$$

$$\vec{c}_2^* = \vec{c}_m - \frac{m_1}{m_1 + m_2}\vec{c}_r^* \quad (2.30)$$

Based on these equations, it is seen that the post-collision velocities are also anti-

parallel in the center of mass frame of reference.

In addition, the conservation of angular momentum requires that the projected distance between post-collision velocities be equal to the projected distance between the pre-collision velocities. Equations 2.27, 2.28 and 2.29, 2.30 show that:

$$m_1 \vec{c}_1^2 + m_2 \vec{c}_2^2 = (m_1 + m_2) \vec{c}_m^2 + m_r \vec{c}_r^2 \quad (2.31)$$

$$m_1 \vec{c}_1^{*2} + m_2 \vec{c}_2^{*2} = (m_1 + m_2) \vec{c}_m^2 + m_r \vec{c}_r^{*2} \quad (2.32)$$

where  $m_r$ , defined as being the reduced mass, is given by:

$$m_r = \frac{m_1 m_2}{m_1 + m_2} \quad (2.33)$$

By comparing Equations 2.31 and 2.32 with Equation 2.24, it is seen that the magnitude of the relative velocity does not change in the collision process, i.e.,

$$\vec{c}_r^* = \vec{c}_r \quad (2.34)$$

As  $\vec{c}_m$  and  $\vec{c}_r$  can be calculated from the pre-collision velocities, then the determination of post-collision velocities is reduced to calculating the change in direction of the  $\chi$  relative to the velocity vector. If  $\vec{F}$  is the force between two spherically symmetric points, and  $\vec{r}_1$  and  $\vec{r}_2$  their position vectors, then the equations of motion of the molecules are as following:

$$m_1 \ddot{\vec{r}}_1 = \vec{F} \quad (2.35)$$

$$m_1 \ddot{\vec{r}}_2 = -\vec{F} \quad (2.36)$$

By combining these two equations, one has,

$$m_1 m_2 (\ddot{\vec{r}}_1 - \ddot{\vec{r}}_2) = (m_1 + m_2) \vec{F} \quad (2.37)$$

By denoting the relative velocity vector by  $\vec{r}$ , then one obtains,

$$m_r \ddot{\vec{r}} = \vec{F} \quad (2.38)$$

In this way, the motion of the molecule of mass  $m_1$  relative to the molecule of mass  $m_2$  is equivalent to the movement of the molecule of mass  $m_r$  relative to a fixed center of force.

For completeness, the aforementioned transformations are illustrated in Fig. 2.4. According to these plots, the transformation from the center of mass coordinate system changes a three-dimensional trajectory into a two-dimensional trajectory, which is symmetric about the apse line AA'. The two trajectories are reduced to one in the further transformation to the reduced mass frame of reference, and this trajectory remains symmetrical about the transformed apse line, which passes through the scattering center **O**.

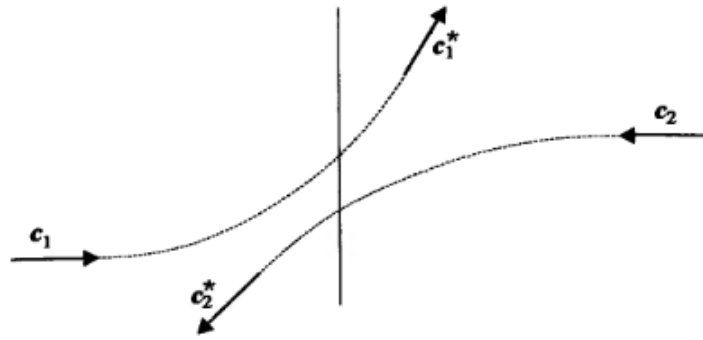
This symmetry reflects the symmetry of the equations related to the pre-collision and post-collision velocities. Another consequence of this symmetry becomes apparent if one considers a collision between two molecules of velocities  $c_1^*$  and  $c_2^*$ . In this way, the separation of their undisturbed trajectories in the center of mass frame of reference is again equal to **b**. This collision results in a post-collision velocities of  $c_1$  and  $c_2$  and is called the inverse of the original or direct collision.

### 2.2.5 Internal Degrees-of-Freedom

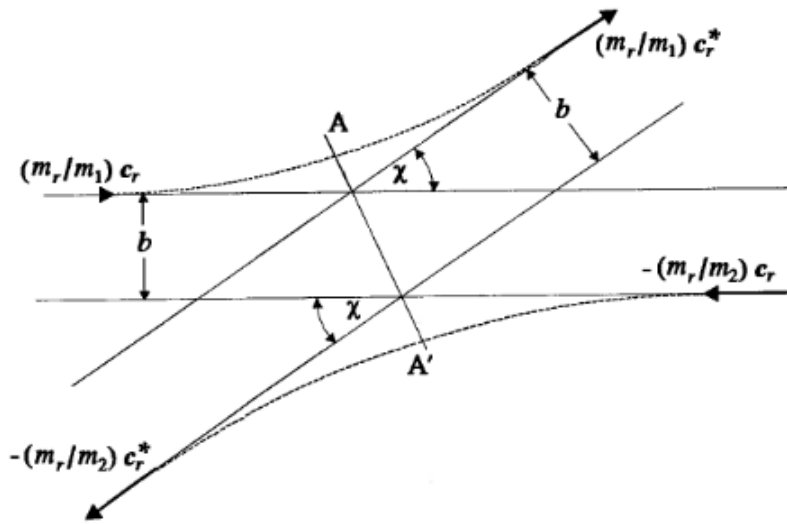
Thermal non-equilibrium is one of the most significant phenomena observed in a rarefied flow. For polyatomic gases, for polyatomic gases, the transfer of energy to and from the internal modes has to be considered. However, energy transfer among translational, rotational and vibrational degrees of freedom cannot be accurately predicted using simple collision models.

The internal energy transfer between the various modes is usually implemented into the DSMC method by the phenomenological model, LB model, introduced by Borgnakke and Larsen (BORGNAKKE; LARSEN, 1975). The essential feature of this model is that a fraction  $\phi$  of translational collisions are assumed to be inelastic, and the remaining  $(1 - \phi)$  collisions are considered as elastic. The fraction  $\phi$  can be interpreted as the average probability of rotational or vibrational energy exchange for translational collisions. This average probability can be determined from measured

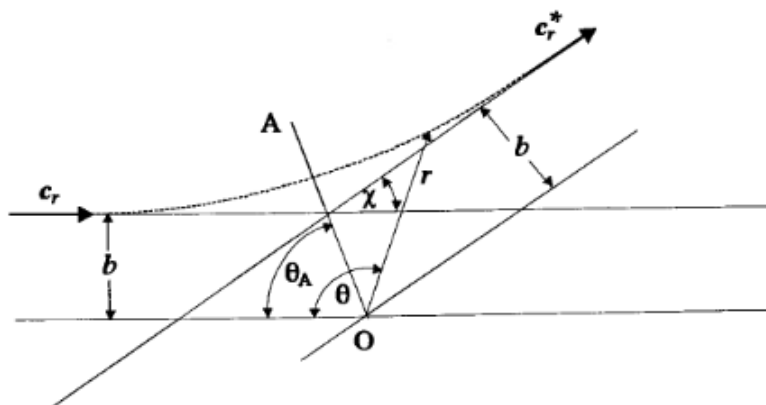
Figure 2.4 - Schematic of the binary collisions. (a) Representation of a planar collision. (b) Binary collision in the center of mass frame of reference, and (c) Interaction of reduced mass particle with a fixed scattering center.



(a)



(b)



(c)

SOURCE: BIRD (1994).

relaxation times.

### 2.2.6 Relaxation Rate

The relaxation time is a function of the local flow properties and can be related to a relaxation number (or collision number)  $Z$ . The relaxation or collision number  $Z$  is usually defined by,

$$Z = \frac{\tau}{\tau_c} \quad (2.39)$$

where  $\tau$  is the relaxation time and  $\tau_c$  is the mean collision time. The relaxation or collision number is the average number of molecular collisions that are required for a particular mode to attain equilibrium energy. Therefore, once this number is determined, the average probability  $\phi$  for each mode in a given collision is conveniently defined as,

$$\phi = \frac{1}{Z} \quad (2.40)$$

The collision procedure for a particular mode is applied in  $1/Z$  of the relevant collisions. The relaxation collision numbers are set as part of the data for each molecular species. These collision numbers are often an arbitrary function of temperature. However, it has been uncertain whether the relevant DSMC procedures can be based on effective collision temperatures, or whether they must be based on the macroscopic temperature.

The molecules in an intermolecular collision are unaware of the macroscopic temperature of the gas and all DSMC procedures should be based entirely on the microscopic properties of these molecules. To achieve this, procedures that employ temperature dependent physical data generally introduce a “collision temperature” that is based on the relative translational energy and some proportion of the internal energy of the molecules in the collision. This collision temperature is not uniquely defined and the procedures must satisfy physical constraints such as the eventual equipartition of energy between the modes as well as the establishment of the equilibrium distribution and compositions.

The DSMC procedures for intermolecular collisions employ a cross-section that is a function of the relative translational energy. The LB model for rotational and

vibrational excitation assumes that only a fraction of the molecules is inelastic. An attempt was made to make the model physically more realistic by making a fraction energy assignment in every collision. However, this led to violation of detailed balancing and there appears to be no alternative to an “inelastic fraction” that is based on the relevant relaxation collision number. If this number is temperature dependent, it is necessary to either introduce a collision temperature or employ the macroscopic temperature. The use of the collision temperature (BIRD, 1994) does not lead to any problems with the classical models and the appropriate inelastic fraction is generally close to the inverse of the collision number (BIRD, 2008).

### 2.2.6.1 Rotational Relaxation Rate

Traditionally, DSMC calculations use the rotational collision number  $Z_R$  around 5. This means that, on average, a molecule rotationally relaxes once every five collisions. In general, this is a good approximation in engineering problems. However, more realistic models for rotational collision number as a function of the translational temperature or translational energy have been proposed (BOYD, 1990a; BOYD, 1990b; BOYD, 1990c).

The following continuum expression for the rotational collision number was obtained by Parker (PARKER, 2004):

$$Z_r = \frac{(Z_r)_\infty}{1 + \frac{\pi^{3/2}}{2} \left(\frac{\Theta^*}{T_{coll}}\right)^{1/2} + \left(\frac{\pi^2}{4} + \pi\right) \frac{\Theta^*}{T_{coll}}} \quad (2.41)$$

where  $\Theta^*$  (characteristic temperature of the intermolecular potential), and  $(Z_r)_\infty$  (the limiting value) are constants. The values of  $(Z_r)_\infty$  and  $\Theta^*$  are chosen in order to obtain the best correspondence between Parker’s expression and the results of Lord and Mates (LORD; MATES, 1970). In their analysis, Lord and Mates (LORD; MATES, 1970) found that nonequilibrium between the translational and rotational modes affects the rotational collision number. In order to consider the behavior of the model under nonequilibrium conditions it is useful to regard the temperature  $T_{coll}$  as the weighted average of the translational and rotational temperatures. It has been shown by Boyd (BOYD, 1990d) that Eq. 2.41 may be reproduced in a discrete particle simulation by assuming that the probability of energy exchange is a function of the relative velocity of collision  $c_r$  (BOYD, 1990a).

Lumpkin (LUMPKIN et al., 1991) have observed that the mechanisms of energy trans-

fer employed in the DSMC calculation affect the rate of energy transfer. It is shown that the value of the collision number used in DSMC will be approximately half of that determined experimentally and employed in a continuum computation. They found the following relation,

$$Z_R^{DSMC} = \frac{Z_R^{Cont}}{1 + \frac{\zeta_R}{\zeta_T}} \quad (2.42)$$

where  $\zeta_R$  and  $\zeta_T$  are the rotational and translational degrees of freedom, respectively.

### 2.2.6.2 Vibrational Relaxation Rate

The vibrational relaxation number  $Z_V$  is also computed as a function of the flow properties. The relaxation number can be easily determined if the collision frequency and the relaxation time are known (Equation 2.39). The relaxation time of the vibrational mode is usually at least an order of magnitude larger than those associated with the rotational mode of a molecule. In DSMC applications, a vibrational relaxation number  $Z_V$  of the order of 50 has been employed. This means that, on average, vibrational relaxation occurs for one in every fifty collisions. The Borgnakke-Larsen method can be applied to the vibrational modes through either a classical or quantum procedure. In the classical procedure, the vibrational energy is treated as a continuous distribution described by a number of vibrational degrees of freedom  $\zeta_V$ , which is fixed. In the quantum procedure, the discrete nature of vibrational spectrum is taken into account, since the vibrational spectrum of real molecules is characterized by large gaps between the neighboring energy levels. The quantum procedure allows sampling of post-collision vibrational energy levels from the discrete form of the Simple Harmonic Oscillator (SHO). This procedure does not require the value of  $\zeta_V$  to be estimated for the whole flowfield. Instead,  $\zeta_V$  varies according to the local energy content of the flow.

Both procedures are discussed at length by Bird (BIRD, 1994)). Vibrational relaxation number as a function of the collision energy is presented by Boyd and Bergemann (BOYD, 1990d; BOYD, 1991; BERGEMANN; BOYD, 1994) and as a function of temperature by Hash and Hassan (HASSAN; HASH, 1993). However, with the collision temperature that had employed in the classical model, equipartition was not achieved. This led to the statement that vibrational equipartition could be achieved with the quantum model only if the vibrational collision number was based on the macroscopic temperature. The vibrational collision number is extremely dependent

on the temperature and the use of a uniform value in a DSMC cell, means that significant effects due to the distribution of collision energies within that cell are not taken into account. This problem has been solved by considering the collision temperature quantized in the same fashion as the vibrational energy and not otherwise dependent on the collision energy. With this procedure, exact equipartition is achieved (BIRD, 2008). The definition of the collision temperature based only on the relative translational energy in the collision follows as (BIRD, 2013):

$$T_{coll} = \frac{m_r c_r^2}{(5 - 2\omega)k} \quad (2.43)$$

However the energy exchange model corresponding to the classical Larsen-Borgnakke (*LB*) model, energy redistribution is based on the sum of the translational energy and a single internal mode. So the appropriate collision temperature based on *LB* energy redistribution is given by:

$$T_{coll} = \frac{1/2m_r c_r^2 + \varepsilon_{int}}{(5/2 + \zeta_{int} - \omega)k} \quad (2.44)$$

where  $\zeta_{int}$  is the number of internal degrees of freedom and  $\varepsilon_{int}$  is the internal energy.

The definition in Eqs. 2.44 is preferred because temperature is a measure of energy and, to define a temperature, the energy is divided by the product of the Boltzmann constant and the “effective” number of degrees of freedom that takes the degree of excitation into account. However, the *LB* selection is based on the physical degrees of freedom, irrespective of the degree of excitation, and, for a partially excited mode, Eq. 2.44 leads to a temperature that is too low (BIRD, 2013). Bird (BIRD, 2002)(BIRD et al., 2011) has shown that equipartition is achieved if the local collision energy is quantized in the same way as the energy of the relevant vibrational mode. Bird (BIRD, 2008) has also shown that the collision temperature should be employed when setting all temperature dependence parameters.

Consider the binary collision of two polyatomic DSMC simulating particles *P* and *Q*. Each particle in the collision pair is considered in turn and the following steps are undertaken (SCANLON et al., 2011):

- Calculate the pre-collision energy of particle *P*,  $E_{c,P}$ , which is the sum of the relative translational energy between *P* and *Q* and the vibrational

energy of particle  $P$  is:

$$E_{c,P} = E_{t,PQ} + E_{v,P} \quad (2.45)$$

- Determine the maximum possible quantum vibrational level for the particle  $P$ ,  $i_{max,P}$ , following the collision:

$$i_{max,P} = \left\lfloor \frac{E_{c,P}}{k\Theta_{v,P}} \right\rfloor \quad (2.46)$$

where  $k$  is the Boltzmann constant and  $\Theta_{v,P}$  is the characteristic vibration temperature. The brackets in the Eq. 2.46 indicate that  $i_{max,P}$  is “quantized” by truncating its value to an integer.

- A desired feature in the DSMC methodology is that numerical process should be not dependent on any macroscopic information. The two molecules in a collision have no knowledge of the overall macroscopic temperature, and, if highly non-equilibrium flows are to be resolved sufficiently. The procedures for energy redistribution in a collision should be based entirely on the energies and impact parameters associated with that collision. In order to adhere to this microscopic principle, a “quantized collision temperature”,  $T_{coll}$  is defined which is based on  $E_{c,P}$  as:

$$T_{coll,P} = \frac{i_{max,P}\Theta_{v,P}}{7/2 - \omega_P} \quad (2.47)$$

The Millican-White (MILLIKAN; WHITE, 2004) theory predicts that the product of the pressure and the vibrational collision time is proportional to the exponential of a constant times the minus one third power of the temperature. This leads (BIRD, 1994) to a vibrational collision number defined as:

$$Z_v = (C_1/T^\omega)exp(C_2T^{-1/3}) \quad (2.48)$$

where  $C_1$  and  $C_2$  are constants. The values of the constants that best fit to experimental data were provided for typical gases. Nevertheless, a problem with Millikan-White data is that the collision number goes to a nonphysical value less than unity before the dissociation temperature is reached. There is a strong case for setting the vibrational collision number to unity at the characteristic temperature of dissociation  $\Theta_d$ , and it is then possible to specify the vibrational collision number through

a single value  $Z_{v,ref}$  at the reference temperature  $T_{ref}$ . The expression for the vibrational collision number is then (SCANLON et al., 2011) (BIRD, 2008) (BIRD, 2013):

$$Z_v = \left( \frac{\Theta_d}{T_{coll,P}} \right)^\omega \left[ Z_{ref} \left( \frac{T_{ref}}{\Theta_d} \right)^\omega \right] \left[ \left( \frac{\Theta_d}{T_{coll,P}} \right)^{1/3} - 1 \right] / \left[ \left( \frac{\Theta_d}{T_{ref}} \right)^{1/3} - 1 \right] \quad (2.49)$$

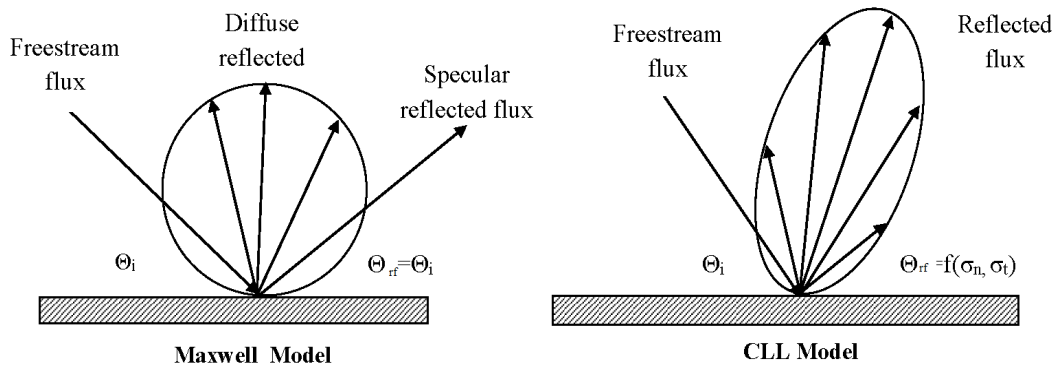
where  $\Theta_d$  is the characteristic temperature of dissociation,  $\omega$  is the temperature exponent of viscosity,  $Z_{ref}$  is a reference vibrational collision number, evaluated at an arbitrary reference temperature  $T_{ref}$ . The value of  $T_{ref}$  should be representative of the range of temperatures expected in the application.

### 2.2.7 Boundary Conditions

The determination of the properties at the vehicle surface, and in particular the aerodynamic forces and moments, and the convective heat transfer, is the most important outcome from many DSMC analysis of hypersonic flows. The surface properties are of course very sensitive to the model assumed in DSMC for gas-surface interaction (BOYD, 2014). Modeling the interaction of gas molecules with a solid surface plays an important role in the DSMC simulation. However, there is no model of gas-surface interaction that is adequate over a wide range of factors for all combinations of gases and surfaces. For instance, some analytical and numerical simulations (PIEKOS, 1995) (XUE et al., 2000) are based on the assumption of diffuse reflections with full thermal and momentum accommodation. The fully diffuse reflection is a common gas-surface interaction in which the particles reflect from the surface with new velocity components that are sampled from Maxwellian distributions characterized by the wall temperature (note that the velocity component normal to the surface is sampled from a biased Maxwellian distribution)(BOYD, 2014). Another method employed is the Cercignani-Lampis-Lord (CLL) gas-surface model (LORD, 1991b). The CLL model is a more sophisticated method and has a stronger theoretical basis, such as using a reciprocity relation, and offers more control through use of additional parameters (BOYD, 2014). Fig. 2.5 displays a schematic comparison of the Maxwell reflection model and the CLL reflection model. The CLL model has also been extended for covering diffuse scattering with partial energy accommodation. In addition, for simulating the accommodation of vibrational energy of a diatomic molecule modeled as simple harmonic oscillator (LORD, 1991a), and an anharmonic oscillator (LORD, 1994).

In order to calculate the aerodynamic forces in the DSMC method, it is neces-

Figure 2.5 - Drawing illustrating the Maxwell reflection model and CLL reflection model.



SOURCE: Leite (2009).

sary to setting the velocity distributions functions for the molecules reflected from the surface. A simplified representation of this function is used, which must take into account the major features of gas-surface interaction. In general, these features are obtained from experiments (force action and angular distribution of escaped molecules). In this sense, one of the oldest and most widely used distribution functions for the reflected molecules is due to Maxwell, which proposed two models – specular and diffuse reflection – for the interaction of an equilibrium gas with a solid surface that maintain equilibrium.

In the diffuse model, the particle internal energies are also sampled from the appropriate equilibrium distribution, using the wall temperature (BOYD, 2014). Also, the velocity of each molecule after reflection is independent of its velocity before reflection. However, the velocities of the reflected molecules as a whole are distributed in accordance with the half-range Maxwellian or equilibrium for the molecules that are directed away from the surface. Equilibrium diffuse reflection requires that both the surface temperature and the temperature associated with the reflected Maxwellian gas be equal to the gas temperature. A gas generally has a velocity component parallel to a surface, and this means that the stagnation temperature in a gas differs from the static temperature. For other than fully specular reflection, the distribution function for the incoming molecules will be different from that for the reflected molecules, and the distribution function for the molecules near the surface will not

be Maxwellian. Also, the energy of a molecule relative to the surface before it strikes the surface will generally be different from the energy relative to the surface after it has been reflected from the surface, so that the process is inelastic (BIRD, 2013).

The opposite limit to diffuse reflection is the specular reflection in which is perfectly elastic, meaning that the only change to the particle properties is its velocity component normal to the surface that is simply reversed in sign (BOYD, 2014). Specularly reflecting surface is functionally identical to a plane of symmetry (BIRD, 2013). Many DSMC computations use an accommodation coefficient,  $\alpha$ , to simulate a combination of diffuse and specular reflections such that  $\alpha = 1$  is fully diffuse, and  $\alpha = 0$  is fully specular. This approach is sometimes referred to as the Maxwell model for gas-surface interaction. It has been found (BIRD, 2013) that, for surfaces that are encountered in engineering problems, there is generally good agreement with calculations as the molecules are assumed to reflect diffusely at the surface temperature, and generally require a value in the range of  $\alpha = 0.8 - 0.9$  (BOYD, 2014).

The general requirement, at a molecular level, for equilibrium between a solid surface and a gas is that the interaction should satisfy the reciprocity condition. This is a relationship between the probability of a gas-surface interaction with a particular set of incident and reflected velocities and the probability of the inverse interaction. It may be written (CERCIGNANI, 1988) as:

$$\mathbf{c}_{rf} \cdot \mathbf{e} P(-\mathbf{c}_{rf}, -\mathbf{c}_i) \exp\left(\frac{-E_{rf}}{kT_w}\right) = -\mathbf{c}_i \cdot \mathbf{e} P(\mathbf{c}_i, \mathbf{c}_{rf}) \exp\left(\frac{-E_i}{kT_w}\right) \quad (2.50)$$

The unit vector  $\mathbf{e}$  has been taken normal to the surface which is at temperature  $T_w$ .  $P(c_1, c_2)$  is the probability that a molecule incident on a surface with velocity  $c_1$  leaves with velocity  $c_2$ , and  $E$  is the energy of the molecule. This condition is related to the law of detailed balance and is satisfied by both the diffuse and specular models for a gas in equilibrium with a surface. While most DSMC applications deal with non-equilibrium situations, the procedures for gas-surface interactions must be such that reciprocity is satisfied when they are applied to equilibrium situations (BIRD, 2013).

Finally, at inlet and outlet boundaries, the physical states of particles should be determined to avoid poorly formulated inflow and outflow treatment (PIEKOS; BREUER, 1996; ANDERSON, 1989). The most probable molecular thermal velocity of the introduced molecule is determined in accordance with the temperature given at inlet. The

thermal velocity components perpendicular to the inlet and outlet boundaries are assigned to the incoming particles. Other variables at both inlet and outlet boundaries have to be specified from the states of particles inside the flowfield (XUE et al., 2000).



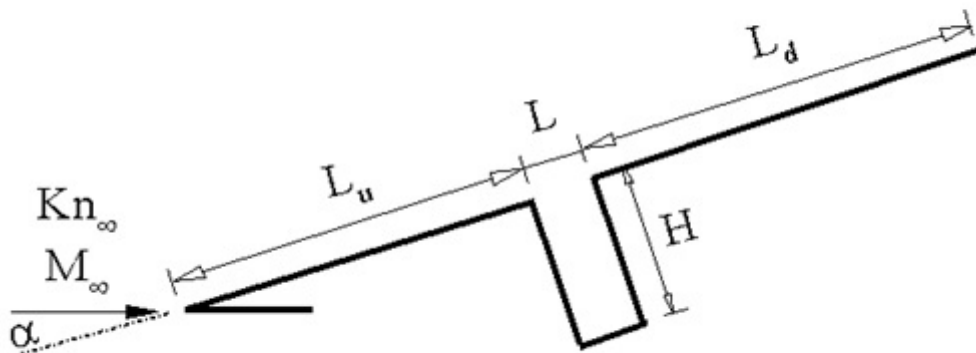
### 3 COMPUTATIONAL PROCEDURE

#### 3.1 Geometry Definition

The present investigation was undertaken in an attempt to investigate the angle-of-attack impact on the flowfield structure and on the aerodynamic surface properties of a hypersonic flow on a gap, which represents a discontinuity on the surface of reentry vehicles.

By considering that the nose radius  $R$  of a reentry vehicle (see Fig. 1.1) is orders of magnitude larger than the gap depth  $H$  or the gap length  $L$ , then one has that  $H/R$  or  $L/R \ll 1$ . In this scenario, a discontinuity on the surface of a reentry vehicle may be modeled by a gap with depth  $H$  and length  $L$  on a flat plate. In addition, an understanding of the angle-of-attack impact on the flowfield structure can be gained by comparing the flowfield behavior of a flat-plate with a gap to that of a flat-plate without a gap.

Figure 3.1 - Drawing illustrating the gap configuration.



A schematic view of the model employed as well as the important geometric and physical parameters is illustrated in Fig. 3.1. Referring to Fig. 3.1,  $M_\infty$  represents the freestream Mach number,  $Kn_\infty$  stands for the Knudsen number,  $\alpha$  the angle of

Table 3.1 - Geometric characteristics for the gaps.

Cases	$L(mm)$	$H(mm)$	$L/H$	$L_u(mm)$	$L_d(mm)$
A	3	3	1	46.43 ( $50\lambda_\infty$ )	46.43 ( $50\lambda_\infty$ )
B	3	6	1/2	46.43 ( $50\lambda_\infty$ )	46.43 ( $50\lambda_\infty$ )
C	3	9	1/3	46.43 ( $50\lambda_\infty$ )	46.43 ( $50\lambda_\infty$ )
D	3	12	1/4	46.43 ( $50\lambda_\infty$ )	46.43 ( $50\lambda_\infty$ )

attack,  $L_u$  the length of gap upstream surface,  $L$  the gap length,  $H$  the gap depth and  $L_d$  the length of the gap downstream surface. It was assumed gap  $L/H$  ratios of 1, 1/2, 1/3, and 1/4, which correspond to the gap length  $L$  of 3 mm and a gap depth  $H$  of 3, 6, 9, and 12 mm, respectively. It was also considered that the flat-plate is infinitely long but only the total length  $L_u + L + L_d$  is investigated. In this fashion, for the cases investigated in this work  $L_u$ ,  $L$ ,  $L_d$  and  $H$  are tabulated in Table 3.1. In addition, the depth  $H$  of 3, 6, 9 and 12 mm correspond to depth  $H$  of  $3.23\lambda_\infty$ ,  $6.46\lambda_\infty$ ,  $9.69\lambda_\infty$  and  $12.92\lambda_\infty$ , where  $\lambda_\infty$  is the freestream mean free path for an altitude of 70 km, defined in the subsequent subsection.

### 3.2 Numerical Simulation Conditions

In principle, as discussed in Chapter 2, the Boltzmann equation is the governing equation in the transition flow regime. The Boltzmann equation (CERCIGNANI, 1988) is a nonlinear integro-differential equation, closed with respect to the one-particle distribution function, which in turns determines the density of molecules in a six-dimensional phase space of particle coordinates and velocities. In order to avoid the difficulty of a direct solution of the Boltzmann equation, the DSMC method has been considered as one of the alternative approaches for solving the Boltzmann equation by simulating the behavior of individual simulated molecules. The DSMC method has been considered as the appropriate choice for problems involving complex multidimensional flows of rarefied hypersonic aerothermodynamics.

The study at hand considers the DSMC code as developed by Bird (BIRD, 1994). In this code, molecular collisions are modeled by using the Variable Hard Sphere (VHS) molecular model, and the No-Time-Counter (NTC) method as a collision-sampling technique. The energy exchange between kinetic and internal modes is controlled by the Larsen-Borgnakke (LB) phenomenological model (BORGNAKKE; LARSEN, 1975). The inelastic collisions ensure the energy exchange between the internal modes, rotation and vibration one. In addition, the model tends to push the

internal energy distributions toward their equilibrium state. Furthermore, collision numbers, which correspond to the number of collisions necessary, on average, for a molecule to undergo relaxation, were assumed to have a temperature dependence, as mentioned earlier, and defined by Boyd (BOYD, 1990a) for rotation mode and by Bird (BIRD, 2008) for vibration mode. Moreover, simulations are performed by considering air as the working fluid with two chemical species,  $N_2$  and  $O_2$ . Chemical reactions, dissociation and recombination, were not considered.

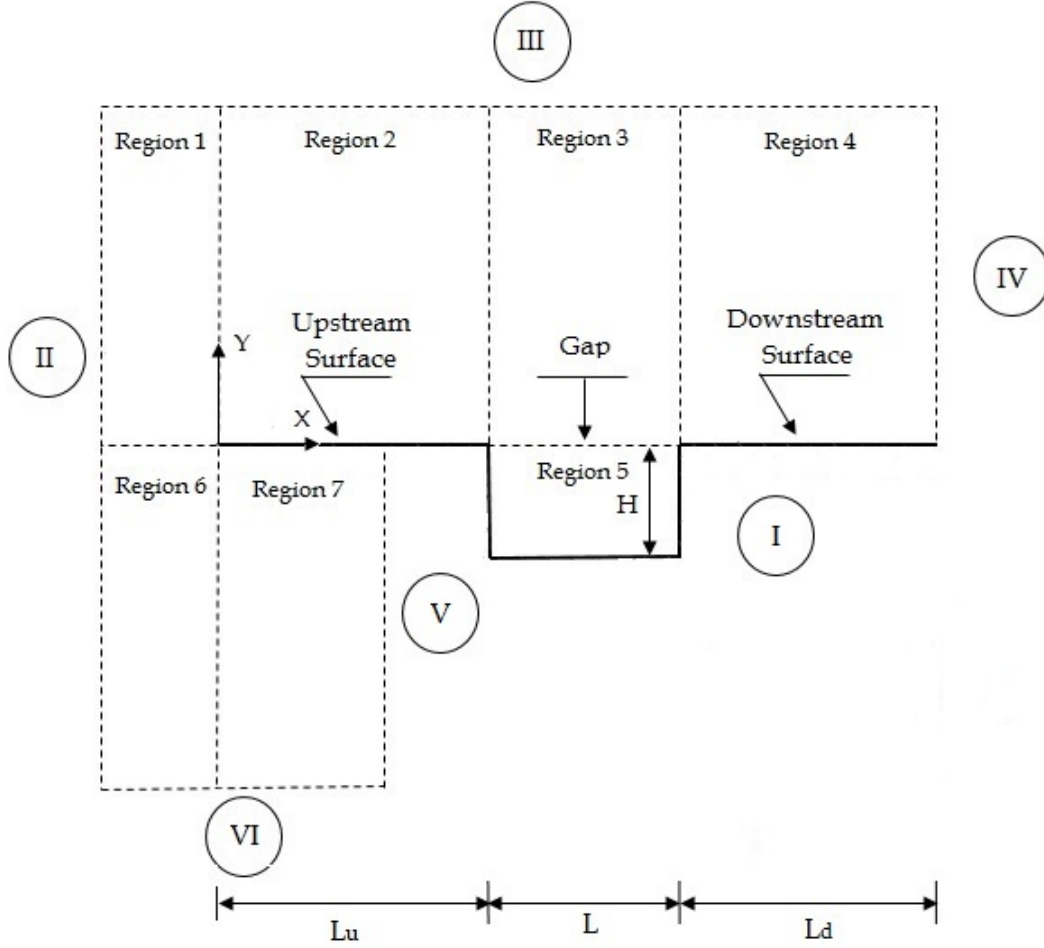
The freestream coefficient of viscosity  $\mu_\infty$  and the mean free path  $\lambda_\infty$  used in the present simulation are evaluated from a consistent definition (BIRD, 1986) by using the VHS molecular model with the temperature exponent  $\omega$  (Eq. 2.12) equal to 0.77 and 0.74 for  $O_2$  and  $N_2$ , respectively. Table 3.2 summarizes the air characteristics used in the present DSMC calculations.

Table 3.2 - Working fluid properties for DSMC simulations.

Properties	Values	Unity
Working fluid	$N_2 + O_2$	
Molecular weight	28.96	<i>kg/kgmole</i>
Molecular mass of $O_2$	$5.312 \times 10^{-26}$	<i>kg</i>
Molecular mass of $N_2$	$4.650 \times 10^{-26}$	<i>kg</i>
Molecular diameter $O_2$	$4.070 \times 10^{-10}$	<i>m</i>
Molecular diameter $N_2$	$4.170 \times 10^{-10}$	<i>m</i>
Moles fraction of $O_2$	0.237	
Moles fraction of $N_2$	0.763	
Viscosity index of $O_2$	0.77	
Viscosity index of $N_2$	0.74	
Degrees of freedom of $O_2$	5 a 7	
Degrees of freedom of $N_2$	5 a 7	

The computational domain, which represents the physical domain, is large enough so that body disturbances do not reach the upstream and side boundaries, where the freestream conditions are specified. In order to implement the particle collisions, the computational domain around the gap is divided into an arbitrary number of regions, which are subdivided into computational cells. The cells are further subdivided into subcells, two subcells/cell in each coordinate direction. In this way, collision partners are selected from the same subcell for the establishment of the collision rate, while the cell provides a convenient reference for the sampling of the macroscopic gas properties. The flowfield is divided into a number of regions and each one of them

Figure 3.2 - Drawing illustrating the computational domain.



has a separated value of time step  $\Delta t$  and a scaling factor  $F_N$ , which relates the number of real molecules to the number of simulated particles (SHU et al., 2005). The ratio of these two quantities,  $F_N$  and  $\Delta t$ , is the same in every region. The cell dimensions must be such that the change in flow properties across each cell is small; hence, the cell dimension is less than the local mean free path. Also, time is advanced in discrete steps such that each step is small in comparison with the mean collision time. A view of the computational domain is depicted in Fig. 3.2.

According to Fig. 3.2, side I is defined by the gap surface. Diffuse reflection with complete thermal accommodation is the condition applied to this side. Sides II and III are freestream sides through which simulated molecules can enter and exit.

Finally, the flow at the downstream outflow boundaries, side IV, V, and VI, are predominantly supersonic and vacuum condition is specified. At these boundaries, simulated molecules can only exit. The choice of vacuum is normally used when the velocity of the gas through these boundaries is supersonic. For flows with Mach number equal to or greater than three (BIRD, 1994), the molecules entering to the computational domain through the boundary can be neglected.

For completeness, the mesh generation, the effect of the mesh resolution, and the verification and validation process employed in the present account are discussed in the next chapter.

### 3.3 Freestream and Flow Conditions

Freestream conditions employed in the present simulations are those given by Paolicchi (PAOLICCHI, 2010), tabulated in Table 3.3. These conditions represent those experienced by a reentry vehicle at an altitude of 70 km.

The freestream velocity  $U_\infty$  is assumed to be constant at 7546.5  $m/s$ , which corresponds to a freestream Mach number  $M_\infty$  of 25. The wall temperature  $T_w$  is assumed to be constant at 880  $K$ . This temperature is chosen to be representative of the surface temperature near to the stagnation point of a reentry capsule, and it is also assumed to be uniform on the gap surface. It should be remarked in this context that the surface temperature is low compared to the stagnation temperature  $T_o$  of the air, i.e.,  $T_w/T_o = 0.013$ . This assumption,  $T_w = 880 K$ , seems reasonable since practical surface material will probably be destroyed if the surface temperature is allowed to approach the stagnation temperature.

Under the aforementioned conditions, the overall Knudsen number,  $Kn_\infty$ , by con-

Table 3.3 - Freestream flow conditions.

Properties	Values	Unit
Velocity ( $U_\infty$ )	7546.5	$m/s$
Temperature ( $T_\infty$ )	219.69	$K$
Pressure ( $p_\infty$ )	5.582	$N/m^2$
Density ( $\rho_\infty$ )	$8.753 \times 10^{-5}$	$Kg/m^3$
Number density ( $n_\infty$ )	$1.819 \times 10^{21}$	$m^{-3}$
Viscosity ( $\mu_\infty$ )	$1.455 \times 10^{-5}$	$Ns/m^2$
Mean free path ( $\lambda_\infty$ )	$9.285 \times 10^{-4}$	$m$

sidering the gap depth  $H$  as the characteristic length, corresponds to 0.3095, 0.1548, 0.1032 and 0.0774 for depth  $H$  of 3, 6, 9 and 12  $mm$ , respectively. In addition, the Reynolds number  $Re_\infty$  is around 121.7, 243.4, 365.1 and 486.8 for  $H$  of 3, 6, 9 and 12  $mm$ , respectively, also based on conditions in the undisturbed stream. Finally, in order to account for the angle-of-attack impact, simulations were conducted by assuming  $\alpha$  of 10, 15, and 20 degrees. It is important to recall that simulations with zero-degree angle of attack were investigated earlier by Paolicchi ([PAOLICCHI, 2010](#)).

## 4 VERIFICATION AND VALIDATION PROCESS

The processes of verification and validation are the primary means to assess accuracy and reliability in computational simulations. The fundamental procedure of the verification process is to identify and quantify errors in the computational model and its solution. The fundamental procedure of validation process is to assess how accurately the computational results compare with the experimental data, with quantified error and uncertainty estimates for both.

With this perspective in mind, the processes of verification and validation in the DSMC code consist of four basic steps; (1) verification by increasing the number of computational cells, (2) verification by increasing the number of simulated particles, (3) verification by increasing the time step, and (4) validation by comparing with experimental data or numerical results available in the literature. In this fashion, the purpose of this Chapter is to discuss at length these four basic steps.

### 4.1 Computational Requirements

Currently, the DSMC method has been the most appropriate for modeling complex flows in the transition flow regime. For computing and tracking the path of the molecules, it is necessary a computational mesh that simulates the physical space of the problem. The mesh allows detecting movement and collisions between molecules, while the computer stores their position coordinates, velocities and energies. In order to do that, the computational mesh is used as a reference in the selection process of the collision pairs, and for sampling and averaging macroscopic flowfield properties. In the last decades, some alternative mesh generation schemes have been developed in order to cover different body shapes as well as to reduce the computational cost. For instance, the body-fitted coordinate system implemented by Abe (ABE, 1993) and Sohn et al. (SOHN et al., 2010), multi-level Cartesian mesh proposed by Rault (RAULT, 1994) and by Zhang and Schwartzentruber (ZHANG; SCHWARTZENTRUBER, 2012), the transfinite interpolation method made by Olynick et al. (OLYNICK et al., 1989), and a Iterative Method for unstructured dynamic-grid proposed by Wu et al. (WU et al., 2009).

In general, these mesh generation schemes have advantages and disadvantages such as a low cost during the movement of simulated particles, the use of cells with non-uniform size in regions where the gradients are more intense, and application in simulation of complex geometries. An advantage of the body-fitted over the cartesian mesh is a possibility of minimizing the computational domain size by adapting the

domain shape to an expected disturbed area. The mesh cell structure can therefore be irregular with regard to the shape of the cells and there can be discontinuities in the mesh lines that define the cell (continuum methods generally require a near orthogonal mesh structure with no discontinuities). Wilmoth (WILMOTH et al., 1996) and Nance (NANCE et al., 1997) discussed in details the advantages of each scheme, in terms of accuracy, computational efficiency and ease of use.

Three primary constraints on the DSMC method must be considered when evaluating computational requirements: (1) the simulation time step must be less than the local average collision time, (2) the cell size must be smaller than the local mean free path, and (3) the number of simulated particles per cell must be roughly constant in order to preserve collision statistics, since it is very important to obtain sufficient collisions in the computation.

As pointed by Bird (BIRD, 1994), an important assumption in the DSMC method is that the gas is dilute, meaning that the average molecular diameter is much smaller than the average spacing between molecules in the gas. This assumption allows that the molecular motion be decoupled from the molecular collisions over a small local time interval. Thus, the successful application of the method requires that the time step must be a fraction of the average time between collisions, as well the linear size of a collision cell should be usually not greater than the local mean free path,  $\lambda$ . Violation of this requirement can lead to a significant distortion of flow properties.

In order to simulate the collisions, the present numerical DSMC investigation employs a cartesian mesh consisting of uniform cells where the computational domain is usually a rectangular cartesian box. The use of rectangular cells has a main advantage in the sense that to be simple and effective in the particle indexing process in cells, whereas the use of a body-fitted mesh or another, which requires tracing or sorting of particles, increases the computational cost. This rectangular regular cells are divided into small cells depending on the flow pattern. Typically, closer to the body surface, the smallest cells are located (an order of or smaller than one third of the local mean free path). In order to adequately model the physics of interest, the number of molecules in the simulation must be greater than a certain number. To obtain accurate collision statistics, it is desirable to have 20 - 30 computational molecules in each cell (ALEXANDER et al., 2000). However, it is difficult to maintain this requirement when the density distribution in the computational domain is no longer uniform. As pointed out by Kannenberg and Boyd (KANNENBERG; BOYD, 2000), the number of molecules in the cell varies inversely with the gas density.

Therefore high-density regions will tend to have few molecules, while low-density regions will have a large number of molecules resulting in over resolution in the flow domain. In order to overcome this difficulty, a variable scaling factor  $F_N$  is used to control the distribution of computational molecules within the grid.  $F_N$  is the ratio of real molecules and computational or simulated molecules.

In this context, the computational effort is substantially reduced by subdividing the flowfield into an arbitrary number of regions where the time step  $\Delta t$  and the scaling factor  $F_N$  remain constant within a region, but they can vary from one region to another one. The combination of subdividing the flowfield into regions along with the use of variable cell sizes provides the flexibility to substantially reduce the total number of molecules used in the simulation and also resolves the flow gradients. It is important to mention that although  $F_N$  and  $\Delta t$  can vary from region to region, the ratio  $F_N/\Delta t$  must be the same for all regions in order to conserve mass across region boundaries in the flow. More details for estimating the computational requirements of DSMC simulations are presented at length by Rieffel (RIEFFEL, 1999) and by Cyril and Boyd (CYRIL; BOYD, 2015).

## 4.2 Computational Mesh Generation

In order to generate the computational grid, the grid generation scheme, proposed by Bird (BIRD, 1994) in his G2 algorithm, was employed. Proceeding in a manner analogous to the Bird treatment, the physical domain is divided into a number of arbitrary four-sided regions, as shown in Fig. 3.2. Along the boundaries, point distributions are generated in such way that the number of points on each opposite side is the same. In the following, the cell structure is defined by joining the corresponding points on each side by straight lines and then dividing each of these lines into segments which are joined to form the system of quadrilateral cells. The point distribution can be controlled by a number of different distribution functions which allow the concentration of points in areas where high flow gradients or small mean free paths are expected. In addition, the point distributions may be chosen independently for each region.

## 4.3 Computational Mesh Adaption

In order to improve the solution accuracy and the grid efficiency, a mesh adaptation technique is also adopted in the present study. Initially, calculation is made on a coarse mesh until a converged solution is obtained. Afterwards, the value of adaptation indicators is examined for each cell based on the flow properties, such as the

ratio of the mean free path to the cell size, the ratio of the time step to the time related to the collision frequency. The main steps for the mesh adaptation employed in this study are summarized as follows: (1) an initial region and cell mesh structure are generated from consideration of the freestream conditions, (2) assumed values of  $F_N$  are chosen for each region,  $\Delta t$  are then estimated subject to the condition that the ratio  $F_N/\Delta t$  be the same for all regions, (3) these parameters are iteratively modified until an acceptable number of computational molecules, cell size distribution, and simulation time step are obtained.

#### 4.4 DSMC Test Case

The problem of a hypersonic flow over a flat plate was selected as a test case in order to elucidate the requirements posed on the verification and validation processes related to the DSMC code. The flat-plate model has been selected because both experimental data and numerical simulations are available in the open literature for comparison. In doing so, it is instructive to examine in the present work two different flat plates as DSMC test cases. One of them corresponds to experimental and numerical investigations carried out by Lengrand et al. (LENGRAND et al., 1992) for a hypersonic flow over a sharp flat plate. The other one corresponds to a numerical study conducted by Dogra et al. (DOGRA et al., 1989) for a rarefied flow past a flat plate at incidence.

According to Lengrand et al. (LENGRAND et al., 1992), the experimental work considered a flat plate of 100 mm of length with 100 mm of width and sharp leading edge. Two angle of incidence, 0 and 10 degrees, were considered to perform the experiments. Nitrogen, used as the working gas, was generated by the freejet expansion from a distance of the flat plate resulting in a freestream Mach number of 20.2, temperature of 13.32 K and pressure of 0.06831 N/m<sup>2</sup>. The flat-plate surface temperature,  $T_w$ , was 290 K. The flow conditions were chosen among those that could be obtained in the SR3 wind tunnel of Centre National de la Recherche Scientifique (CNRS). Table 4.1 presents the freestream conditions.

In addition to this experimental work, Lengrand et al. (LENGRAND et al., 1992) investigated numerically this hypersonic flat-plate flow by employing the DSMC method. Molecular collisions were treated by the VHS model associated with the Larsen-Borgnakke model for rotation-translation energy exchange. By considering the temperature level, vibration mode was neglected. The gas-surface interaction was treated by the Maxwell's model with a single accommodation coefficient.

Table 4.1 - Freestream flow conditions

Properties	Value	Unit(SI)
Mach number ( $M_\infty$ )	20.2	
Velocity ( $U_\infty$ )	1503	$m/s$
Number density ( $n_\infty$ )	$3.716 \times 10^{20}$	$m^{-3}$
Density ( $\rho_\infty$ )	$1.7256 \times 10^{-5}$	$kg/m^3$
Pressure ( $p_\infty$ )	0.06831	$N/m^2$
Temperature ( $T_\infty$ )	13.32	$K$
Stagnation temperature	1100	$K$
Mean free path ( $\lambda_\infty$ )	$2.35 \times 10^{-3}$	$m$
Angle of attack ( $\alpha$ )	0 and 10	$deg$

SOURCE: LENGRAND et al. (1992).

Also of great significance in the present verification and validation processes is the numerical investigation of a hypersonic flat-plate flow conducted by Tsuboi et al. (TSUBOI et al., 2004). Tsuboi et al. examined a hypersonic flow over a flat plate with 100 mm of length and 100 mm of width. The plate had a leading-edge angle of 20 degrees and thickness of 5 mm. Simulation conditions are those employed in the experimental work conducted by Lengrand et al. (LENGRAND et al., 1992). Simulations were performed by employing the DSMC method, along with the Dynamic Molecular Collision (DMC) model (TOKUMASU; MATSUMOTO, 1999) for gas-gas collisions. In addition, it was employed the diffuse reflection for gas-surface interactions and the null collision technique for collision frequency. According to Tsuboi et al. (TSUBOI et al., 2004), the DMC model for nitrogen molecules is able to capture the non-equilibrium characteristics in the rarefied gas flow below 2000K.

In the same fashion, Dogra et al. (DOGRA et al., 1989) conducted DSMC simulations of a rarefied flow past a flat plate at 40-degree angle of incidence. The study considered a flat plate with 1 m of length and zero thickness. The flow conditions simulated were those experienced by the Shuttle Orbiter during re-entry at 7.5 km/s. These conditions correspond to an altitude of 90 km, freestream Mach number of 27.2, freestream temperature of 188 K and density of  $3.418 \times 10^{-6}$ . The flat-plate surface temperature,  $T_w$ , was 1000 K. The flat-plate surface was assumed to be diffused with full thermal accommodation. In addition, the freestream Knudsen number is 0.023. The Table 4.2 summarizes the freestream conditions.

In order to assess the overall performance of the DSMC code employed in this study,

Table 4.2 - Freestream flow conditions

Properties	Value	Unit(SI)
Altitude	90	<i>km</i>
Velocity ( $U_\infty$ )	7500	<i>m/s</i>
Density ( $\rho_\infty$ )	$3.418 \times 10^{-6}$	<i>kg/m<sup>3</sup></i>
Temperature ( $T_\infty$ )	188	<i>K</i>
Angle of attack ( $\alpha$ )	40	<i>deg</i>

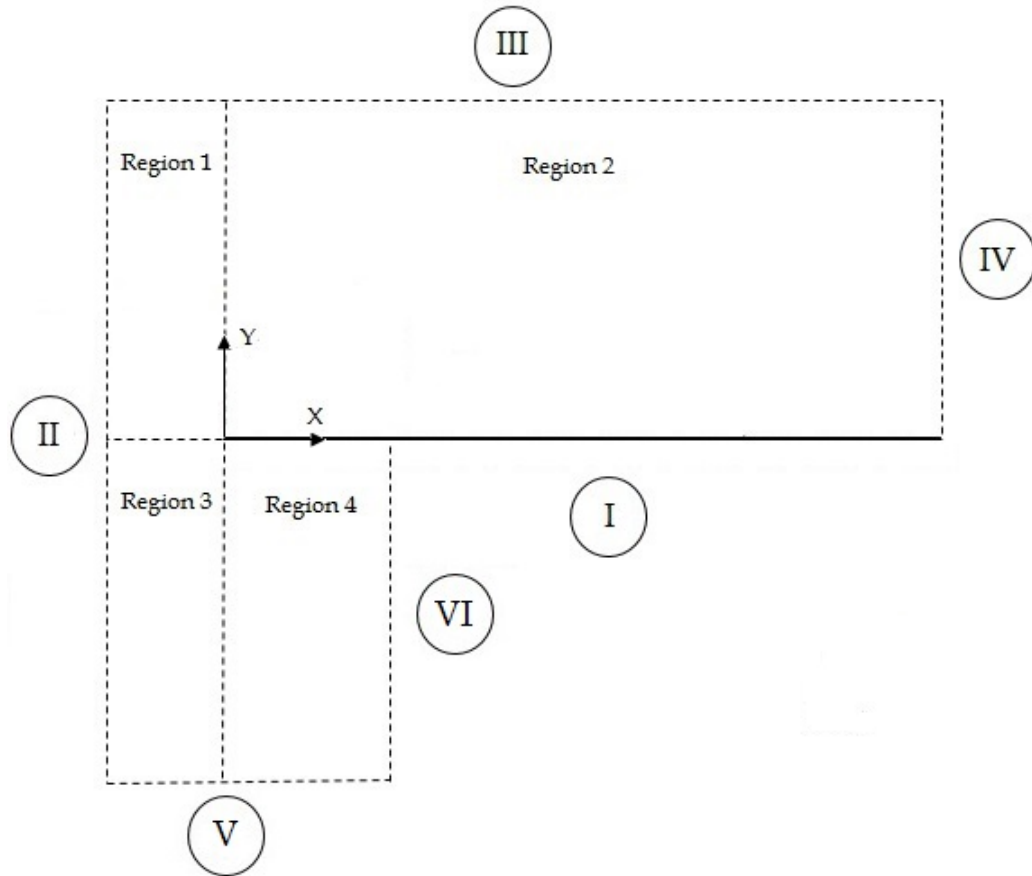
SOURCE: (DOGRA et al., 1989).

the freestream flow conditions and the geometric parameters, for the purpose of the validation processes, are those given by the experimental and numerical investigations conducted by Lengrand et al. (LENGRAND et al., 1992), as shown in Table 4.1. It is important to remark that this investigation was numerically reproduced by Tsuboi et al. (TSUBOI et al., 2004). In the computational solution reproduced in this work, it was assumed that the flat plate is immersed in a uniform stream flowing to the plate at 20-degree of incidence. The flat plate was modeled as one with zero thickness and length of  $100\lambda_\infty$ .

The computational domain used for the simulation was made large enough so that flat-plate disturbances did not reach the upstream and side boundaries, where simulation conditions were specified. The undisturbed freestream boundary conditions were imposed at  $5\lambda_\infty$  upstream of the plate leading edge, and the boundaries normal to the plate extended to a distance of  $30\lambda_\infty$  from the plate surface. This computational domain was divided into four regions, which were subdivided into computational cells, more precisely, quadrilateral cells. The cells were subdivided into subcells, two subcells/cell in each coordinate direction. A schematic view of the computational domain around the flat plate used for the DSMC test case is displayed in Fig. 4.1.

Based on this figure, side I is the flat-plate surface. Diffuse reflection with complete thermal accommodation is the condition applied to this side. Sides II, III, and V are freestream sides through which simulated molecules can enter and exit. The uniform flow is entering the left boundary, side II, at a freestream Mach number of 27.2. The flow at the downstream outflow boundaries, sides IV and VI, are predominantly supersonic and vacuum condition was specified. In this fashion, simulated molecules can only exit at these boundaries.

Figure 4.1 - Drawing illustrating the flat-plate computational domain.



Still referring to Fig. 4.1, region 1 consisted of 30 cells along  $x$ -direction (side III) 70 cells along  $y$ -direction (side II). Region 2 consisted of 320 cells by 100 cells along  $x$ - and  $y$ -directions, respectively. Similarly, region 3 and region 4 have 30 cells by 70 cells and 50 cells by 70 cells along the  $x$ - and  $y$ -directions, respectively. This computational mesh was defined as being the standard case. In addition to this mesh, two other meshes, defined by coarse and fine, were used to study the sensitivity of the computations to the mesh resolution.

#### 4.4.1 Effect of Mesh Resolution

It is firmly established that insufficient grid resolution near the body surface can reduce significantly the accuracy of predicted aerodynamic heating and forces acting on the body surface. Hence, the aerodynamic surface properties, such as heat trans-

fer, pressure and skin friction coefficients, are used as the representative parameters for the grid sensitivity study.

Table 4.3 - Number of cells in the ( $x$ -direction) and [ $y$ -direction] for the flat-plate case.

Region	Coarse	Standard	Fine
1	(15) [70] - (30) [35]	(30) [70]	(60) [70] - (30) [140]
2	(160) [100] - (320) [50]	(320) [100]	(640) [100] - (320) [200]
3	(15) [70] - (30) [35]	(30) [70]	(60) [70] - (30) [140]
4	(25) [70] - (50) [35]	(50) [70]	(100) [70] - (50) [140]
Total Cells	19850	39700	79400

The effect of altering the mesh resolution in the  $x$ - and  $y$ -direction was investigated for three different computational meshes, defined by coarse, standard, and fine. The coarse and fine meshes correspond, respectively, to 50% less and 100% more cells with respect to the standard mesh. As a base of comparison, Table 4.3 tabulates the number of cells employed for each region in these meshes. It is important to remark that each mesh was made up of non-uniform cell spacing in both coordinate directions. In addition, the effect of altering the mesh resolution was examined separately for each coordinate direction.

The effect of changing the number of cells in the  $x$ -direction on pressure  $C_p$ , skin friction  $C_f$  and heat transfer  $C_h$  coefficients is illustrated in Fig. 4.2. In this set of plots, the dimensionless length  $X$  corresponds to the length  $x$  normalized by the freestream mean free path  $\lambda_\infty$ . Based on this set of plots, it is clearly seen that the calculated results are not affected to the range of cell spacing considered for the  $x$ -direction in the cases defined by coarse, standard and fine meshes.

A similar examination was made in the  $y$ -direction. The sensitivity of the calculated results to cell size variations in the  $y$ -direction is displayed in Fig. 4.3. In this figure, a new series of three simulations, with mesh in the region 2 of 320 cells fixed in the  $x$ -direction, and 35, 70 and 140 cells in the  $y$ -direction, are compared. The cell spacing in both directions is again nonuniform. According to this figure, the results for three independent meshes are approximately the same, indicating that the standard mesh is essentially grid independent. For the standard case, the cell size in the  $y$ -direction is always less than the local mean free path in the vicinity of the surface. The comparison shows that the effect of cell variations over these

quantities was negligible for the cases investigated in the present work, indicating that the standard mesh is essentially independent of the cell size.

#### 4.4.2 Effect of Variation on the Number of Simulated Particles

A similar analysis was made for the number of molecules. The sensitivity of the calculated results to number of molecules variations is demonstrated in Fig. 4.4. The standard mesh corresponds to a total of 476,400 molecules. Two new cases using the same mesh were investigated. These new cases correspond to, on average, 238,200 and 952,800 molecules in the entire computational domain. The number of molecules was increased by changing the scaling factor  $F_N$  defined earlier. It is clearly seen that the results are the same for the three cases investigated, indicating that the number of simulated particles for the standard mesh, 476,400 molecules is enough for the code validation process.

#### 4.4.3 Effect of Downstream Boundary Condition

Vacuum was defined as the boundary condition on sides IV and VI (see Fig. 4.1) in the computational domain. The vacuum option is usually adopted when the gas velocity through the boundary condition is supersonic, more precisely, for a flowfield with a Mach number equal to or greater than three (BIRD, 1994). As a result, the flux of molecules across the boundary condition into the computational domain can be neglected. Nevertheless, close to the wall, molecules may not be moving at supersonic speed. Consequently, in this subsonic region close to the wall, there is an interaction between the flow and the downstream boundary. In order to determine the extend of the upstream effect of this imposed downstream vacuum boundary conditions, calculations were made for two other plates with different lengths, i.e.,  $80 \lambda_\infty$  and  $120 \lambda_\infty$ . A comparison of the aerodynamic surface quantities calculated for three different flat-plate sizes is illustrated in Fig. 4.5.

According to this set of plots, it is observed that the vacuum boundary condition present a minor effect in the heat transfer coefficient, followed by the skin friction coefficient, and, finally, for the pressure coefficient. Based on the distribution for the skin friction and pressure coefficients, it is clearly noticed that the upstream disturbance imposed by the vacuum condition is around  $30 \lambda_\infty$ .

### 4.5 Experimental and Numerical Comparisons

Having completed the discussion of verification process, the attention is turned to the validation process. In doing so, this section presents comparisons of two test cases

Figure 4.2 - Effect of altering the cell size in  $x$ -direction on pressure (top), skin friction (middle) and heat transfer (bottom) coefficients.

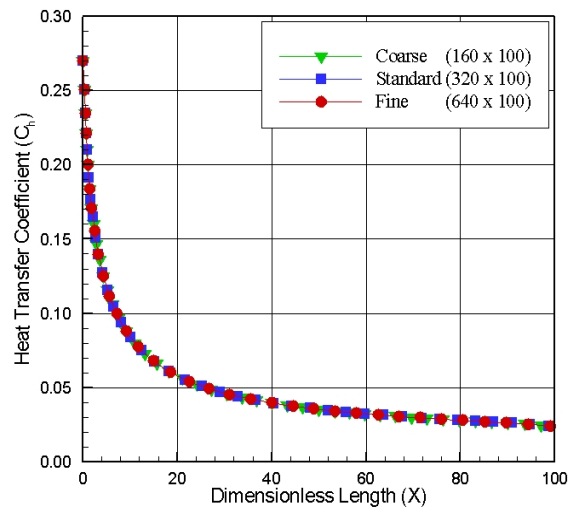
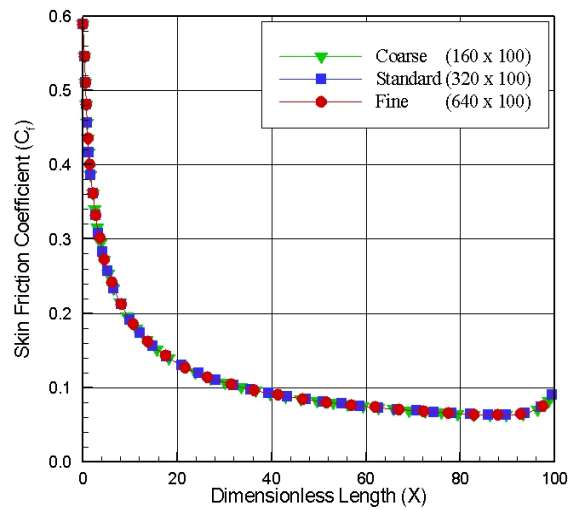
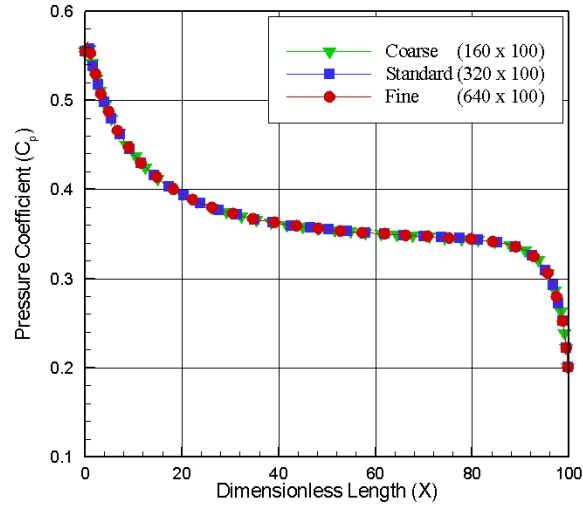


Figure 4.3 - Effect of altering the cell size in  $y$ -direction on pressure (top), skin friction (middle) and heat transfer (bottom) coefficients.

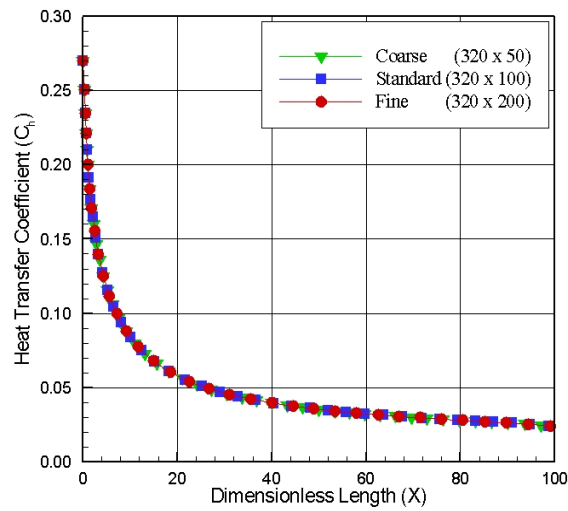
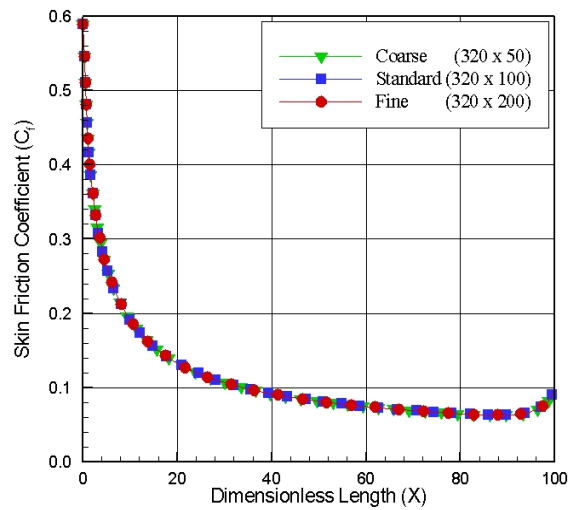
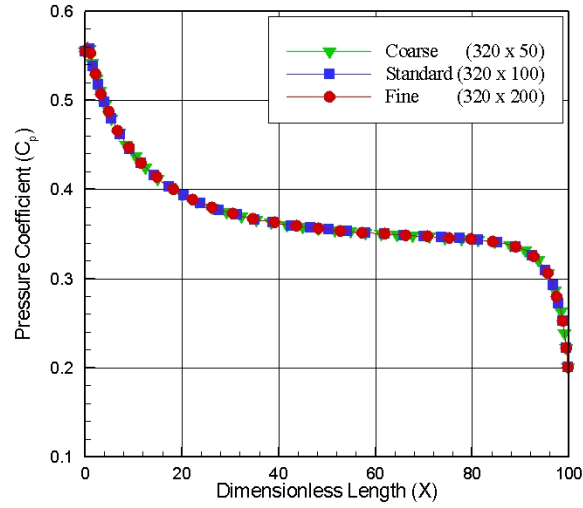


Figure 4.4 - Effect of altering the number of simulated particles on pressure (top), skin friction (middle) and heat transfer (bottom) coefficients.

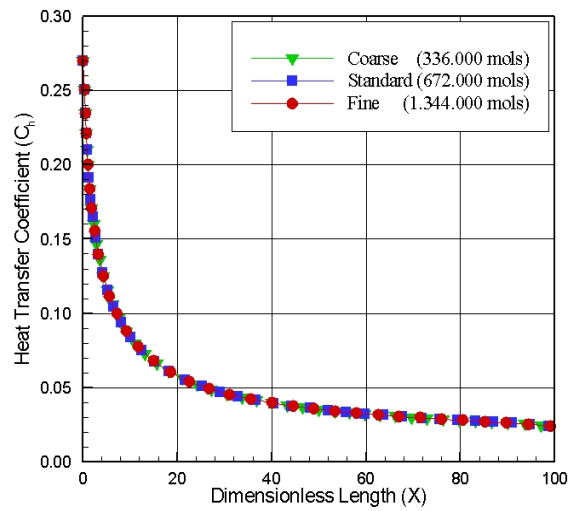
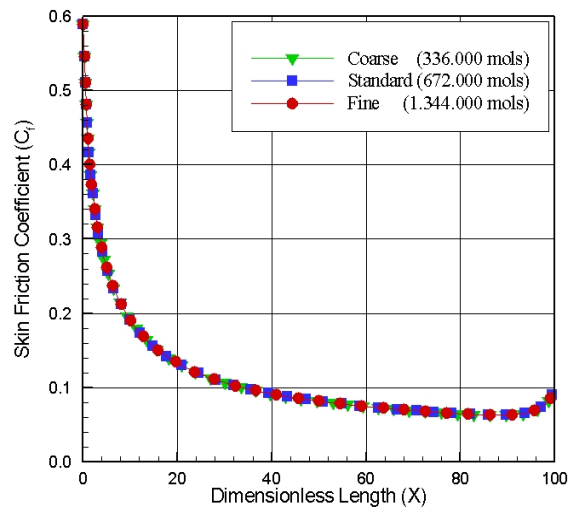
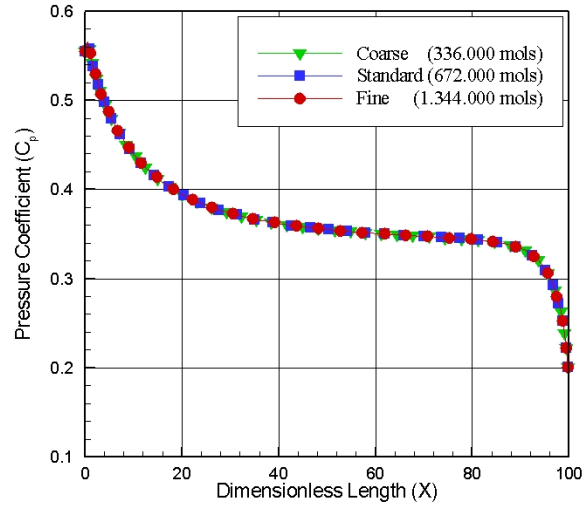
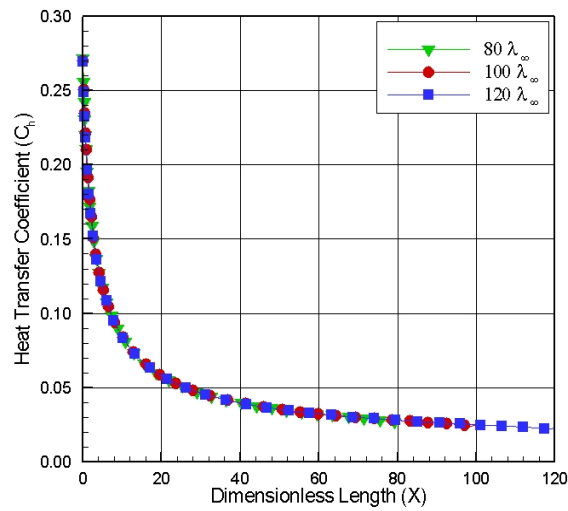
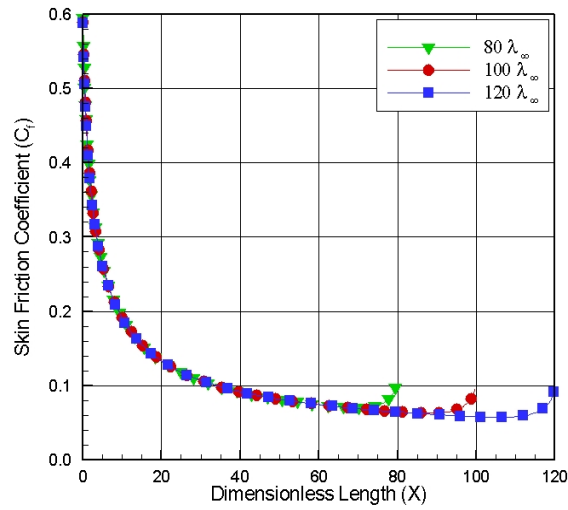
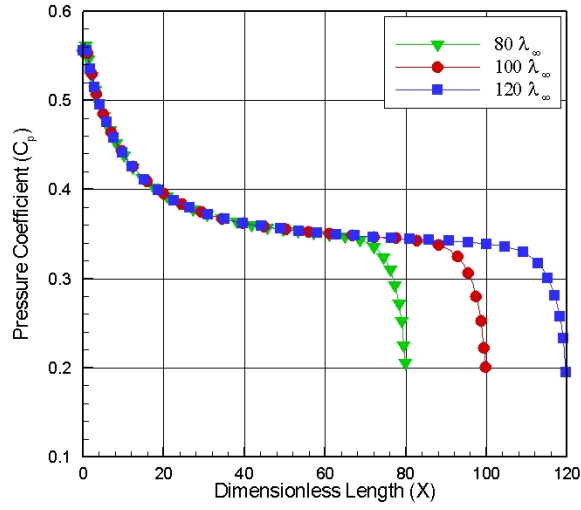


Figure 4.5 - Effect of altering the length of the flat-plate on pressure (top), skin friction (middle) and heat transfer (bottom) coefficients.



with experimental and numerical results for a flat-plate given by (1) Lengrand et al. (LENGRAND et al., 1992), that was numerically reproduced by Tsuboi et al. (TSUBOI et al., 2004) by using the DSMC method, and (2) a numerical study conducted by Dogra et al. (DOGRA et al., 1989) for a rarefied flow past a flat plate at incidence. Freestream flow conditions used in the DSMC code for the comparisons with the two cases are those tabulated in Tables 4.1 and 4.2.

#### 4.5.1 First Test Case

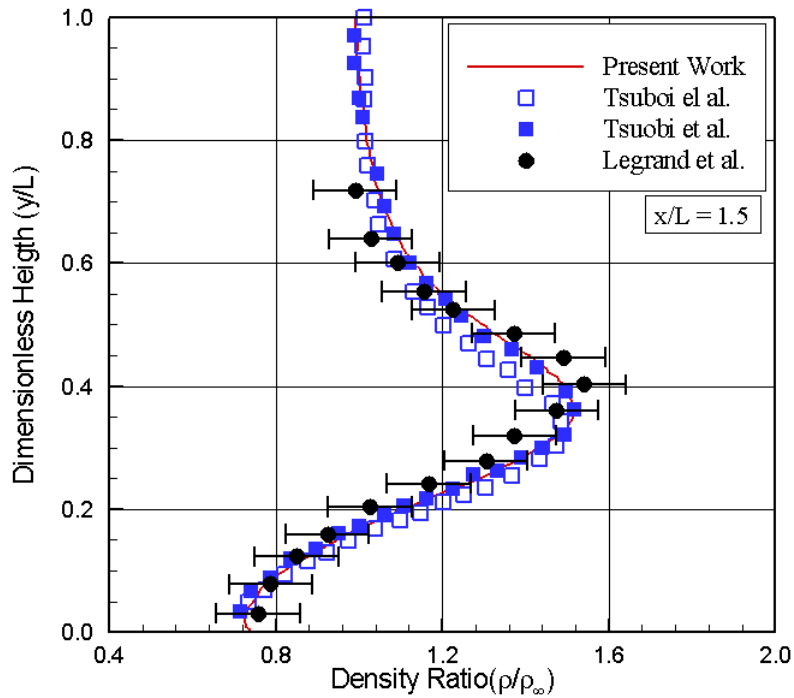
The first test case was developed in order to reproduce the results for a rarefied hypersonic flow over a flat-plate that was conducted experimentally by Lengrand et al. (LENGRAND et al., 1992) and reproduced numerically by Tsuboi and Matsumoto (TSUBOI; MATSUMOTO, 2001), as defined earlier in subsection 4.4.

Density ratio,  $\rho/\rho_\infty$ , profile normal to the flat plate surface is illustrated in Fig. 4.6 for section  $x/L = 1.5$  along the flat plate surface. In this plot, solid line stands for the present DSMC results, filled and empty square symbols represent numerical data for 0-degree and 20-degree leading-edge bevel angle, respectively, obtained by Tsuboi et al. (TSUBOI et al., 2004), and filled circle symbol represents experimental data obtained by Lengrand et al. (LENGRAND et al., 1992) with uncertainty of 10%. Based on this figure, it is observed that results obtained in this work present an excellent agreement as compared to experimental and numerical DSMC results obtained by Lengrand et al. (LENGRAND et al., 1992) and by Tsuboi et al. (TSUBOI et al., 2004).

In the following, Fig. 4.7 displays the wall pressure distribution along the flat plate. In this plot, wall pressure  $p_w$  is normalized by the freestream pressure  $p_\infty$ , and the distance  $x$  along the plate is normalized by the plate length  $L$ . Again, solid line stands for the present DSMC results, filled and empty square symbols represent numerical data for 0-degree and 20-degree leading-edge bevel angle, respectively, obtained by Tsuboi et al. (TSUBOI et al., 2004), and filled circle symbol represents experimental data obtained by Lengrand et al. (LENGRAND et al., 1992). In addition, filled and empty triangles correspond to DSMC results by considering the fraction  $f$  of inelastic collisions of 0.5 and 1.0, respectively, also simulated by Lengrand et al. (LENGRAND et al., 1992). Also, it is important to remark that wall pressure definition is given by Equation (5.6), Chapter 5.

According to Fig. 4.7, it is clearly noticed that the DSMC results present a good agreement only at the vicinity of the flat-plate leading edge, as compared to the experimental data. Far from the flat-plate leading edge, DSMC results overpredict

Figure 4.6 - Density ratio ( $\rho/\rho_\infty$ ) profile at section  $x/L = 1.5$  along the flat plate surface.

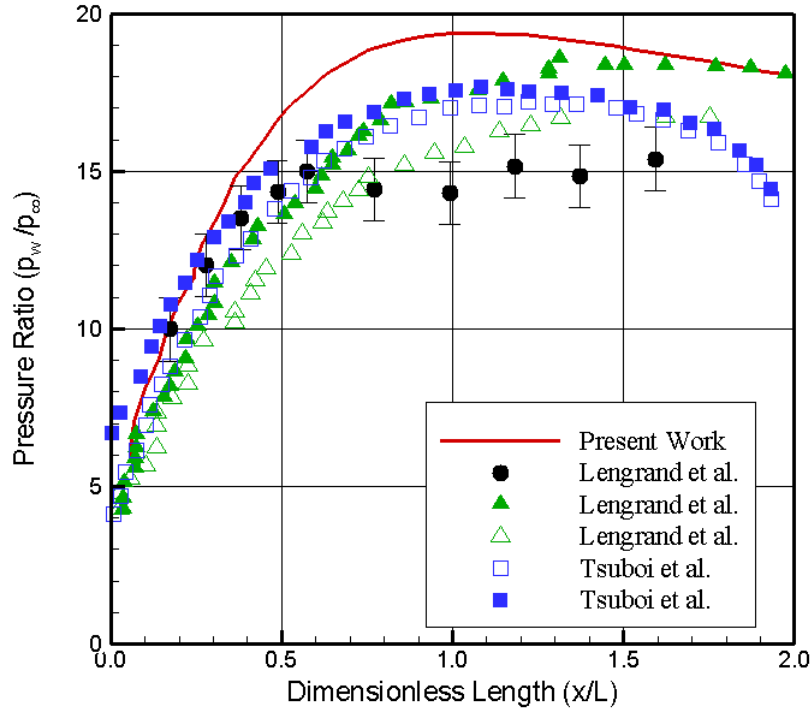


Filled circle: experimental data; filled square: 0-degree leading-edge bevel angle; empty square: 20-degree leading-edge bevel angle.

the experimental data for wall pressure. These differences are attributed to different numerical conditions, such as, molecular collision model, energy exchange model, and gas-surface interaction model, used between the current DSMC test case, the numerical data given by Lengrand et al. (LENGRAND et al., 1992), and the numerical DSMC investigation given by Tsuboi et al. (TSUBOI et al., 2004).

In what follows, Fig. 4.8 demonstrates the translational and rotational temperature distribution along the flat plate for the first row of cells immediately adjacent to flat plate. In this plot, translational temperature  $T_T$  and rotational temperature  $T_R$  are normalized by the freestream pressure  $T_\infty$ , and the distance  $x$  along the plate is normalized by the plate length  $L$ . In addition, solid and dashed lines stand for the present DSMC results, square and circle symbols represent numerical data for 0-degree and 20-degree leading-edge bevel angle, respectively, obtained by Tsuboi et al. (TSUBOI et al., 2004). Based on this plot, it is seen a good agreement of the present DSMC results with DSMC simulations given Tsuboi et al. (TSUBOI et al., 2004).

Figure 4.7 - Wall pressure ( $p_w/p_\infty$ ) distribution along the flat plate surface.



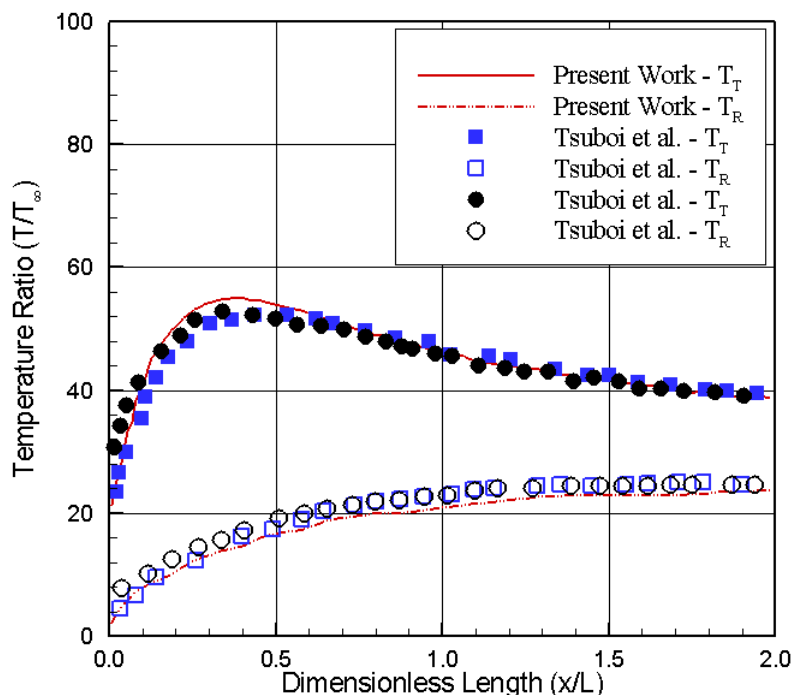
Filled circle: experimental data; filled square: 0-degree leading-edge bevel angle; empty square: 20-degree leading-edge bevel angle; filled triangle:  $f = 0.5$ ; empty triangle:  $f = 1.0$ .

#### 4.5.2 Second Test Case

The second test case, a rarefied hypersonic flow over a flat-plate at 40-degree of incidence, was simulated in order to reproduce the DSMC results obtained by Dogra et al. (DOGRA et al., 1989), as defined earlier in subsection 4.4. Results for three different locations along the flat-plate surface are presented for density, overall kinetic temperature and tangential velocity.

Density, overall kinetic temperature, and tangential velocity profiles normal to the flat plate surface are exhibited in Figs. 4.9, 4.10, and 4.11 for three sections along the flat-plate surface. In this set of plots, density  $\rho$  is normalized by the freestream density  $\rho_\infty$ , the overall kinetic temperature  $T_O$  is normalized by freestream temperature  $T_\infty$ , and tangential velocity  $u$  is normalized by  $U_\infty \cos \alpha$ , where  $\alpha$  is the angle of attack, 40 degrees. In addition, empty symbols stands for the present DSMC results and filled symbols represent DSMC results obtained by Dogra et al. (DOGRA et al., 1989). Also, it is important to mention that overall kinetic temperature  $T_O$

Figure 4.8 - Translational ( $T_T/T_\infty$ ) and rotational ( $T_R/T_\infty$ ) temperature distribution along the flat plate surface.



Square symbols: 0-degree leading-edge bevel angle; circle symbols: 20-degree leading-edge bevel angle.

is defined for a nonequilibrium gas as the weighted mean of the translational and internal temperatures, as given by Equation (5.1), Chapter 5.

According to this set of plots, it is observed that results obtained in this work present a good agreement as compared to numerical DSMC results obtained by Dogra et al. (DOGRA et al., 1989) for stations  $x/L$  of 0.1 and 0.5. However, for station  $x/L$  of 0.9, significant differences are observed in the overall kinetic temperature (small difference for density and tangential velocity) inside the shock layer. These differences are attributed to two effects: (1) the vacuum condition assumed as the downstream boundary condition, as explained in subsection 4.4.3, where the upstream disturbance seems to be larger than 10% of the plate length; (2) differences in the simulations conditions between the present DSMC simulations and those conducted by Dogra et al. (DOGRA et al., 1989), for instance, the recombination of Nitrogen and Oxygen atoms promoted by the flat-plate surface.

Figure 4.9 - Density ratio ( $\rho/\rho_\infty$ ) profiles normal to the plate surface for three locations along the plate surface.

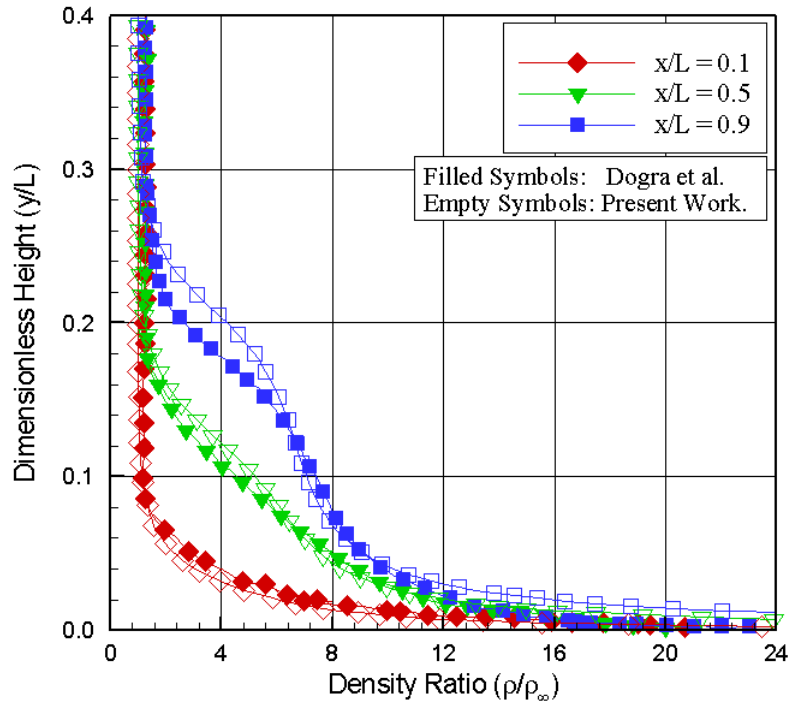


Figure 4.11 - Tangential velocity ratio ( $u/U_\infty \cos \alpha$ ) profiles normal to the plate surface for three locations along the plate surface.

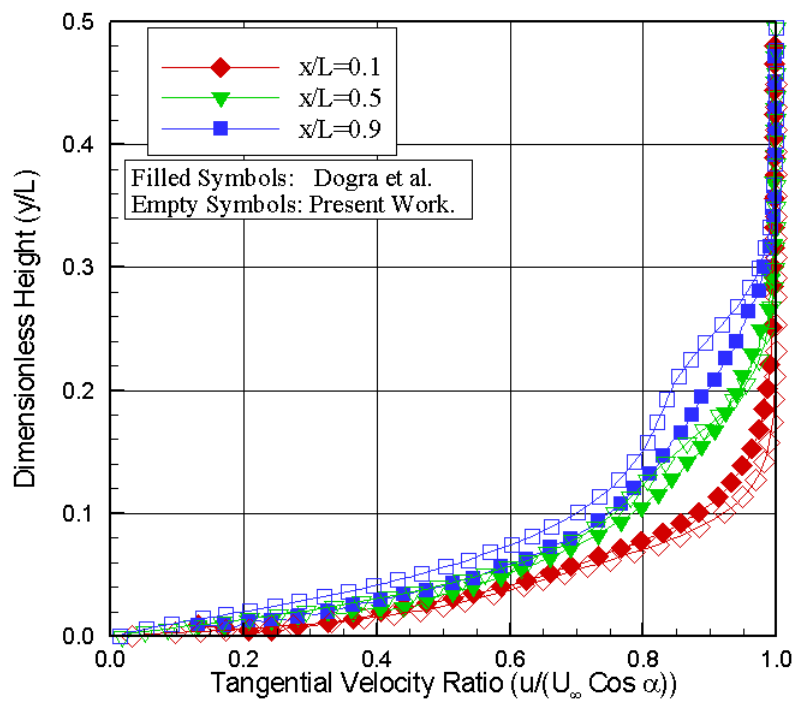
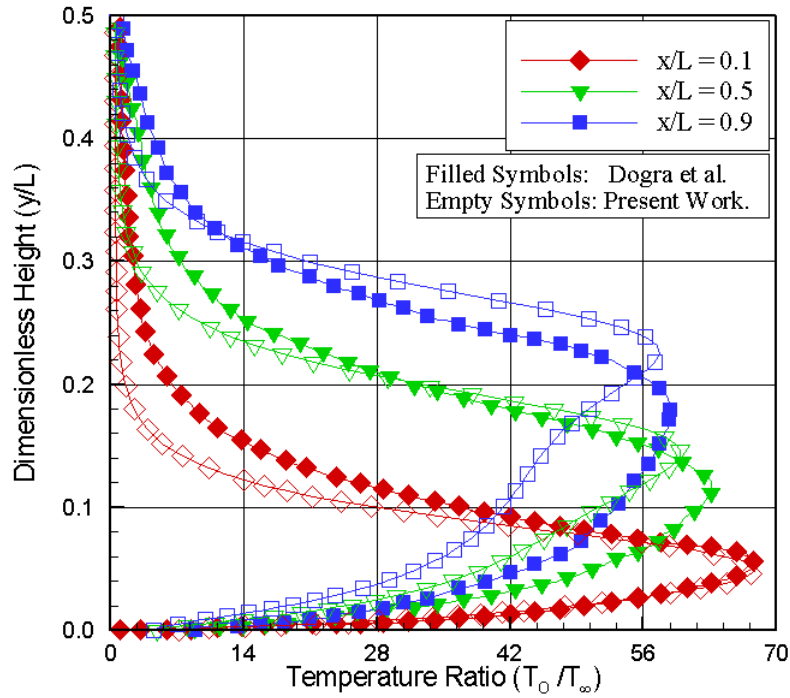


Figure 4.10 - Overall kinetic temperature ratio ( $T_O/T_\infty$ ) profiles normal to the plate surface for three locations along the plate surface.



#### 4.6 Gap Case

The verification procedures employed previously in the DSMC Test Case, section 4.4, were also employed to the gap configuration, defined in Chapter 3. In doing so, simulations were performed with computational meshes that met the general requirements for the DSMC method already presented in sections 4.1 to 4.3.

In this context, this section presents the analysis in order to verify the grid resolution and the influence of the number of simulated particles on the aerodynamic surface quantities, such as heat transfer, pressure, and skin friction coefficients, for a gap defined by  $L/H$  ratio of 1 and 10-degree angle of attack. A similar procedure was employed in the grid independence study for the other cases.

As was pointed out earlier, cell dimensions are more critical in the direction with high gradients. For a gap configuration, as illustrated in Fig. 3.2, the gradients are important in the direction normal to the gap surfaces and inside of it. Computer simulations were performed by considering computational meshes containing cells

distributed in seven regions. Table 4.4 tabulates the number of cells employed in the seven regions for a coarse, a standard, and a fine mesh for a gap defined by  $L/H$  ratio of 1 and 10-degree angle of attack.

The effect of altering the cell size in the  $x$ -direction was investigated for a coarse and a fine mesh with, respectively, 50% less and 100% more cells with respect to the standard mesh. Figures 4.12, 4.13, and 4.14 illustrate the cell size effects on pressure, skin friction, and heat transfer coefficients, respectively. In this group of plots,  $X$  is the length  $x$  normalized by the freestream mean free path  $\lambda_\infty$ , and  $Y_H$  is the height  $y$  normalized by the gap height  $H$ . In addition, the left-column plots refer to the distribution of the surface quantities along the gap upstream and downstream surfaces, i.e., surfaces S1 and S5, while the right-column plots correspond to the distribution on the surfaces inside the gap, i.e., surfaces S2, S3, and S4. According to this set of plots, the effect of changing the cell size in the  $x$ -direction on the aerodynamic surface quantities was rather insensitive to the range of cell spacing considered for the standard and fine meshes.

In analogous fashion, an examination was made in the  $y$ -direction with a coarse and a fine mesh with, respectively, 50% less and 100% more cells with respect to the standard mesh, as shown in Table 4.4. Figures 4.15, 4.16, and 4.17 illustrate the cell size effects on pressure, skin friction, and heat transfer coefficients, respectively, due to changes on the cell size in the  $y$ -direction only. Based in this set of plots, it is noticed that the effect of changing the cell size in the  $y$ -direction on the aerodynamic surface quantities was also insensitive to the range of cell spacing considered for the standard and fine meshes.

A similar examination was made for the dependence of the standard mesh on the number of molecules. The standard mesh for the gap  $L/H = 1$  case corresponds to a total of 950,000 molecules. Two new cases using the same mesh were investigated. These two new cases correspond to 475,000 and 1,900,000 molecules in the entire computational domain, i.e, cases with 50% less and 100% more cells with respect to the standard mesh. The influence of the number of molecules on pressure, skin friction, and heat transfer coefficients is displayed in Figs. 4.18, 4.19, and 4.20, respectively. As these cases presented the same results for the aerodynamic surface quantities, hence the standard mesh with a total of 950,000 molecules is considered enough for the computation of the flowfield properties. For illustration purpose, Fig. 4.21 demonstrates the standard mesh for the gap  $L/H = 1$  case. In these plots,  $X$  and  $Y$  are the length  $x$  and height  $y$  normalized by the freestream mean free path

$\lambda_\infty$ .

Table 4.4 - Number of cells in the ( $x$ -direction) and [ $y$ -direction] for the gap case of the  $L/H = 1$  and 10-degree angle of attack.

Region	Coarse	Standard	Fine
1	(15)[70] – (30)[35]	(30)[70]	(60)[70] – (30)[140]
2	(75)[100] – (150)[50]	(150)[100]	(300)[100] – (150)[200]
3	(25)[100] – (50)[50]	(50)[100]	(100)[100] – (50)[200]
4	(75)[100] – (150)[50]	(150)[100]	(300)[100] – (150)[200]
5	(25)[50] – (50)[25]	(50)[50]	(100)[50] – (50)[100]
6	(15)[70] – (30)[35]	(30)[70]	(60)[70] – (30)[140]
7	(25)[70] – (50)[35]	(50)[70]	(100)[70] – (50)[140]
#Cells	22,600	45,200	90,400

Figure 4.12 - Effect of variation in the cell size in the  $x$ -direction in pressure coefficient for  $L/H = 1$  case.

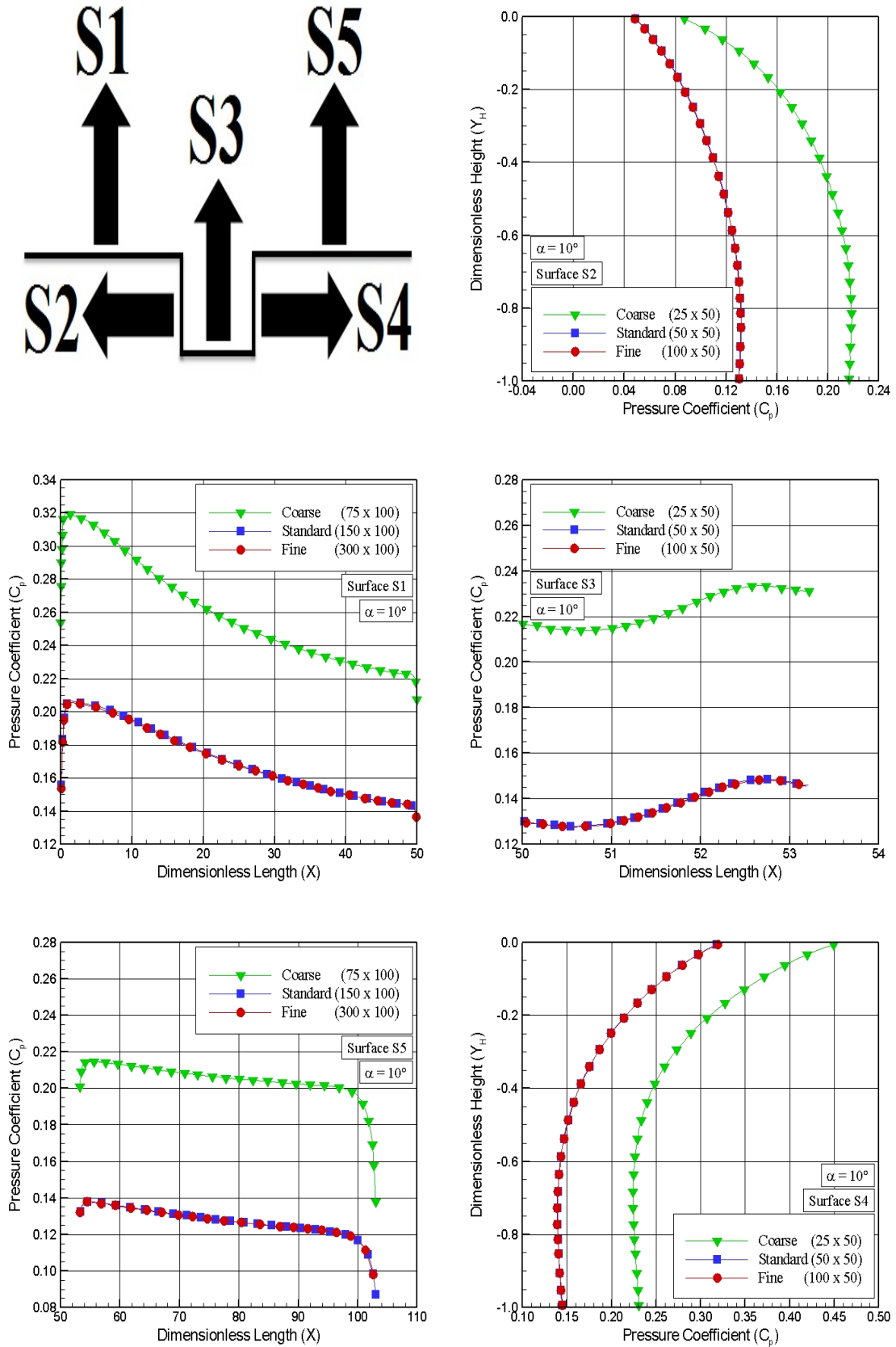


Figure 4.13 - Effect of variation in the cell size in the  $x$ -direction in skin friction coefficient for  $L/H = 1$  case.

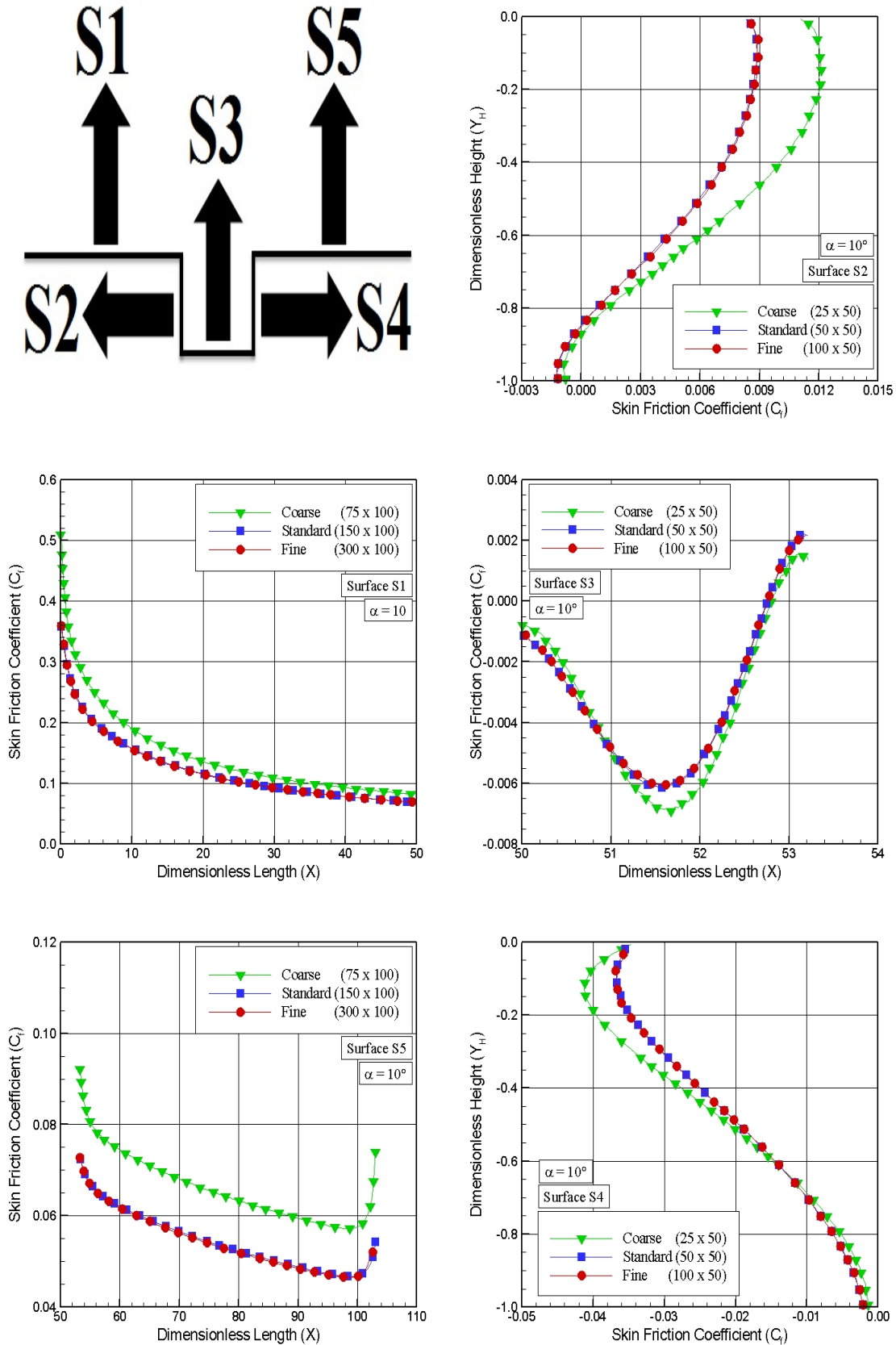


Figure 4.14 - Effect of variation in the cell size in the  $x$ -direction in heat transfer coefficient for  $L/H = 1$  case.

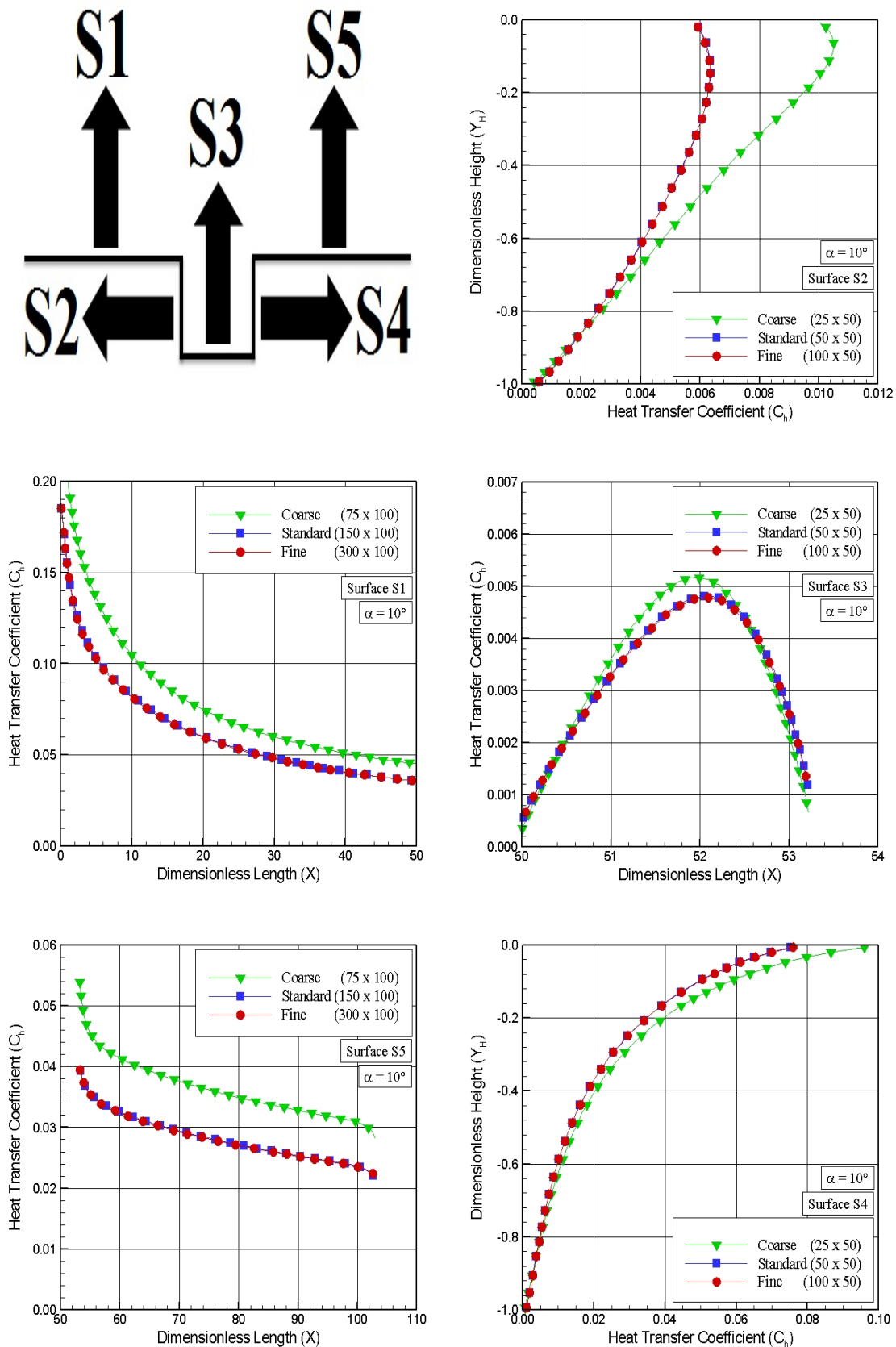


Figure 4.15 - Effect of variation in the cell size in the  $y$ -direction in pressure coefficient for  $L/H = 1$  case.

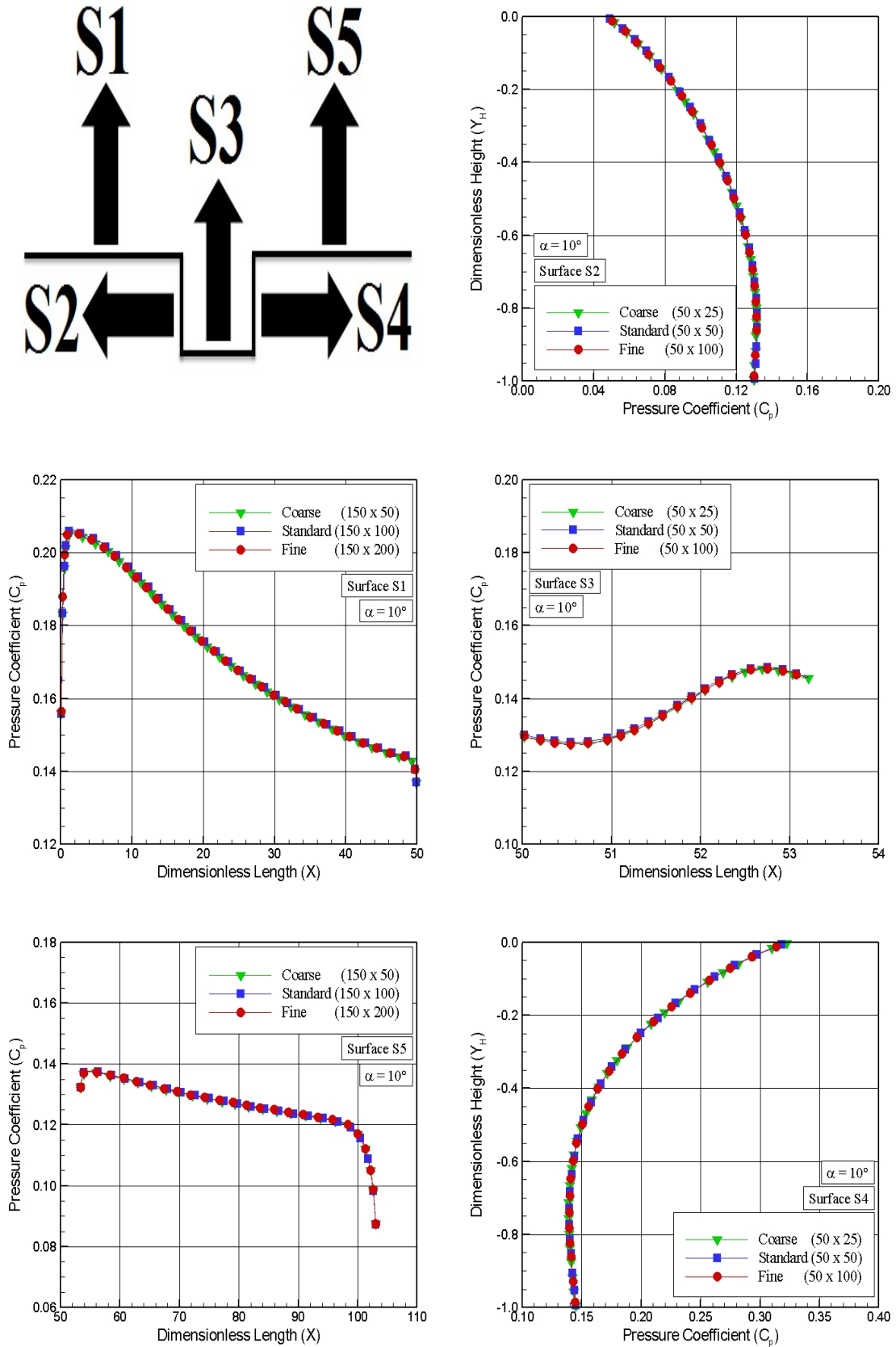


Figure 4.16 - Effect of variation in the cell size in the  $y$ -direction in skin friction coefficient for  $L/H = 1$  case.

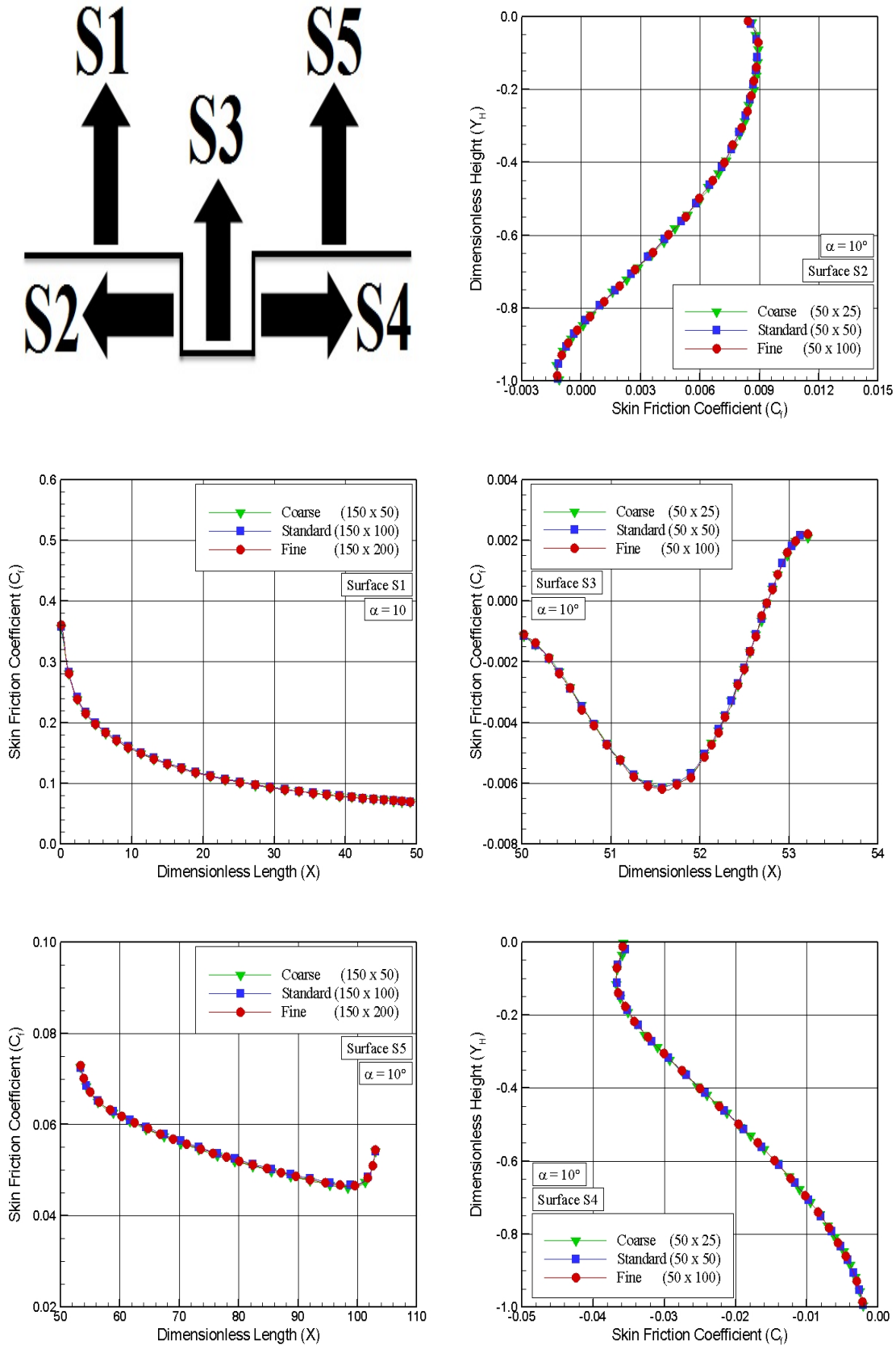


Figure 4.17 - Effect of variation in the cell size in the  $y$ -direction in heat transfer coefficient for  $L/H = 1$  case.

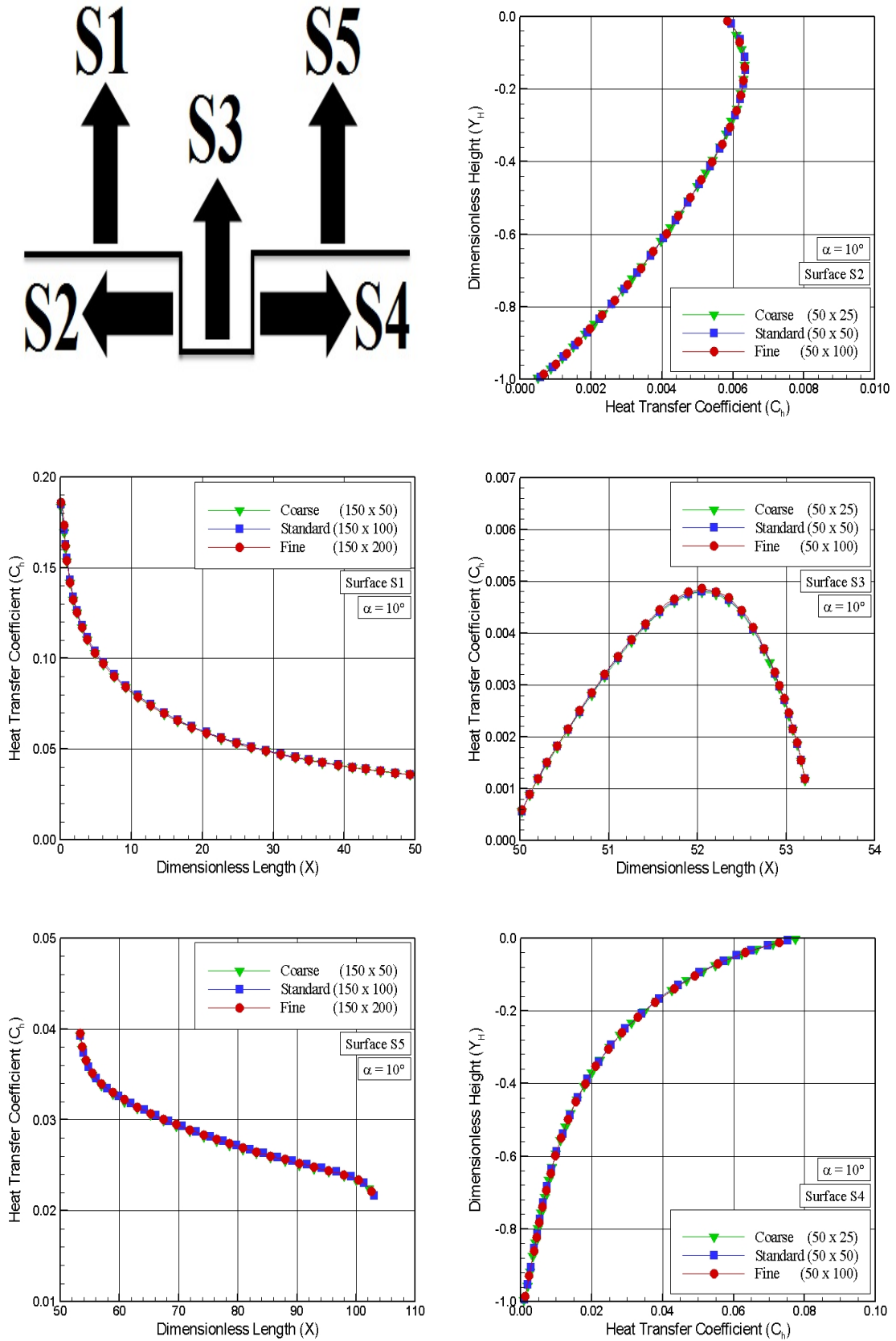


Figure 4.18 - Effect of variation in the number of molecules in pressure coefficient for  $L/H = 1$ .

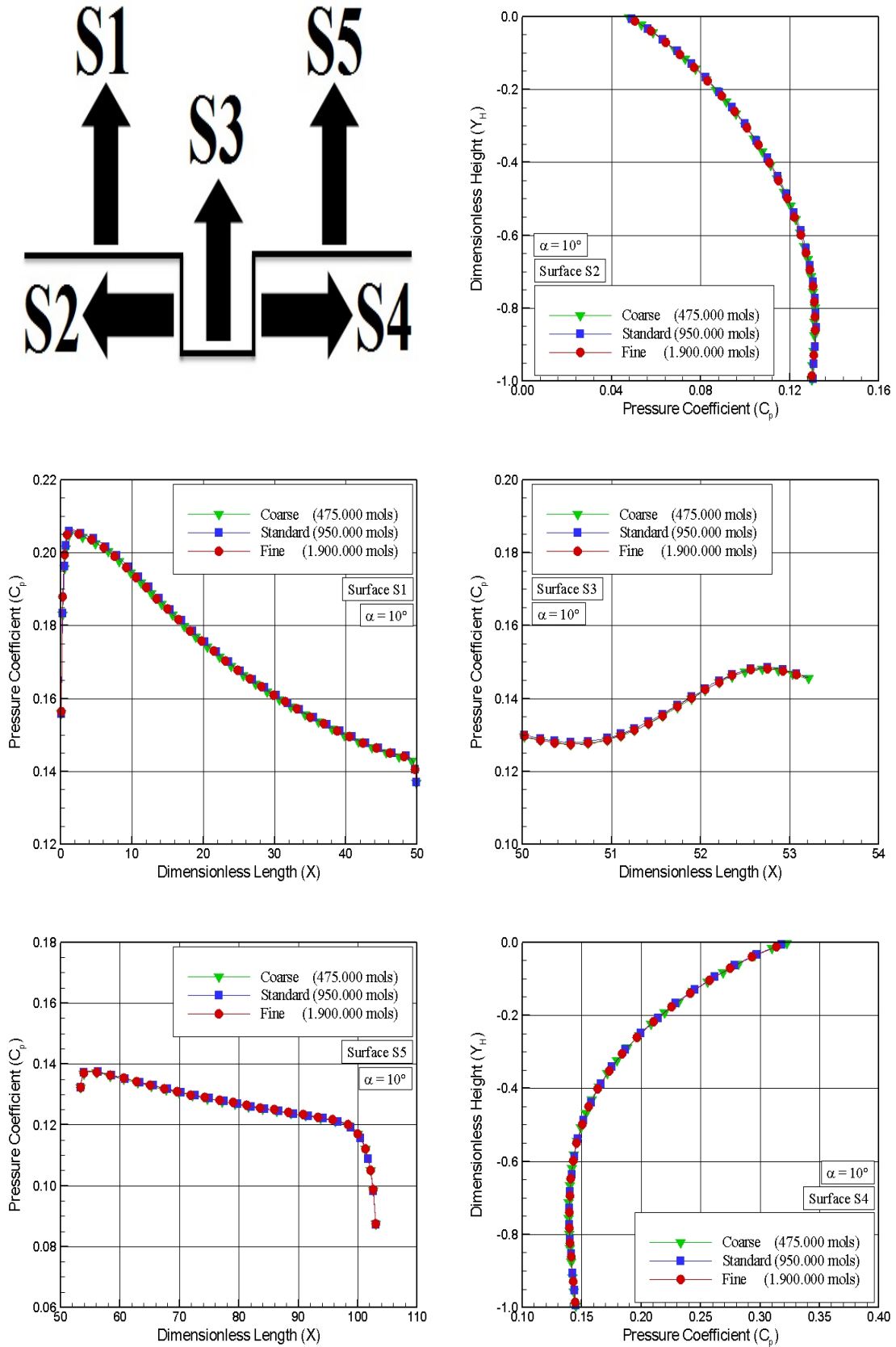


Figure 4.19 - Effect of variation in the number of molecules in skin friction coefficient for  $L/H = 1$ .

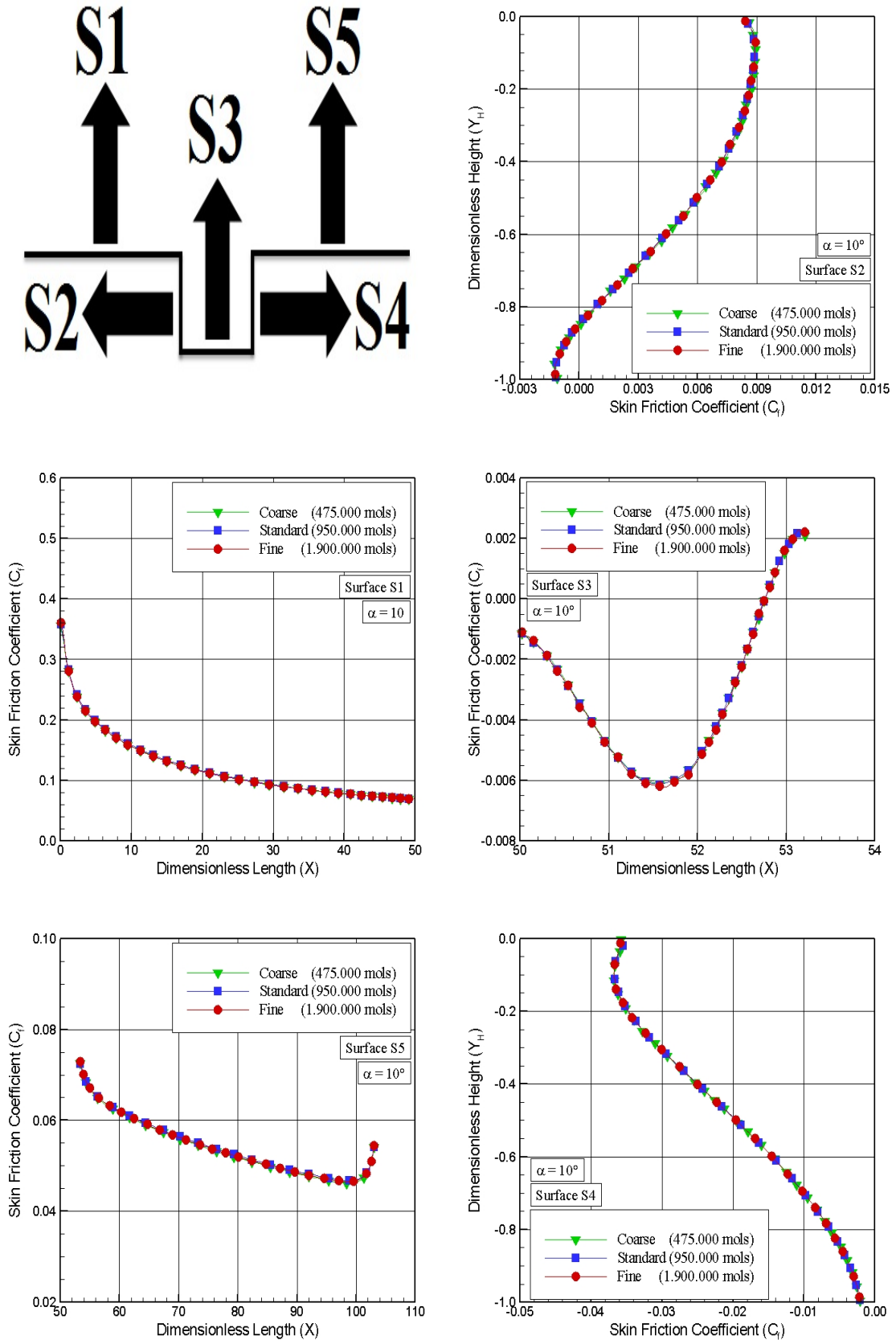


Figure 4.20 - Effect of variation in the number of molecules in heat transfer coefficient for  $L/H = 1$ .

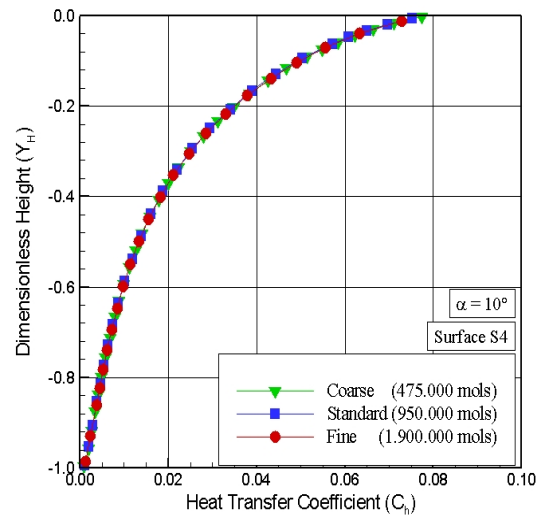
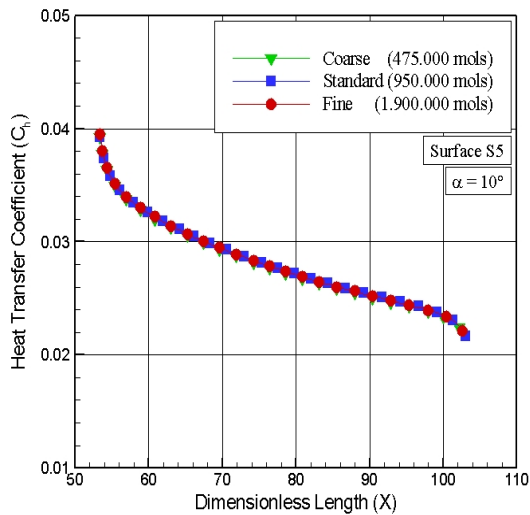
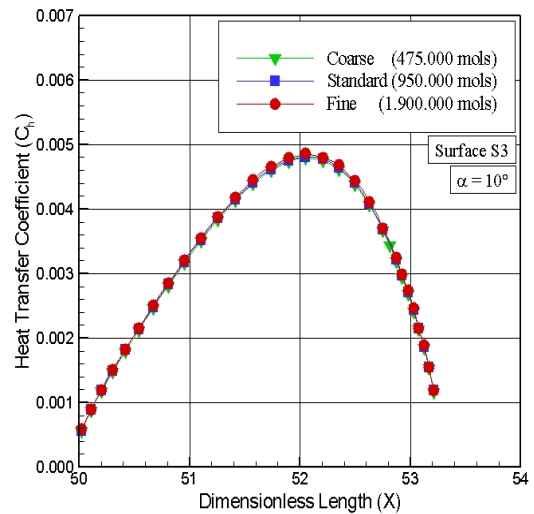
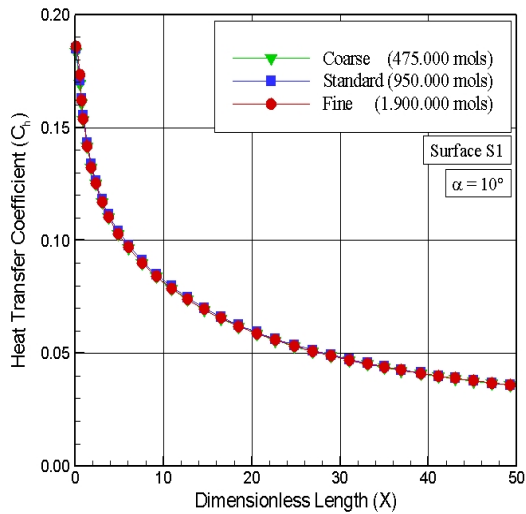
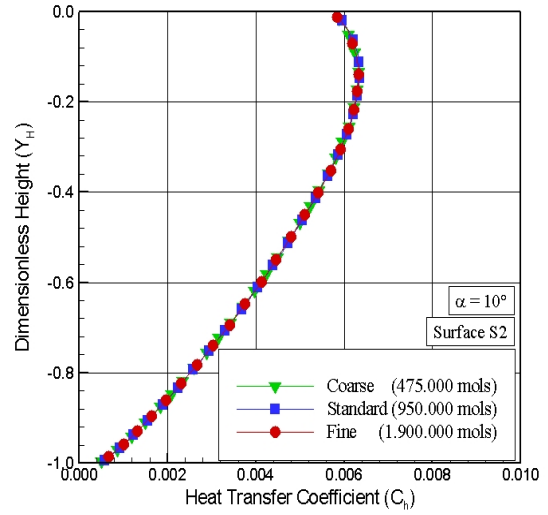
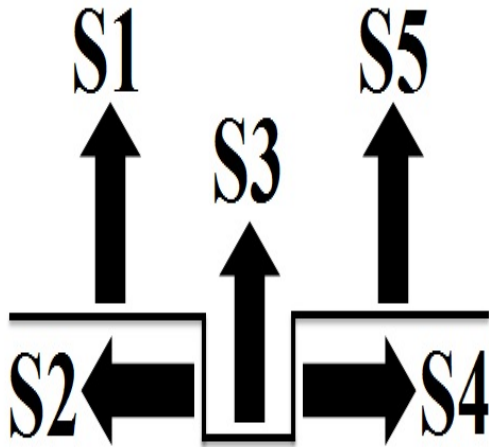
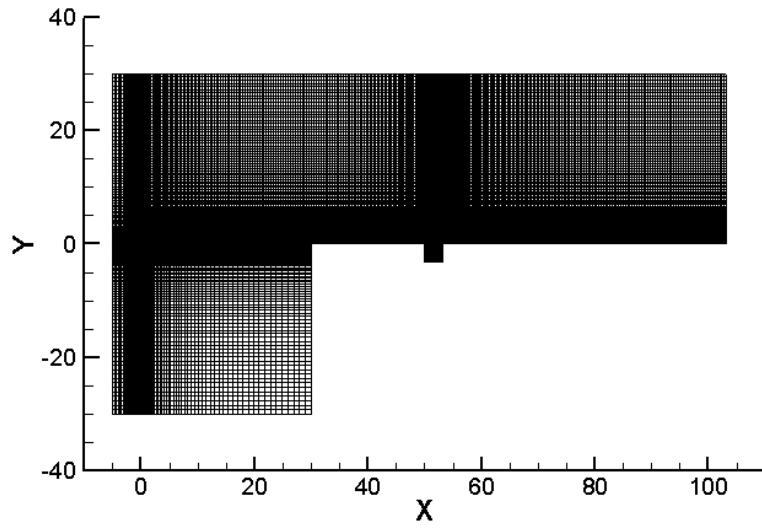
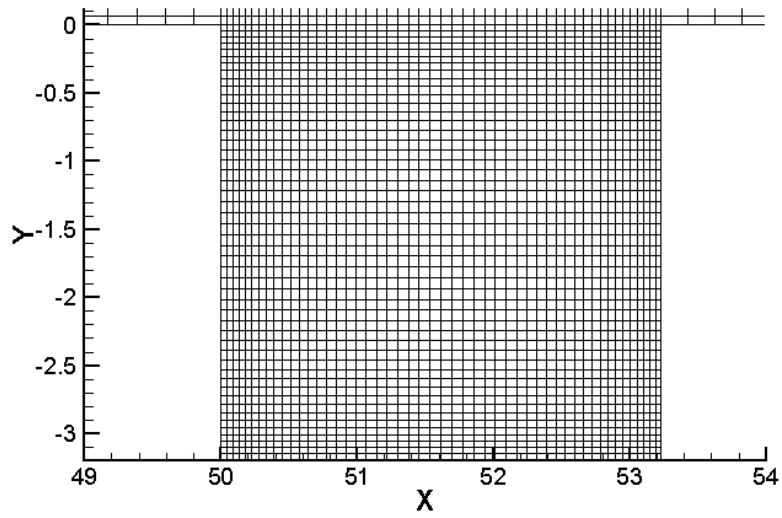


Figure 4.21 - A Drawing illustrating the cell distribution for (a) the standard mesh for the gap configuration with  $L/H = 1$  and 10-degree angle of attack, and (b) a magnified view of region R5.



(a)



(b)



## 5 COMPUTATIONAL RESULTS AND DISCUSSION

The study described in this work was undertaken with the objective of investigating the effects of the gap  $L/H$  ratio and the angle of attack  $\alpha$  for a hypersonic gap flow in the transition flow regime. In doing so, the purpose of this Chapter is to discuss and to compare differences in the flowfield structure as well as in the aerodynamic surface quantities due to variations on these two parameters,  $L/H$  ratio and  $\alpha$ .

### 5.1 Flowfield Structure

In order to present the DSMC results coherently, this section focuses on the calculations of the primary properties obtained from DSMC simulations. The primary properties of particular interest in this dissertation are velocity, density, pressure and kinetic temperatures.

#### 5.1.1 Velocity Field

Tangential velocity profiles for two sections outside the gap and their dependence on gap  $L/H$  ratio are illustrated in Fig. 5.1. In this set of plots, the tangential velocity  $u$  is normalized by the freestream velocity  $U_\infty$ ,  $Y$  stands for the height  $y$  normalized by the freestream mean free path  $\lambda_\infty$ , and  $X'_L$  represents the distance  $(x - L_u - L/2)$  normalized by the gap length  $L$ . Therefore, the two stations  $X'_L$  of -1 (left-column plots) and 1 (right column plots) correspond, respectively, to sections immediately upstream and downstream the gap position by a distance of  $L/2$ . In addition, for comparison purpose, the tangential velocity ratio profiles for the flat-plate case, i.e., a plate without a gap, are presented in the same plots as a solid line.

According to Fig. 5.1, it is observed that tangential velocity profiles for the gap  $L/H$  ratio and angle of attack  $\alpha$  investigated are identical to those for the flat-plate cases, indicating that the presence of the gaps does not influence the flowfield immediately upstream and downstream the gaps. It should be also observed that the tangential velocity  $u \rightarrow u_\infty$  as  $Y \rightarrow \infty$ . Therefore, because of the flow incidence,  $u_\infty$  varies as a function of the angle of attack  $\alpha$ ,  $u_\infty \rightarrow U_\infty \cos\alpha$  as  $Y \rightarrow \infty$ . As a result,  $u_\infty$  decreases with increasing the angle of attack, as shown in the plots.

Still referring to Fig. 5.1, particular attention should be paid to the magnitude of the tangential velocity at  $Y = 0$ . It is clearly noted that the velocity ratio  $u/U_\infty$  is not zero at the wall; there is a slip velocity, a characteristic of a rarefied flow. As a result, the condition  $u/U_\infty = 0$  does not apply in a rarefied flow at the wall. Another interesting characteristic in these plots is the similarity of the velocity profiles along

the body surface. This is an indication that the velocity profiles may be expressed in terms of functions that, in appropriate coordinates, may be independent of one of the coordinate directions. However, no attempts have been done to find such functions.

Effects on the tangential velocity profiles for two sections outside the gap due to changes on the angle of attack  $\alpha$  are demonstrated in Fig. 5.2 for gap  $L/H$  ratio of 1, 1/2, and 1/4. As a base of comparison, results for zero-degree angle of attack obtained by Paolicchi (PAOLICCHI, 2010) are presented in this set of plots. It is clearly seen that velocity profiles for the two sections outside the gap, for the angle of attack investigated, are identical to those for zero-degree angle of attack obtained by Paolicchi (PAOLICCHI, 2010), when the velocity  $u$  is normalized by  $U_\infty \cos\alpha$ .

Tangential velocity profiles inside the gaps for three sections  $X'_L$  are displayed in Fig. 5.3 parameterized by the gap  $L/H$  ratio. In this set of diagrams, the dimensionless height  $Y_H$  represents the height  $y$  normalized by the gap height  $H$ . The three sections  $X'_L$  of -0.25, 0.0, and 0.25 define, respectively, a section at the vicinity of the gap backward face, in the middle of the gap, and at the vicinity of the gap forward face. In addition, left- and right-column diagrams correspond to  $u/U_\infty$  for angle of attack  $\alpha$  of 10 and 20 degrees, respectively. Results for 15 degrees are intermediate, and they will not be shown.

On examining first the left-column diagrams, for 10-degree angle of incidence, it is noticed the tangential velocity profiles present a similar behavior for the three sections  $X'_L$ , i.e., the velocity ratio  $u/U_\infty$  is high at the top of the gap,  $Y_H = 0$ , becomes negative in the upper half portion of the gap,  $Y_H > -0.4$ , and then tends to zero toward the bottom of the gaps with decreasing the gap  $L/H$  ratio.

At section  $X'_L$  of -0.25, the velocity ratio  $u/U_\infty$  changes from positive to negative values at section  $Y_H$  of -0.371, -0.202, -0.134, and -0.101 for  $L/H$  ratio of 1, 1/2, 1/3, and 1/4, respectively. Nevertheless, when these values are normalized by the freestream mean free path  $\lambda_\infty$ , i.e., dimensionless height  $Y$ , one has -1.196, -1.303, -1.301, and -1.303, for  $L/H$  ratio of 1, 1/2, 1/3, and 1/4, respectively. On the other hand, at section  $X'_L$  of 0.25, velocity ratio changes to  $Y_H$  of -0.393, -0.209, -0.139, and -0.104 for  $L/H$  ratio of 1, 1/2, 1/3, and 1/4, respectively. Again, in terms of dimensionless height  $Y$ , they correspond to -1.271, -1.349, -1.350, and -1.348, for  $L/H$  ratio of 1, 1/2, 1/3, and 1/4, respectively. Therefore, it is firmly established that the thickness of the separated boundary layer is basically constant for  $L/H < 1$ , and slightly increases from section  $X'_L = -0.25$  to  $X'_L = 0.25$ .

Figure 5.1 - Tangential velocity ratio ( $u/U_\infty$ ) profiles for two sections outside the gaps and for angle of attack  $\alpha$  of 10, 15 and 20 degrees, parameterized by the gap  $L/H$  ratio.

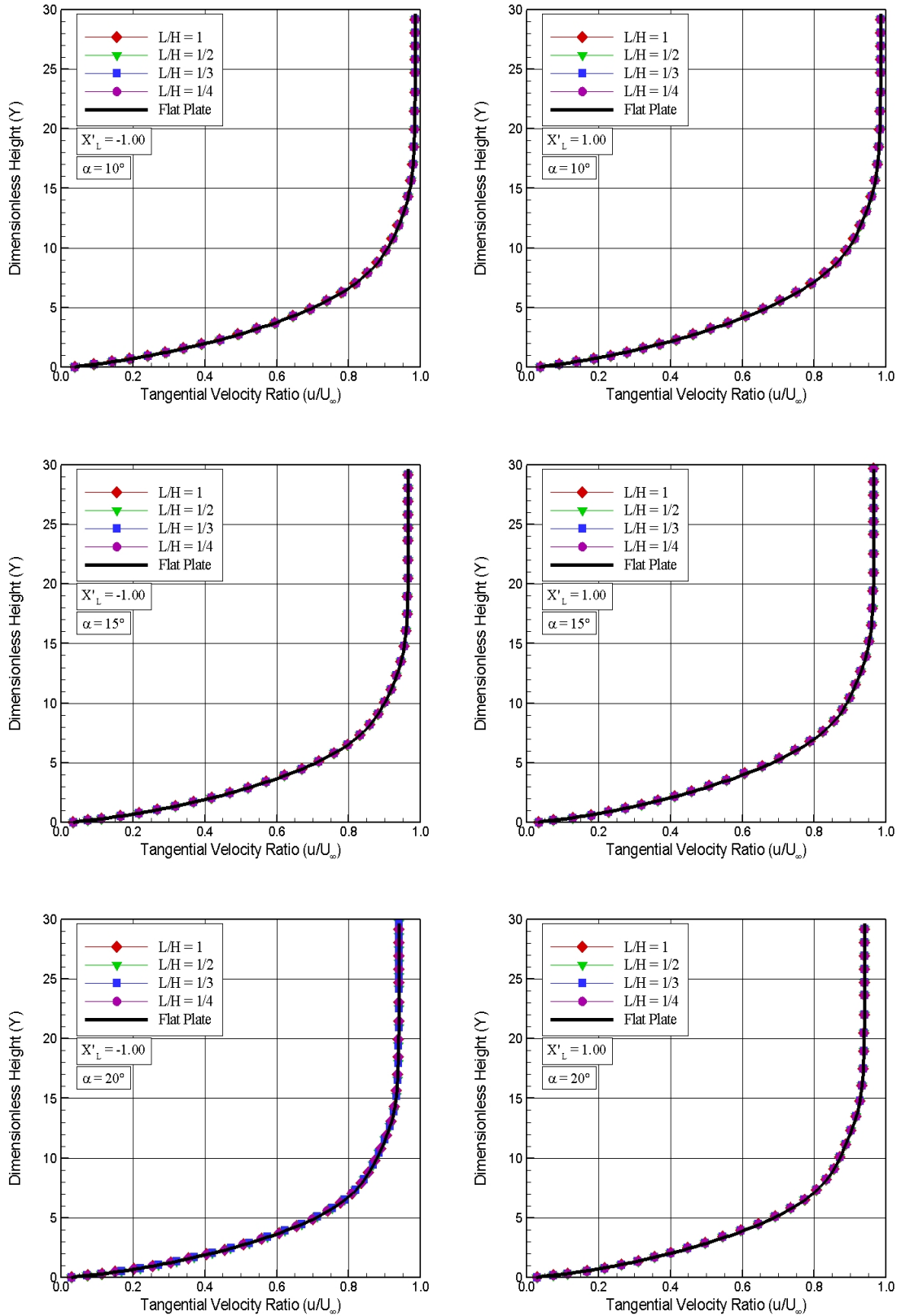
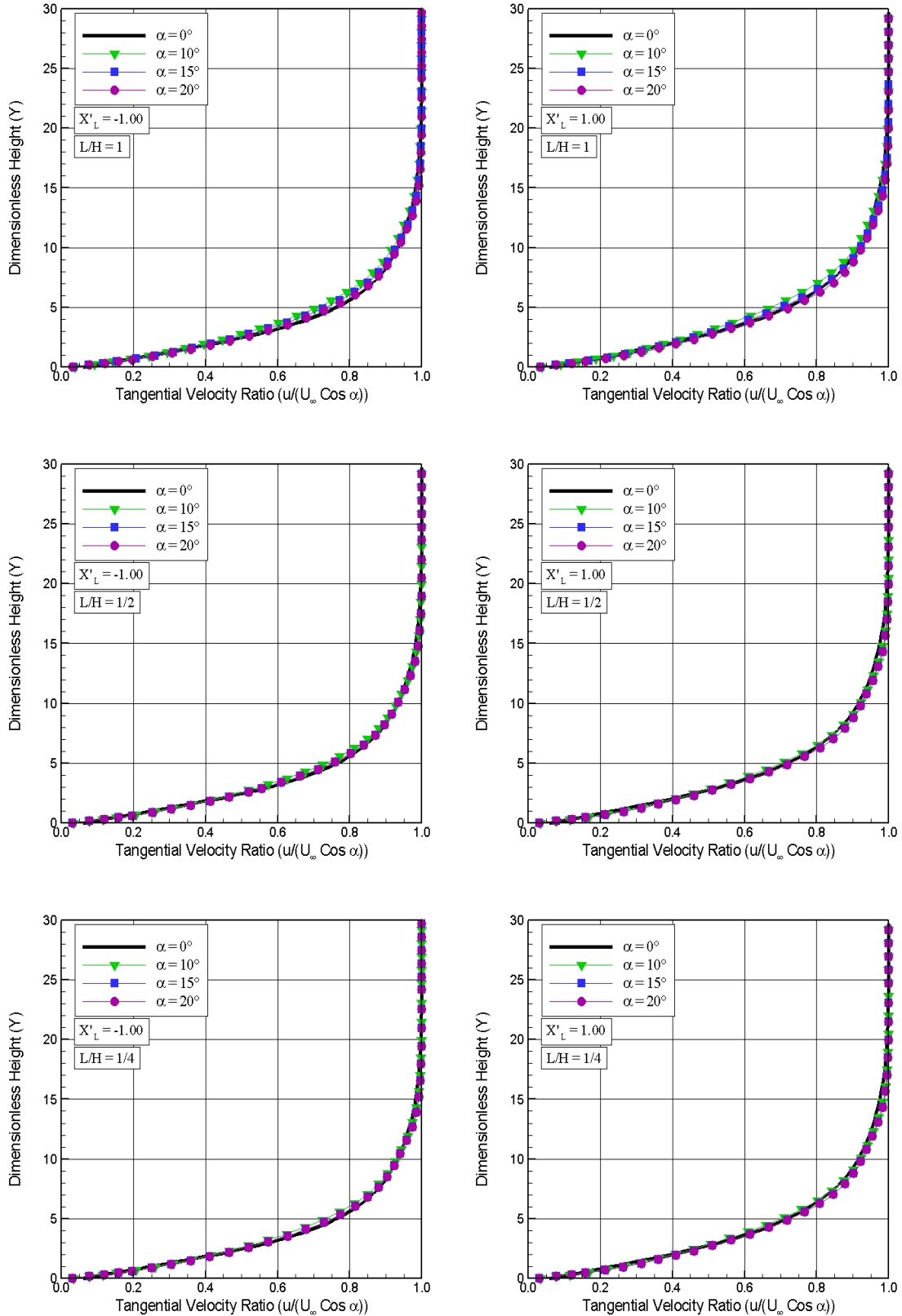


Figure 5.2 - Tangential velocity ratio ( $u/(U_\infty \cos \alpha)$ ) profiles for two sections outside the gaps and for  $L/H$  ratio of 1, 1/2, and 1/4, parameterized by the angle of attack  $\alpha$ .



Turning next to the right-column diagrams, for 20-degree angle of incidence, it is observed the tangential velocity profiles present a similar behavior for the three  $X'_L$  of -0.25, 0.0, and 0.25, in the sense that the velocity ratio  $u/U_\infty$  is high at the top of the gap, it becomes negative in the upper half portion of the gap, and then tends to zero toward the bottom of the gap with decreasing the gap  $L/H$  ratio. Nevertheless, the maximum value for the tangential velocity ratio at the top of the gap slightly increased as the angle of attack  $\alpha$  increased from 10 to 20 degrees. The reason for that is because the body is becoming blunter for the oncoming freestream molecules with increasing the angle of attack.

For comparison purpose, for 20-degree angle of attack, at section  $X'_L$  of -0.25,  $u/U_\infty$  changes from positive to negative values at section  $Y_H$  of -0.364, -0.191, -0.126, and -0.096 for  $L/H$  ratio of 1, 1/2, 1/3, and 1/4, respectively. At section  $X'_L$  of 0.25, velocity ratio changes to  $Y_H$  of -0.377, -0.196, -0.130, and -0.098 for  $L/H$  ratio of 1, 1/2, 1/3, and 1/4, respectively. In terms of dimensionless height  $Y$ , this set of values correspond to -1.176, -1.235, -1.225, and -1.238, and -1.217, -1.264, -1.259, and -1.266, for  $L/H$  ratio of 1, 1/2, 1/3, and 1/4, respectively.

The influence of the angle of attack  $\alpha$  on the tangential velocity ratio  $u/U_\infty$  inside the gap is exhibited in Figs. 5.4 and 5.5 for the same three sections  $X'_L$ , parameterized by the gap  $L/H$  ratio. In these plots, results for zero-degree angle of attack, obtained by Paolicchi (PAOLICCHI, 2010), are shown for comparison purpose. According to these plots, a small change in the tangential velocity ratio is observed as the angle of attack increases from 0 to 10 degrees, especially for  $L/H$  of 1. However, by visual inspection, no changes are observed in the tangential velocity ratio as the angle of attack increases from 10 to 20 degrees.

Normal velocity profiles inside the gaps for three sections  $Y_H$  are demonstrated in Fig. 5.6 as a function of the streamwise distance  $X'_L$ , parameterized by the gap  $L/H$  ratio. In this set of plots, the normal velocity  $v$  is normalized by the freestream velocity  $U_\infty$ , and the three sections  $Y_H$  correspond to the transverse sections defined by -0.25, -0.50, and -0.75, i.e., a section close to the top, in the middle, and close to the bottom of the gap, respectively. In addition, left- and right-column plots correspond to  $v/U_\infty$  for angle of attack of 10 and 20 degrees, respectively.

According to these plots, it is clearly seen that near the gap backward face,  $X'_L \cong -0.4$ , the normal velocity ratio profiles present positive values for the gap  $L/H$  ratio investigated in the upper half portion of the gap, meaning that the flow is moving upward. Conversely, at the vicinity of the gap forward face,  $X'_L \cong 0.4$ , the

Figure 5.3 - Tangential velocity ratio ( $u/U_\infty$ ) profiles for three sections inside the gaps as a function of the dimensionless height  $Y_H$ , parameterized by the gap  $L/H$  ratio. Left- and right-column plots correspond to angle of attack  $\alpha$  of 10 and 20 degrees, respectively.

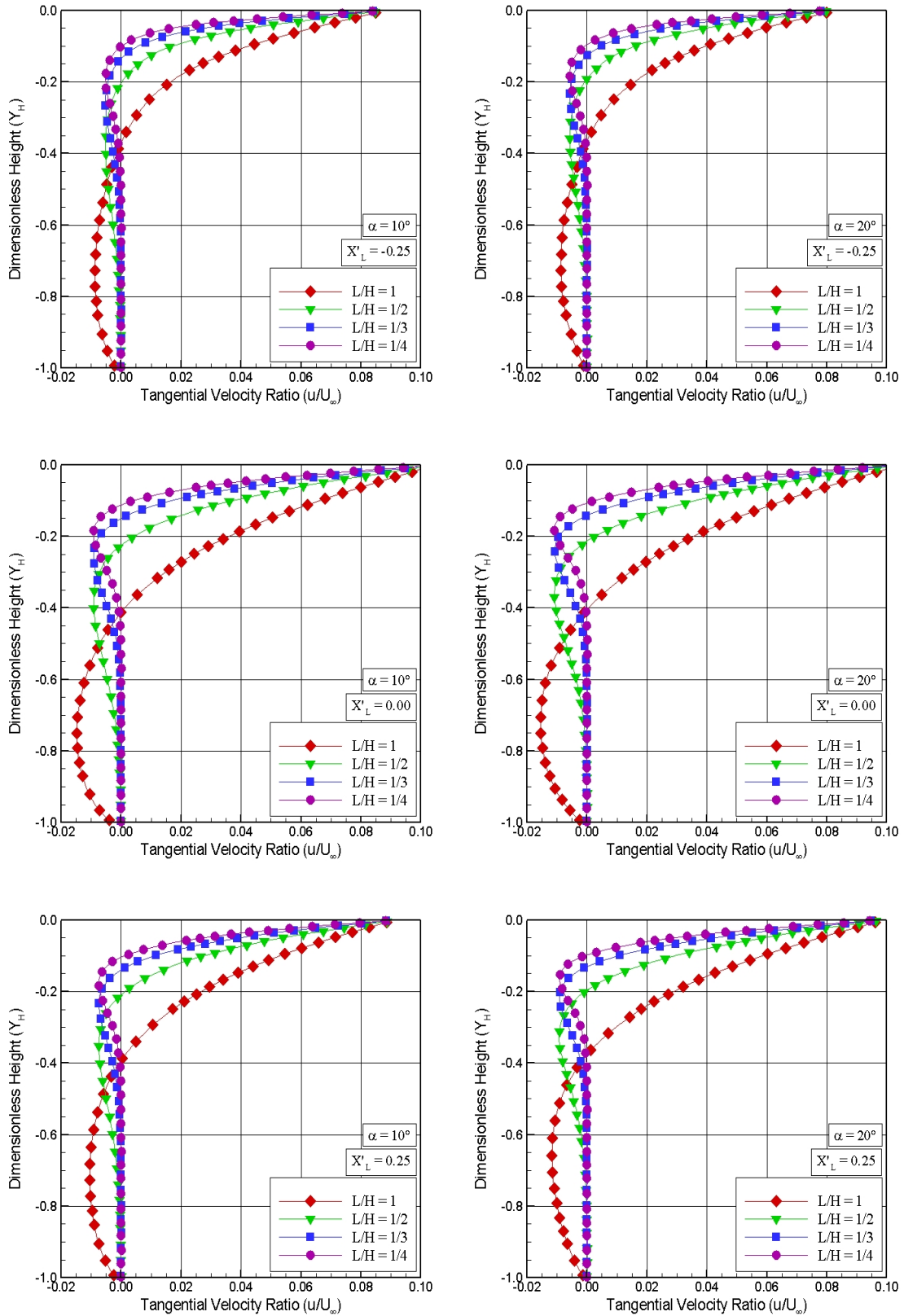


Figure 5.4 - Tangential velocity ratio ( $u/U_\infty$ ) profiles for three sections inside the gaps as a function of the dimensionless height  $Y_H$ , parameterized by the angle of attack  $\alpha$ . Left- and right-column plots correspond to gap  $L/H$  ratio of 1 and  $1/2$ , respectively.

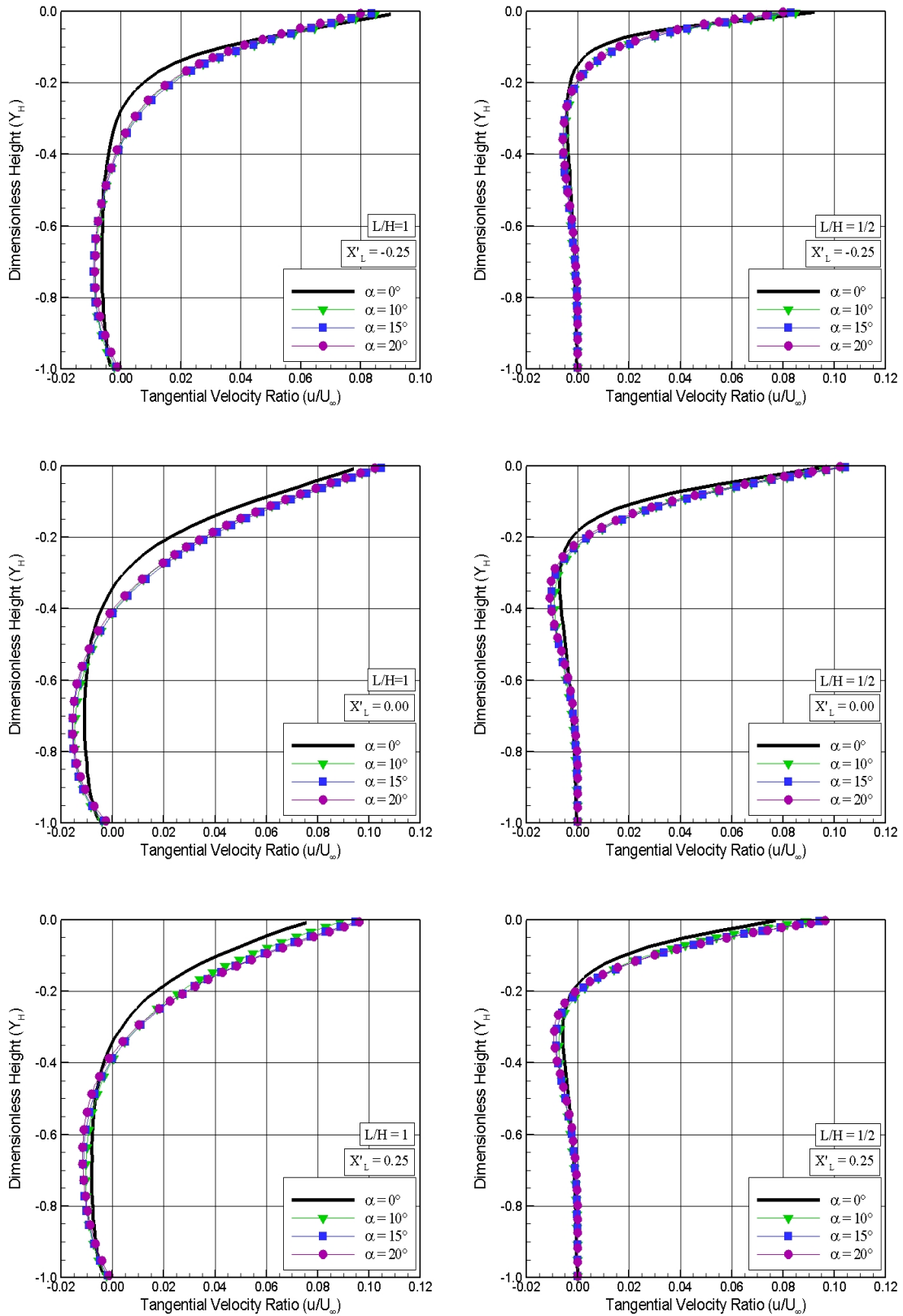


Figure 5.5 - Tangential velocity ratio ( $u/U_\infty$ ) profiles for three sections inside the gaps as a function of the dimensionless height  $Y_H$ , parameterized by the angle of attack  $\alpha$ . Left- and right-column plots correspond to gap  $L/H$  ratio of  $1/3$  and  $1/4$ , respectively.

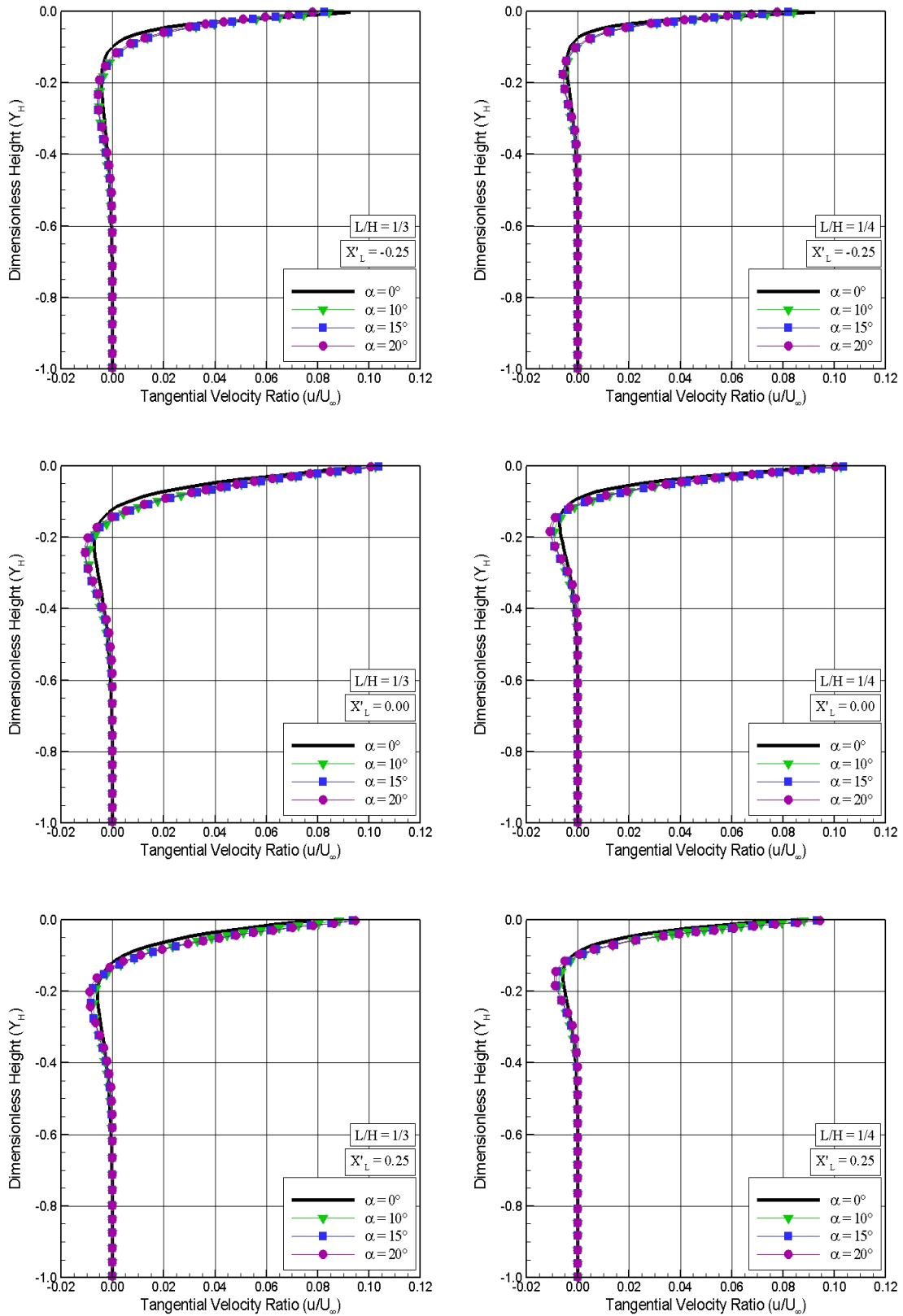
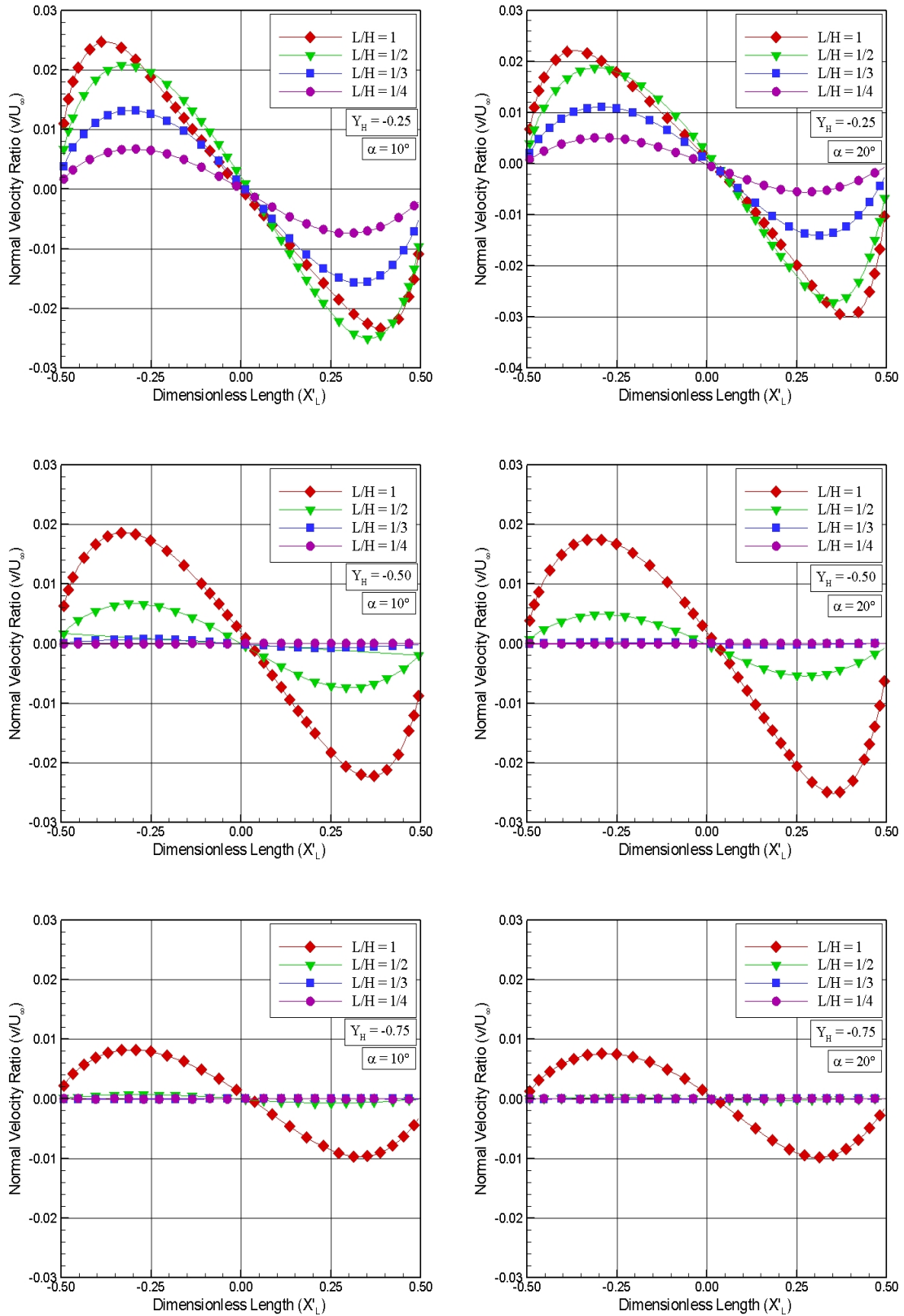


Figure 5.6 - Normal velocity ratio ( $v/U_\infty$ ) profiles for three transverse sections inside the gaps as a function of the dimensionless length  $X'_L$ , parameterized by the gap  $L/H$  ratio. Left- and right-column plots correspond to angle of attack  $\alpha$  of 10 and 20 degrees, respectively.



normal velocity ratio profiles present negative values, indicating that the flow is moving downward. Therefore, based on the two opposite behaviors for the normal velocity ratio, it may be inferred in passing that there is a region of a clockwise circulating flow. In addition, of particular interest is the behavior of the normal velocity ratio profiles near the bottom surface of the gaps, i.e.,  $Y_H = -0.75$ . It is quite apparent that the  $v$ -velocity component is around zero, indicating that there is no a recirculation region at the vicinity of the gap floor for  $L/H < 1$ . Moreover, no significant differences are observed in the normal velocity ratio profiles as the angle of attack increases from 10 to 20 degrees.

In attempting to assess the angle of attack impact on the normal velocity ratio inside the gap, Figs. 5.7 and 5.8 illustrate the normal velocity ratio,  $v/U_\infty$ , as a function of the streamwise distance  $X'_L$  for the same three transverse sections  $Y_H$ . As a base of comparison, results for zero-degree angle of attack, obtained by Paolicchi (PAOLICCHI, 2010), are shown in this set of plots.

Based on this set of plots, it is noted that the normal velocity ratio increases with increasing the angle of attack at the vicinity of the gap backward and forward faces in the upper half portion of the gap. As mentioned earlier, the body is becoming blunter for the oncoming freestream molecules with increasing the angle of attack. In addition, this increase is more significant close to the gap forward face than to the gap backward face. The reason for that is because the flow experiences an expansion close to the backward face and a compression close to the forward face.

In the following, based on the aforementioned behavior for the tangential and normal velocity ratio inside the gap, it becomes instructive to take a closer look at the recirculation region. In this scenario, streamline traces inside the gaps are depicted in Fig. 5.9. In this set of diagrams, the  $L/H$  ratio decreases from 1 (left side) to  $1/4$  (right side), and the angle of attack increases from 10 (top) to 20 (bottom) degrees.

Referring to Fig. 5.9, it is clearly noticed that the flow within the gaps is characterized by a primary recirculation system. For the  $L/H = 1$  case, the recirculation region fills the entire gaps for the angle-of-attack range investigated. For the  $L/H < 1$  cases, the recirculation region does not fill the entire gaps. In addition, a secondary recirculation region appears in the gaps with increasing the angle of attack  $\alpha$ . Furthermore, the primary recirculation region seems to be of the same size, by visual inspection, as the angle of attack increases from 10 to 20 degrees.

It may be recognized from this set of diagrams that, for the  $L/H < 1$  cases, the

Figure 5.7 - Normal velocity ratio ( $v/U_\infty$ ) profiles for three transverse sections inside the gaps as a function of the dimensionless length  $X'_L$ , parameterized by the angle of attack  $\alpha$ . Left- and right-column plots correspond to gap  $L/H$  ratio of 1 and 1/2, respectively.

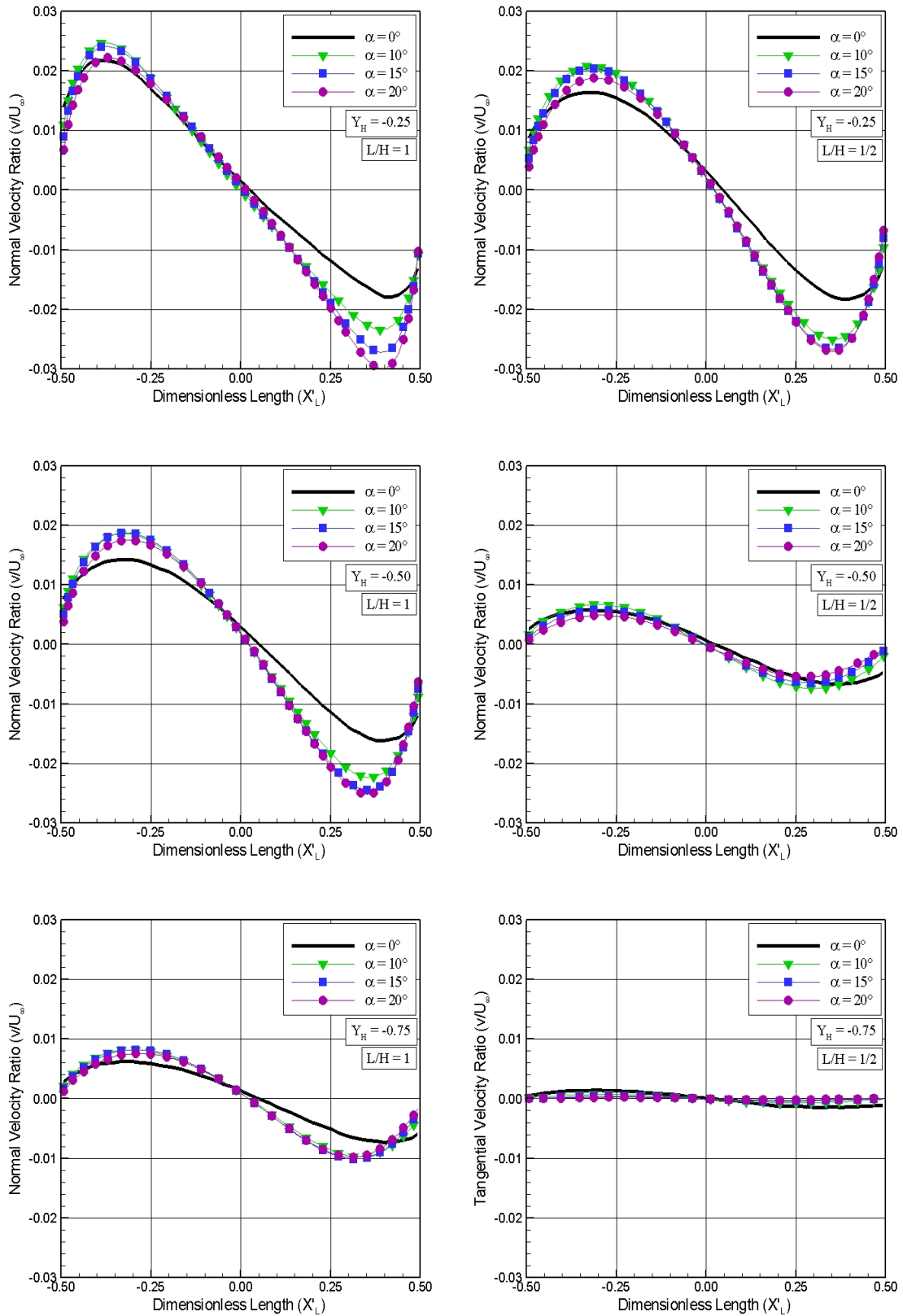


Figure 5.8 - Normal velocity ratio ( $v/U_\infty$ ) profiles for three transverse sections inside the gaps as a function of the dimensionless length  $X'_L$ , parameterized by the angle of attack  $\alpha$ . Left- and right-column plots correspond to gap  $L/H$  ratio of 1/3 and 1/4, respectively.

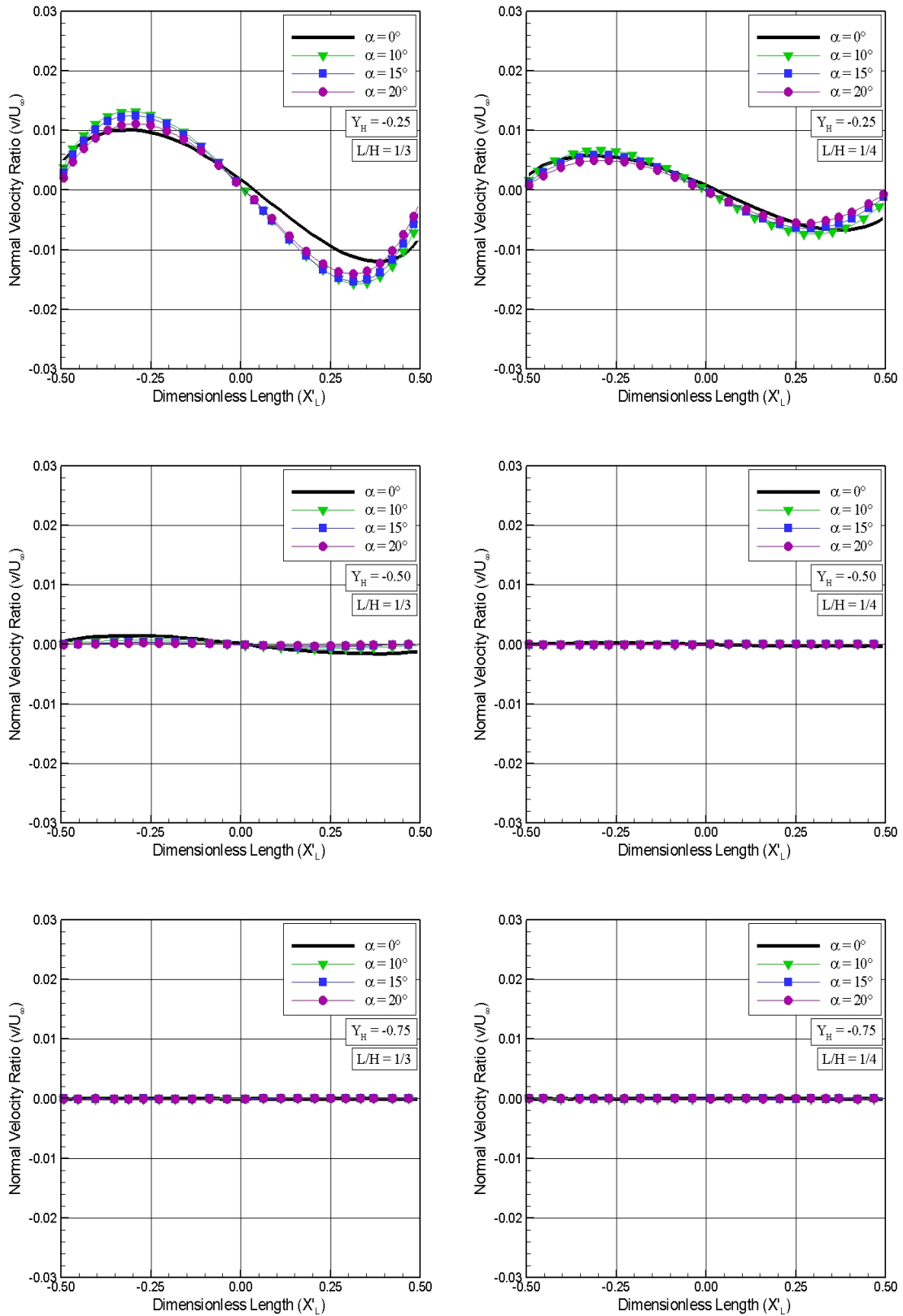
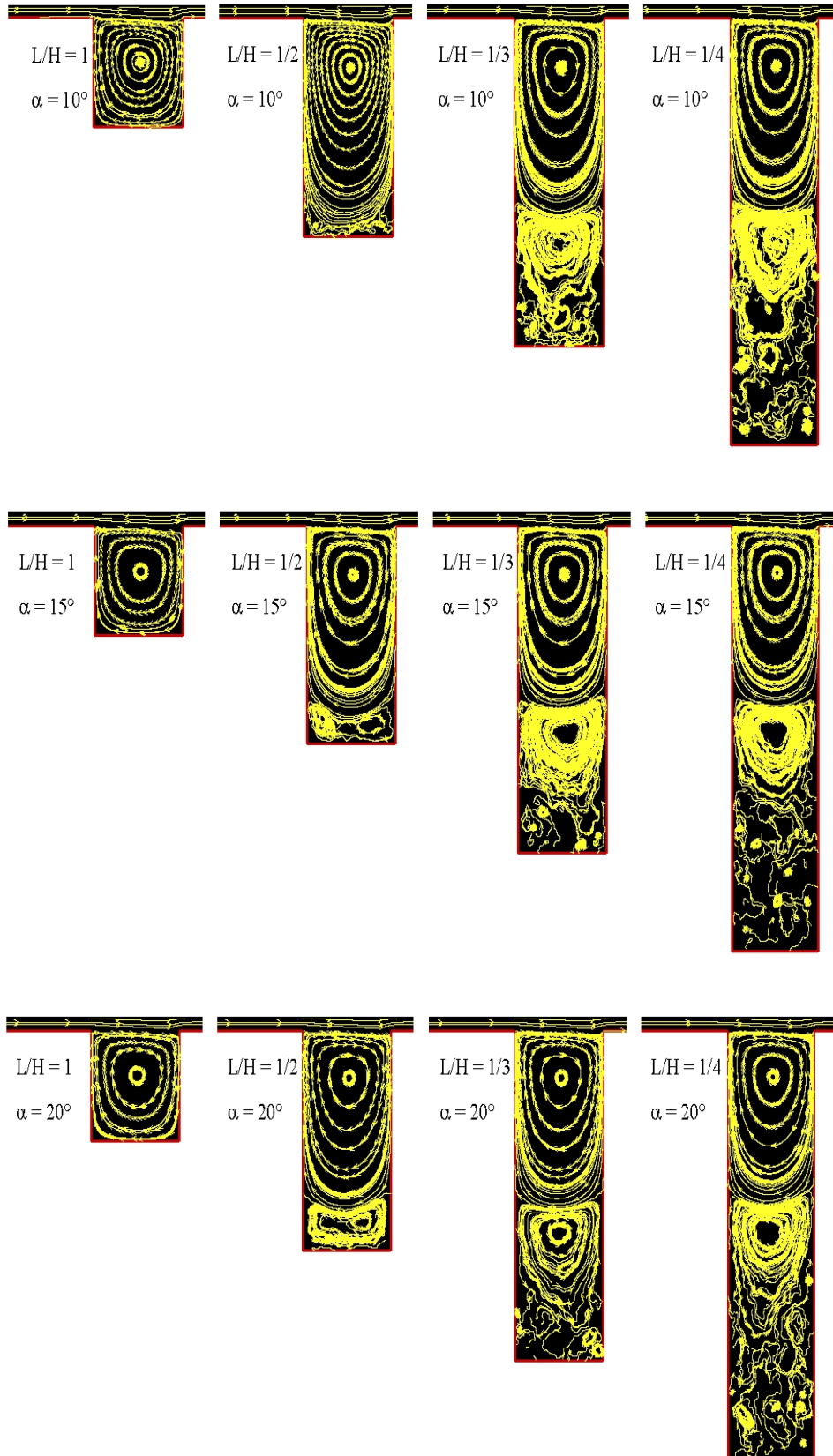


Figure 5.9 - Distribution of streamline traces inside the gaps for  $L/H$  of 1 (left), 1/2, 1/3, and 1/4 (right), with angle attack  $\alpha$  of 10 (top), 15, and 20 (bottom) degrees.



gap flow topology differs from that obtained by Paolicchi (PAOLICCHI, 2010) for zero-degree angle of attack (Fig. 1.5). Moreover, the flow topology observed here in a rarefied environment differs from that usually observed in the continuum flow regime, as defined in Chapter 1 (Fig. 1.4).

### 5.1.2 Density Field

The impact on the density profiles due to changes on gap  $L/H$  ratio for two sections outside the gap are illustrated in Fig. 5.10. In this set of plots, the density  $\rho$  is normalized by the freestream density  $\rho_\infty$ . Again,  $Y$  stands for the height  $y$  normalized by the freestream mean free path  $\lambda_\infty$ , and the two stations  $X'_L$  of -1 (left-column plots) and 1 (right column plots) correspond, respectively, to sections immediately upstream and downstream the gap as defined earlier. In addition, as a base of comparison, density ratio profiles for the flat-plate case are presented in the same plots.

Based on Fig. 5.10, it is noticed that, similar to tangential velocity profiles, density ratio profiles for the gap  $L/H$  ratio and angle of attack  $\alpha$  investigated are basically identical to those for the flat-plate cases, indicating that the presence of the gaps does not influence the flowfield immediately upstream the gap, section  $X'_L = -1$ . However, for section  $X'_L = 1$ , density ratio profiles for the gaps are slightly different from that for the flat-plate case at the vicinity of the wall, indicating that the presence of the gaps is still felt at least a half-gap length downstream the gaps.

The influence of the angle of attack  $\alpha$  on the density ratio for two sections outside the gap is demonstrated in Fig. 5.11 for gap  $L/H$  ratio of 1, 1/2, and 1/4. For comparison purpose, results for zero-degree angle of attack obtained by Paolicchi (PAOLICCHI, 2010) are presented in this set of plots. According to these plots, it is clearly seen that density ratio increases significantly with increasing the angle of attack  $\alpha$ . The reason for that is because, for the oncoming freestream molecules, the body is changing from an aerodynamic sharp one to a blunt body with increasing the angle of attack.

Still referring to Fig. 5.11, it is observed that the density ratio undergoes significant changes in the direction perpendicular to the surface. The density ratio is high adjacent to the wall,  $Y \approx 0$ , and rapidly decreases to a minimum value inside a layer of thickness around two to three freestream mean free paths. For instance, for the case of zero-degree angle of attack, the density ratio is less than one. It means that the density  $\rho$  is smaller than the freestream density  $\rho_\infty$ . This behavior, the gas

Figure 5.10 - Density ratio ( $\rho/\rho_\infty$ ) profiles for two sections outside the gaps and for angle of attack  $\alpha$  of 10, 15 and 20 degrees, parameterized by the gap  $L/H$  ratio.

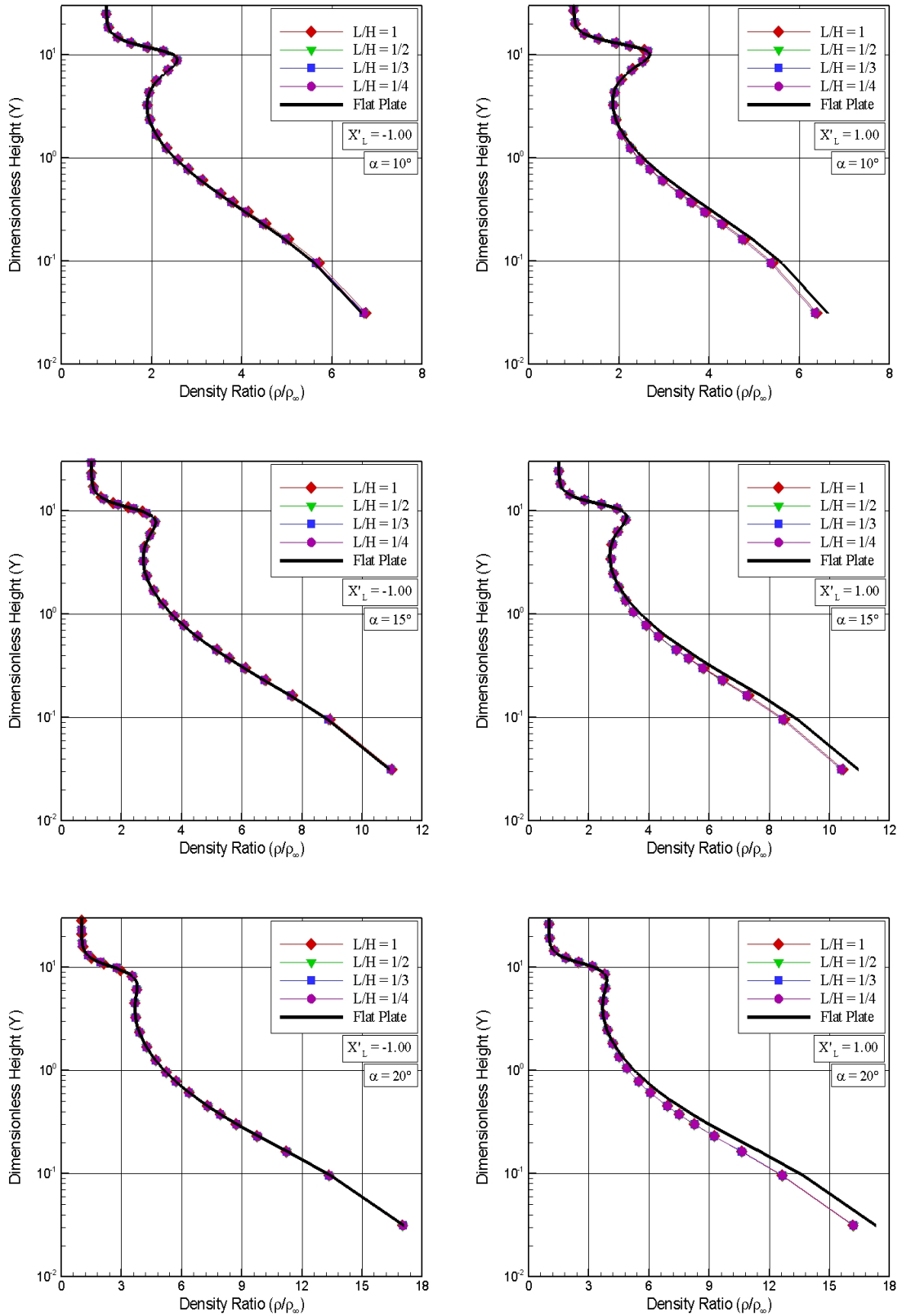
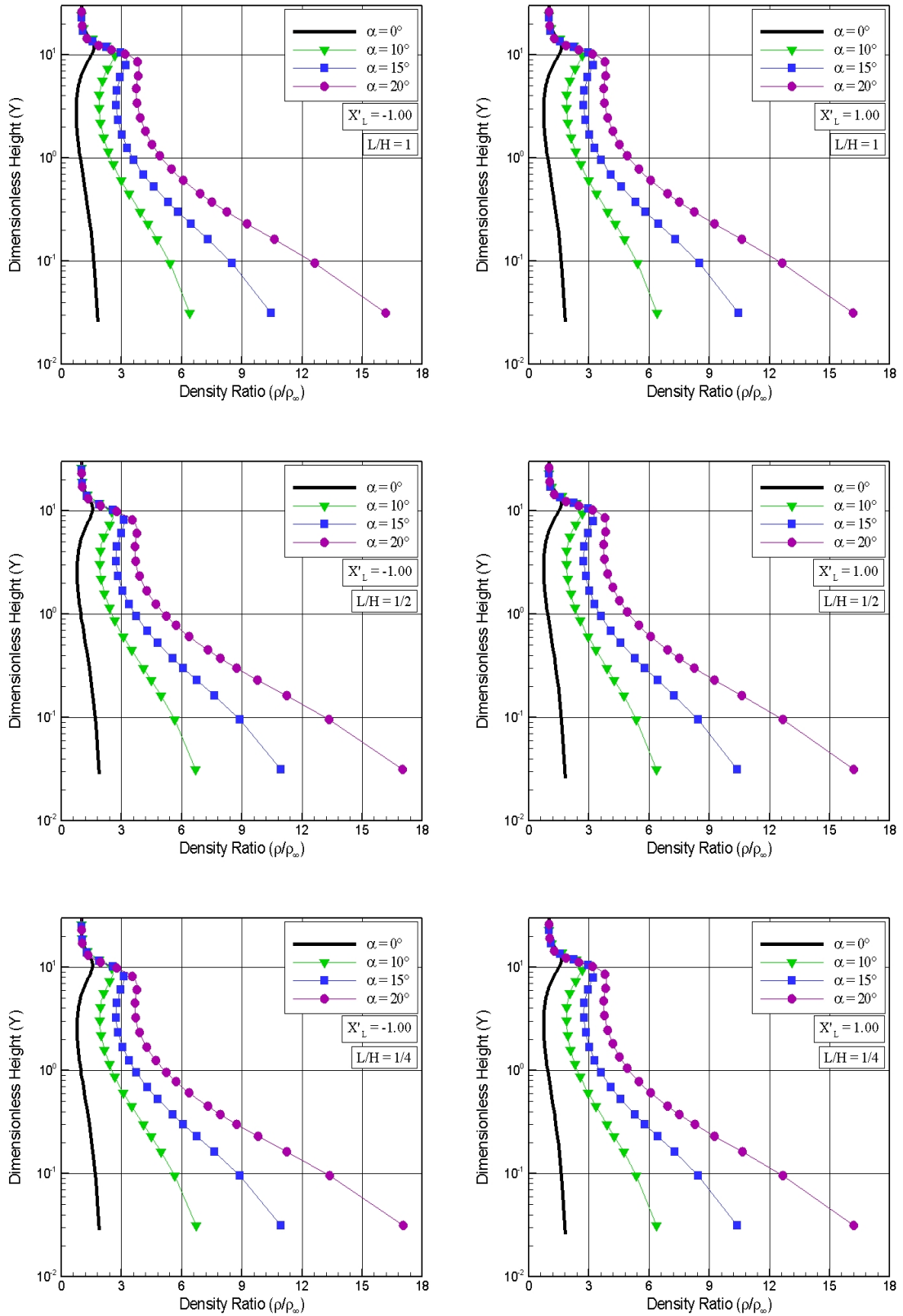


Figure 5.11 - Density ratio ( $\rho/\rho_\infty$ ) profiles for two sections outside the gaps and for  $L/H$  ratio of 1, 1/2, and 1/4, parameterized by the angle of attack  $\alpha$ .



near the body surface be much denser and cooler (see next sections) than the gas in the rest of the boundary layer, is observed when the body surface is very much colder than the stagnation temperature of the oncoming gas. Afterwards, as  $Y$  increases, the density ratio increases significantly inside the shock wave, reaching a maximum value that depends on the angle of attack  $\alpha$ . After that, the density decreases and reaches the freestream density value as  $Y \rightarrow \infty$ .

Density profiles for three sections  $X'_L$  inside the gap are displayed in Fig. 5.12, parameterized by the gap  $L/H$  ratio. In this group of plots, again,  $Y_H$  stands for the height  $y$  normalized by the gap height  $H$ . The three sections  $X'_L$  of -0.25, 0.0, and 0.25 correspond, respectively, to a section close to the gap backward face, in the middle of the gap, and at the vicinity of the gap forward face. In addition, left- and right-column diagrams correspond to density ratio for angle of attack  $\alpha$  of 10 and 20 degrees, respectively.

According to this group of plots, it is quite apparent that density ratio profiles present a similar pattern for the three sections  $X'_L$  as well as for the angle of attack range investigated. It is observed that the density ratio inside the gap increases from the top of the gap,  $Y_H = 0$ , to the bottom of the gap,  $Y_H = -1$ , for the  $L/H$  ratio investigated. In addition, it is also observed that, for  $L/H < 1$ , the density ratio basically tends to a same value at the bottom of the gap with decreasing the  $L/H$  ratio. Also, at the bottom of the gap, density ratio increases significantly with increasing the angle of attack  $\alpha$ . This is an expected behavior in the sense that more molecules enter into the gap with increasing the angle of attack  $\alpha$ . As a base of comparison,  $\rho/\rho_\infty$  reaches a maximum value around 16, 25, and 38, for angle of attack of 10, 15, and 20 degrees, respectively.

The sensitive in the density ratio inside the gap due to changes on the angle of attack is exhibited in Figs. 5.13 and 5.14 for the same three sections  $X'_L$ , parameterized by the gap  $L/H$  ratio. In addition, for comparison purpose, results for zero-degree angle of attack, obtained by Paolicchi (PAOLICCHI, 2010), are shown in this set of plots. It is recognized from this set of plots that density ratio increases significantly with increasing the angle of attack as compared to the case for zero-degree angle of incidence. As mentioned earlier, the amount of molecules entering into the gap increases with increasing the angle of attack.

In the following, in an effort to emphasize points of interest related to the density field, Fig. 5.15 displays the distribution of density ratio,  $\rho/\rho_\infty$ , along with streamline traces inside the gaps. This family of plots covers all the cases investigated for gap

Figure 5.12 - Density ratio ( $\rho/\rho_\infty$ ) profiles for three sections inside the gaps as a function of the dimensionless height  $Y_H$ , parameterized by the gap  $L/H$  ratio. Left- and right-column plots correspond to angle of attack  $\alpha$  of 10 and 20 degrees, respectively.

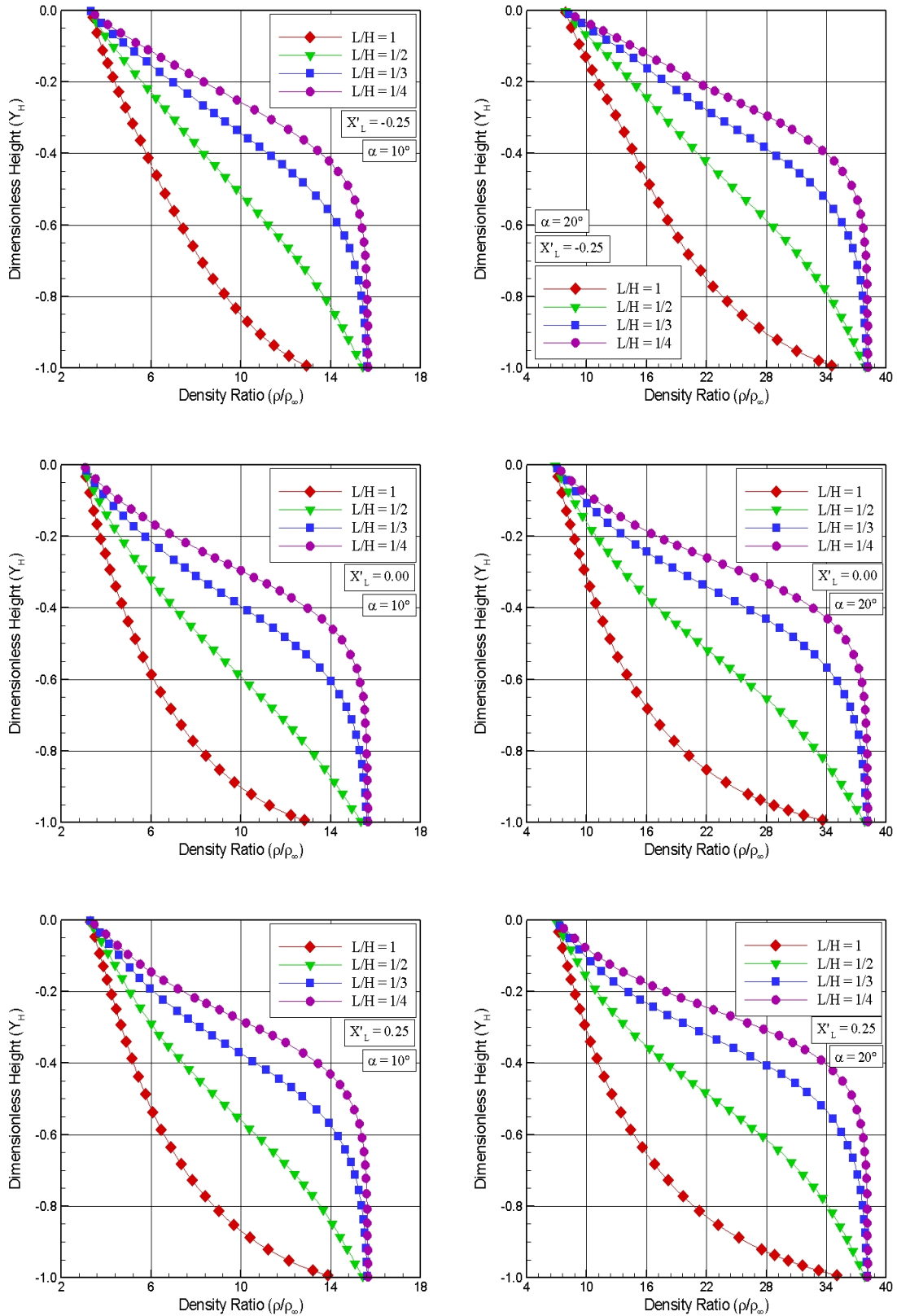


Figure 5.13 - Density ratio ( $\rho/\rho_\infty$ ) profiles for three sections inside the gaps as a function of the dimensionless height  $Y_H$ , parameterized by the angle of attack  $\alpha$ . Left- and right-column plots correspond to gap  $L/H$  ratio of 1 and  $1/2$ , respectively.

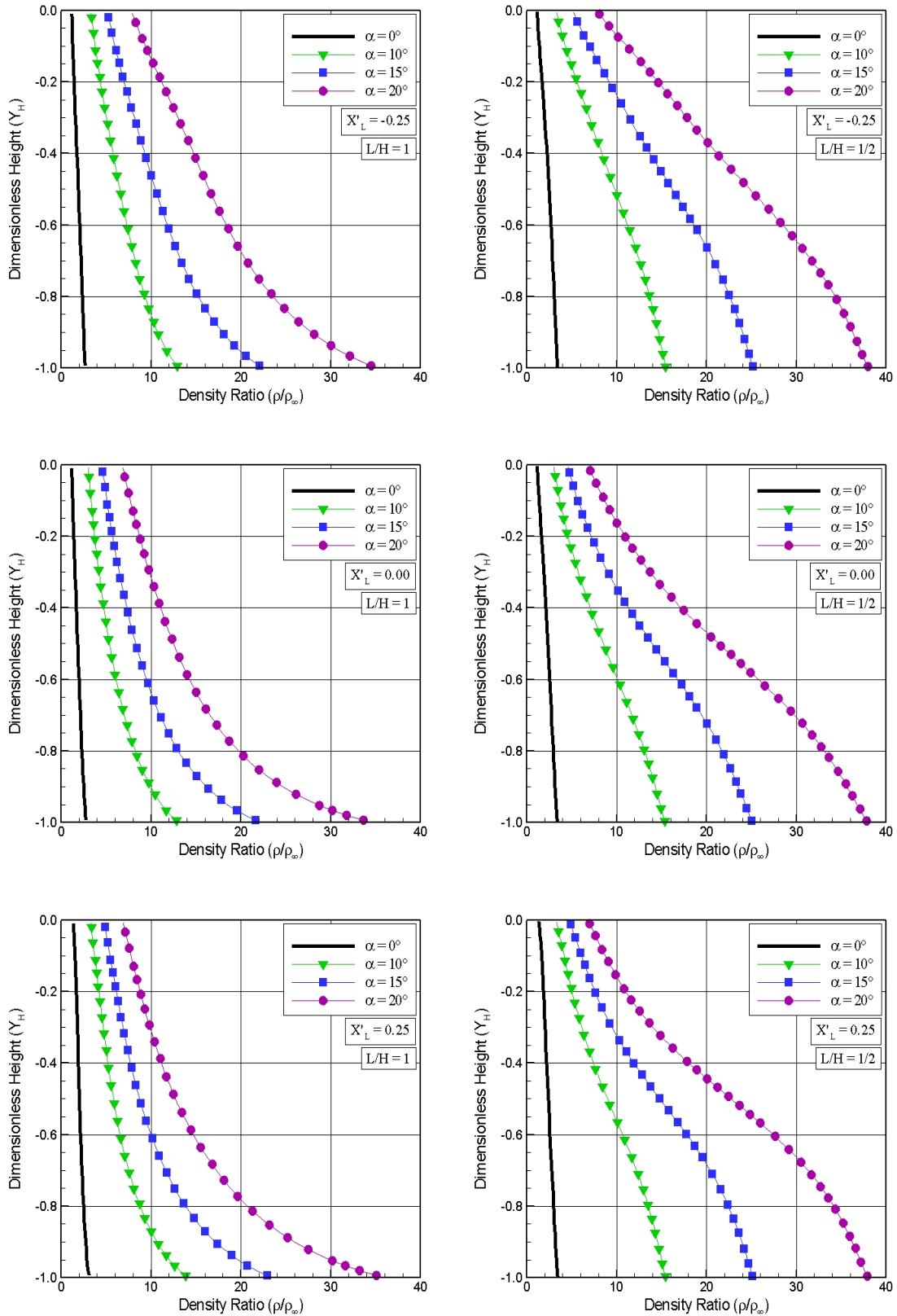


Figure 5.14 - Density ratio ( $\rho/\rho_\infty$ ) profiles for three sections inside the gaps as a function of the dimensionless height  $Y_H$ , parameterized by the angle of attack  $\alpha$ . Left- and right-column plots correspond to gap  $L/H$  ratio of 1/3 and 1/4, respectively.

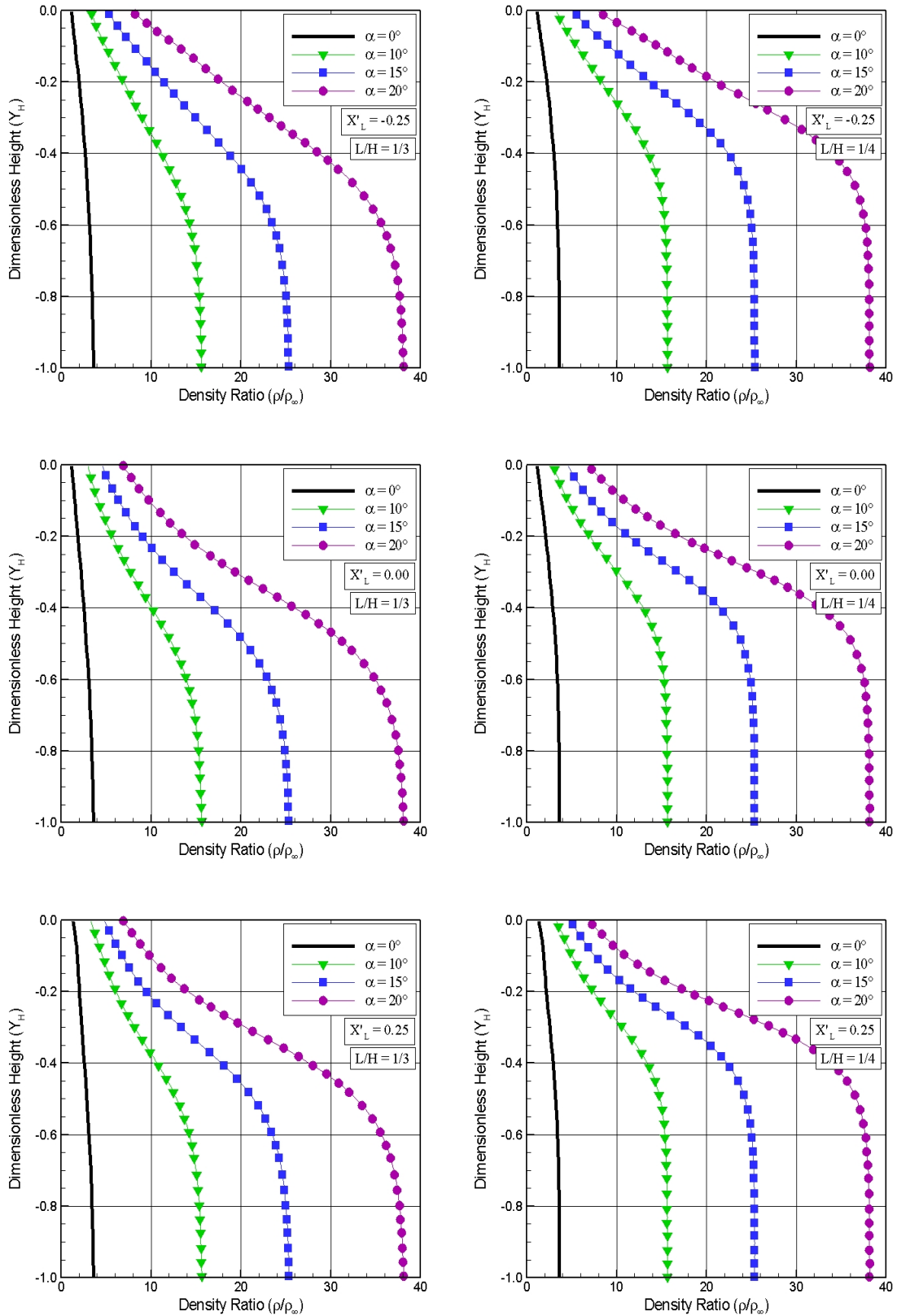
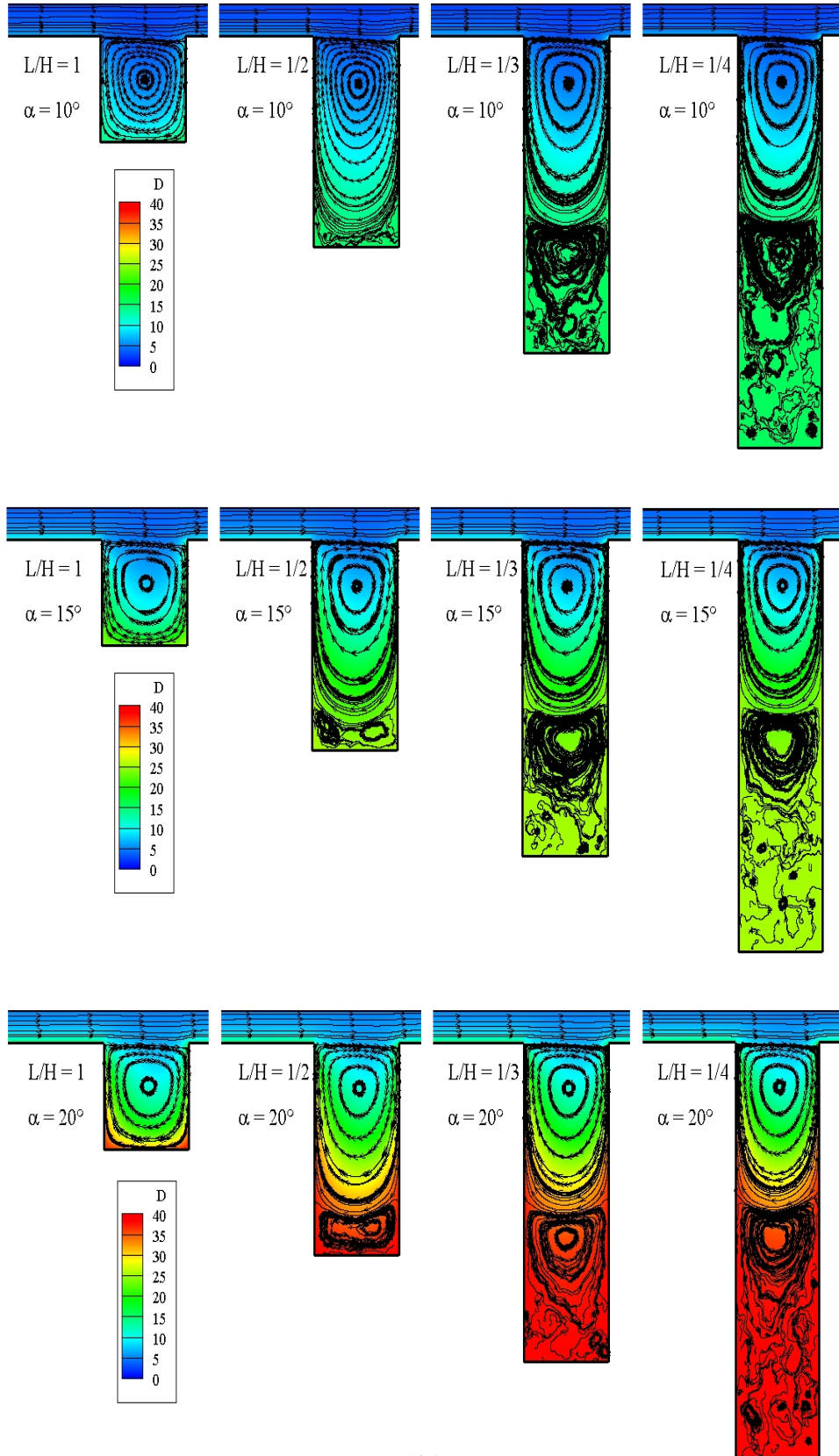


Figure 5.15 - Distribution of density ratio ( $\rho/\rho_\infty$ ) along with streamline traces inside the gaps for  $L/H$  ratio of 1 (left), 1/2, 1/3 and 1/4 (right), with angle attack  $\alpha$  of 10 (top), 15, and 20 degrees (bottom).



$L/H$  ratio and angle of attack  $\alpha$ . According to these plots, it is seen that, the density ratio increases inside the gaps with increasing the angle of attack  $\alpha$ . In addition, it is also seen, by visual inspection, that the recirculation region did not undergo significant changes with increasing the angle of attack  $\alpha$ , for the gap  $L/H$  ratio investigated.

### 5.1.3 Pressure Field

The influence of the  $L/H$  ratio on pressure profiles for two sections outside the gap,  $X'_L$  of -1 and 1, is exhibited in Fig. 5.16 as a function of the dimensionless height  $Y$ . In this set of diagrams, pressure  $p$  is normalized by the freestream pressure  $p_\infty$ ,  $X'_L$  and  $Y$  are dimensionless length and height, respectively, as defined previously in the density profiles. Moreover, for comparative purpose, pressure ratio profiles for the flat-plate case are also exhibited in the same diagrams.

On examining Fig. 5.16, it is observed that, similar to tangential velocity and density profiles, pressure ratio profiles for the gap  $L/H$  ratio and angle of attack  $\alpha$  investigated are basically identical to those for the flat-plate cases, indicating that the presence of the gap does not affect the flowfield immediately upstream the gap, section  $X'_L = -1$ . However, for section  $X'_L = 1$ , pressure ratio profiles are slightly different from those for the flat-plate case in the shock layer, indicating that the presence of the gap is still felt at least a half-gap length downstream the gap position. This is in contrast to the behavior observed for density ratio profiles, where density profiles are slightly different from that for the flat-plate case at the vicinity of the wall.

The impact on the pressure profiles due to variations on the angle of attack  $\alpha$  for two sections  $X'_L$  outside the gap is demonstrated in Fig. 5.17 for gap  $L/H$  ratio of 1, 1/2, and 1/4. Again, results for  $L/H$  ratio of 1/3 are intermediate, and they are not shown in this figure. Once more, for comparison purpose, results for zero-degree angle of attack obtained by Paolicchi (PAOLICCHI, 2010) are presented in this set of plots.

Based on Fig. 5.17, it is noticed that pressure ratio increases significantly close to the wall,  $Y \cong 0$ , with increasing the angle of attack  $\alpha$ . Similar to the behavior for density ratio profiles, the reason for this significant pressure increase is because the body is changing from an aerodynamic sharp body to a blunt body for the oncoming freestream molecules, as the angle of attack increases from 0 to 20 degrees. Then, for the range  $0 < Y < 3$ , pressure ratio slightly increases in the shock layer, where

Figure 5.16 - Pressure ratio ( $p/p_\infty$ ) profiles for two sections outside the gaps and for angle of attack  $\alpha$  of 10, 15 and 20 degrees, parameterized by the gap  $L/H$  ratio.

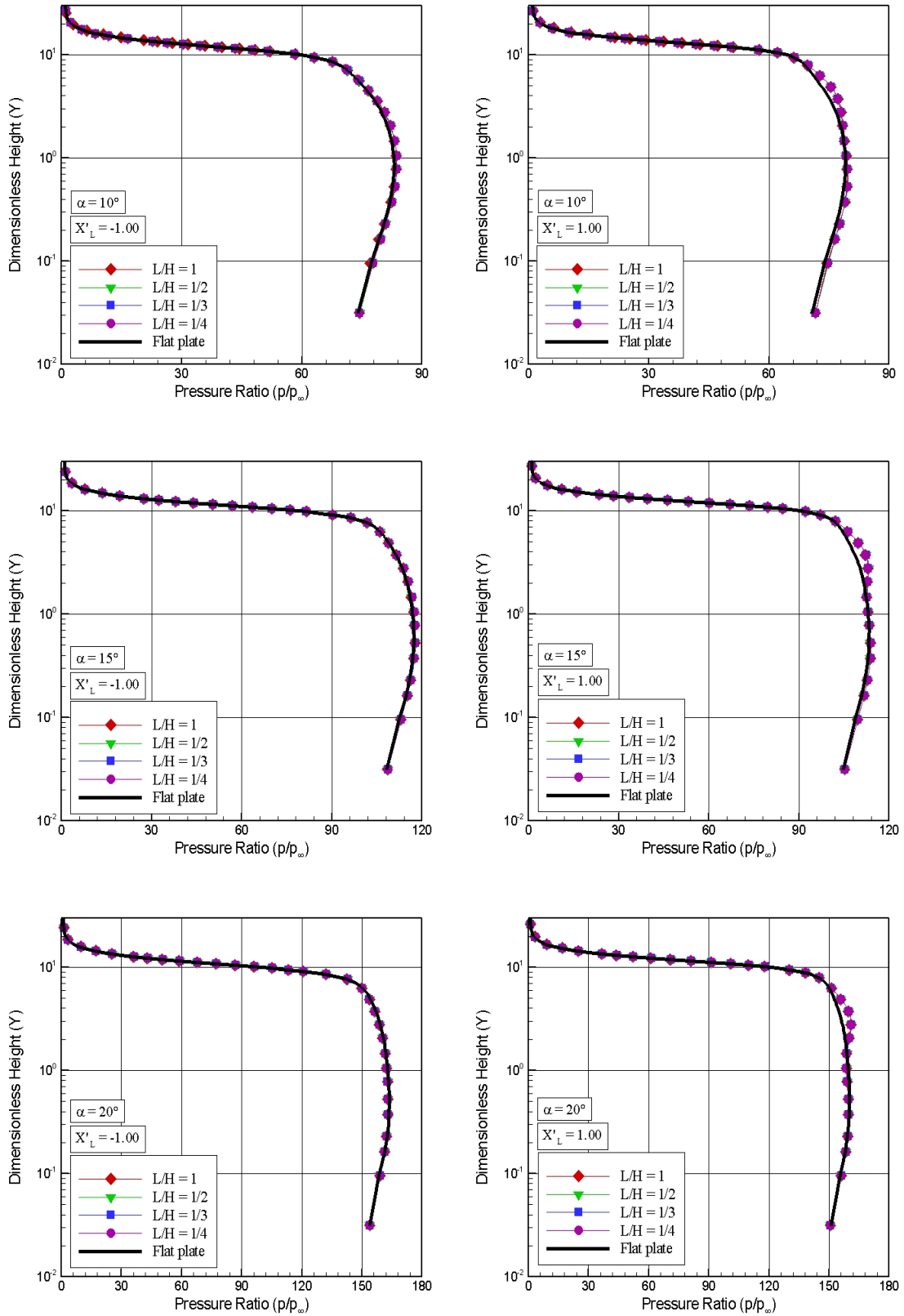


Figure 5.17 - Pressure ratio ( $p/p_\infty$ ) profiles for two sections outside the gaps and for  $L/H$  ratio of 1, 1/2, and 1/4, parameterized by the angle of attack  $\alpha$ .

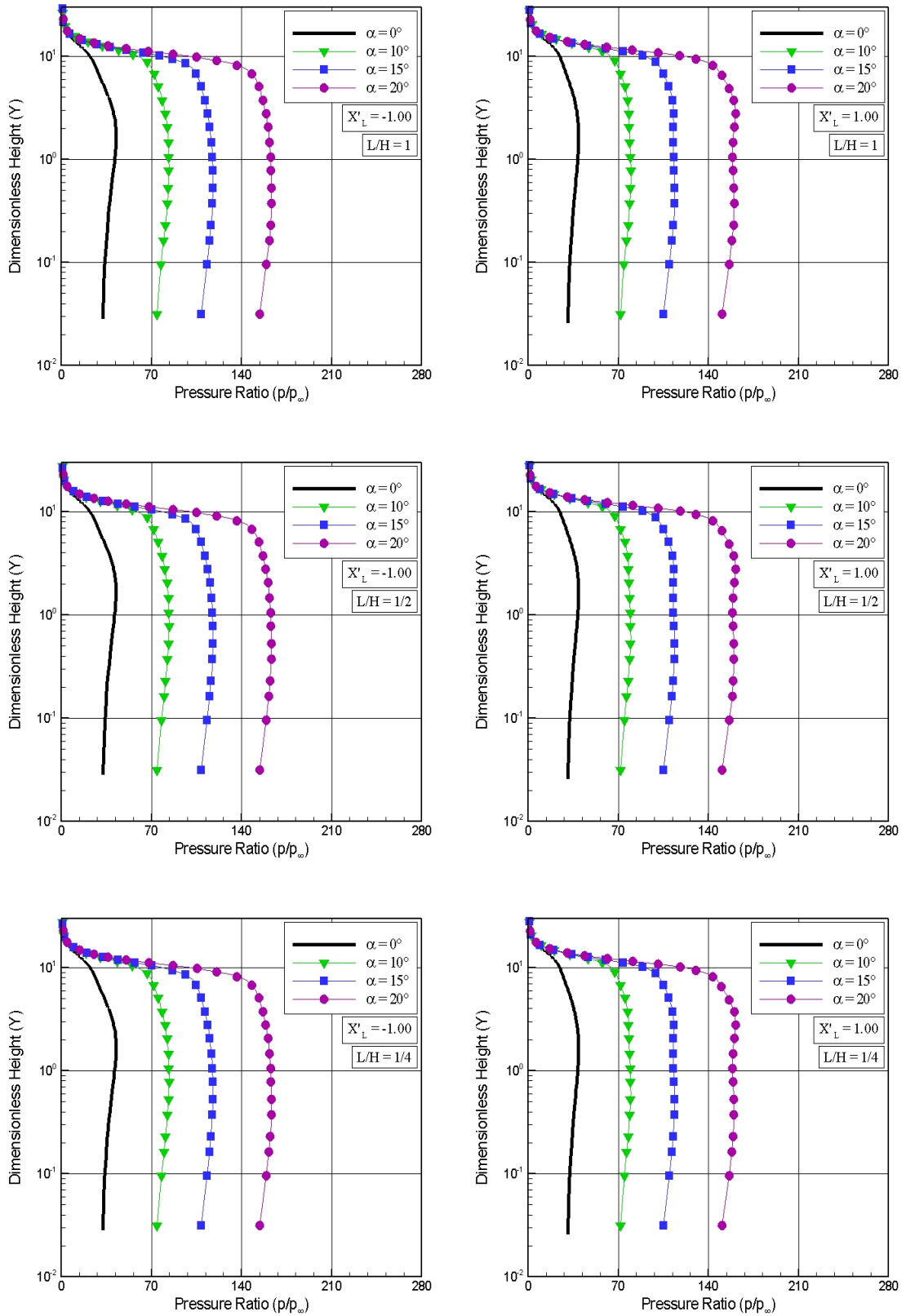
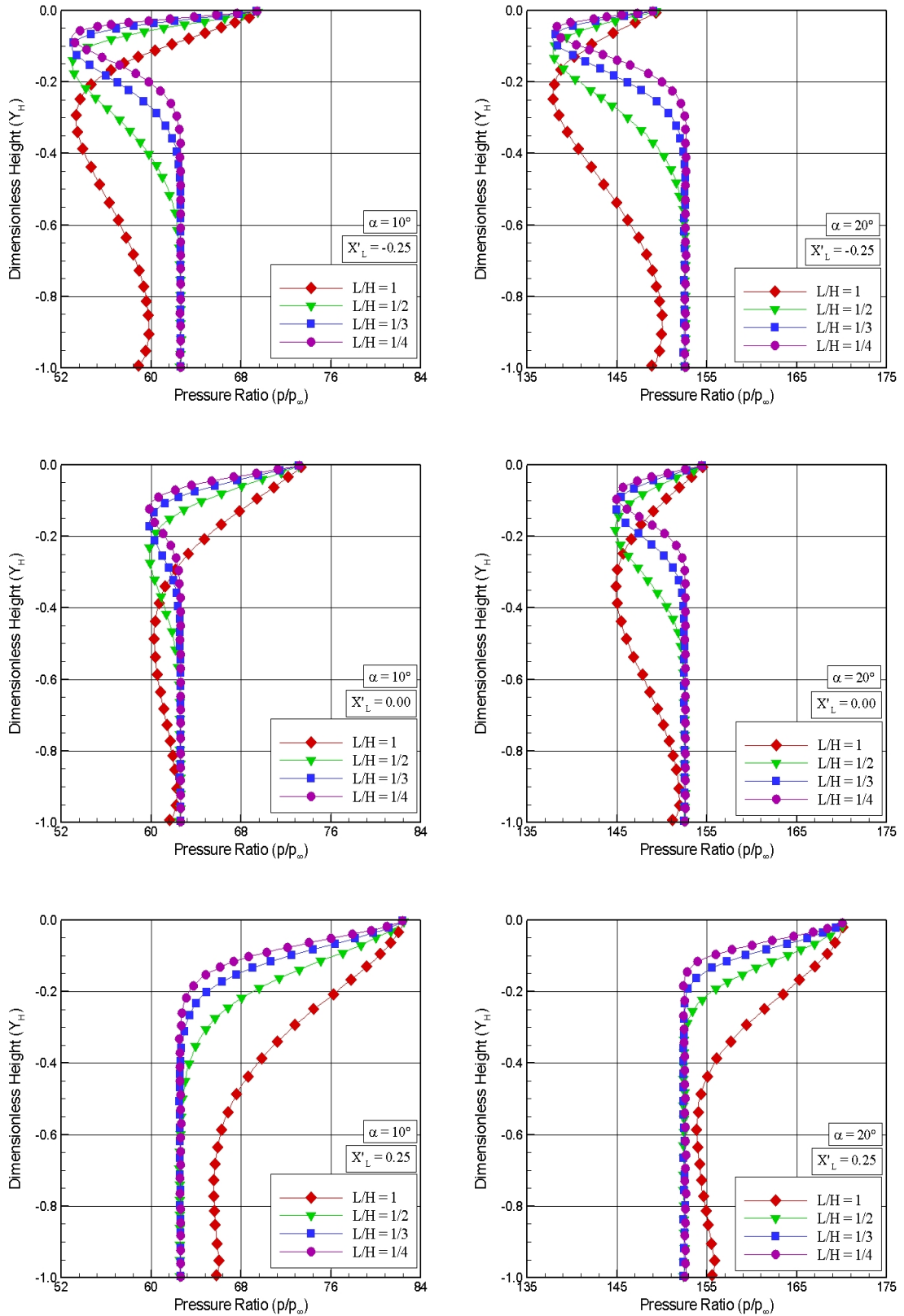


Figure 5.18 - Pressure ratio ( $p/p_\infty$ ) profiles for three sections inside the gaps as a function of the dimensionless height  $Y_H$ , parameterized by the gap  $L/H$  ratio. Left- and right-column plots correspond to angle of attack  $\alpha$  of 10 and 20 degrees, respectively.



pressure ratio reaches the maximum value. Afterwards, as  $Y \rightarrow \infty$ , pressure ratio drops off, outside the shock layer, and the pressure  $p$  reaches the freestream pressure  $p_\infty$ .

Pressure ratio profiles inside the gap are illustrated in Fig. 5.18 as a function of the dimensionless height  $Y_H$  for three sections  $X'_L$ . In these plots, the dimensionless height  $Y_H$  represents the height  $y$  normalized by the gap height  $H$ . Again, the three sections  $X'_L$ , -0.25, 0.0, and 0.25, correspond, respectively, to a section at the vicinity of the gap backward face, in the middle of the gap, and at the vicinity of the gap forward face. In addition, left- and right-column diagrams correspond to  $p/p_\infty$  for angle of attack  $\alpha$  of 10 and 20 degrees, respectively.

Looking first at the left-column plots, for 10-degree angle of incidence, it is observed that the pressure ratio inside the gaps decreases from the top of the gap,  $Y = 0$ , to the bottom of the gap,  $Y = -1$ , for the  $L/H$  ratio investigated. However, the pressure ratio behavior for section  $X'_L$  of -0.25 is different from that for section  $X'_L$  of 0.25. For section  $X'_L$  of -0.25, close to the gap backward face, the pressure ratio presents a maximum value at the top of the gap. Then, it decreases to a minimum value in the upper portion of the gap,  $-0.4 < Y < 0$ . Afterwards, the pressure ratio increases again and reaches a constant value up to the bottom of the gap, for  $L/H < 1$  cases. In contrast, for section  $X'_L$  of 0.25, close to the gap forward face, the pressure ratio presents a maximum value at the top of the gap. Then, it decreases to a minimum value, and reaches a constant value up to the bottom of the gap. This behavior is explained by the fact that the flow experiences an expansion at the vicinity of the gap backward face and a compression at the vicinity of the gap forward face.

Turning next to the right-column plots, for 20-degree angle of incidence, it is observed that the pressure ratio behavior is similar to that for 10-degree angle of incidence for the  $L/H$  ratio investigated. However, the maximum values for the pressure ratio for 20-degree angle are around one order of magnitude larger than those for 10-degree angle.

The impact on the pressure ratio due to changes in the angle of attack is exhibited in Figs. 5.19 and 5.20 for the same three sections  $X'_L$ , parameterized by the gap  $L/H$  ratio. Again, as a base of comparison, results for zero-degree angle of attack, obtained by Paolicchi (PAOLICCHI, 2010), are shown in this set of plots. It is clearly noted from this set of plots that pressure ratio increases significantly with increasing the angle of attack, as compared to the case for zero-degree angle of attack. At the

Figure 5.19 - Pressure ratio ( $p/p_\infty$ ) profiles for three sections inside the gaps as a function of the dimensionless height  $Y_H$ , parameterized by the angle of attack  $\alpha$ . Left- and right-column plots correspond to gap  $L/H$  ratio of 1 and  $1/2$ , respectively.

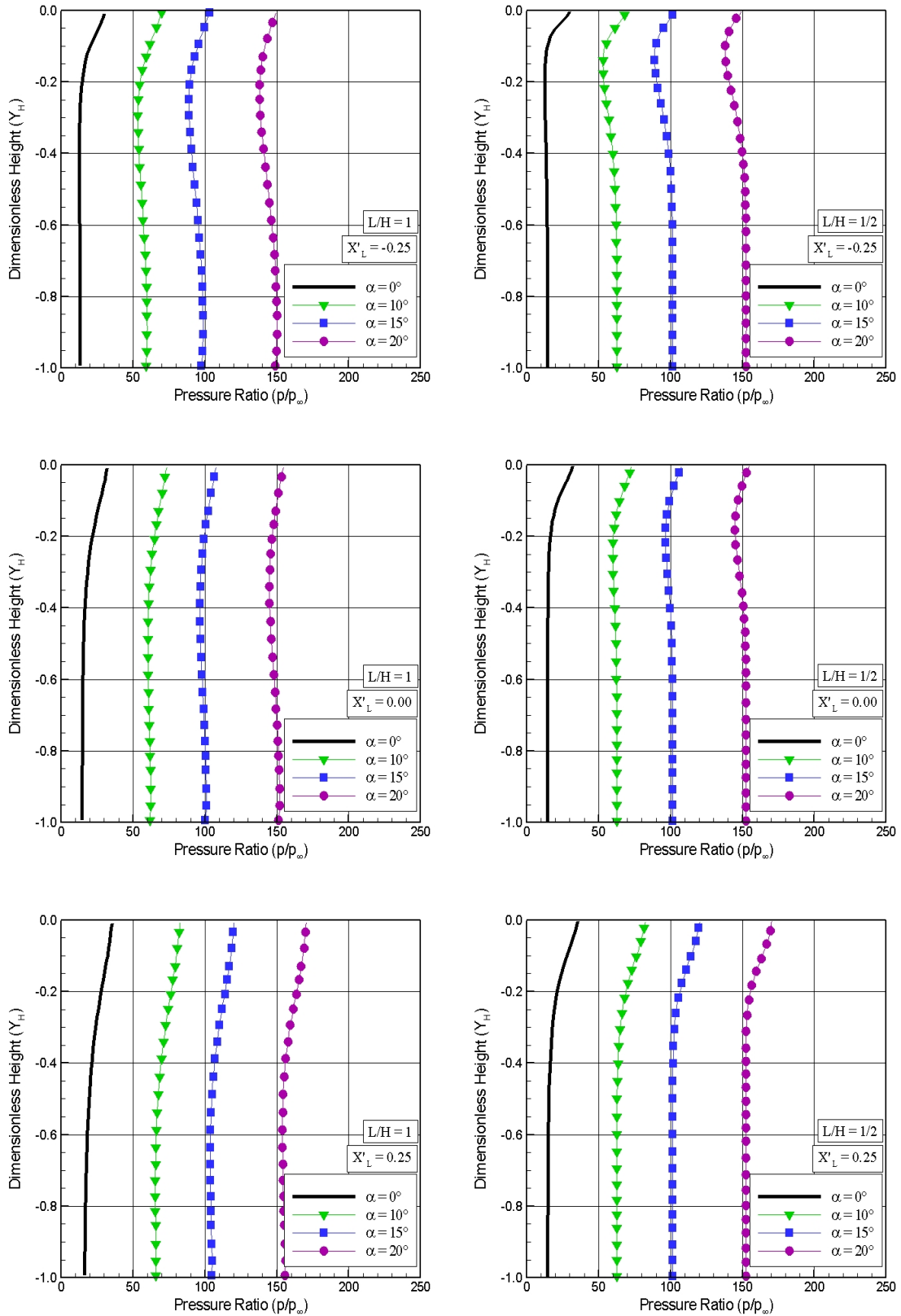


Figure 5.20 - Pressure ratio ( $p/p_\infty$ ) profiles for three sections inside the gaps as a function of the dimensionless height  $Y_H$ , parameterized by the angle of attack  $\alpha$ . Left- and right-column plots correspond to gap  $L/H$  ratio of  $1/3$  and  $1/4$ , respectively.

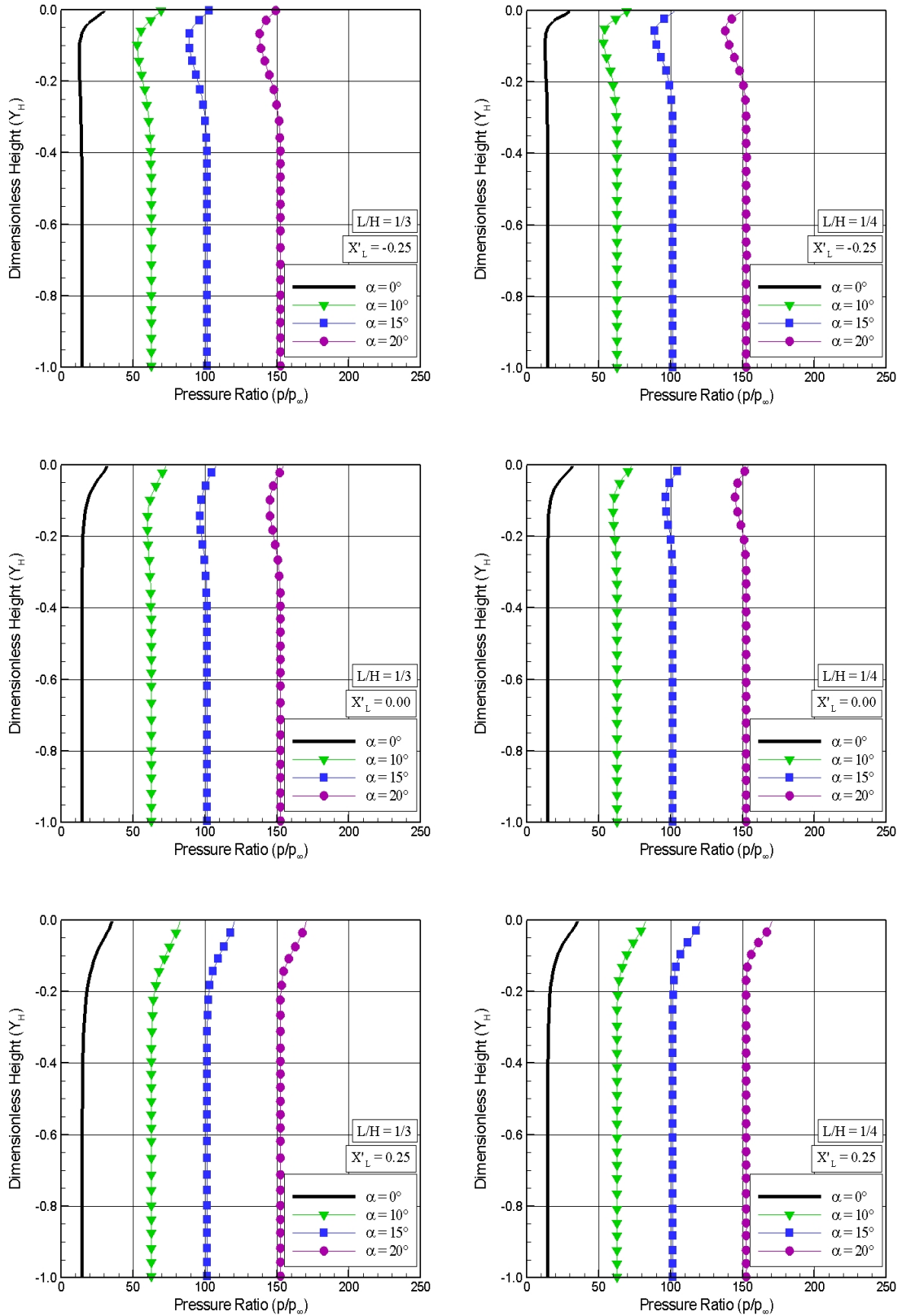
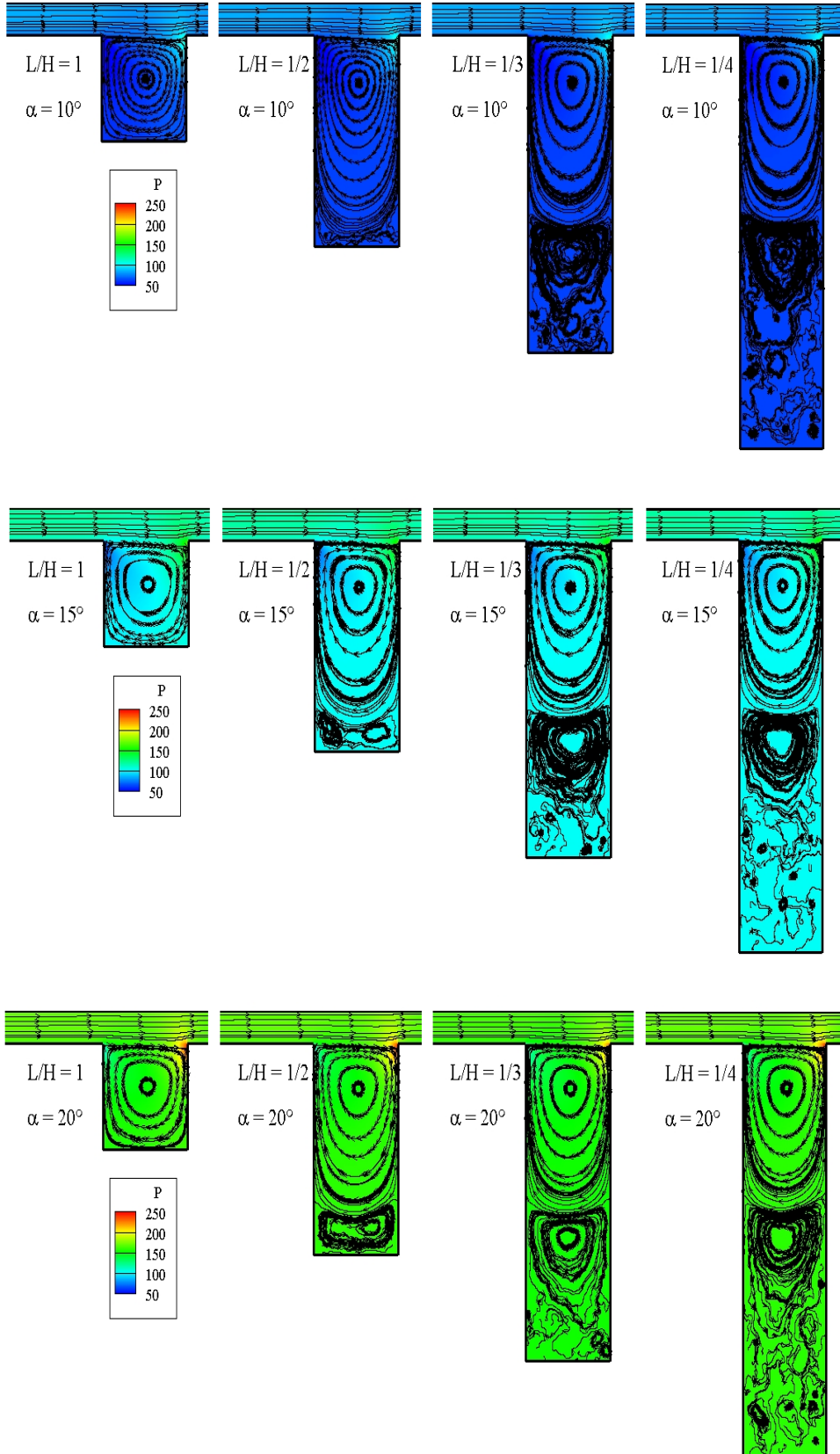


Figure 5.21 - Distribution of pressure ratio ( $p/p_\infty$ ) along with streamline traces inside the gaps for  $L/H$  ratio of 1 (left), 1/2, 1/3 and 1/4 (right), with angle attack  $\alpha$  of 10 (top), 15, and 20 degrees (bottom).



bottom of the gap, it is seen that pressure ratio increases one order of magnitude when the angle of attack increases from 0 to 20 degrees. For comparison purpose, at the bottom of the gap, pressure ratio achieves approximately maximum value of 11, 60, 100, and 150, for angle of attack of 0, 10, 15, and 20 degrees. This increase in the pressure ratio is related to the increase in the amount of molecules entering into the gap, as a consequence of increasing the angle of attack.

In what follows, in attempting to bring out the essential features of the pressure behavior inside the gaps, Fig. 5.21 illustrates the distribution of pressure ratio,  $p/p_\infty$ , along with streamline traces. According to this group of plots, it is clearly seen that the maximum value for pressure ratio takes place at the vicinity of the corner on the gap forward face. In addition, the maximum value increases with increasing the angle of attack. As mentioned earlier, the reason for that is because the flow experiences a compression on this face of the gap.

#### 5.1.4 Kinetic Temperature Field

In a diatomic or polyatomic gas in complete thermodynamic equilibrium, the translational temperature is equal to the temperature related to the internal modes, i.e., rotational, vibrational, or electronic temperatures, and it is identified as thermodynamic temperature. Conversely, in a thermodynamic non-equilibrium gas, an overall temperature is defined as the weighted mean of the translational and internal temperatures (BIRD, 1994) as being,

$$T_O = \frac{\zeta_T T_T + \zeta_R T_R + \zeta_V T_V}{\zeta_T + \zeta_R + \zeta_V} \quad (5.1)$$

where  $T$  and  $\zeta$  stand for the temperature and the degree of freedom, respectively, and subscripts  $T$ ,  $R$  and  $V$  refer to translation, rotation and vibration, respectively.

Translational, rotational, and vibrational temperatures are obtained to each cell in the computational domain by the following equations,

$$T_T = \frac{1}{3k} \sum_{j=1}^N \frac{(mc^2)_j}{N} \quad (5.2)$$

$$T_R = \frac{2 \bar{\epsilon}_R}{k \zeta_R} \quad (5.3)$$

$$T_V = \frac{\Theta_V}{\ln(1 + \frac{k\Theta_V}{\bar{\epsilon}_V})} \quad (5.4)$$

where  $k$  is the Boltzmann constant,  $\Theta_V$  is the characteristic temperature of vibration, and  $\bar{\epsilon}_R$  and  $\bar{\epsilon}_V$  are, respectively, rotation and vibration average energies in each cell.

Under the aforementioned definitions, the dependence of the kinetic temperature due to changes on the  $L/H$  ratio is demonstrated in Fig. 5.22 for two sections outside the gap,  $X'_L$  of -1 and 1. In this set of diagrams, kinetic temperature ratio stands for the translational temperature  $T_T$ , rotational temperature  $T_R$ , vibrational temperature  $T_V$ , and overall temperature  $T_O$  normalized by the freestream temperature  $T_\infty$ . In addition, temperature profiles are only shown for  $L/H$  of 1 and 1/4. Results for  $L/H$  of 1/2 and 1/3 are intermediate, and they will not be shown.

On examining Fig. 5.22, it is quite apparent that thermodynamic non-equilibrium occurs outside the gaps, as shown by the lack of equilibrium between the translational and internal kinetic temperatures. Thermal non-equilibrium occurs when the temperatures associated with the translational, rotational, and vibrational modes of a polyatomic gas are different. In this framework, the overall temperature, defined by Equation 5.1, is equivalent to the thermodynamic temperature only under thermal equilibrium conditions. In addition, the ideal gas equation of state does not apply to this temperature in a non-equilibrium situation.

Still examining Fig. 5.22, it is firmly established that, by visual inspection, no significant changes are observed in the temperature ratio profiles due to variations on the  $L/H$  ratio, since  $L/H$  of 1 and 1/4 represent, respectively, the largest and the smallest values investigated.

Proceeding in a manner analogous to the earlier treatment to velocity, density, and pressure profiles, Fig. 5.23 illustrates a comparison of the kinetic temperature ratio only for the gap with  $L/H$  of 1 and the flat-plate case at section  $X'_L$  of -1 and 1. Based on this group of plots, it is noticed that, similar to tangential velocity, density, and pressure profiles for the angle of attack  $\alpha$  investigated, temperature ratio profiles are basically identical to those for the flat-plate cases, indicating that the presence of the gap does not influence the flowfield immediately upstream the gap, section  $X'_L = -1$ . However, for section  $X'_L = 1$ , temperature ratio profiles for the gap are slightly different from that for the flat-plate cases at the vicinity of the wall, indicating that the presence of the gaps is still felt at least a half-gap length

downstream of the gap.

Of particular interest in Fig. 5.23 is the behavior of the temperature ratio profiles in the body off direction. It is seen that, in the undisturbed freestream far from the flat-plate,  $Y \rightarrow \infty$ , the translational and internal kinetic temperatures have the same value and are equal to the thermodynamic temperature. Approaching the flat-plate,  $Y \approx 3$ , the translational kinetic temperature rises to well above the rotational and vibrational temperatures and reaches a maximum value that is basically the same for the angle of attack range investigated. Since a large number of collisions is necessary to excite the vibration mode of the molecules, from the ground state to the upper state, the vibrational temperature is seen to increase much more slowly than rotational temperature. Still further toward the flat-plate surface,  $Y \approx 0$ , the translational kinetic temperature decreases, and reaches a constant value on the wall that is above the wall temperature  $T_w (\approx 4T_\infty)$ , resulting in a temperature jump as defined in continuum formulation (GUPTA et al., 1985). Furthermore, the difference between translational temperature and internal temperatures at the vicinity of the flat-plate surface also indicates that the thermodynamic equilibrium is not achieved in the boundary layer.

In order to assess the overall behavior of the kinetic temperature ratio profiles inside the gaps, Fig. 5.24 illustrates the temperature ratio profiles for three sections,  $X'_L$  of -0.25, 0.0, and 0.25. In this set of plots, left- and right-column plots correspond to density ratio for angle of attack  $\alpha$  of 10 and 20 degrees, respectively. Results for  $L/H$  of 1/2 and 1/3 are intermediate, and they will not be shown. In addition, filled and empty symbols stand for gap  $L/H$  ratio of 1 and 1/4, respectively.

According to this set of plots, it is observed that the kinetic temperature ratio  $T/T_\infty$  decreases from the top of the gap and basically reaches a constant value on the gap bottom surface, which corresponds to the wall temperature  $T_w (\approx 4T_\infty)$ . At the bottom surface, it is seen that the flow is in thermal equilibrium, once the rotation and vibration temperatures are equal to the translational temperature. It is important to recall that, the density increased at the vicinity of the gap bottom surface, as shown in Fig. 5.12. As a result, the local mean free path decreased and the mean collision frequency increased and, therefore, the flow reached the thermal equilibrium.

In the results that follow, it proves helpful to present the distribution of temperature inside the gaps. In doing so, Fig. 5.25 displays the distribution of overall temperature ratio,  $T_O/T_\infty$ , along with streamline traces for the entire range of  $L/H$  ratio and

Figure 5.22 - Kinetic temperature ratio ( $T/T_\infty$ ) profiles for two sections outside the gaps and for angle of attack  $\alpha$  of 10, 15 and 20 degrees, parameterized by the gap  $L/H$  ratio.

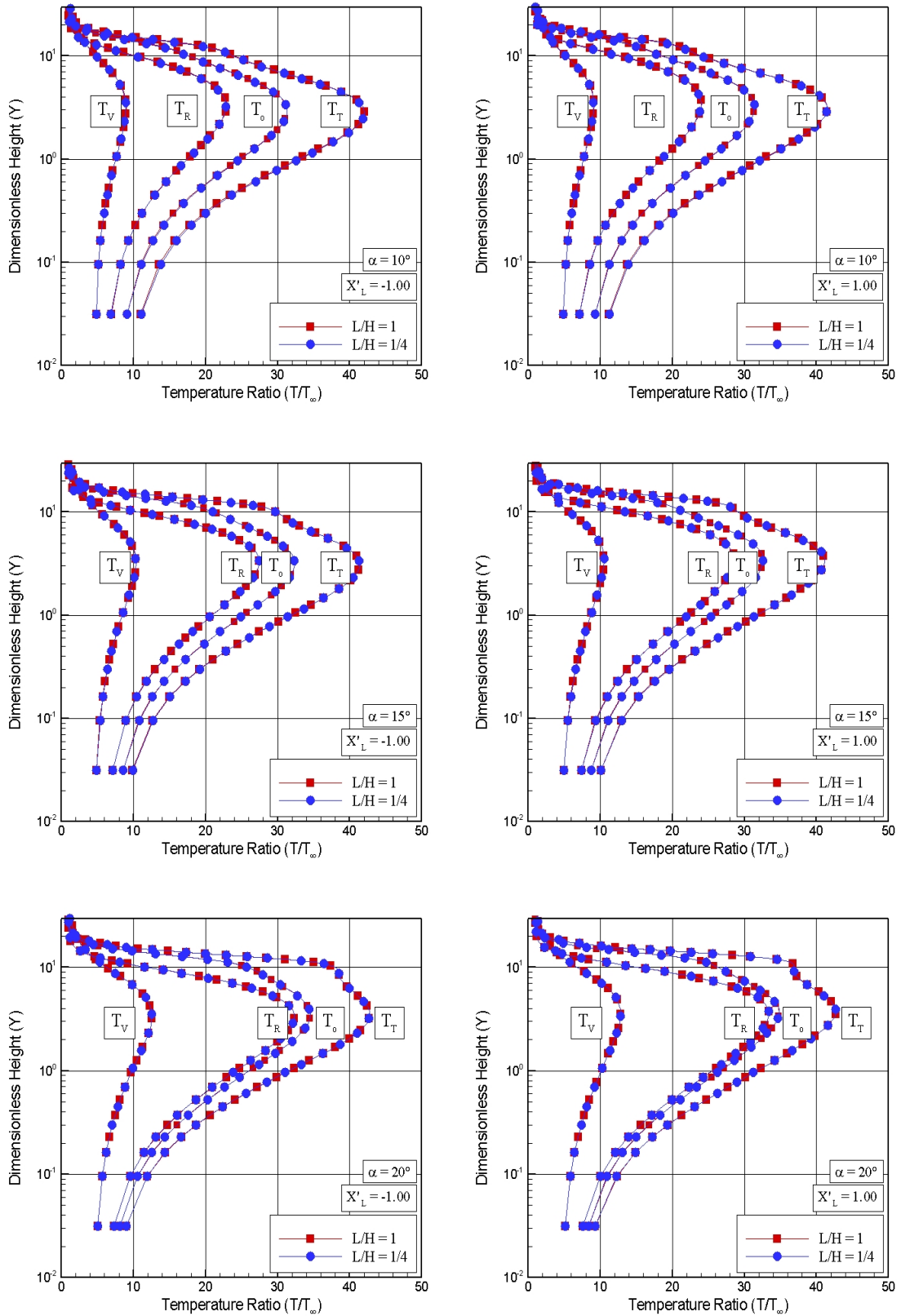


Figure 5.23 - Comparison of the kinetic temperature ratio ( $T/T_\infty$ ) profiles for the gap  $L/H$  ratio of 1 and the flat-plate at two sections outside the gap for angle of attack  $\alpha$  of 10, 15 and 20 degrees.

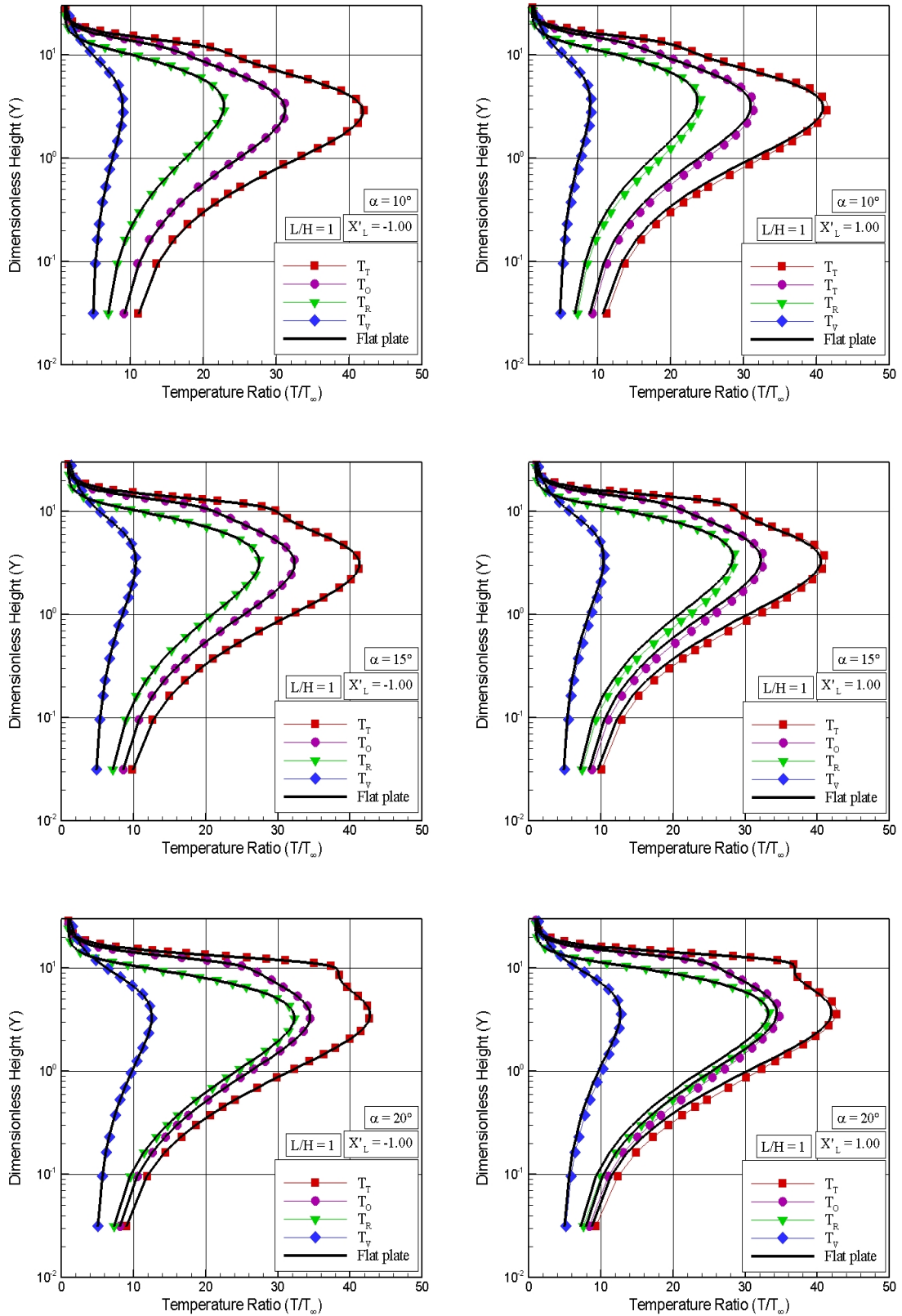


Figure 5.24 - Kinetic temperature ratio ( $T/T_\infty$ ) profiles for three sections inside the gaps as a function of the dimensionless height  $Y_H$ , parameterized by the gap  $L/H$  ratio. Left- and right-column plots correspond to angle of attack of 10 and 20 degrees, respectively.

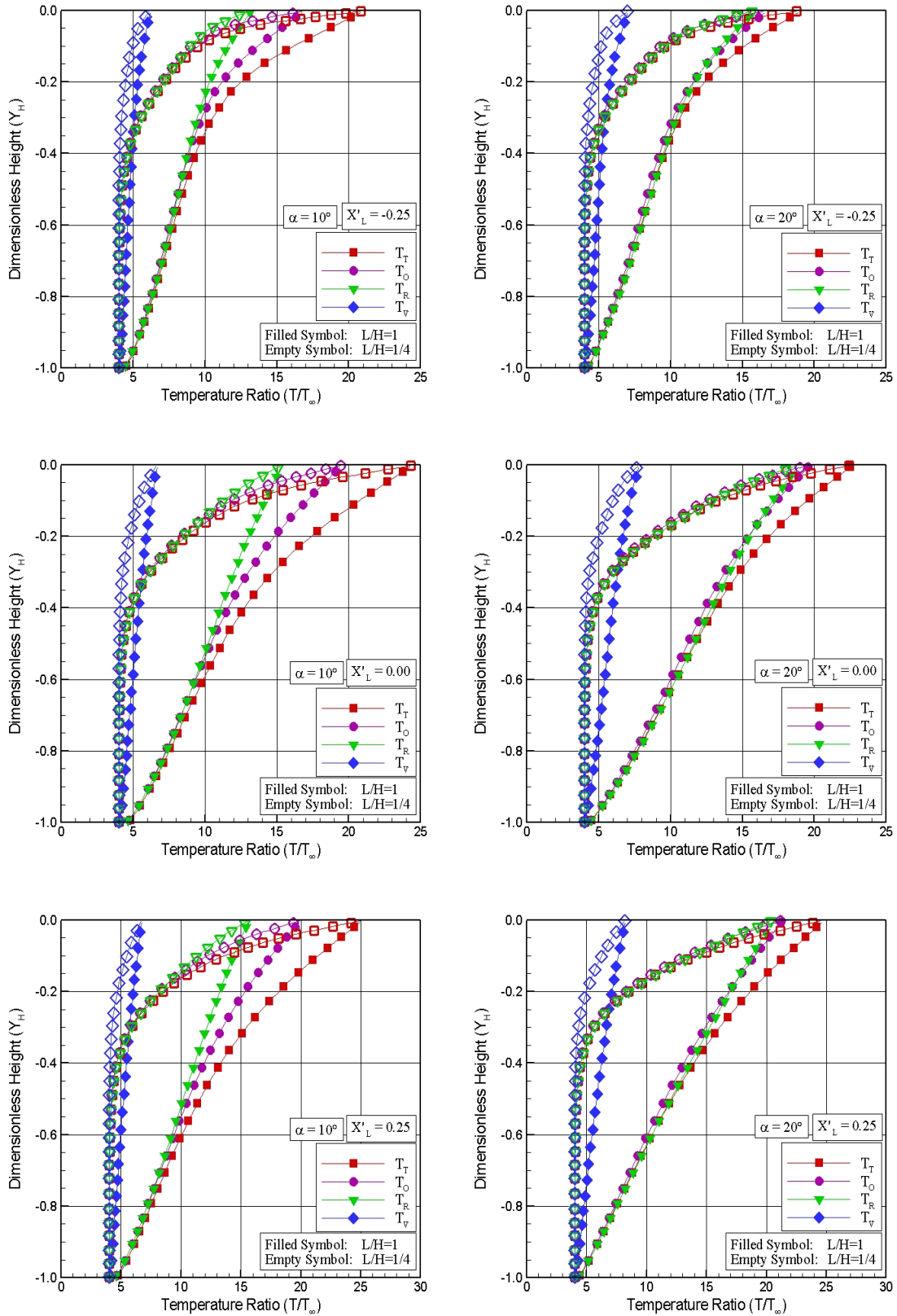
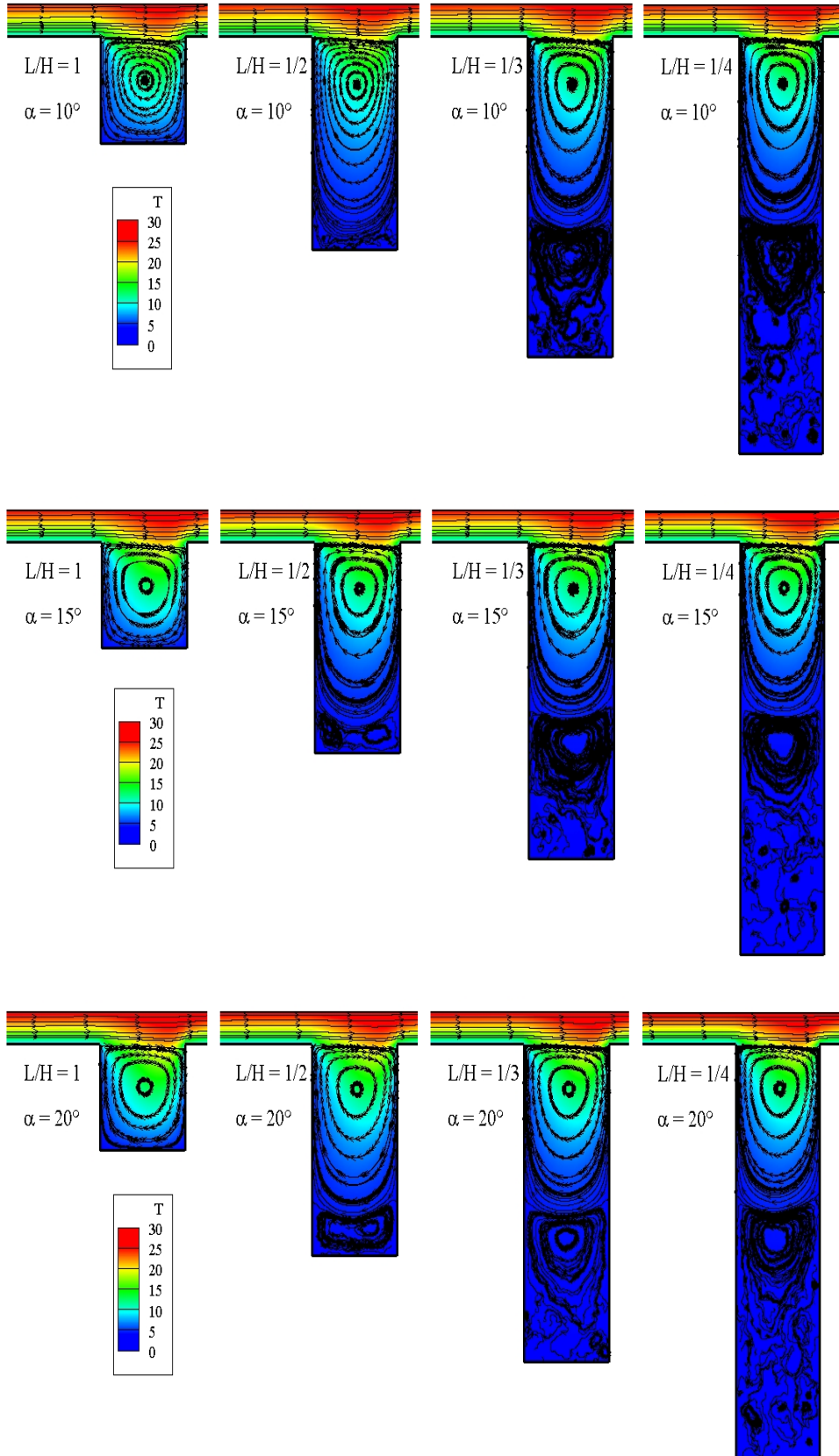


Figure 5.25 - Distribution of overall temperature ratio ( $T_O/T_\infty$ ) along with streamline traces inside the gaps for  $L/H$  ratio of 1 (left), 1/2, 1/3 and 1/4 (right), with angle attack  $\alpha$  of 10 (top), 15, and 20 degrees (bottom).



angle of attack  $\alpha$  investigated. According to these plots, the distribution of overall temperature inside the gaps is similar one to each other with decreasing the gap  $L/H$  ratio. In addition, the same behavior is observed as the angle of attack  $\alpha$  increases from 10 to 20 degrees.

## 5.2 Aerodynamic Surface Quantities

The purpose of this section is to discuss and to compare differences in the aerodynamic surface quantities due to variations on the gap  $L/H$  ratio and on the angle of attack  $\alpha$ . Aerodynamic surface properties of particular interest in this work are the number flux, pressure, skin friction and heat transfer coefficients.

### 5.2.1 Number Flux

Effects of the gap  $L/H$  ratio on the number flux are illustrated in Figs. 5.26 and 5.27 for angle of attack of 10 and 20 degrees, respectively. In this group of plots,  $N_f$  represents the number flux  $N$  normalized by  $n_\infty U_\infty$ , where  $n_\infty$  is the freestream number density and  $U_\infty$  is the freestream velocity. In addition,  $X$  is the length  $x$  normalized by the freestream mean free path  $\lambda_\infty$ , and  $Y_H$  is the height  $y$  normalized by the gap height  $H$ . Furthermore, the left-column plots refer to the distribution of the number flux along the gap upstream and downstream surfaces, i.e., surfaces S1 and S5, while the right-column plots correspond to the distribution on the surfaces inside the gap, i.e., surfaces S2, S3, and S4. Results for angle of attack of 15 degrees are intermediate, and they are not shown in this group of plots. As a base of comparison, the number flux distribution for the flat-plate case is also illustrated in this group of plots.

On examining first the left-column plots, it is noticed that the number flux behavior to the surfaces outside the gap basically follows that presented by the flat-plate case for the  $L/H$  ratio investigated in this work. Except very close to the gap position, no upstream disturbance is caused by the presence of the gap. Along surface S5, no appreciable changes, as compared to the flat-plate case, are observed in the number flux distribution, excepted at the vicinity of the gap shoulder, i.e., at the surface-S4/surface-S5 junction. On the other hand, this small effect at the vicinity of the gap shoulder increases with increasing the angle of attack. Due to the flow expansion on the gap shoulder the density is low in this region. As a result, the number flux to the surface is low. Another feature that deserves attention is the significant drop in the number flux at the end of surface S5. This reduction is due to vacuum condition used as the boundary condition at the end of the computational domain, as explained in

## Chapter 3.

Turning next to right-column plots, for the backward face, surface S2, the number flux is low at the gap shoulder, surface-S1/surface-S2 junction, it increases gradually along the surface up to the corner at the bottom surface, surface S3, where it reaches the maximum value. In addition, this maximum value increases significantly with increasing the angle of attack. Along the gap floor, surface S3, the number flux behavior also relies on  $L/H$  ratio and on the angle of attack. It is observed that it increases with decreasing the  $L/H$  ratio and with increasing the angle of attack  $\alpha$ . Nevertheless, it seems to reach a constant value for  $L/H < 1/2$ . Finally, along the forward face, surface S4,  $N_f$  basically increases from the corner, at the bottom surface, up to the top of the gap. This behavior is in contrast to that observed for the backward face. In fact, this is an expected behavior in the sense that it is directly related to the flow recirculation inside the gaps, as pointed out earlier. Due to the clockwise flow recirculation, at the vicinity of the surface S4, density is higher than that close to the surfaces S2 and S3. Therefore, a larger flux of molecules colliding to this surface is expected.

In order to gain some insight into the physics, it becomes instructive to examine the differences in the number flux distribution due to the angle-of-attack effect. In this fashion, Figs. 5.28 and 5.29 demonstrate the distribution of the number flux along the five gap surfaces, parameterized by the angle of attack  $\alpha$ , and for gap  $L/H$  ratio of 1 and 1/4, respectively. Results for the other gap  $L/H$  ratio are intermediate, and they will not be shown in this set of plots. It should be mentioned in this context that results for zero-degree angle of attack in these plots were obtained earlier by Paolicchi (PAOLICCHI, 2010).

Base on this group of plots, it is clearly noticed that the number flux increases significantly with increasing the angle of attack. This is an expected behavior in the sense that density increases inside the gaps with the angle-of-attack rise, for the  $L/H$  ratio investigated. In addition, as the angle of attack increases from 0 to 20 degrees, the body geometry changes aerodynamically from a sharp body to a blunt body for the oncoming flow. As a result, the geometry becomes less streamlined and the collision frequency of the molecules with the surfaces increases. Therefore, the number flux to the gap surfaces increases.

Figure 5.26 - Dimensionless number flux ( $N_f$ ) distribution along the gap surfaces parameterized by the gap  $L/H$  ratio for 10-degree angle of attack.

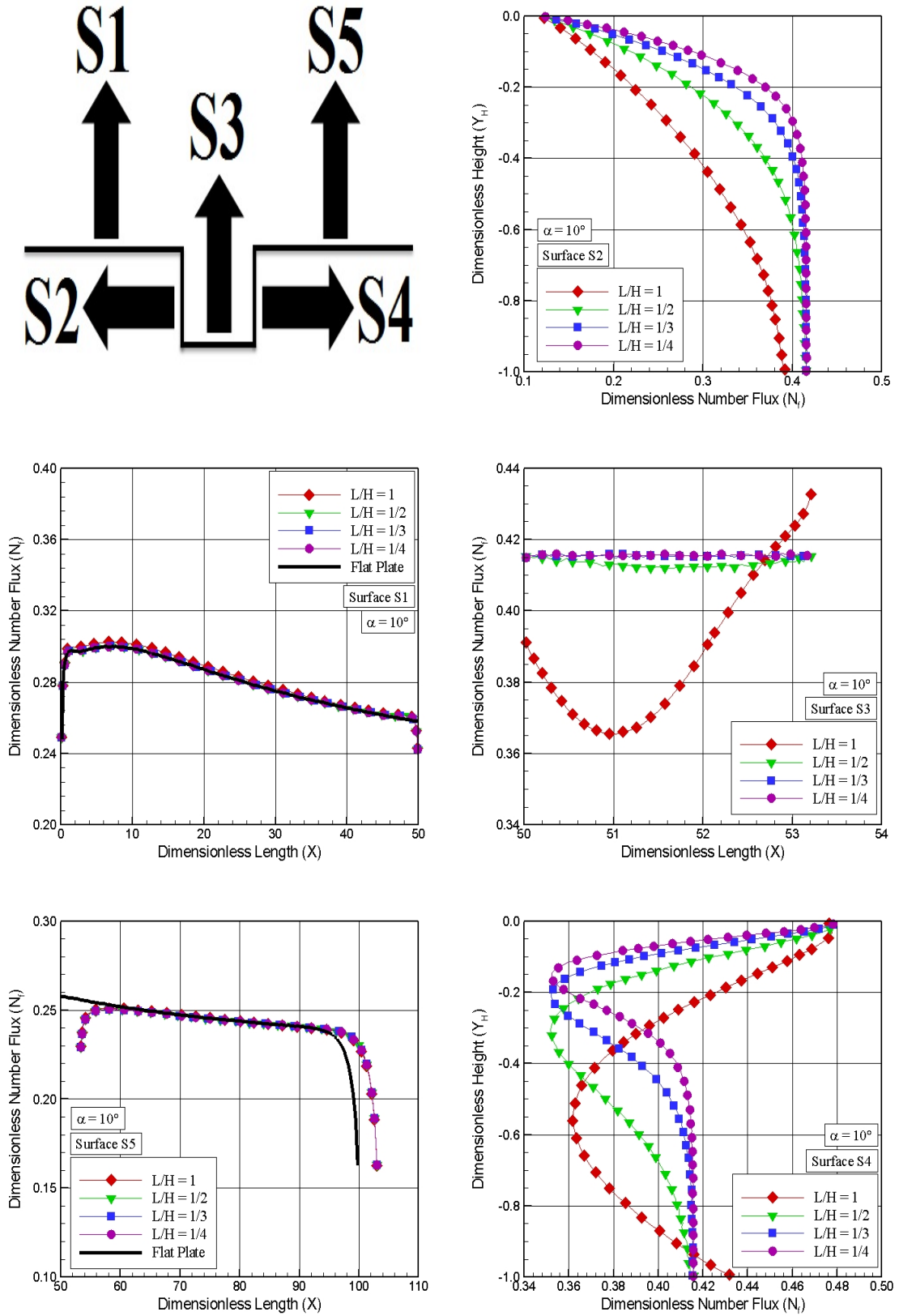


Figure 5.27 - Dimensionless number flux ( $N_f$ ) distribution along the gap surfaces parameterized by the gap  $L/H$  ratio for 20-degree angle of attack.

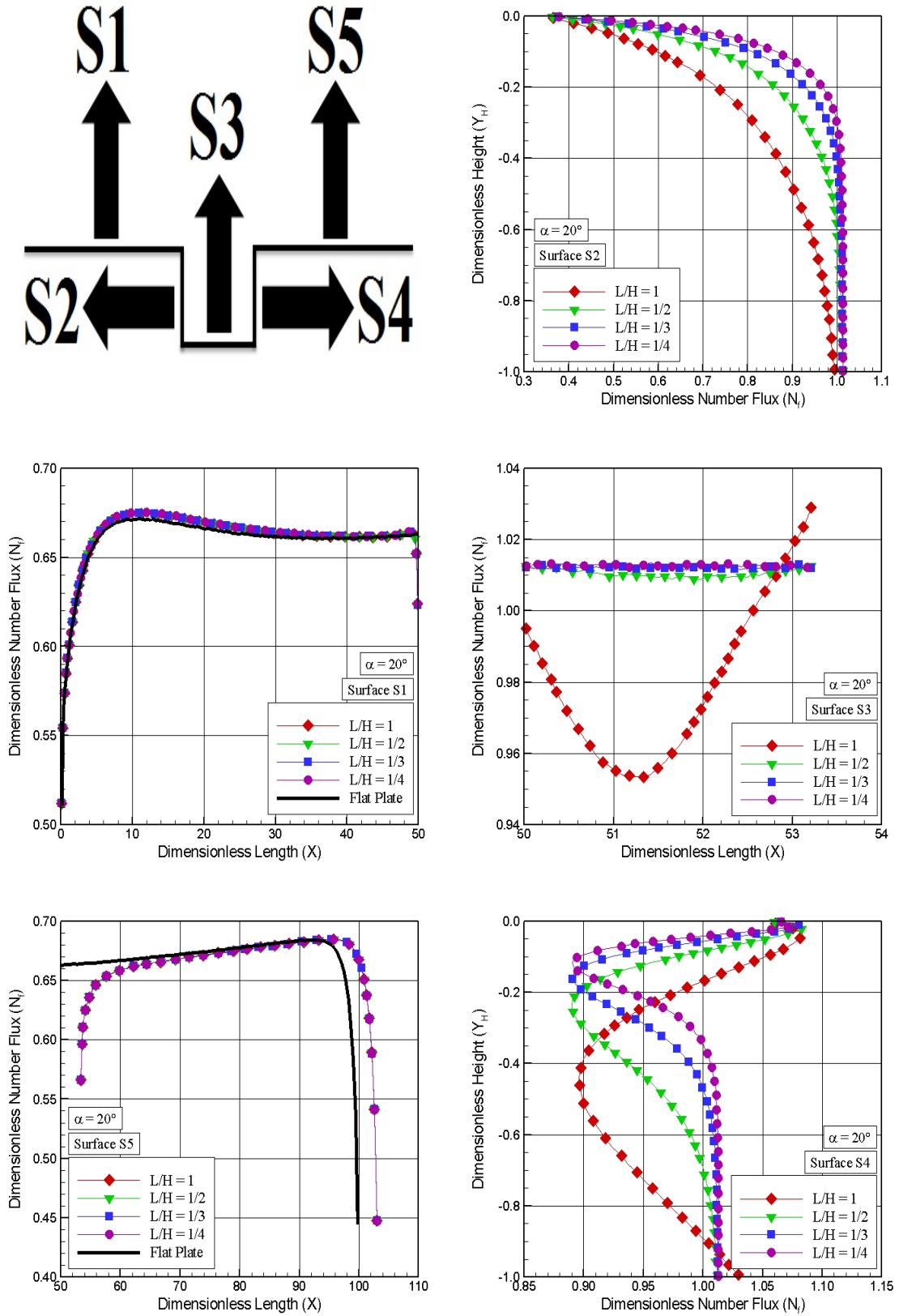


Figure 5.28 - Dimensionless number flux ( $N_f$ ) distribution along the gap surfaces parameterized by the angle of attack  $\alpha$  for gap  $L/H$  ratio of 1.

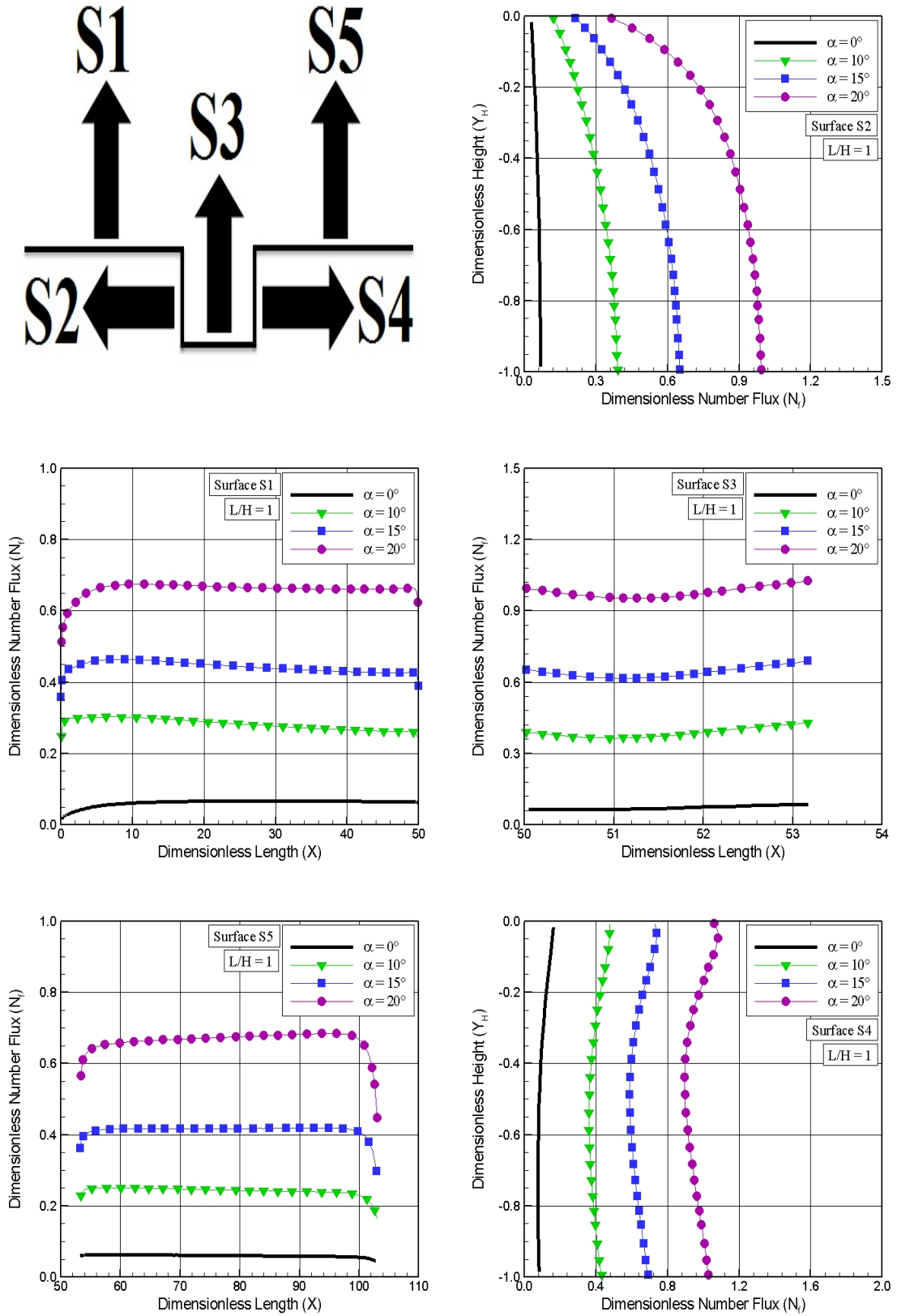
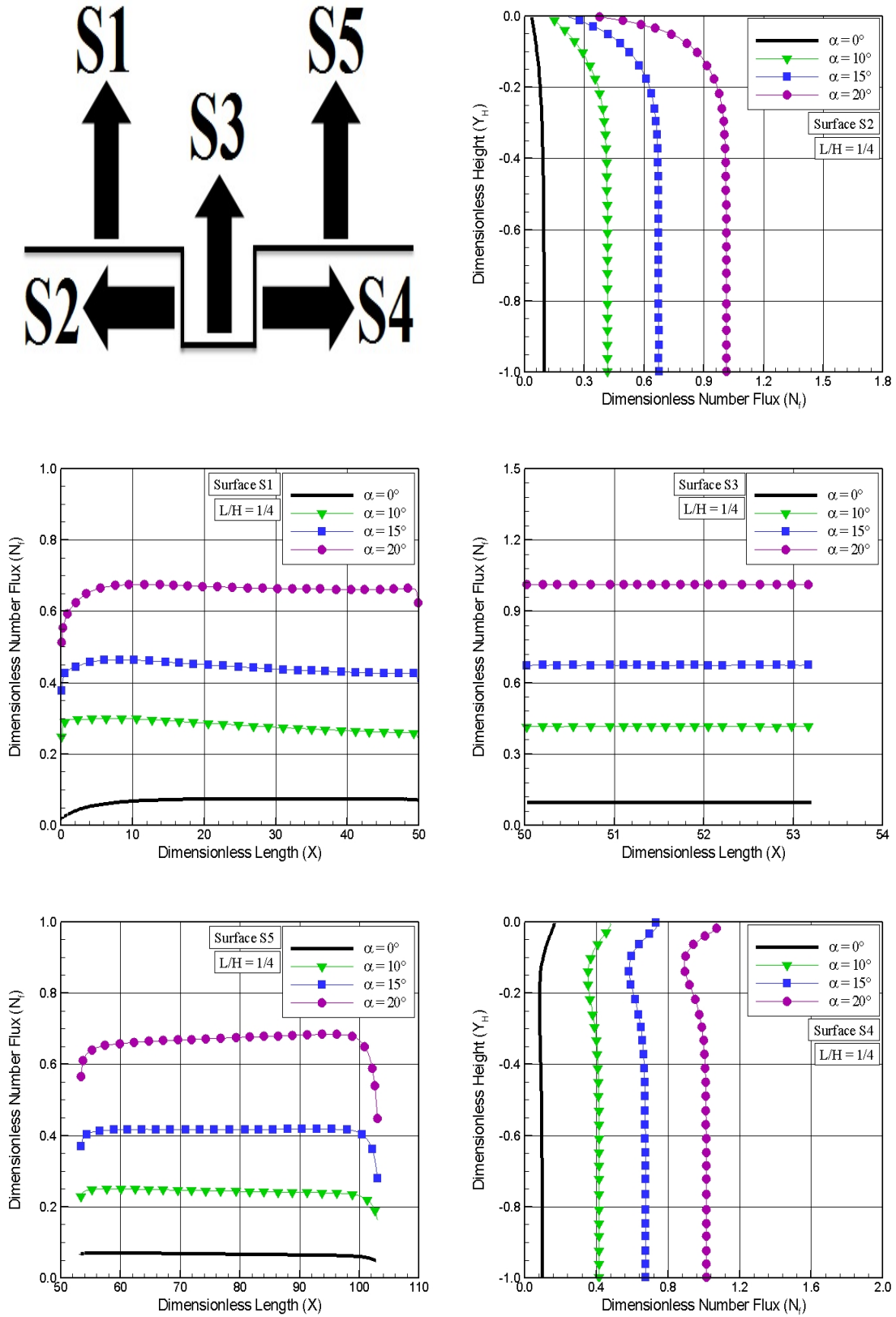


Figure 5.29 - Dimensionless number flux ( $N_f$ ) distribution along the gap surfaces parameterized by the angle of attack  $\alpha$  for gap  $L/H$  ratio of 1/4.



### 5.2.2 Pressure Coefficient

The pressure coefficient  $C_p$  is defined as follows,

$$C_p = \frac{p_w - p_\infty}{\frac{1}{2}\rho_\infty U_\infty^2} \quad (5.5)$$

where  $p_w$  is the wall pressure.

The wall pressure  $p_w$  on the body surface is calculated by the sum of the normal momentum fluxes of both incident and reflected molecules at each time step. A flux is regarded as positive if it is directed toward the body surface. Therefore, the wall pressure  $p_w$  is given by the following expression,

$$p_w = p_i - p_r = \frac{F_N}{A\Delta t} \sum_{j=1}^N \{[(mv)_j]_i - [(mv)_j]_r\} \quad (5.6)$$

where  $F_N$  is the number of real molecules represented by a single simulated molecule,  $\Delta t$  is the time step,  $A$  stands for the surface area,  $N$  is the number of molecules colliding with the surface by unit time and unit area,  $m$  is the mass of the molecules, and  $v$  is the velocity component of the molecule  $j$  in the surface normal direction. Subscripts  $i$  and  $r$  refer to incident and reflect molecules.

The behavior of the pressure coefficient due to changes on the gap  $L/H$  ratio is displayed in Figs. 5.30, and 5.31 for angle of attack of 10 and 20 degrees, respectively. Again, left-column plots in these figures refer to the distribution of the pressure coefficient along the gap upstream and downstream surfaces, i.e., surfaces S1 and S5, while the right-column plots correspond to the distribution on the surfaces inside the gap, i.e., surfaces S2, S3, and S4.

Referring to the left-column plots in these figures, it is clearly noticed that the pressure coefficient  $C_p$  follows the same trend as that presented for the number flux in the sense that, along surfaces S1 and S5, the pressure coefficient presents the same behavior for the flat-plate case, except at the vicinity of the gap shoulders. At the vicinity of these shoulders, a significant reduction in the pressure coefficient is observed when compared to the pressure coefficient for the flat-plate case. The reason for that is due to the flow expansion around these shoulders. Moreover, this

pressure decrease is associated to the significant reduction in the number flux, as shown in Figs. 5.26 and 5.27.

Turning to the right-column plots in these figures, the pressure coefficient  $C_p$  basically follows a similar behavior as that presented by the number flux in the sense that, for the backward face, surface S2, it is low at the shoulder,  $Y_H = 0$ , and increases downward along the surface, reaching the maximum value at the bottom, station  $Y_H = -1$ . In what follows, for the gap floor, surface S3, the pressure coefficient distribution relies on the gap  $L/H$  ratio. For the  $L/H = 1$  case,  $C_p$  increases along the surface, and reaches the maximum value at the vicinity of the surface-S3/surface-S4 junction. Nevertheless, for  $L/H < 1$  cases, the pressure coefficient is basically constant along the surface. Finally, along the forward face, surface S4, the pressure coefficient behavior is in contrast to that observed along surface S2 in the sense that  $C_p$  presents the lower value at the station  $Y_H = -1$ , and increases monotonically upward along the surface, reaching the peak value at the shoulder,  $Y_H = 0$ . This behavior is explained by the fact that the flow within the gaps is characterized by the appearance of a recirculation region. According to the flow topology, Fig. 5.9, the streamline pattern shows that the flow is characterized by a primary vortex system for  $L/H$  ratio investigated, where a clockwise recirculation structure fills the entire gap for the  $L/H = 1$  case. Conversely, for the  $L/H < 1$  cases, the recirculation region does not fill the entire gaps. Consequently, the pressure coefficient is basically constant along the gap floor for the  $L/H < 1$  cases.

Proceeding in a manner analogous to number flux, Figs. 5.32 and 5.33 display the distribution of the pressure coefficient  $C_p$  along the five gap surfaces, parameterized by the angle of attack  $\alpha$ , for gap  $L/H$  ratio of 1 and 1/4, respectively. It is clearly noticed from this set of plots that pressure coefficient  $C_p$  increases significantly with the angle-of-attack rise. As a base of comparison, for zero-degree angle of attack, the maximum value for  $C_p$  is around to 0.0392 at a station  $X = 23.9$  from the leading edge, along surface S1, independently of the gap  $L/H$  ratio. In contrast, this maximum value increases to 0.206, 0.321, and 0.459, at station  $X$  of 1.61, 0.97, and 0.51, for angle of attack of 10, 15, and 20 degrees, respectively. It is observed that the maximum value approaches the leading edge of the plate with increasing the angle of attack. As mentioned earlier, with increasing the angle of attack, the body geometry changes aerodynamically from a sharp body to a blunt body for the oncoming flow. As a result, the geometry becomes less streamlined and the collision frequency of the molecules with the surfaces increases, therefore, pressure coefficient increases.

Figure 5.30 - Pressure coefficient ( $C_p$ ) distribution along the gap surfaces parameterized by the gap  $L/H$  ratio for 10-degree angle of attack.

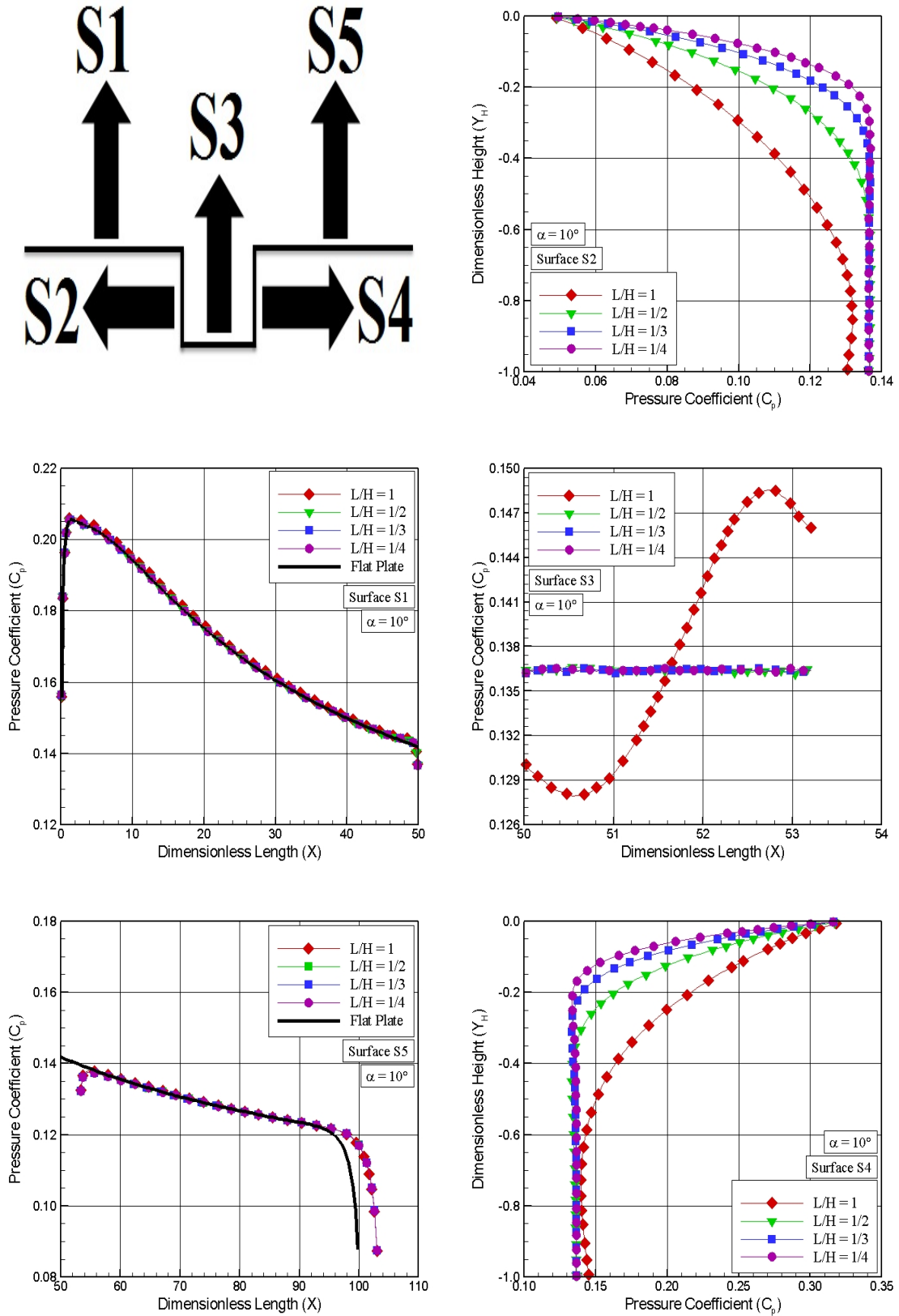


Figure 5.31 - Pressure coefficient ( $C_p$ ) distribution along the gap surfaces parameterized by the gap  $L/H$  ratio for 20-degree angle of attack.

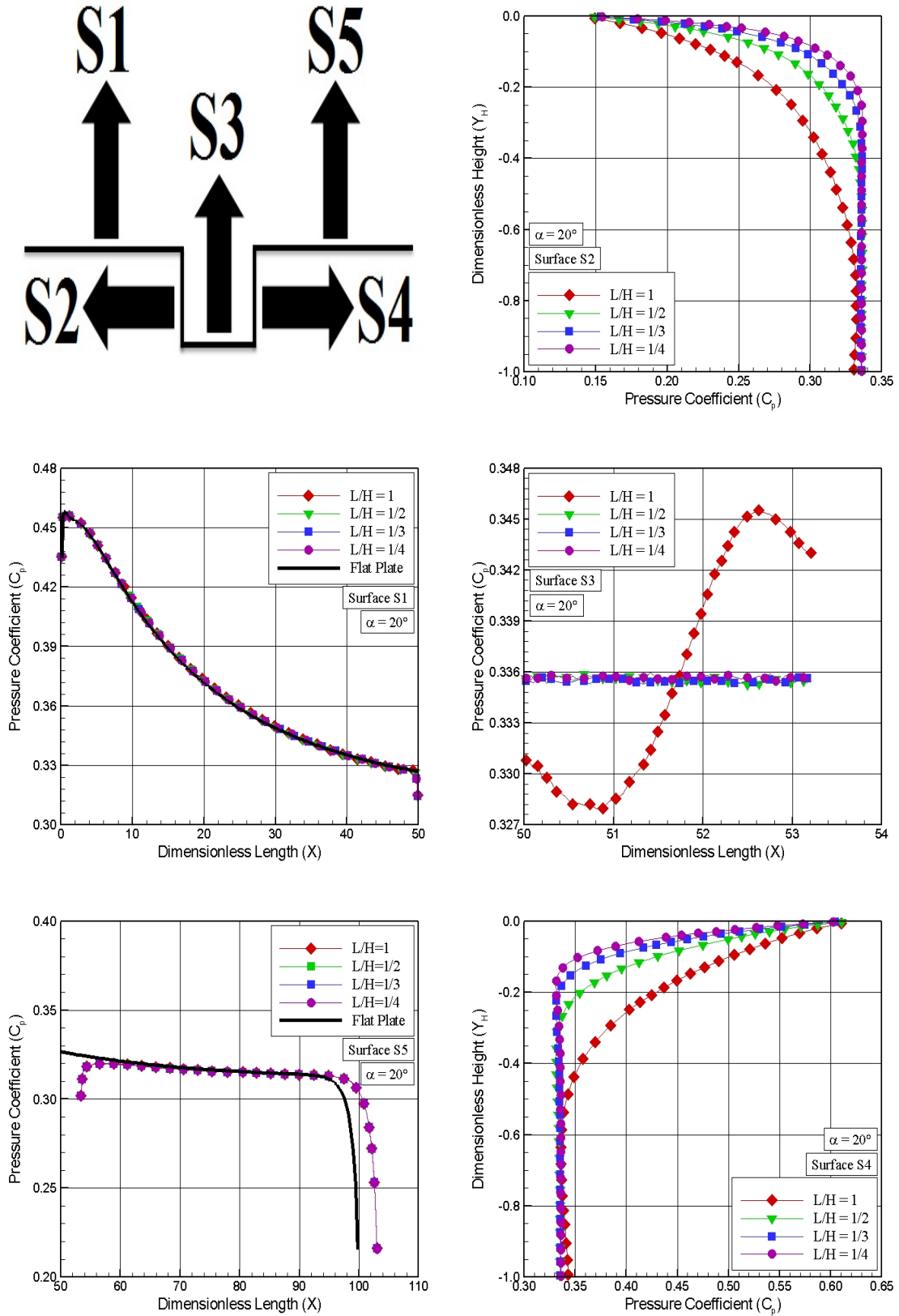


Figure 5.32 - Pressure coefficient ( $C_p$ ) distribution along the gap surfaces parameterized by the angle of attack  $\alpha$  for gap  $L/H$  ratio of 1.

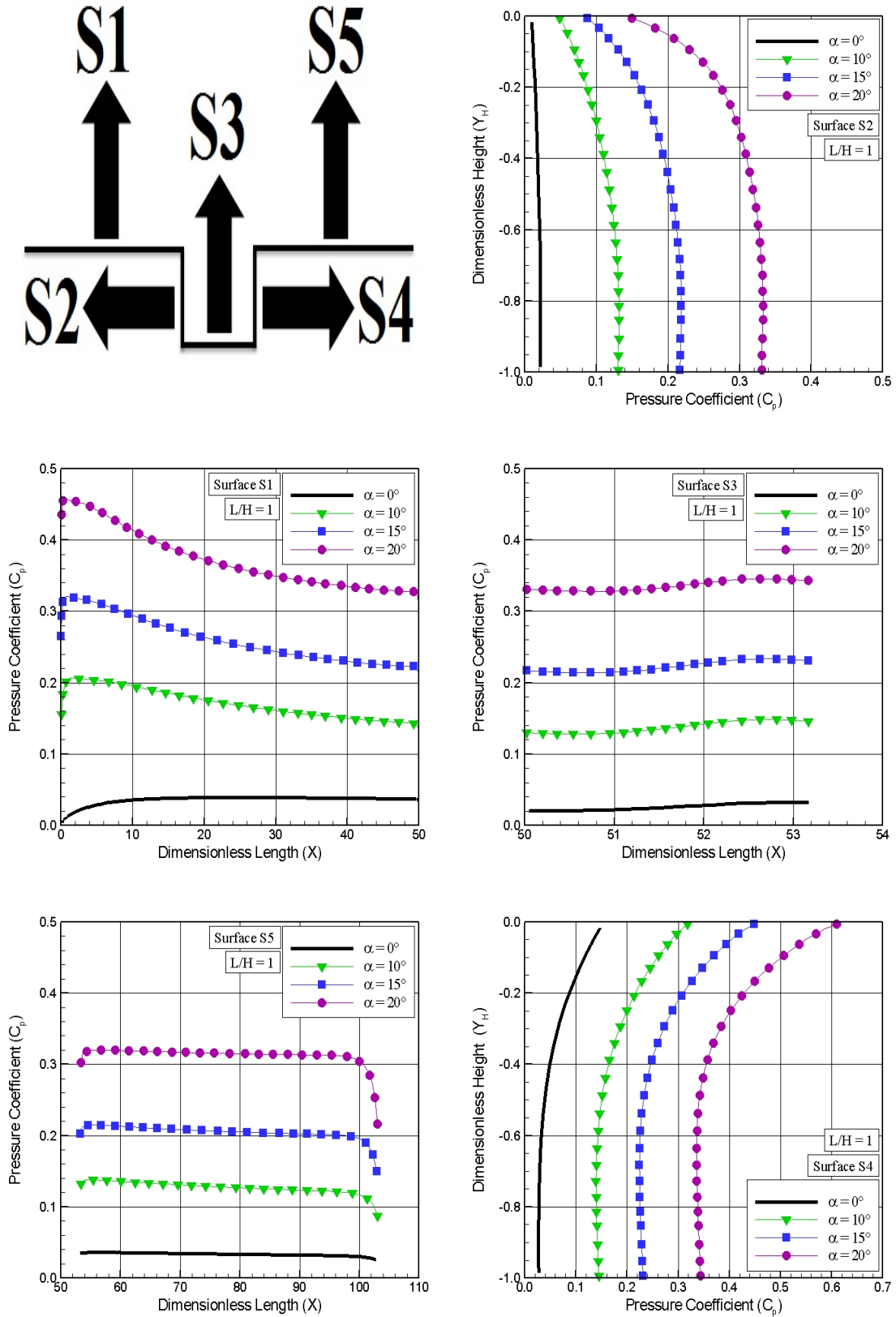
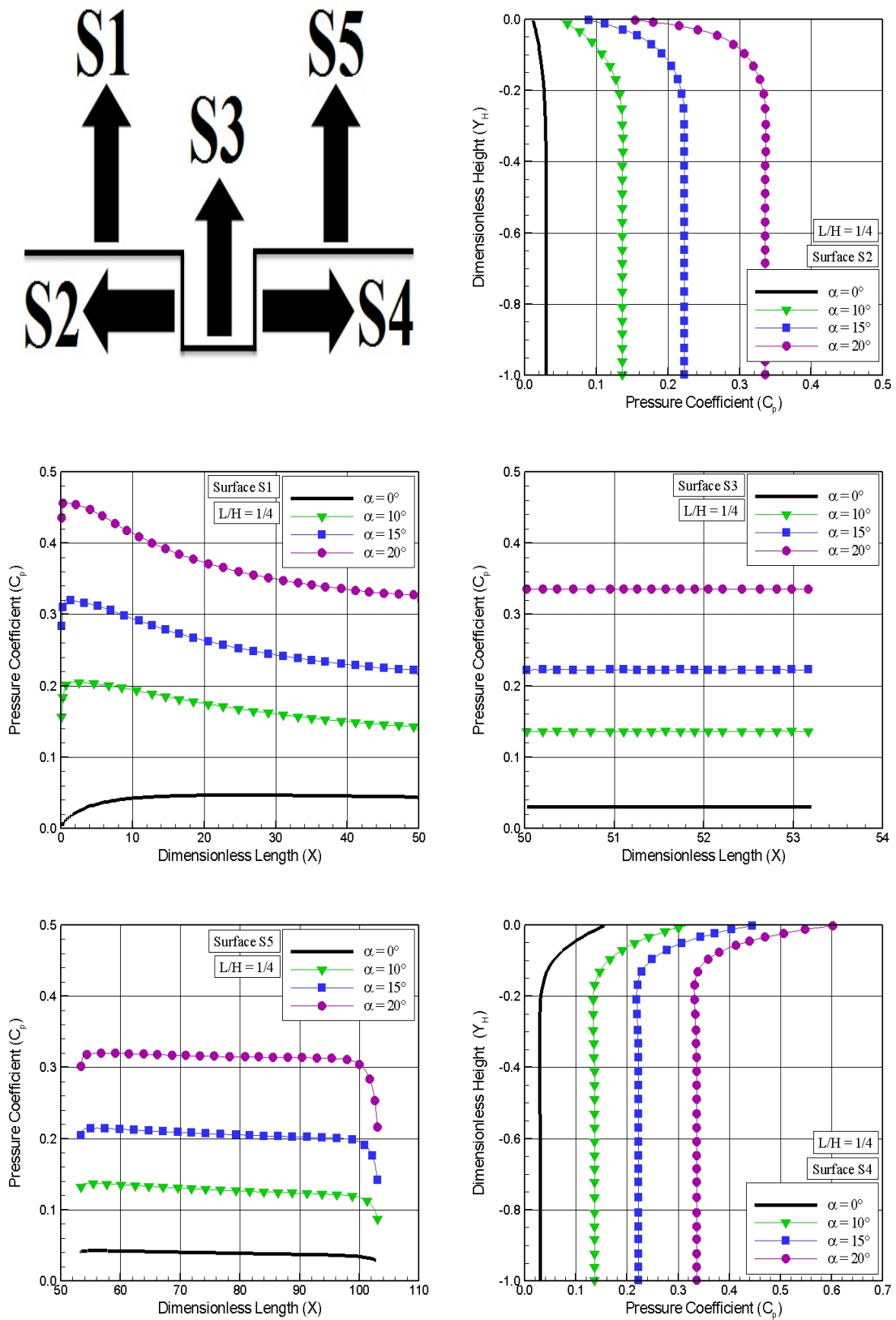


Figure 5.33 - Pressure coefficient ( $C_p$ ) distribution along the gap surfaces parameterized by the angle of attack  $\alpha$  for gap  $L/H$  ratio of 1/4.



In the following, it proves instructive to compare the maximum values for the pressure coefficient observed in the gaps with that for a smooth surface, i.e., a flat plate without a gap, for the corresponding angle of attack. For comparative purpose, independently of the gap  $L/H$  ratio, the peak value for  $C_p$  is around 0.147, 0.318, 0.448, and 0.610, for angle of attack of 0, 10, 15, and 20 degrees, respectively, observed at the gap corner, surface-S4/surface-S5 junction, for the conditions investigated. For the flat-plate cases, the maximum value for  $C_p$  is around to 0.0392, 0.206, 0.321, and 0.459, at station  $X$  of 23.9, 1.61, 0.97, and 0.51, from the leading edge, along surface S1, for angle of attack of 0, 10, 15, and 20 degrees, respectively. Therefore, the  $C_p$  peak values for the gaps are around 3.76, 1.54, 1.40, and 1.33 times larger than the peak values for a smooth surface at 0, 10, 15, and 20 degrees of incidence, respectively. Consequently, the presence of the gaps on the vehicle surface can not be ignored in a vehicle design.

### 5.2.3 Skin Friction Coefficient

The skin friction coefficient  $C_f$  is defined as follows,

$$C_f = \frac{\tau_w}{\frac{1}{2}\rho_\infty U_\infty^2} \quad (5.7)$$

where  $\tau_w$  is the shear stress on the body surface.

The shear stress  $\tau_w$  on the body surface is calculated by the sum of the tangential momentum fluxes of both incident and reflected molecules impinging on the surface at each time step by the following expression,

$$\tau_w = \tau_i - \tau_r = \frac{F_N}{A\Delta t} \sum_{j=1}^N \{[(mu)_j]_i - [(mu)_j]_r\} \quad (5.8)$$

where  $u$  is the velocity component of the molecule  $j$  in the surface tangential direction. Subscripts  $i$  and  $r$  refer to incident and reflect molecules, respectively.

It is worthwhile to note that, for the special case of diffuse reflection, the gas-surface interaction model adopted in present work, the reflected molecules have a tangential moment equal to zero, since the molecules essentially lose, on average, their tangen-

tial velocity components. In this fashion, the contribution of  $\tau_r$  in Equation. 5.8 is equal to zero.

The gap  $L/H$  ratio effects on the skin friction coefficient along all surfaces are illustrated in Figs. 5.34 and 5.35 for angle of attack of 10 and 20 degrees, respectively. According to the left-column plots, along surface S1, the value of  $C_f$  starts from a maximum value near the leading edge and decreases monotonically downstream along the body surface, for the conditions investigated. This maximum value increases with the angle-of-attack rise. In addition, the skin friction coefficient  $C_f$  for the flat plate with a gap is basically the same as that of the flat-plate case, i.e., a flat plate without a gap. At the vicinity of the gap position, more precisely at the gap shoulder at station  $X = 50$ , no upstream effect is observed on the skin friction coefficient, by visual inspection. In contrast, along surface S5, it is noticed that the skin friction coefficient  $C_f$  is larger than that for the flat-plate case, especially at the vicinity of the gap downstream corner, defined by the surface-S4/surface-S5 junction. It is perhaps worth noting that this behavior, at the vicinity of the gap downstream corner, is in contrast to that observed for the pressure coefficient. Finally, as the flow moves downstream along surface S5, the skin friction coefficient  $C_f$  reaches the value observed for the flat-plate case.

On examining the right-column plots in these figures, for backward face, surface S2, the skin friction coefficient in general presents the peak value close to the shoulder,  $Y_H = 0$ . Then, it decreases along the upper half part of the surface, and basically reaches a constant value along the lower half part of the surface. In what follows, for the gap floor, surface S3, the skin friction coefficient is negative at the vicinity of the surface-S2/surface-S3 junction, and becomes positive at the vicinity of the surface-S3/surface-S4 junction. Nevertheless, as the  $L/H$  ratio increases,  $C_f = 0$  is observed along the entire surface. Afterwards, along the forward face, surface S4, the skin friction coefficient starts from zero at the vicinity of the surface-S3/surface-S4 junction and decreases negatively up to a minimum value close to the shoulder,  $Y_H = 0$ .

A feature of particular interest in these set of plots is the change from positive to negative value in the skin friction coefficient  $C_f$ . Usually, the condition  $C_f = 0$  may indicate the presence of a backflow, an attachment or reattachment point in the flow in a two-dimensional problem, as pointed out by Kim and Setoguchi (KIM; SETOGUCHI, 2007) and Deepak et al. (DEEPAK et al., 2010). In the present work, this change is directly related to the clockwise recirculation region inside the gaps.

Figure 5.34 - Skin friction coefficient ( $C_f$ ) distribution along the gap surfaces parameterized by the gap  $L/H$  ratio for 10-degree angle of attack.

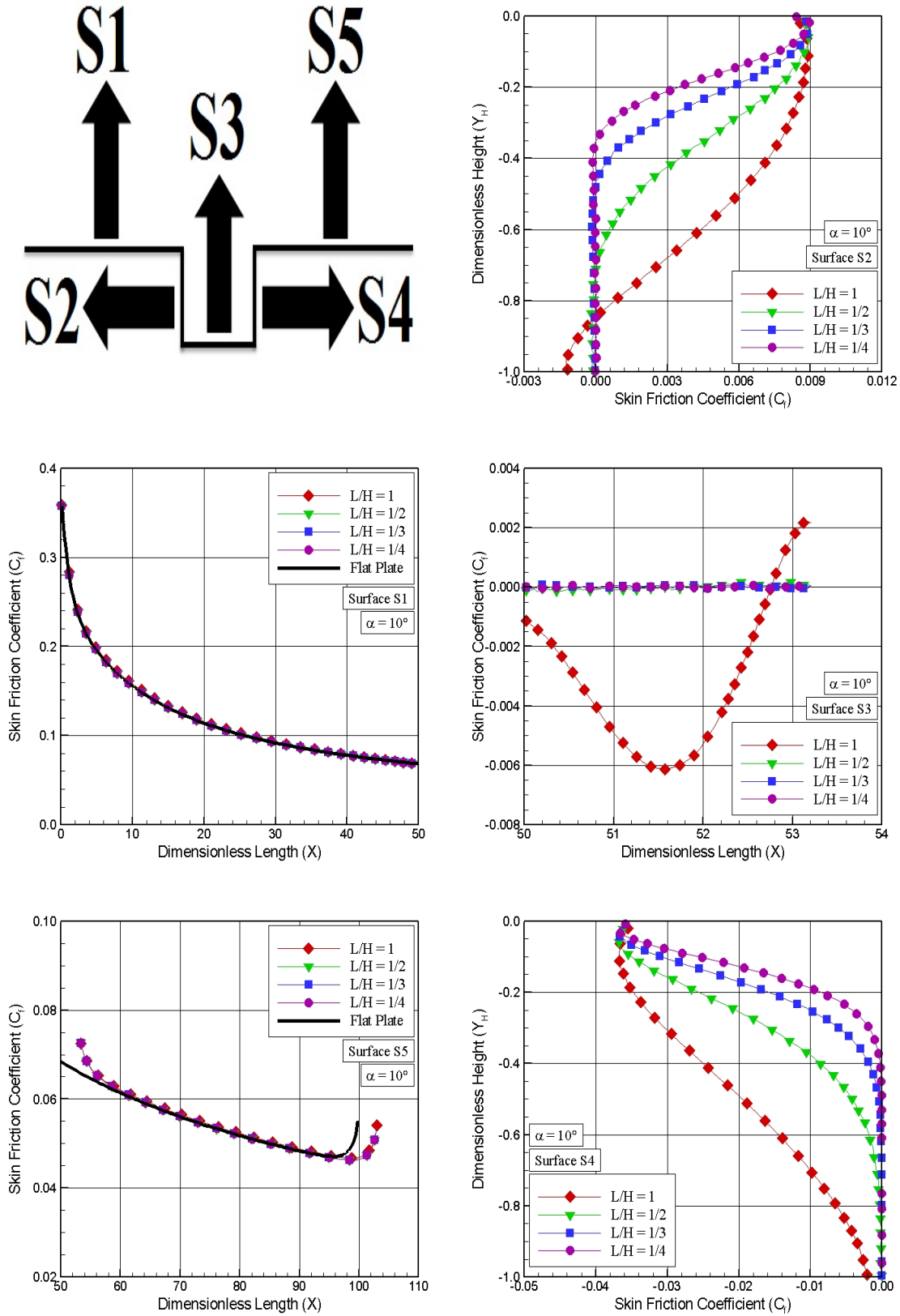


Figure 5.35 - Skin friction coefficient ( $C_f$ ) distribution along the gap surfaces parameterized by the gap  $L/H$  ratio for 20-degree angle of attack.

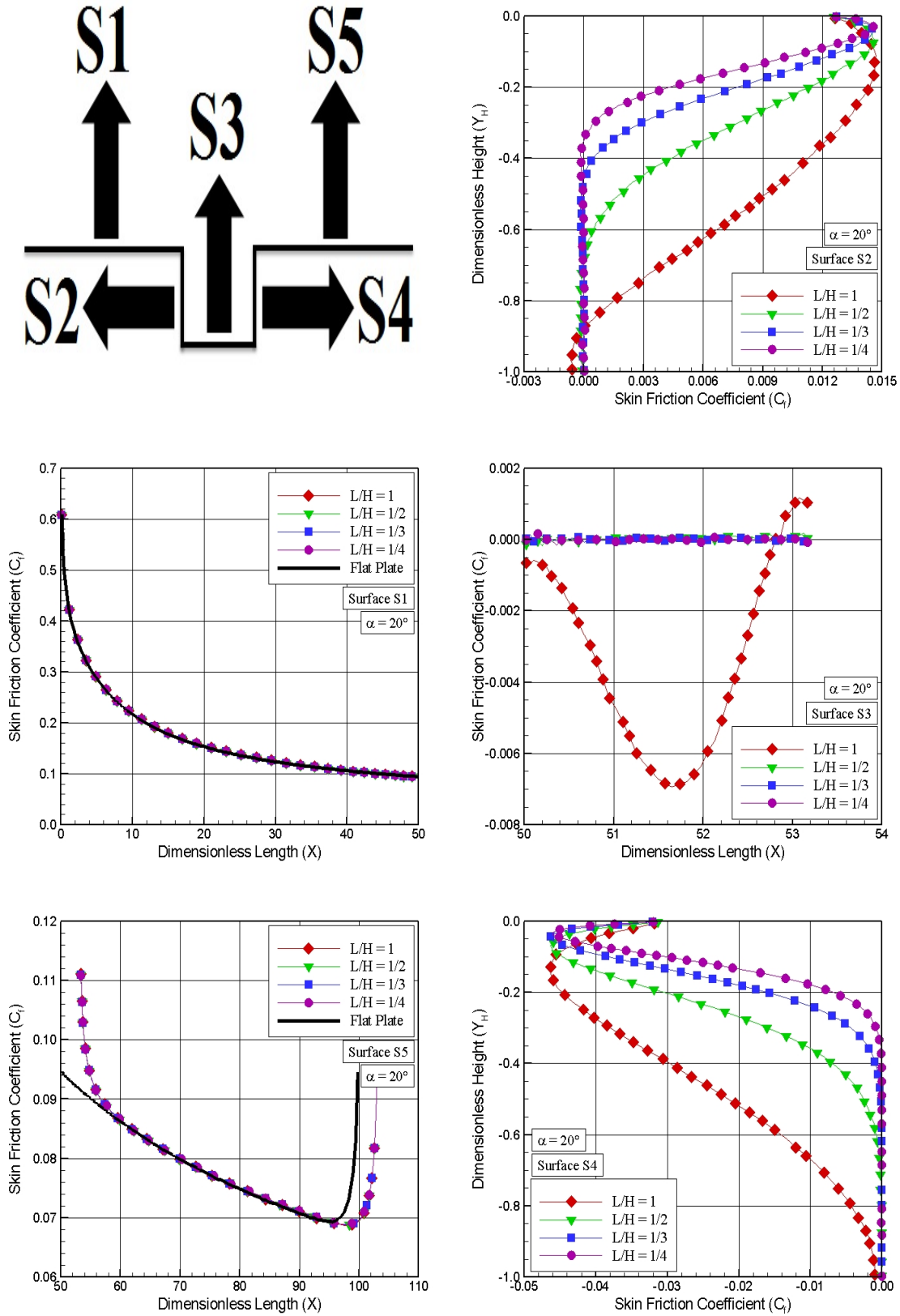


Figure 5.36 - Skin friction coefficient ( $C_f$ ) distribution along the gap surfaces parameterized by the angle of attack  $\alpha$  for gap  $L/H$  ratio of 1.

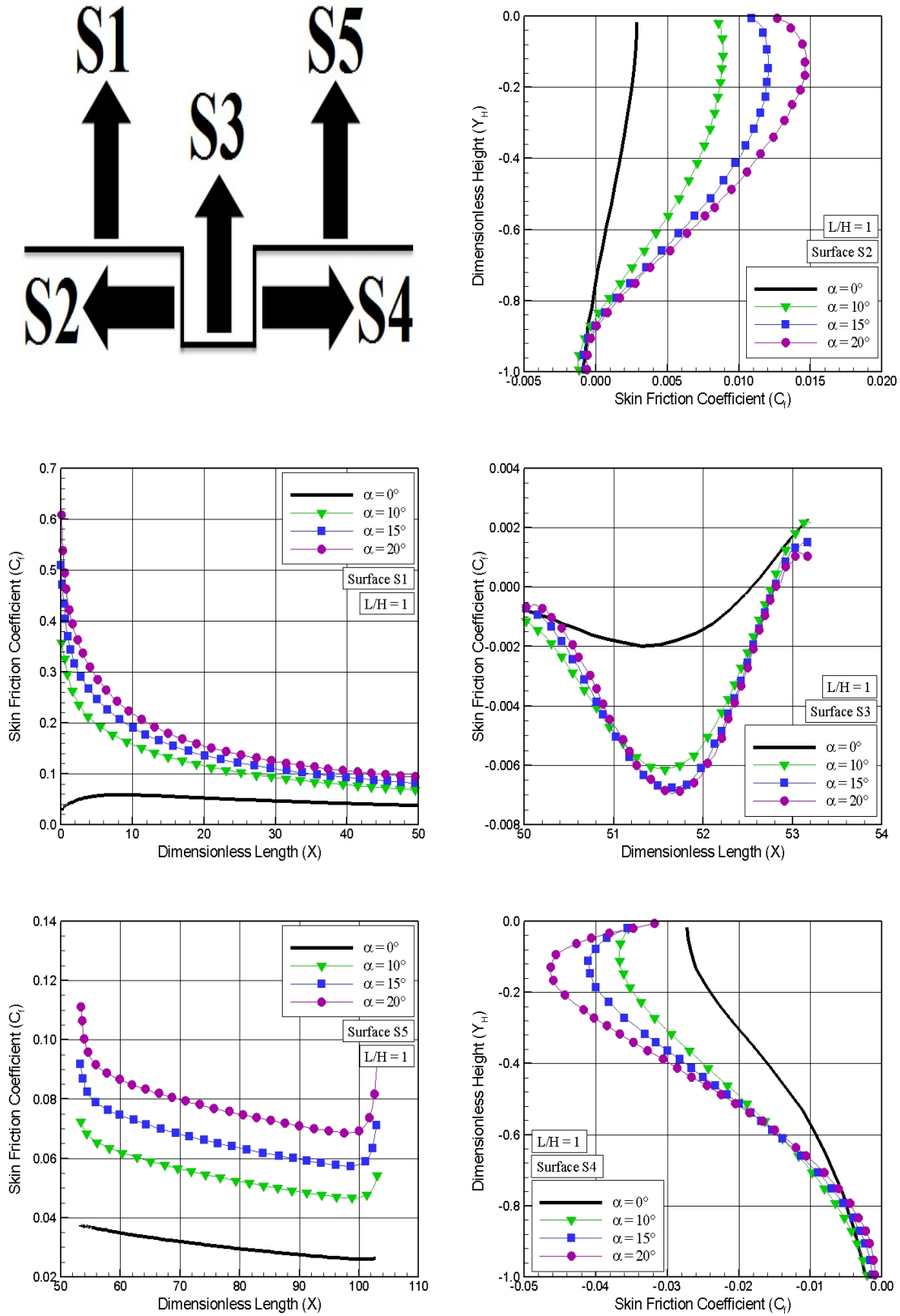
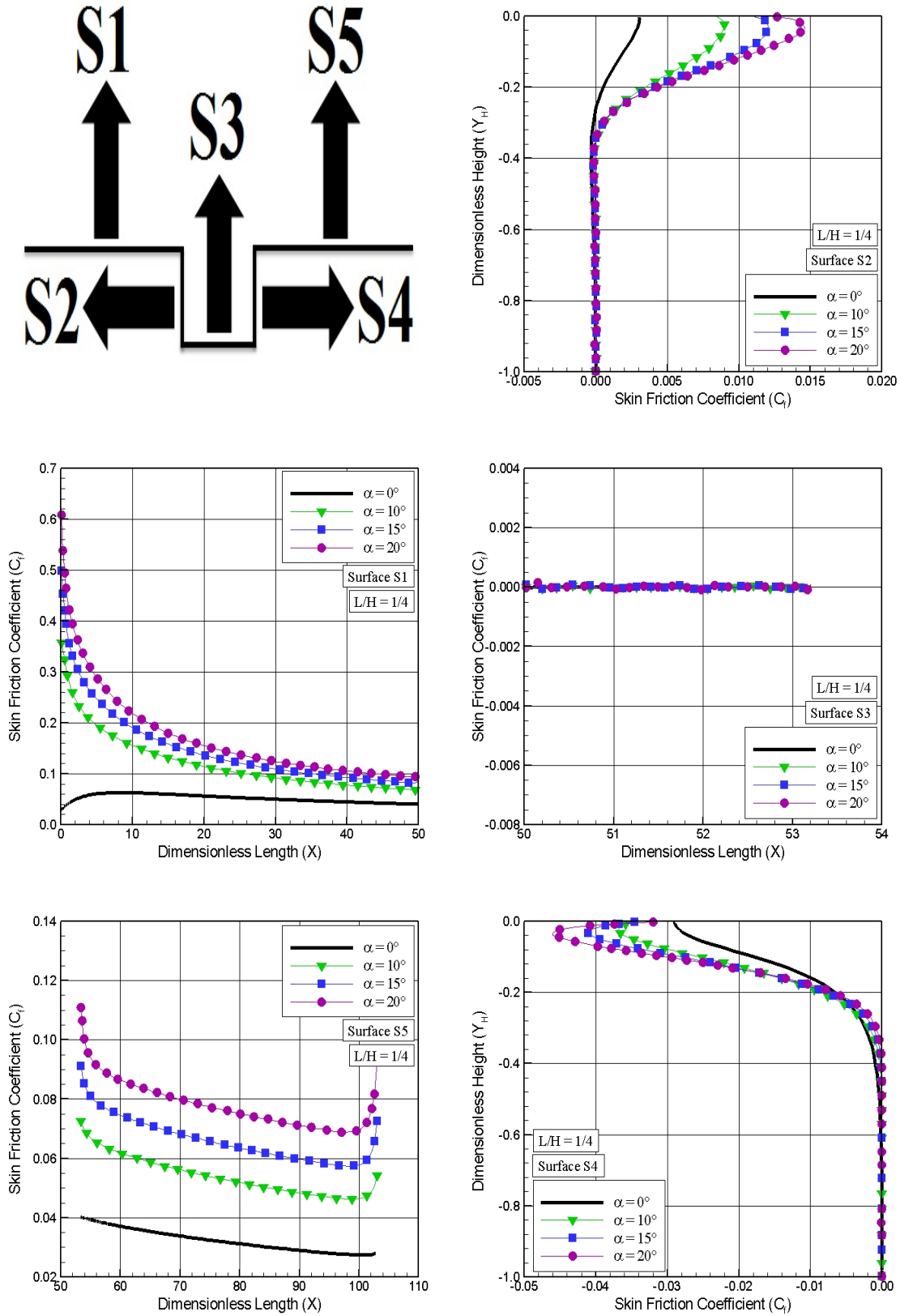


Figure 5.37 - Skin friction coefficient ( $C_f$ ) distribution along the gap surfaces parameterized by the angle of attack  $\alpha$  for gap  $L/H$  ratio of 1/4.



For the  $L/H$  ratio and angle of attack investigated, the flowfield structure inside the gaps was defined primarily by one vortex system. This is in contrast to the gap flowfield structure usually observed in the continuum flow regime. In continuum flow regime, the gap flow topology is defined by the development of a column of counter-rotating vortices within the gap caused by the main stream flow, where the number of vortices is approximately given by the ratio  $H/L$ . In addition, alternating hot spots are developed in the gap when the vortices directionally align and impinge on the gap sidewall (EVERHART et al., 2006).

Having a clear qualitative picture of the skin friction coefficient due to the effects of the gap  $L/H$  ratio, the attention is turned to the angle of attack effects. In doing so, Figs. 5.36 and 5.37 demonstrate the distribution of the skin friction coefficient  $C_f$  along the five gap surfaces, parameterized by the angle of attack  $\alpha$ , for gap  $L/H$  ratio of 1 and 1/4, respectively. It is quite apparent from this set of plots that skin friction coefficient  $C_f$  increases significantly with increasing the angle-of-attack. For comparison purpose, for zero-degree angle of attack, the maximum value for  $C_f$  is around to 0.063 at the station  $X = 8.02$  from the leading edge, along surface S1, independently of the gap  $L/H$  ratio. Conversely, this maximum value increases to 0.358, 0.509, and 0.607, at the leading edge of the flat plate, for angle of attack of 10, 15, and 20 degrees respectively.

Finally, by taking a closer look at these skin friction coefficient results, it is recognized from these plots that the peak values for  $C_f$  along surfaces S1 are larger than those observed for the pressure coefficient. As a result, tangential forces, associated with the shear stress, are larger than normal forces, related to the wall pressure.

#### 5.2.4 Heat Transfer Coefficient

The heat transfer coefficient  $C_h$  is defined as follows,

$$C_h = \frac{q_w}{\frac{1}{2}\rho_\infty U_\infty^3} \quad (5.9)$$

where  $q_w$  is the heat flux to the body surface.

The heat flux  $q_w$  is calculated by the net energy flux of the molecules impinging on the surface. The net heat flux  $q_w$  is related to the sum of the translational, rotational and vibrational energies of both incident and reflected molecules as defined by,

$$q_w = q_i - q_r = \frac{F_N}{A\Delta t} \left\{ \sum_{j=1}^N \left[ \frac{1}{2} m_j c_j^2 + e_{rj} + e_{vj} \right]_i - \sum_{j=1}^N \left[ \frac{1}{2} m_j c_j^2 + e_{rj} + e_{vj} \right]_r \right\} \quad (5.10)$$

where  $c$  is the velocity of the molecules,  $e_r$  and  $e_v$  stand for rotational and vibrational energies, respectively.

The gap  $L/H$  ratio impact on the heat transfer coefficient along all surfaces is displayed in Figs. 5.38 and 5.39 for angle of attack of 10 and 20 degrees, respectively. Based on the left-column plots, the value of  $C_h$  along surface S1 starts from a peak value at the leading edge and decreases monotonically downstream along the body surface, for the conditions investigated. This peak value increases with increasing the angle of attack  $\alpha$ . In addition, no upstream effect is observed on the heat transfer coefficient along surface S1, since the heat transfer coefficient for the flat-plate with a gap is basically the same as that of the flat-plate case, i.e., a flat-plate without a gap, even at the vicinity of the gap position, station  $X = 50$ . Conversely, along surface S5, it is clearly seen that the heat transfer coefficient  $C_h$  is larger than that for the flat-plate case, especially at the vicinity of the gap downstream corner, defined by the surface-S4/surface-S5 junction. Again, this peak value increases with increasing the angle of attack  $\alpha$ . This behavior, at the vicinity of the gap downstream corner, is similar to that observed for the skin friction coefficient. Nevertheless, it is in contrast to that observed for the pressure coefficient. Finally, as the flow moves downstream along surface S5, the heat transfer coefficient  $C_h$  recovers the value observed for the flat-plate case.

Focusing on the right-column plots in these figures, for backward face, surface S2, the heat transfer coefficient follows the same trend as that presented by the skin friction coefficient in the sense that, in general, it presents the peak value close to the shoulder,  $Y_H = 0$ . Afterwards, it decreases along the upper half part of the surface, and basically reaches a constant value along the lower half part of the surface. In the following, for the gap floor, surface S3, the heat transfer coefficient exhibits very low values, around two order of magnitude smaller than the peak value observed in surface S1. Then, along the forward face, surface S4, the heat transfer coefficient starts from zero at the vicinity of the surface-S3/surface-S4 junction and increases up to a maximum value close to the shoulder,  $Y_H = 0$ .

Figure 5.38 - Heat transfer coefficient ( $C_h$ ) distribution along the gap surfaces parameterized by the gap  $L/H$  ratio for 10-degree angle of attack.

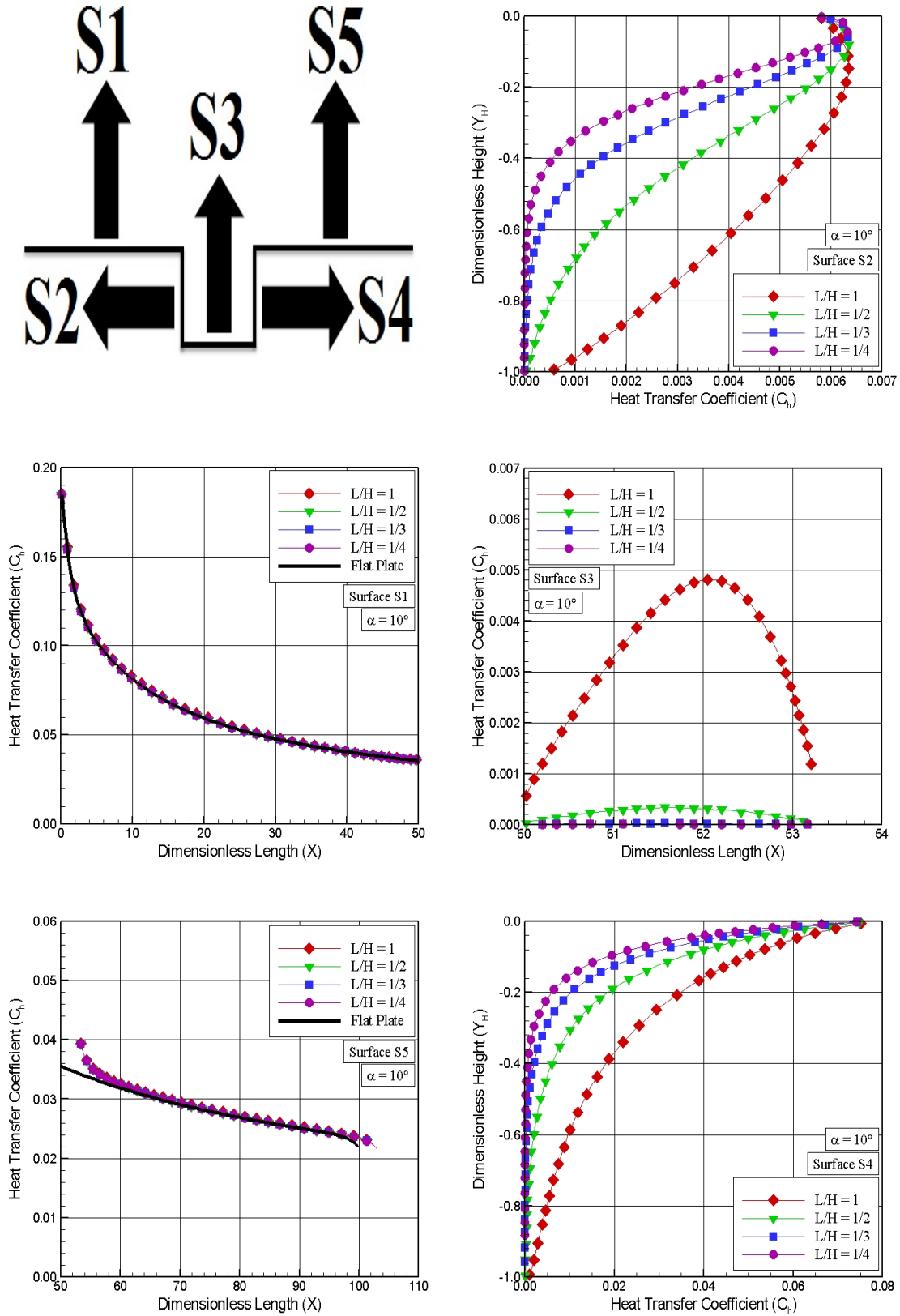


Figure 5.39 - Heat transfer coefficient ( $C_h$ ) distribution along the gap surfaces parameterized by the gap  $L/H$  ratio for 20-degree angle of attack.

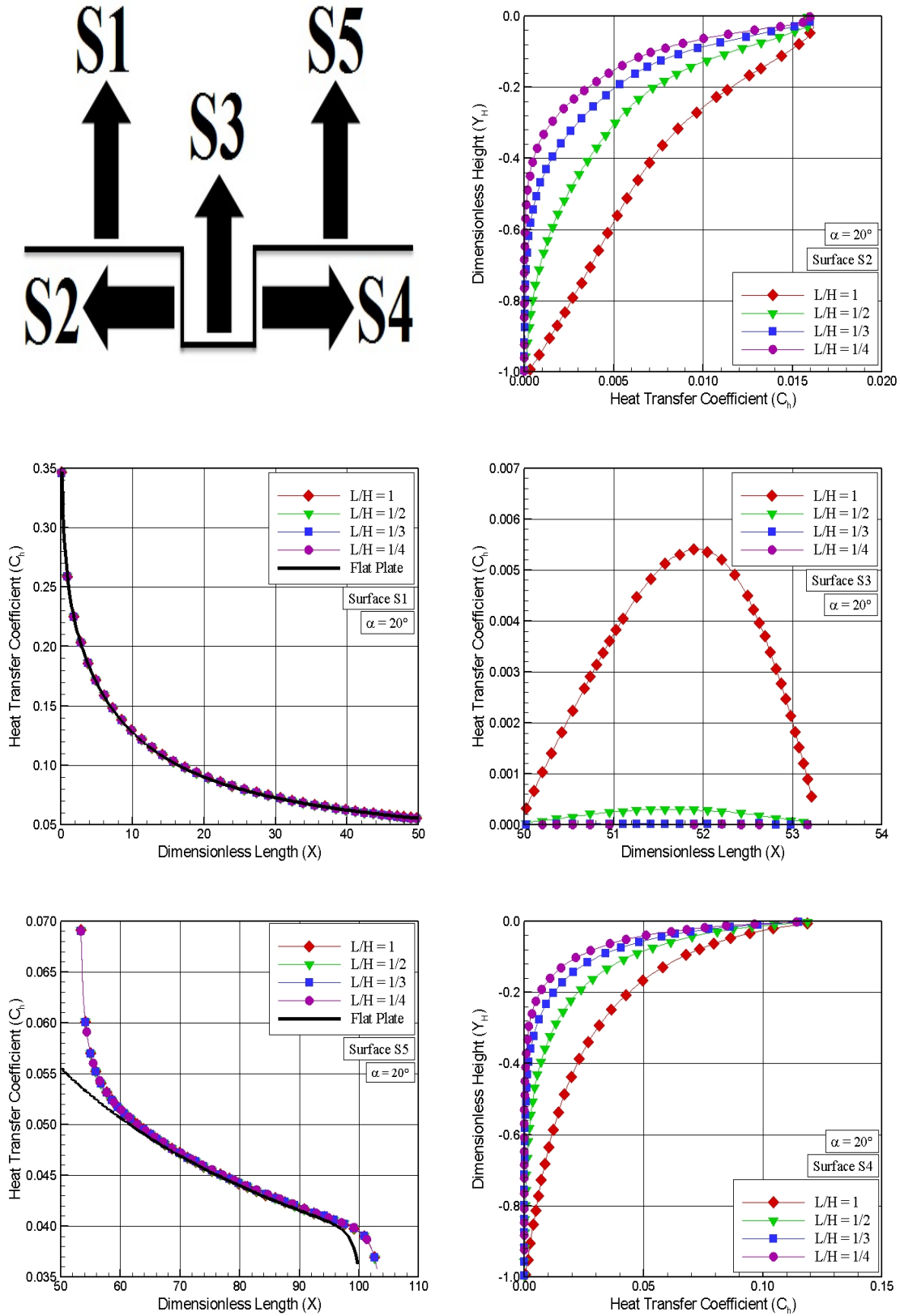


Figure 5.40 - Heat transfer coefficient ( $C_h$ ) distribution along the gap surfaces parameterized by the angle of attack  $\alpha$  for gap  $L/H$  ratio of 1.

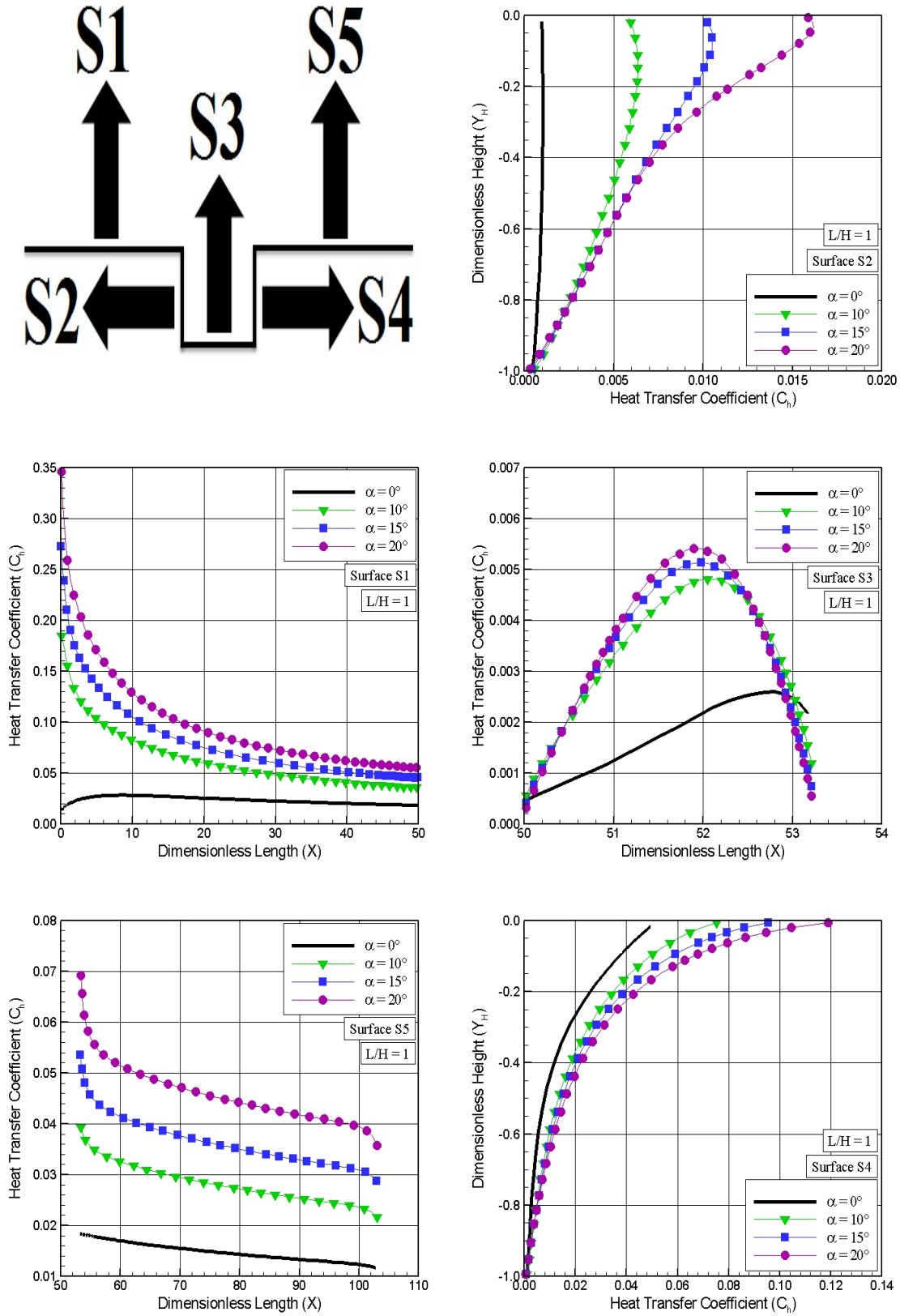
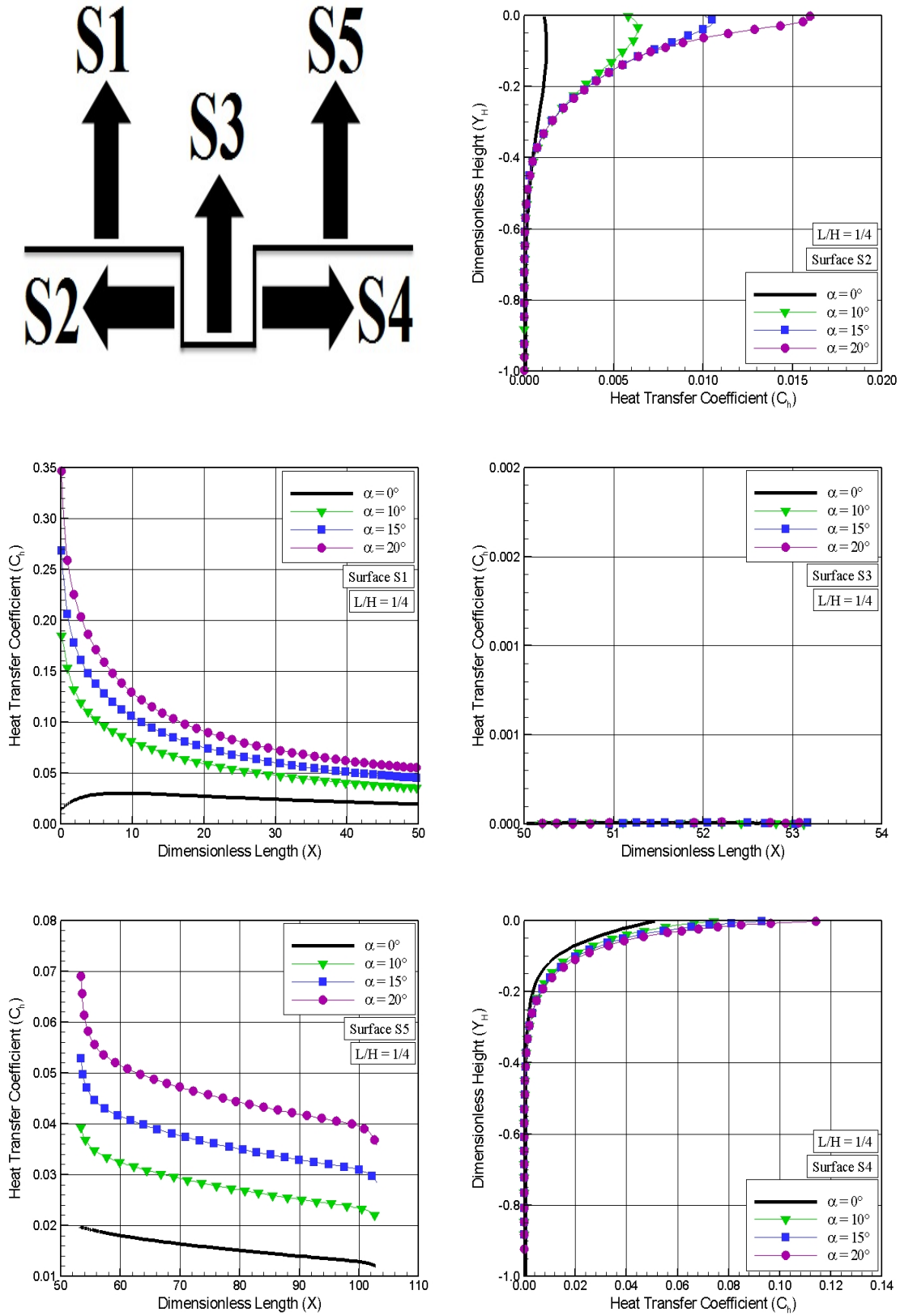


Figure 5.41 - Heat transfer coefficient ( $C_h$ ) distribution along the gap surfaces parameterized by the angle of attack  $\alpha$  for gap  $L/H$  ratio of 1/4.



For the time being, a critical assessment of the angle-of-attack effects is provided by Figs. 5.40 and 5.41. These figures display the distribution of the heat transfer coefficient  $C_h$  along the five gap surfaces, parameterized by the angle of attack  $\alpha$ , for gap  $L/H$  ratio of 1 and  $1/4$ , respectively. Based on this set of plots, it is accepted without questions that changes on the angle of attack affect the heat transfer coefficient to the gap surfaces, not only outside but also inside the gap surfaces. As a matter of comparison, for zero-degree angle of attack, the maximum heat transfer coefficient to surface S1 is  $C_h = 0.029$  that takes place at section  $X = 8.8$ . Due to the presence of the gap in the flat-plate, the peak value for heat transfer to surface S4 is  $C_h = 0.054$ , which takes place at the vicinity of the surface-S4/surface-S5 junction. Therefore, for the same freestream conditions, the peak value of  $C_h$  for the gaps is approximately twice of that for a smooth surface. As a result, for zero-degree angle of attack, the presence of the gap in the surface of a hypersonic vehicle may not be ignored. On the other hand, for angle of attack of 10, 15 and 20 degrees, peak values for  $C_h$  on surface S1 are 0.185, 0.272, and 0.346, respectively, and they occur at the leading edge, for the conditions investigated in this work. In addition, along surface S4, the peak values for  $C_h$  are 0.075, 0.095, and 0.119 for angle of attack of 10, 15 and 20 degrees, respectively. Consequently, in the design of a hypersonic vehicle at incidence, the presence of a gap may be ignored in terms of heat flux to the vehicle surface.



## 6 CONCLUSIONS

### 6.1 Concluding Remarks

In this work, a computational analysis has been carried out in order to investigate a hypersonic rarefied two-dimensional flow over a gap, by employing the Direct Simulation Monte Carlo method. The simulations provided information concerning the nature of the flow on gaps resulting from variations in the length-to-depth ( $L/H$ ) ratio, defined by 1, 1/2, 1/3, and 1/4, and on the angle of attack, defined by 10, 15, and 20 degrees. A detailed description of the primary flowfield properties, such as velocity, density, pressure and temperature, and of the aerodynamic surface properties, such as number flux, pressure coefficient, heat transfer coefficient and skin friction coefficient, was presented by a numerical method that properly accounts for non-equilibrium effects. Overall performance results for the gaps are compared with those obtained on a flat plate without gaps for the corresponding angle of attack.

It was observed that the gap  $L/H$  ratio did not disturb significantly the primary flowfield properties far upstream and far downstream, as compared to the freestream mean free path, and the domain of influence along the upstream and downstream surfaces outside the gap did not increase with increasing the  $L/H$  ratio as well as the angle of attack. Conversely, significant changes in the primary flowfield properties were observed inside the gaps with increasing the angle of attack of the flow.

It was found that the flow topology inside the gap with incidence is slightly different from that for zero-degree angle of incidence. The analysis showed that the recirculation region inside the gaps is a function of the  $L/H$  ratio. For the  $L/H$  of 1, the flow structure was characterized by a primary vortex system, with the recirculation region filling the entire gaps, similar to that for the zero-degree angle of incidence. For the  $L/H < 1$ , it was observed that the recirculation region does not fill the entire gaps, and a second recirculation region was formed with increasing the angle of attack, in contrast to that for zero-degree angle of incidence. In addition, even at incidence, the gap flow topology observed here in a rarefied environment differs from that usually observed in the continuum flow regime, as showed in Chapter 1, for the conditions investigated in this work.

Also of great significance in this study was the heat flux to and forces acting on the gap surface, due to pressure and shear stress. The results showed that both depended on the  $L/H$  ratio and the angle of attack  $\alpha$ , for the range investigated. It was found that the maximum values for the heat transfer, pressure and skin

friction coefficients inside the gaps took place on the gap forward face. Maximum values for pressure coefficient  $C_p$  are around 3.76, 1.54, 1.40, and 1.33 times larger than the peak values for a smooth surface at 0, 10, 15, and 20 degrees of incidence, respectively. It was also found that, maximum values for heat transfer coefficient inside the gaps increased with increasing the angle of attack. Nevertheless, it was observed that these maximum values are smaller than those observed in a flat-plate without gap for the corresponding angle of attack. Consequently, in terms of heat flux, the presence of the gaps on the vehicle surface can be ignored in the vehicle design. Conversely, in terms of pressure, the presence of the gaps on the vehicle surface can not be ignored in the vehicle design.

## 6.2 Future Work

The present work has described an initial investigation on discontinuities on the surface of hypersonic vehicles represented by a rarefied hypersonic flow over a gap at incidence. Although this investigation has taken into account a representative range for the  $L/H$  ratio and angle of attack  $\alpha$ , a number of improvements to a realistic investigation on surface discontinuities is still desirable.

In this investigation, diffuse reflection was used as the gas-surface interaction model. This model assumes that the molecules are reflected equally in all directions, quite independently of their incident speed and direction. However, as a space flight vehicle is exposed to a rarefied environment over a considerable time, a departure from the diffuse model is observed, resulting from the colliding molecules that clean the surface of the vehicle, which becomes gradually decontaminated. Molecules reflected from clean surfaces show lobular distribution in direction. In this way, incomplete surface accommodation effects might provide more insight into the sensitivity of the aerodynamic surface properties to gas-surface model.

The DSMC method has been used to assess the flowfield structure on the gap by considering constant wall temperature. In a realistic design, temperature not only changes along the body surface but also inside the gap. In this scenario, simulations that take into account the conjugate heat transfer problems seems to be a challenge.

Finally, chemical reaction effect, Mach number effect, as well geometrical effect, i.e., blunt leading edge, different length for the distance  $L_u$  in front of the gap or different geometric combinations, seems to be important.

## REFERENCES

- ABE, T. Generalized scheme of the no-time-counter scheme for the DSMC in rarefied gas flows analysis. **Computers and Fluids**, Elsevier, v. 22, n. 2, p. 253–257, 1993. 28, 49
- AKIRA, S. **Introduction to practice of molecular simulation**. [S.l.]: Elsevier Inc., 2011. 15
- ALDER, B. J.; WAINWRIGHT, T. E. Studies in molecular dynamics. **Journal of Chemical and Physics**, v. 31, n. 2, p. 459–466, 1957. 15
- \_\_\_\_\_. Molecular dynamics by electronic computers. **Transport Processes in Statistical Mechanics**, Ed. I. Prigogine, New York, Interscience, v. 27, p. 97–131, 1958. 15
- ALEXANDER, F. J.; GARCIA, A. J.; ALDER, B. J. Cell size dependence of transport coefficients in stochastic particle algorithms. **Physics of Fluids**, v. 10, p. 1540–1542, 1998. 17
- \_\_\_\_\_. Erratum: Cell size dependence of transport coefficients in stochastic particle algorithms. **Physics of Fluids**, v. 12, p. 731, 2000. 17, 50
- ANDERSON, J. D. **Hypersonic and high temperature gas dynamics**. New York: McGraw-Hill, 1989. 40
- ATKINSON, N. Best images from sts-134, endeavours final mission, part 1. **Space and astronomy news**, 2015. 2
- ATVARS, K.; KNOWLES, S. A. R. K.; LAWSON, N. J. Experimental and computational investigation of an "open" transonic flow. **Aerospace Engineering**, p. 357, 2009. 7
- BERGEMANN, F.; BOYD, I. D. Rarefied gas dynamics: theory and simulation: new discrete vibrational energy model for the direct simulation Monte Carlo. **Progress in Astronautics and Aeronautics**, p. 174–183, 1994. 35
- BERTIN, J. J.; CUMMINGS, R. M. Critical hypersonic aerothermodynamic phenomena. **Annual Review of Fluid Mechanics**, v. 38, p. 129–157, 2006. 2
- BERTIN, J. J.; GOODRICH, W. D. Aerodynamic heating for gaps in laminar and transitional boundary layers. In: AIAA AEROSPACE SCIENCES MEETING

AND EXHIBIT, 18th., 1980, Houston, Texas. **Proceedings...**  
Pasadena, CA, U.S.A., 1980. 8

BERTIN, J. J.; KEISNER, A. Effect of step and/or gap tile misalignment on shuttle transition. **Aerospace Engineering Report**, NASA-CR-151833, n. 79N10118, 1978. 7

BERTRAM, M. H.; WIGGS, M. M. Effect of surface distortions on the heat transfer to a wing at hypersonic speeds. **AIAA Journal**, v. 1, n. 6, p. 1313–1319, 1963. 7

BERTRAN, M. H.; WEINSTEIN, L. M.; CARY JR., A. M.; ARRINGTON, J. P. Heat transfer to wavy wall in hypersonic flow. **AIAA Journal**, v. 5, n. 10, p. 1767–1767, 1967. 7

BIRD, G. Direct simulation and the Boltzmann equation. **Physics of Fluids**, AIP Publishing, v. 13, n. 11, p. 2676, 1970. 16

\_\_\_\_\_. Monte-Carlo simulation in an engineering context. **Progress in Astronautics and Aeronautics**, v. 74, p. 239–255, 1981. 23, 25

\_\_\_\_\_. Perception of numerical methods in rarefied gasdynamics. **Progress in Astronautics and Aeronautics**, v. 117, p. 211–226, 1989. 28

\_\_\_\_\_. A criterion for the breakdown of vibrational equilibrium in expansions. **Physics of Fluids**, AIP Publishing, v. 14, n. 5, p. 1732–1735, 2002. 36

\_\_\_\_\_. A comparison of collision energy-based and temperature-based procedures in DSMC. In: INTERNATIONAL SYMPOSIUM ON RAREFIED GAS DYNAMICS, 26th. **Proceedings...** Kyoto, Japan: Edited by T.Abe, 2008. v. 1084, p. 245–250. 34, 36, 38, 45

BIRD, G.; LEVIN, D. A.; WYSONG, I. J.; GARCIA, A. L. Chemical reactions in DSMC. In: AIP CONFERENCE, 1th. **Proceedings...** Pacific Grove, EUA: American Institute of Physics, 2011. v. 1333, p. 1195. 36

BIRD, G. A. Molecular gas dynamics. **Annual Review of Fluid Mechanics**, [S.l.]: Clarendon Press, Oxford, 1976. 16, 28

\_\_\_\_\_. Low-density aerothermodynamics. **Progress in Astronautics and Aeronautics**, v. 103, 1986. 14, 17, 23, 45

\_\_\_\_\_. **Molecular gas dynamics and the Direct Simulation of gas flows.** [S.l.]: Clarendon Press, Oxford, 1994. 16, 17, 18, 20, 21, 22, 26, 32, 34, 35, 37, 44, 47, 50, 51, 57, 110

\_\_\_\_\_. **The DSMC Method, version 1.2.** [S.l.]: The university of Sydney, 2013. 16, 24, 36, 38, 40

BOGDONOFF, S. M.; KEPLER, C. E. Separation of a supersonic turbulent boundary layer. **Journal of the Aeronautical Sciences**, v. 22, n. 6, p. 414–430, 1955. 7

BORGNAKKE, C.; LARSEN, P. Statistical collision model for Monte Carlo simulation of polyatomic gas mixture. **Journal of Computational Physics**, v. 18, p. 405–420, 1975. 31, 44

BOYD, I. D. Analysis of rotational nonequilibrium in standing shock waves of nitrogen. **AIAA Journal**, v. 28, n. 11, p. 1997–1999, 1990a. 34, 45

\_\_\_\_\_. Monte Carlo study of vibrational relaxation process. **17th Int. Symposium on Rarefied Gas Dynamics**, Ed. A. E. Beylich, p. 792–799, 1990b. 34

\_\_\_\_\_. Rotational and vibrational nonequilibrium effects in rarefied hypersonic flow. **Journal of Thermophysics and Heat Transfer**, v. 4, p. 478–484, 1990c. 34

\_\_\_\_\_. Rotational-translational energy transfer in rarefied nonequilibrium flows. **Physics of Fluids**, A2(3), p. 447–452, 1990d. 34, 35

\_\_\_\_\_. Analysis of vibrational-translational energy transfer using the direct simulation Monte Carlo method. **Physics of Fluids**, A3(7), p. 1785–1791, 1991. 35

\_\_\_\_\_. Computation of hypersonic flows using the direct simulation Monte Carlo method. **Journal of Spacecraft and Rockets**, v. 52, n. 1, p. 38–53, 2014. 28, 38, 39, 40

BOYD, I. D.; CHEN, G.; CANDLER, G. V. Prediction failure of the continuum fluid equations in the transition hypersonic flows. **Physics of Fluids**, v. 7, n. 1, p. 210–219, 1995. 14

BREWER, R. A.; SAYDAH, A. R.; NESTLER, D. E.; E., F. D. Thermal performance evaluation of RSI panel gaps for space shuttle orbiter. **Journal of Spacecraft**, v. 10, n. 1, p. 23–28, 1973. 7

BURNETT, D. The distribution of molecular velocities and the mean motion in a non-uniform gas. In: LONDON MATHEMATICAL SOCIETY. **Proceedings...** London, 1936. p. 382–435. 14

CATLETT, M. R. **Flow Induced Noise from Turbulent Flow over Steps and Gaps**. — Virginia Polytechnic Institute and State University, 2010. 7

CERCIGNANI, C. The Boltzmann equation and its applications. **Springer-Verlag**, New York, 1988. 15, 40, 44

CHAPMAN, S.; COWLING, T. G. **The mathematical theory of non-uniform gases**. [S.l.]: Cambridge University press, 1970. 14

CHENG, H. K.; EMMANUEL, G. Perspective on hypersonic nonequilibrium flows. **AIAA Journal**, v. 33, n. 3, p. 385–400, 1995. 15

COMEAX, K. A.; MACCORMACK, R. W.; CHAPMAN, D. R. An analysis of the Burnett equations based on the second law of thermodynamics. In: AIAA AEROSPACE SCIENCE MEETING AND EXHIBIT, 33rd. **Proceedings...** [S.l.]: AIAA Paper 95-0415, 1995. 14, 15

CYRIL, G.; BOYD, I. D. An analysis of the convergence of the direct simulation Monte Carlo method. **Computational Physics**, n. 281, p. 449–472, 2015. 51

DEEPAK, N. R.; GAI, S. L.; NEELY, A. J. A computational study of high enthalpy flow over a rearward facing step. In: AIAA AEROSPACE SCIENCES MEETING INCLUDING THE NEW HORIZONS FORUM AND AEROSPACE EXPOSITION, 48th. **Proceedings...** Orlando, FL, 2010. 130

DOGRA, V. K.; MOSS, J. N.; PRICE, J. M. Rarefied flow past a flat plate at incidence. **Rarefied gas dynamics: Theoretical and computational techniques, Progress in Astronautics and Aeronautics**, Edited by E. P. Muntz, D. P. Weaver, and D. H. Campbell, v. 118, p. 567–581, 1989. 52, 53, 54, 62, 64, 65

DOMINIK, M.; JÜRIG, H. **AB Initio molecular dynamics: Basic theory and advanced methods**. [S.l.]: Cambridge University Press, 2009. 15

DUNAVANT, J. C.; THROCKMORTON, D. A. Aerodynamic heat transfer to RSI tile surfaces and gap intersections. **Journal of Spacecraft and Rockets**, v. 11, p. 437–440, 1974. 7, 8

ESTEVE, M.; REULET, P.; MILLAN, P. Flow field characterisation within a rectangular cavity. In: INTERNATIONAL SYMPOSIUM APPLICATIONS OF LASER TECHNIQUES TO FLUID MECHANICS, 10th. **Proceedings...** [S.l.], 2000. 7

EVERHART, J. L.; ALTER, S. J.; MERSKI, N. R.; WOOD, W. A.; PRABHU, R. K. Pressure gradient effects on hypersonic flow heating. In: AIAA AEROSPACE SCIENCES MEETING AND EXHIBIT, 44th. **Proceedings...** [S.l.]: Paper 2006-0185, 2006. 7, 9, 10, 135

FISCKO, K. A.; CHAPMAN, D. R. Hypersonic shock structure with Burnett terms in the viscous stress and heat transfer. **AIAA Thermophysics, Plasmadynamics and Lasers Conference**, 1988. 14

\_\_\_\_\_. Comparison of Burnett, super-Burnett and Monte Carlo solutions for hypersonic shock structure, rarefied gas dynamics: Theoretical and computational techniques. **AIAA Progress in Astronautics and Aeronautics**, Paper 88-2733, v. 118, p. 374–395, 1989. 14

FRENKEL, D.; SMIT, B. **Understanding molecular simulation from algorithms to applications**. [S.l.]: Computational Science Series, 2009. 15

GAD-EL-HAK, M. The fluid mechanics of microdevices the freeman scholar lecture. **Journal of Fluids Engineering.**, v. 121, n. 5, p. 5–33, 1999. 6

GADD, G. E. A theoretical investigation of laminar separation in supersonic flow. **Journal of the Aeronautical Sciences**, v. 24, n. 10, p. 759–784, 1957. 7

GAI, S.; MILTHORPE, J. F. Hypersonic high-enthalpy flow over a blunt-stepped cone. In: AIAA, V.1, 20th. **Proceedings...** [S.l.]: International Symposium on Shock Waves, 1995. p. 234–244. 7

GROTOWSKY, I. M. G.; BALLMANN, J. Numerical investigation of hypersonic step-flows. **Shock Waves**, v. 10, p. 57–72, 2000. 7

GUPTA, R.; SCOTT, C.; MOSS, J. Rarefied gas dynamics: Thermal design of aeroassisted orbital transfer vehicles, progress in astronautics and aeronautics. Ed. H. F. Nelson, v. 96, p. 465–490, 1985. 112

- HAO, J.; WANG, M.; JI, M.; WANG, K. Flow noise induced by small gaps in low-Mach-number turbulent boundary layers. **Physics of Fluids**, n. 25, 2013. 7
- HARVEY, J. K. Direct Simulation Monte Carlo method and comparison with experiment, rarefied gas dynamics: Thermophysical aspect of re-entry flows. **Progress in Astronautics and Aeronautics, AIAA**, Washington, DC, v. 103, p. 25–43, 1986. 16
- \_\_\_\_\_. A review of a validation exercise on the use of the DSMC method to compute viscous/inviscid interaction in hypersonic flow. In: AIAA THERMOPHYSICS CONFERENCE, 36th. **Proceedings...** Orlando: Paper 2003-3643, 2003. 16
- HARVEY, J. K.; GALLIS, M. A. Review of code validation studies in high-speed low-density flows. **Journal of Spacecraft and Rockets**, v. 37, p. 8–20, 2000. 16
- HASSAN, H. A.; HASH, D. B. A generalized hard-sphere model for Monte Carlo simulation. **Physics of Fluids A: Fluid Dynamics**, AIP Publishing, v. 5, n. 3, p. 738–744, 1993. 35
- HAVILAND, J. K. The solution of two molecular flow problems by the Monte Carlo method. **Methods in Computational Physics**, v. 4, p. 109–209, 1965. 15
- HAVILAND, J. K.; LAVIN, M. L. Application of Monte Carlo method to heat transfer in rarefied gases. **Physics of Fluids**, v. 5, p. 1399–1405, 1962. 15
- HINDERKS, M.; RADESPIEL, R.; GULHAN, A. Simulation of hypersonic gap flow with consideration of fluid structure interaction. In: AIAA FLUID DYNAMICS CONFERENCE AND EXHIBIT, 34th. **Proceedings...** [S.l.]: AIAA Paper 2004-2238, 2004. 7, 8
- HINDERSKS, M.; RADESPIEL, R. Investigation of hypersonic gap flow of a reentry nose cap with consideration of fluid structure interaction. In: AIAA AEROSPACE SCIENCES MEETING AND EXHIBIT, 44th. **Proceedings...** [S.l.]: AIAA Paper 2006-0188, 2006. 7
- HIRSCHFELDER, J. O.; CURTISS, C. F.; BIRD, R. B. **Molecular theory of gases and liquids**. New York, EUA: Wiley, 1954. 27
- HOLDEN, M.; P., W. T. A review of experimental studies for DSMC and Navier-Stokes code validation in laminar regions of shock/shock and shock/boundary layer interaction including real gas effects in hypervelocity flows. **Progress in Astronautics and Aeronautics, AIAA**, 2003. 16

- JACKSON, A. P.; SOLTANI, S.; HILLIER, R. Estudy of two- and three-dimensional separation at hypersonic speeds. In: AIAA AEROSPACE SCIENCES MEETING AND EXHIBIT, 37th. **Proceedings...** London, 1999. 7
- JAKUBOWSKI, A. K.; LEWIS, C. H. Experimental study of supersonic laminar base flow with and without suction. **AIAA Journal**, v. 11, n. 12, p. 1670–1677, 1973. 7
- KANNENBERG, K. C.; BOYD, I. Strategies for efficient particle resolution in the direct simulation Monte Carlo method. **Computational Physics**, v. 157, p. 727–745, 2000. 50
- KEON-YOUNG, Y.; AGARWAL, R. K.; BALAKRISHNAN, R. Beyond Navier-Stokes: Burnett equations for flows in the continuum-transition regime. **Physics of Fluids**, v. 13, n. 10, p. 3061–3086, 2001. 14
- KIM, H. D.; SETOGUCHI, T. Shock-induced boundary layer separation. In: INTERNATIONAL SYMPOSIUM ON EXPERIMENTAL AND COMPUTATIONAL AEROTHERMODYNAMICS OF INTERNAL FLOWS, 8th. **Proceedings...** Lyon, France, 2007. 130
- KOURA, K. Null-collision technique in the direct simulation Monte Carlo method. **Physics of Fluids**, AIP Publishing, v. 29, n. 11, p. 3509–3511, 1986. 28
- \_\_\_\_\_. Improved null-collision technique in the direct simulation Monte Carlo method: application to vibrational relaxation of nitrogen. **Computers and Mathematics with Applications**, Elsevier, v. 35, n. 1, p. 139–154, 1998. 28
- LEE, C. J. Unique determination of solutions to the Burnett equations. **AIAA Journal**, v. 32, n. 4, p. 985–990, 1994. 14
- LEITE, P. **Direct molecular simulation of step influence on a reentry vehicle surface**. 164 p. Master Thesis in Engineering and Space Technology - Combustion and Propulsion — National Institute for Space Research, São José dos Campos- SP, Brazil, 2009. Disponível em: <<http://urlib.net/8JMKD3MGP8W/35TNLKS>>. 39
- LENGRAND, J.; ALLÉGRE, J.; CHPOUN, A.; RAFFIN, M. Rarefied hypersonic flow over a sharp flat plate: Numerical and experimental results. In: RAREFIED GAS DYNAMICS: SPACE SCIENCES AND ENGINEERING, PROGRESS IN ASTRONAUTICS AND AERONAUTICS, V.160. **Proceedings...** Meudon, France: B. D. Shizgal and D. P. Weaver, 1992. p. 276–284. 52, 53, 54, 62, 63

LIN, L.-S.; CHEN, Y.-C.; LIN, C.-A. Multi relaxation time lattice Boltzmann simulations of deep lid driven cavity flows at different aspect ratios. **Computers and Fluids**, p. 233–240, 2011. 7

LIU, N.; YIN-KWEE, E. N. The impacts of the-step size in the application of the direct simulation Monte Carlo method to ultra thin gas film lubrication. **Journal of Micromechanics and Microengineering**, v. 12, p. 567–573, 2002. 18

LORD, J. A.; MATES, R. E. Rotational relaxation in nonpolar diatomic gases. **Physics of Fluids**, AIP Publishing, v. 13, n. 2, p. 291–308, 1970. 34

LORD, R. Application of the Cercignani-Lampis scattering kernel to direct simulation Monte Carlo method. In: 158 INTERNATIONAL SYMPOSIUM ON RAREFIED GAS DYNAMICS, 17th. **Proceedings...** Aachen, Germany: Edited by ED.A.E.Beylich, 1991. p. 1427–1433. 38

\_\_\_\_\_. Some extensions to the Cercignani–Lampis gas-surface scattering kernel. **Physics of Fluids A: Fluid Dynamics**, AIP Publishing, v. 3, n. 4, p. 706–710, 1991. 38

\_\_\_\_\_. Direct simulation of rarefied hypersonic flow over a flat plate with incomplete surface accommodation. **Progress in Astronautics and Aeronautics**, American Institute of Aeronautics and Astronautics, v. 160, p. 221, 1994. 38

LUMPKIN; E., F.; HAAS, B. L.; BOYD, I. D. Resolution of differences between collision number definitions in particle and continuum simulations. **Physics of Fluids**, A3(9), p. 2282–2284, 1991. 34

LUMPKIN III, F. E.; CHAPMAN, D. R. Accuracy of the Burnett equations for hypersonic real gas flows. **Journal of Thermophysics and Heat Transfer**, v. 6, n. 3, p. 419–425, 1992. 14

MAZAHERI, A.; WOOD, W. A. Heating augmentation for short hypersonic protuberances. **Journal of Spacecraft and Rockets**, v. 2, p. 284–291, 2009. 7

McCARTY, J. Hypersonic blunt-body gas dynamics. **Modern Development Gas Dynamics**, Edited by W. H. T. Loh, Plenum press, New York, p. 183–234, 1969. 6

MILLIKAN, R. C.; WHITE, D. R. Systematics of vibrational relaxation. **The Journal of Chemical Physics**, AIP Publishing, v. 39, n. 12, p. 3209–3213, 2004. 37

- NANBU, K. Theoretical basis of the direct simulation Monte Carlo method. In: INTERNATIONAL SYMPOSIUM ON RAREFIED GAS DYNAMICS, 15th. **Proceedings...** Grado, Italy, 1986. p. 369–383. 28
- NANCE, R. P.; WILMOTH, R. G.; HASSAN, H. A. Comparison of grid-definition schemes for Monte Carlo simulations. **Thermophysics and Heat Transfer**, AIAA paper 96-1812, New Orleans, Louisiana, v. 11, n. 2, p. 296–303, 1997. 50
- NARIS, S.; VALOUGEORGIS, D. The driven cavity flow over the whole range of the Knudsen number. **Physics of Fluids**, v. 097106, n. 17, 2005. 7
- NESTLER, D. E.; SAYDAH, A. R.; AUXER, W. L. Heat transfer to steps and cavities in hypersonic turbulent flow. **AIAA Journal**, v. 7, n. 7, p. 1368–1370, 1969. 7
- NICOLL, K. M. A study of laminar hypersonic cavity flows. **AIAA Journal**, v. 2, n. 9, p. 1535–1541, 1964. 7
- OHMACHI, Y.; SUZUKI, K. Study on hypersonic flow over flat plate with channels. **American Institute of Aeronautics and Astronautics**, p. 27–30, 2011. 7
- OLYNICK, D. P.; MOSS, J. N.; HASSAN, H. A. Grid generation and adaptation for the direct simulation Monte Carlo method. **Thermophysics and Heat Transfer**, v. 3, n. 4, p. 368–373, 1989. 49
- ORAN, E.; OH, C.; CYBYK, B. Direct Simulation Monte Carlo: Recent advances and applications. **Annual Review of Fluid Mechanics**, v. 30, n. 1, p. 403–441, 1998. 20
- PALMER, G. E.; PULSONETTI, M.; WOOD, W. A.; ALTER, S.; GNOFFO, P.; TANG, C. Computational assessment of thermal protection system damage experienced during sts-118. **Journal of Spacecraft and Rockets**, v. 46, n. 6, p. 1110–1116, 2009. 3
- PAOLICCHI, L. T. L. C. **Direct molecular simulation of step influence on a reentry vehicle surface**. Master Thesis in Engineering and Space Technology - Combustion and Propulsion — National Institute for Space Research, São José dos Campos- SP, Brazil, 2010. 9, 11, 19, 47, 48, 82, 85, 90, 94, 97, 102, 106, 118
- PARKER, J. Rotational and vibrational relaxation in diatomic gases. **Physics of Fluids**, AIP Publishing, v. 2, n. 4, p. 449–462, 2004. 34

PATIL, D. V.; LAKSHMISHA, k. N.; ROGG, B. Lattice Boltzmann simulation of lid-driven flow in deep cavities. **Computers and Fluids**, v. 35, p. 1116–1125, 2006. 7, 9

PIEKOS, E. **DSMC modeling of micromechanical devices**. PhD Thesis — Massachusetts Institute of Technology, 1995. 38

PIEKOS, E.; BREUER, K. Numerical modeling of micromechanical devices using the direct simulation Monte Carlo method. **Journal of Fluids Engineering**, American Society of Mechanical Engineers, v. 118, n. 3, p. 464–469, 1996. 40

PRASANTH, P.; KAKKASSERY, J. K. Molecular models for simulation of rarefield gas flows using direct simulation Monte Carlo method. **Fluid Dynamics Research**, Elsevier, v. 40, n. 4, p. 233–252, 2008. 20, 22, 25, 26

PULLIN, D. I.; HARVEY, J. K. Direct simulation calculations of the rarefied flow past a forward-facing step. **AIAA Journal**, v. 15, n. 1, p. 124–126, 1977. 7

RAULT, D. F. G. Aerodynamic of the shuttle orbiter at high altitude. **Spacecraft and Rockets**, v. 31, n. 6, p. 944–952, 1994. 49

RIEFFEL, M. A. A method for estimating the computational requirements of DSMC simulations. **Journal of Computational Physics**, v. 149, p. 95–113, 1999. 51

ROM, J.; SEGNER, A. Laminar heat transfer to a two-dimensional backward facing step from the high-enthalpy supersonic flow in the shock tube. **AIAA Journal**, v. 2, n. 2, p. 251–255, 1964. 7

SCANLON, T.; WHITE, C.; SCHUEBLER, M.; BROWN, R.; REESE, J. Thermochemistry modelling in an open-source DSMC code. In: INTERNATIONAL SYMPOSIUM ON SHOCK WAVES, 28th. **Proceedings...** Manchester, U.K., 2011. 36, 38

SCOTT, C. D.; MARAIA, R. J. Gap heating with pressure gradients. In: AIAA THERMOPHYSICS CONFERENCE, 14th. **Proceedings...** Orlando, FL., USA: AIAA, 1979. 7, 8

SHEN, C. **Rarefied gas dynamics: fundamentals, simulations and micro-flows**. New York, EUA: Springer Science & Business Media, 2006. 23

SHU, C.; MAO, X. H.; CHEW, Y. Particle number per cell and scaling factor effect on accuracy of DSMC simulation of micro flows. **International Journal of**

**Numerical Methods of Heat and Fluid Flow**, Emerald Group Publishing Limited, v. 15, n. 8, p. 827–841, 2005. 46

SOHN, I.; LEVIN, D.; MODEST, M. Closely-coupled DSMC hypersonic re-entry flow simulations with photon Monte Carlo radiation. In: AIAA AEROSPACE SCIENCES MEETING INCLUDING THE NEW HORIZONS FORUM AND AEROSPACE EXPOSITION, 44th. **Proceedings...** Orlando, Florida, 2010. 49

TANNEHILL, J. C.; EISLER, G. R. Numerical computation of the hypersonic leading edge problem using the Burnett equations. **Physics of Fluids**, 1976. 14

TOKUMASU, T.; MATSUMOTO, Y. Dynamic molecular collision (DMC) model for rarefied gas flow simulations by the DSMC method. **Physics of Fluids**, AIP Publishing, v. 11, n. 7, p. 1907–1920, 1999. 53

TRAINEAU, J. C.; THIVET, F.; GULHAN, A.; COSSON, E.; SMITH, A.; MARRAFFA, L. Synthesis of the gap heating analysis of the hyflex flight. In: EUROPEAN SYMPOSIUM ON AEROTHERMODYNAMICS FOR SPACE VEHICLES, 50th. **Proceedings...** Cologne, Germany: European Space Agency, 2005. v. 563, p. 635. 7, 9

TSUBOI, N.; MATSUMOTO, Y. DSMC simulation with gas-surface interaction models in hypersonic rarefied flow. **American Institute of Physics, Rarefied Gas Dynamics: 22th International Symposium.**, p. 331–338, 2001. 62

TSUBOI, N.; YAMAGUCHI, H.; MATSUMOTO, Y. Direct Simulation Monte Carlo method on rarefied hypersonic flow around flat plates. **Journal of Spacecraft and Rockets**, v. 41, n. 3, p. 397–405, 2004. 53, 54, 62, 63

VICENTI, W.; KRUGER, C. **Introduction to physical gas dynamics**. New York, EUA: Wiley, 1967. 27

WAGNER, W. A. Convergence proof for bird's direct simulation Monte Carlo method for the Boltzmann equation. **Journal of Statistical Physics**, 1992. 16

WEI, N.; McNamara, J. J.; FRIEDMANN, P. P.; WAAS, A. M. Thermomechanical behavior of damaged TPS including hypersonic flow effects. In: AIAA/AHI SPACE PLANES AND HYPERSONIC SYSTEMS AND TECHNOLOGIES CONFERENCE, 14th. **Proceedings...** [S.l.]: University of Michigan, 2006. 7

WEINSTEIN, I.; AVERY, D. E.; CHAPMAN, A. J. Aerodynamic heating to the gaps and surfaces of simulated reusable-surface-insulation tile arrays in turbulent

flow at Mach 6.6. **NASA TECHNICAL MEMORANDUM**, 1975. NASA TM X-3225. 7, 8

\_\_\_\_\_. \_\_\_\_\_. **NASA TM, National and Space Administration**, Washington, p. X-3225, 1975. 7

WILMOTH, R. G.; LEBEAU, G. J.; CARLSON, A. B. DSMC grid methodologies for computing low-density, hypersonic flows about reusable launch vehicles. In: **AIAA THERMOPHYSICS CONFERENCE**, 31st. **Proceedings...** New Orleans, Louisiana: AIAA paper 96-1812, 1996. p. 17–20. 50

WU, Q.; ZHONG, Y.; YU, S.; HU, J. An iterative method for unstructured dynamic-grid using springs based on LU-SGS. **Computational Physics**, 2009. 49

XU, J.; HUANG, H.; HUANG, G.; MO, S. Numerical simulation of supersonic gap flow. **PLOS ONE**, v. 10, n. 1, p. 16, 2015. 7, 11

XUE, H.; FAN, Q.; SHU, C. Prediction of micro-channel flows using direct simulation Monte Carlo. **Probabilistic Engineering Mechanics**, Elsevier, v. 15, n. 2, p. 213–219, 2000. 38, 41

YEN, S. M. Monte carlo solutions of nonlinear Boltzmann equation for problems of heat transfer in rarefied gases. **International Journal of Heat and Mass Transfer**, 1971. 16

\_\_\_\_\_. Numerical solution of the nonlinear Boltzmann equation for nonequilibrium gas flow problems. **Annual Review of Fluid Mechanics**, 1984. 16

YOSHIO, S. **Molecular Gas Dynamics: Theory, Technique, and Applications**. [S.l.]: Birkhäuser Physics, 2007. 16

ZDANSKI, P.; ORTEGA, M.; NIDE, G.; JR, F. On the flow over cavities of large aspect ratio: A physical analysis. **International Communications in Heat and Mass Transfer**, v. 33, p. 458–466, 2006. 7

ZHANG, C.; SCHWARTZENTRUBER, T. E. Robust cut-cell algorithms for DSMC implementations employing multi-level cartesian grids. **Computers and Fluids**, v. 69, p. 122–135, 2012. 49

ZHONG, X.; MCCORMACK, R. W.; CHAPMAN, D. R. Stabilization of the Burnett equations and application to hypersonic flows. **AIAA Journal**, 1993. 14

## **PUBLICAÇÕES TÉCNICO-CIENTÍFICAS EDITADAS PELO INPE**

### **Teses e Dissertações (TDI)**

Teses e Dissertações apresentadas nos Cursos de Pós-Graduação do INPE.

### **Manuais Técnicos (MAN)**

São publicações de caráter técnico que incluem normas, procedimentos, instruções e orientações.

### **Notas Técnico-Científicas (NTC)**

Incluem resultados preliminares de pesquisa, descrição de equipamentos, descrição e ou documentação de programas de computador, descrição de sistemas e experimentos, apresentação de testes, dados, atlas, e documentação de projetos de engenharia.

### **Relatórios de Pesquisa (RPQ)**

Reportam resultados ou progressos de pesquisas tanto de natureza técnica quanto científica, cujo nível seja compatível com o de uma publicação em periódico nacional ou internacional.

### **Propostas e Relatórios de Projetos (PRP)**

São propostas de projetos técnico-científicos e relatórios de acompanhamento de projetos, atividades e convênios.

### **Publicações Didáticas (PUD)**

Incluem apostilas, notas de aula e manuais didáticos.

### **Publicações Seriadas**

São os seriados técnico-científicos: boletins, periódicos, anuários e anais de eventos (simpósios e congressos). Constam destas publicações o Internacional Standard Serial Number (ISSN), que é um código único e definitivo para identificação de títulos de seriados.

### **Programas de Computador (PDC)**

São a seqüência de instruções ou códigos, expressos em uma linguagem de programação compilada ou interpretada, a ser executada por um computador para alcançar um determinado objetivo. Aceitam-se tanto programas fonte quanto os executáveis.

### **Pré-publicações (PRE)**

Todos os artigos publicados em periódicos, anais e como capítulos de livros.